

Design and verification of a Hydraulic Air Compressor as a CO₂ capture and
sequestration system.

by

Maryam Mahdavi

A thesis submitted in partial fulfillment
of the requirements for the degree of
Doctor of Philosophy (PhD) in Natural
Resources Engineering

The Office of Graduate Studies
Laurentian University
Sudbury, Ontario, Canada

©Maryam Mahdavi, 2023

THESIS DEFENCE COMMITTEE/COMITÉ DE SOUTENANCE DE THÈSE
Laurentian Université/Université Laurentienne
Office of Graduate Studies/Bureau des études supérieures

Title of Thesis Titre de la thèse	Design and verification of a Hydraulic Air Compressor as a CO ₂ capture and sequestration system		
Name of Candidate Nom du candidat	Mahdavi, Maryam		
Degree Diplôme	Doctor of Philosophy		
Department/Program Département/Programme	Natural Resources Engineering	Date of Defence Date de la soutenance	August 17, 2023

APPROVED/APPROUVÉ

Thesis Examiners/Examineurs de thèse:

Dr. Dean Millar
(Supervisor/Directeur(trice) de thèse)

Dr. Meysar Zeinali
(Committee member/Membre du comité)

Dr. Ramesh Subramanian
(Committee member/Membre du comité)

Dr. Francois Caron
(Committee member/Membre du comité)

Dr. Alex Hutchinson
(Committee member/Membre du comité)

Dr. Michael Hitch
(External Examiner/Examineur externe)

Dr. Jeff Shepperd
(Internal Examiner/Examineur interne)

Approved for the Office of Graduate Studies
Approuvé pour le Bureau des études supérieures
Tammy Eger, PhD
Vice-President Research (Office of Graduate Studies)
Vice-rectrice à la recherche (Bureau des études supérieures)
Laurentian University / Université Laurentienne

ACCESSIBILITY CLAUSE AND PERMISSION TO USE

I, **Maryam Mahdavi**, hereby grant to Laurentian University and/or its agents the non-exclusive license to archive and make accessible my thesis, dissertation, or project report in whole or in part in all forms of media, now or for the duration of my copyright ownership. I retain all other ownership rights to the copyright of the thesis, dissertation or project report. I also reserve the right to use in future works (such as articles or books) all or part of this thesis, dissertation, or project report. I further agree that permission for copying of this thesis in any manner, in whole or in part, for scholarly purposes may be granted by the professor or professors who supervised my thesis work or, in their absence, by the Head of the Department in which my thesis work was done. It is understood that any copying or publication or use of this thesis or parts thereof for financial gain shall not be allowed without my written permission. It is also understood that this copy is being made available in this form by the authority of the copyright owner solely for the purpose of private study and research and may not be copied or reproduced except as permitted by the copyright laws without written authority from the copyright owner.

Abstract

As a result of human activities, the level of atmospheric carbon dioxide (CO₂) has increased. Carbon capture and sequestration (CCS) technologies offer an effective approach for mitigating CO₂ from various industrial process to reduce the global climate change effect. These technologies can be integrated into existing infrastructure with minimal disruption. This study reviews on post-combustion CO₂ capture and sequestration techniques, with a specific focus on mineral carbonation process routes and their potential feedstocks. Mineral carbonation is an approach that mimics the natural weathering of rock, in which metal oxide-bearing materials, for instance natural silicate minerals (serpentine, olivine) react with gaseous CO₂ to form solid carbonates. This process takes place on geological time scales, but it can be accelerated by increasing the concentration of CO₂ in a reactor through pressurization of the system.

The purpose of this study was investigation of technical feasibility of a CCS process by means of a hydraulic air compressor (HAC). A series of experiments were conducted on the HAC pilot plant to investigate the potential of the system as a post-combustion CO₂ capture system. Those experiences experimentally verified a one-dimensional steady-state model for two-phase bubbly flow. The verified bubbly flow model was used to compare the hydrodynamics and mass transfer characteristics of HAC downcomers and upward co-current flow bubble column reactors and to predict gas liquid mass transfer coefficients.

The experimental results showed that the HAC is an effective technology for intensification of CCS processes due to its improved mass transfer performance compared to other mass transfer devices. While the high capital cost of HAC construction, following a general Millar (2014) design

paradigm, limits applicability, the horizontal injector loop (HIL), developed in this thesis offers a new apparatus with similar gas compressor performance and reduced height, which would make the concept more accessible for capital restricted projects.

A mathematical dynamic kinetic model is developed to simulate the kinetics of CO₂ absorption into an alkaline solution in the HIL. This model makes a significant contribution in predicting the absorption rate under operating conditions beyond those achievable in experimental tests undertaken. In addition, this model can be used to guide the design of a new reactor and future experiments, making it a valuable tool for CO₂ capture and sequestration activity.

Carbon dioxide capture and sequestration by means of a HIL as a pressurized, continuous chemical reactor was also investigated experimentally. The experimental results demonstrated that the HIL has a credible potential for this purpose. These experiments were also simulated using the dynamic kinetic model, which showed good agreement with the experimental findings. However, some potential improvements to the dynamic kinetic model have been identified to enhance its compatibility with experimental conditions.

Keywords: CO₂ capture and sequestration, mineral carbonation, hydraulic air compressor, horizontal injector loop, two-phase bubbly flow, dynamic kinetic model

Acknowledgments

First and foremost, I would like to thank my supervisor Dr. Dean Millar for his incredible support and mentorship throughout this project. I was extremely lucky to get to know Dean, as he helped me to be more confident and believe more in myself every day.

I would like to acknowledge my committee members, Dr. Ramesh Subramanian, Dr. Meysar Zeinali, Dr. Alex Hutchison, and Dr. François Caron for their time in helping me to finish my PhD work and reading and reviewing the thesis to improve and enhance its quality.

I am extremely grateful for the financial support I received in the form of Ontario Trillium Scholarship (OTS) from Laurentian University and the government of Ontario. I acknowledge receiving Gordon M. Ritcey PhD award (2022) from MetSoc of CIM (Canadian Institute of Mining, Metallurgy and Petroleum), SRK Consulting scholarship (2022), and Parya Scholarship (2020).

Many thanks to my groupmates and friends in HAC team, Stephen Young and Philip Vipond for so many good memories, nice friendships, and their support. I would like to extend my thankfulness to Dr. Caterina Noula her valuable assistance during my laboratory work. I would also like to thank Greg Lakanen from Laurentian University for his important contributions in fabricating the test rig.

Finally, I owe great gratitude to my family, especially my husband, Mohamad, and my sister, Sanaz, for their unwavering support and encouragement throughout my studies.

This thesis is dedicated to Iranian women and their uncommon bravery in their fight against oppression.

I'm proud to share a fraction of my identity with them.

Table of Contents

Thesis Defense Committee	ii
Abstract	iii
Acknowledgments	v
Table of Contents	vii
List of Figures	xi
List of Tables	xv
List of Appendices	xvii
Nomenclature	xviii
Greek Letters	xix
1. Introduction	1
1.1 Mitigating global CO ₂ emissions	1
1.2 Carbon capture and sequestration	2
1.3 Thesis aim and objectives.	11
1.4 Thesis Structure	13
2. A review of mineral carbonation as a post-combustion carbon capture and sequestration ..	15
2.1 Post-combustion CO ₂ capture and sequestration	15
2.2 A review of mineral carbonation routes and feedstocks	20
2.2.1 Process routes of mineral carbonation	21
2.3 Natural mineral feedstock for mineral carbonation	28
2.3.1 Carbonation potential and efficiency of natural silicate rocks.....	30
2.3.2 Studies of mineral carbonation by neutral silicate materials	31
2.4 Alkaline waste materials	37
2.4.1 Carbonation capacity and efficiency of alkaline waste residues	38
2.4.2 Studies of mineral carbonation by alkaline waste materials	40
2.5 Summary	49
3. The direct aqueous mineral carbonation chemical process.....	50
3.1 Reaction equilibria	51
3.1.1 Carbon species arising when CO ₂ is dissolved in water	51
3.1.2 Dissolution of the minerals into solution	60
3.1.3 Formation of calcium carbonate precipitates: nucleation and growth	67
3.2 Kinetics of the reactions.....	70
3.2.1 Mass transfer of CO ₂ gas into the alkaline solution.....	74
3.2.2 Calcium hydroxide dissolution in water	80
3.2.3 Ionic reactions and precipitation of CaCO ₃	83
3.3 Formulation of a dynamical kinetic model of the reactions	85
3.3.1 The differential equations	85
3.3.2 Verification 1: CO ₂ absorption in NaOH solution	88
3.3.3 Verification 2: CO ₂ absorption into alkaline solution (lime-containing oil shale waste ash).....	91
3.3.4 Verification 3: CaCO ₃ precipitation through direct mixing of Ca(OH) ₂ and a solution of dissolved CO ₂	93
3.4 Summary	96

4.	Hydraulic air compressor as a gas-liquid contactor	98
4.1	Bubble column devices and the mass transfer coefficient	102
4.1.1	Effect of temperature on k_{LA}	105
4.1.2	Effect of gas and liquid velocity on k_{LA}	105
4.1.3	Effect of bubble size on k_{LA}	107
4.1.4	Effect of pressure on k_{LA}	107
4.1.5	Effect of solid concentration on k_{LA}	108
4.1.6	Challenges in estimating mass transfer coefficient in bubble columns	109
4.2	Hydraulic air compressor (HAC) developments	110
4.3	The hydrodynamic and mass transfer bubbly flow model of the HAC	114
4.4	HAC systems as mineral carbonation contactors	115
4.4.1	Isothermal compression	116
4.4.2	Pressure gradient varies with the sense of interphase mass transfers	116
4.4.3	Hydrodynamic and mass transfer of HAC downcomer	117
4.4.4	Back-calculation of k_{LA} for HAC downcomer	123
4.5	Summary	126
5.	The Experimental verification of bubbly flow model of the HAC	128
5.1.1	Approach for model verification	129
5.1.2	Experimental control	132
5.1.3	Details of the auxiliary model for the time evolution of dissolved gas species within HAC systems.	133
5.2	Principal dimensions and process flow diagram	137
5.3	Instrumentation	139
5.3.1	Temperature	139
5.3.2	Pressure	139
5.3.3	Water level	140
5.3.4	Water flow rate	140
5.3.5	Gas flow rate	140
5.3.6	Gas composition	141
5.3.7	Dissolved CO ₂ concentration	141
5.4	Experimental methodology	142
5.4.1	Gas sampling	142
5.4.2	Liquid sampling	142
5.4.3	Experimental procedure	143
5.5	Experimental results	144
5.5.1	HAC process operating conditions	144
5.5.2	CO ₂ additions defining experimental set points	146
5.5.3	Time series of experimental observations of CO ₂ concentrations	147
5.6	Comparison of the experimental data with numerical results	153
5.7	Discussion	165
5.7.1	The effect of pH on the CO ₂ concentration in liquid and gas phases	165
5.7.2	Estimating the values of k_{LA} for Baby HAC downcomer	166
5.7.3	HAC as a CO ₂ capture system	169
5.8	Summary	171

6.	Horizontal injector loop test rig	173
6.1	Review of alternative reactors for CO ₂ capture and sequestration process	174
6.1.1	Batch reactor	174
6.1.2	Fluidized bed reactors	176
6.1.3	Rotating packed bed reactors	177
6.2	Horizontal injector loop	178
6.2.1	Description of process flow of the horizontal injector loop	180
6.2.2	Design characteristics of the HIL	182
6.2.3	Instrumentation	187
6.3	Experimental results of operation of the HIL	191
6.3.1	Pump performance	194
6.3.2	Injector performance	196
6.4	Summary	202
7.	Experimental investigation of CO ₂ capture and sequestration by means of HIL	204
7.1	Experimental procedures for CO ₂ carbonation	205
7.1.1	Purpose of experiment	205
7.1.2	Preparation of circulating liquid solutions/suspensions.....	205
7.1.3	Filling the injector loop with liquid	206
7.1.4	Phase I Start-up and steady state operation without CO ₂ being inducted.....	207
7.1.5	Phase II Steady state operation without CO ₂ being inducted.	207
7.1.6	Phase III Admission of the air/CO ₂ mixture	208
7.1.7	Recovery of precipitate	209
7.2	Experimental results.....	210
7.2.1	CO ₂ dissolution in deionized water.....	212
7.2.2	CO ₂ dissolution in Ca(OH) ₂ saturated solution	214
7.2.3	CO ₂ dissolution in Ca(OH) ₂ suspension solution	216
7.2.4	Summary of results from experimental trials.....	224
7.2.5	Mass of suspension solids at the conclusion of each experimental run.	224
7.2.6	XRD analysis of products	225
7.3	Discussion.....	230
7.3.1	Did the reactor operate as intended?.....	230
7.3.2	Problems evident in the results of the experimental runs.	231
7.4	Summary	233
8.	Dynamic simulation of mineral carbonation experiments	235
8.1	Dynamic kinetic model of carbonation experiments	235
8.1.1	The conditions of the experiments	236
8.1.2	Estimating the values of k_{LA} and enhancement factor	238
8.2	Results of dynamic kinetic model.....	240
8.2.1	CO ₂ dissolution in Ca(OH) ₂ saturated solution	240
8.2.2	CO ₂ dissolution in Ca(OH) ₂ suspension solutions.....	245
8.3	Discussion.....	251
8.3.1	Comparison between experimental and modeled results.....	251
8.3.2	Sensitivity analysis.....	255

8.3.3	Potential improvements to the dynamic kinetic model for better agreement with experimental conditions	259
8.4	Summary	261
9.	Discussion	262
9.1	Summary of purpose or findings of prior chapters	262
9.2	Hydrodynamic and mass transfer comparison of HAC downcomers and upward co-current flow bubble column reactors.	263
9.3	The advantage of HAC downcomer over bubble column	271
9.4	Comparison of the HAC and HIL	272
9.5	The HAC or the HIL as a carbon capture and sequestration device	275
9.5.1	CO ₂ mineralization via HAC/HIL	277
9.5.2	Prospects for commercial scale CO ₂ capture and sequestration	278
10.	Conclusions, contributions, and future work	280
10.1	Conclusions	280
10.2	Original contributions	282
10.3	Future work	284
10.4	PhD Journey: learnings and future directions	285
11.	References	286
	Appendix A: Experimental data	310
	Appendix B: Time series of experimental observations of CO ₂ concentrations for experiments A and B	315
	Appendix C: Sample MATLAB Code	317

List of Figures

Figure 1-1: Different approaches to post-combustion CO ₂ capture technologies (Chiang and Pan, 2017a)	4
Figure 1-2: Different methods of post-combustion CO ₂ sequestration	7
Figure 2-1: The ex-situ mineral carbonation process (Veetil and Hitch, 2020a).....	23
Figure 3-1: Solubility of carbon dioxide in water (temperature, pressure effects)(Dodds <i>et al.</i> , 1956)	52
Figure 3-2: Distribution of carbon species as a function of pH (in the presence of P_{CO_2} of 1 atm, and at ambient temperature of 25 °C) (Fioravante <i>et al.</i> , 2019)	59
Figure 3-3: Standard molar free energy of formation for several carbon-related substance at 298 K (Pan <i>et al.</i> , 2015a)	68
Figure 3-4: Schematic of the direct aqueous mineral carbonation mechanism (Ca(OH) ₂ aqueous solution), modified from (Chiang and Pan, 2017b)	73
Figure 3-5: Two film theory. $P_{j,k}$ and $C_{j,k}$ are the partial pressure and molar concentration gas species j at position k respectively (Young, 2017)	75
Figure 3-6: The variations of CO ₂ concentration of the discharge gas and pH	90
Figure 3-7: The variations of CO ₃ ²⁻ and HCO ₃ ⁻ concentrations	90
Figure 3-8: The variation of Ca ²⁺ , CaCO ₃ , and OH ⁻ concentrations according to the time.....	92
Figure 3-9: The slurry of calcium carbonate.....	94
Figure 3-10: The predicted changes in the concentrations of various species over time.	95
Figure 4-1: A simplest form of the bubble column (Majumder, 2016a)	102
Figure 4-2: Types of bubble column contactors / reactors (Abdul Majeed Saed, 2003; Bai, 2010; Jakobsen, 2014).....	104
Figure 4-3: Schematic of the open and closed looped systems of the HAC (Hutchison, 2018a).....	112
Figure 4-4: Concentration profiles of the gas and liquid in the HAC downcomer predicted by the model.....	119
Figure 4-5: Liquid concentration profile of the gas species at the gas-liquid interface in each section of the downcomer	121
Figure 4-6: Variations of gas and liquid molar flow rates in HAC downcomer predicted by the model.....	122
Figure 4-7: The variation of slip velocity and gas density.....	123
Figure 4-8: The variation of mean bubble diameter and interfacial area available for the gas mass transfer.	124
Figure 4-9: Variation of the mass transfer coefficient of CO ₂ in the HAC downcomer.....	125
Figure 5-1: Schematic of the modern style of the hydraulic air compressor and its control volumes, AWMH: air–water mixing horizon, SOWL: separator operating water level, TOWL: tailrace operating water level	130
Figure 5-2: Schematic diagram of the experimental set-up.	138
Figure 5-3: CO ₂ concentration monitored in gas phase and liquid phase during experiment D. Mass flow rates of CO ₂ added for each of the 7 set points are as consecutively listed in Table 5-2. For each set point, average steady state concentrations were computed over the time durations indicated by the horizontal dashed lines.	148
Figure 5-4: CO ₂ concentration monitored in gas phase and liquid phase during experiment C. Mass flow rates of CO ₂ added for each of the 7 set points are as consecutively listed in	

Table 5-2. For each set point, average steady state concentrations were computed over the time durations indicated by the horizontal dashed lines.	149
Figure 5-5: CO ₂ concentration measured at location c (Figure 5-2) during experiment D. Mass flow rates of CO ₂ added for each of the 7 set points are as consecutively listed in Table 5-2.	150
Figure 5-6: Added CO ₂ mass flow rate to the inlet air versus absolute values of CO ₂ concentration of the evolved gas of tailrace tank through experiment D.	153
Figure 5-7: Flowchart of the dynamic scheme used to predict the steady-state concentrations of experiment set points	155
Figure 5-8: CO ₂ concentration in the discharge gas of the Baby HAC versus CO ₂ concentration in the liquid phase of the separator measured and modelled for experiment D. Dynamic equilibrium predictions of individual set points linked with corresponding measured points with solid line segments.....	157
Figure 5-9: Resulting time series of CO ₂ concentrations in the separator and tailrace liquid and addition rates in the downcomer, separator and tailrace predicted by the dynamic equilibrium scheme with the time series of observed CO ₂ liquid concentrations	159
Figure 5-10: CO ₂ concentration in the discharge gas of the Baby HAC versus CO ₂ concentration in the liquid phase of the separator measured and modelled for experiment D. Dynamic equilibrium predictions of individual set points linked with corresponding measured points with solid line segments.....	161
Figure 5-11: Performance of the dynamic equilibrium prediction of the pilot HAC	163
Figure 5-12: The performance of the Young <i>et al.</i> (2022) bubbly flow model predicting the gauge delivery pressure of the pilot HAC.....	164
Figure 5-13: Concentration profiles of the gas and liquid in the Baby HAC downcomer predicted by the model.....	167
Figure 5-14: Variation of mass transfer coefficient of CO ₂ and interfacial areas of the Baby HAC downcomer.....	168
Figure 5-15: Variation of CO ₂ yield and discharge gauge pressure according to the downcomer length.....	170
Figure 6-1: Schematic diagram of the experimental setup of batch reactor for the CO ₂ capture using Ca(OH) ₂ solution as the absorbent. (1) N ₂ cylinder, (2) CO ₂ cylinder, (3) Mass flow controller, (4) gas mixer, (5) temperature controller, (6) Pyrex reactor, (7) sparser, (8) magnetic stirrer, (9) thermometer, (10) pH sensor, (11) electrical conductivity (EC) sensor, (12) pH/EC meter, (13) dehumidifier, (14) sampling pump, (15) gas analyzer, and (16) computer for data acquisition (Han <i>et al.</i> , 2011d)	175
Figure 6-2: Schematic diagram of the experimental setup of fluidized bed reactor for mineral carbonation of alkaline solid wastes (1) gas cylinder; (2) circulating bath; (3) rotameter; (4) slurry reactor; (5) heating jacket; (6) gas distributor; (7) sampling; (8) thermos couple and pH analyzer; and (9) vent to hood (Chang <i>et al.</i> , 2015).	176
Figure 6-3: Schematic diagram of the experimental setup of rotating packed bed (RPB) for the carbonation of fly ash: (1) high-gravity RPB reactor; (2) stirring heating machine; (3) slurry storage tanks; and (4) pump (Pan <i>et al.</i> , 2013)	178
Figure 6-4: The ejector and venturi gas distributors (Trambouze, 2004).....	179
Figure 6-5: The horizontal injector loop.....	181

Figure 6-6: Mazzei injector(“Mazzei venturi Injectors,” 2022)	183
Figure 6-7: The schematic diagram of the horizontal injector loop.....	185
Figure 6-8: The horizontal injector loop with instrument labels (the cloudy liquid visible in the separator is a solution and suspension of Ca(OH) ₂ that progressive reacts with admitted CO ₂ to form CaCO ₃ as experiments proceed).	186
Figure 6-9: Air & CO ₂ mixing tank and its instruments	189
Figure 6-10: Gas suction flow rate versus water flow rate	193
Figure 6-11: The performance curves of the pump and injector	195
Figure 6-12: Configuration of Mazzei injector	197
Figure 6-13: The injector water flow rate according to the inlet pressure.....	199
Figure 6-14: Inlet pressure and outlet dynamic pressure of the injector versus inlet water flow rate.....	200
Figure 7-1: 5-micron filter showing a white slurry at input and a clear fluid at outlet.....	209
Figure 7-2: Variations of discharge CO ₂ and O ₂ concentrations and pH of the D.I. water throughout phases I to III of the experimental of the experimental trial according to the time	213
Figure 7-3: Variation of discharge CO ₂ concentration and pH of the saturated solution according to the time of the experiment E2.....	216
Figure 7-4: Variation of discharge CO ₂ concentration and pH of the suspension solution (1.7C-S) according to the time of the experiment E3	217
Figure 7-5: Variation of discharge CO ₂ concentration and pH of the 2.2C-S suspension solutions according to the time of the experiment	219
Figure 7-6: Variation of discharge CO ₂ concentration and pH of the 2.9C-S suspension solutions according to the time of the experiment E6	221
Figure 7-7: Variation of discharge CO ₂ concentration and pH of the 5C-S suspension solutions according to the time of the experiment	223
Figure 7-8: XRD patterns of Ca(OH) ₂ powder	227
Figure 7-9: XRD patterns of CaCO ₃ produced in the experiments E2, E5, and E8	229
Figure 8-1: Modeling of the variations of discharge CO ₂ concentration and pH of 1C.F solution according to the time to phase III	242
Figure 8-2: Modeling of the variations of Ca ²⁺ , CaOH ⁺ , and CaCO ₃ concentrations of the 1C.F solution according to the time of phase III	243
Figure 8-3: Modeling of the variations of CO ₂ (aq), HCO ₃ ⁻ , and CO ₃ ²⁻ concentrations of the 1C.F solution according to the time of phase III	244
Figure 8-4: Modeling of the variations of discharge CO ₂ concentration and pH of 2.2C.S suspension solution according to the time phase III of experiments (a) E4 and (b) E5	246
Figure 8-5: Modeling of the variations of Ca ²⁺ , CaOH ⁺ , and CaCO ₃ concentrations of the 2.2C.S solution according to the time of phase III of experiment E5.....	247
Figure 8-6: Modeling of the variations of CO ₂ (aq), HCO ₃ ²⁻ , and CO ₃ ²⁻ concentrations of the 2.2C.S solution according to the time of phase III of experiment E5.....	248
Figure 8-7: Modeling of the variations of discharge CO ₂ concentration and pH of 5C.S solution according to the time of phase III	249
Figure 8-8: Modeling of the variations of the concentrations of Ca ²⁺ , CaCO ₃ , and pH of the 5C.S solution according to the time.....	250

Figure 8-9: Modeling of the variations of $\text{CO}_2(\text{aq})$, HCO_3^{2-} , and CO_3^{2-} concentrations of the 5C.S solution according to the time of phase III	251
Figure 8-10: Mass of absorbed CO_2 and versus the mass of $\text{Ca}(\text{OH})_2$ in the solution.....	253
Figure 8-11: Duration of time to reach $\text{pH}=10$ versus the mass of $\text{Ca}(\text{OH})_2$ in the solution.....	253
Figure 9-1: Concentration profiles of the liquid in the HAC downcomer and bubble column predicted by the model.....	266
Figure 9-2: Concentration profiles of the gas in the HAC downcomer and bubble column predicted by the model.....	267
Figure 9-3: Liquid concentration profile of the gas species at the gas-liquid interface in each section of the downcomer	268
Figure 9-4: Liquid concentration profile of the gas species at the gas-liquid interface in each section of the downcomer	269
Figure 9-5: The variation of slip velocity, gas and liquid velocity in the HAC downcomer and bubble column.....	270
Figure 9-6: The mean bubble diameter and interfacial area of the HAC downcomer and bubble column.....	271

List of Tables

Table 1-1: Advantages and disadvantages of CO ₂ capture technologies modified (Leung <i>et al.</i> , 2014; Rao, 2010; T. Wang <i>et al.</i> , 2017; Y. Wang <i>et al.</i> , 2017; Woodall <i>et al.</i> , 2019)	3
Table 1-2: Summary of different CO ₂ sequestration methods (Bobicki <i>et al.</i> , 2012a; Chiang and Pan, 2017a; IPCC, 2005a; Neeraj and Yadav, 2020; Park <i>et al.</i> , 2016; Sipilä <i>et al.</i> , 2008) ...	8
Table 2-1: Summary of emission gas characteristics from post carbon capture CO ₂ source (“Boiler Combustion,” 2022; Ho <i>et al.</i> , 2019; Ho and Wiley, 2016; IPCC, 2005a; Last and Schmick, 2011; Padurean <i>et al.</i> , 2012; Pavri and Moore, 2007; Pellegrini <i>et al.</i> , 2020; Romano <i>et al.</i> , 2013; Song <i>et al.</i> , 2004)	16
Table 2-2: General advantages and disadvantages of post-combustion CO ₂ capture and sequestration (Chiang and Pan, 2017a; Kolawole, 2019; Singh and Dhar, 2019).....	18
Table 2-3: Summary of mineral carbonation process routes (Bobicki <i>et al.</i> , 2012b; Chiang and Pan, 2017b; Wouter, Huijgen and Comans, 2005)	25
Table 2-4: The essential factors for effective direct aqueous carbonation (Chiang and Pan, 2017a)	27
Table 2-5: Potential mineral rocks for mineral carbonation (King, 2022; Lackner <i>et al.</i> , 1995; Sanna <i>et al.</i> , 2014; Yadav and Mehra, 2021).....	30
Table 2-6: Summary of the significant studies of mineral carbonation using natural minerals (DAC = direct aqueous carbonation, DC = direct carbonation, IC = indirect carbonation, CEA= Chemical extraction agent used for metal leaching).....	34
Table 2-7: The examples of alkaline wastes used as feedstock for mineral carbonation collated from Chiang and Pan (2017a), Doucet (2010a), Li (2016), Sánchez-Cotte <i>et al.</i> (2020) and, Sanna <i>et al.</i> (2012)	38
Table 2-8: Main properties and carbonation conversions of waste materials (DC – direct carbonation, DAC – direct aqueous carbonation, IAC – indirect aqueous carbonation, NW – natural weathering, CRW – cold rolling wastewater, DI – deionized water)(Bobicki <i>et al.</i> , 2012b; Reddy <i>et al.</i> , 2019; Sanna <i>et al.</i> , 2014a)	41
Table 3-1: Parameters and constants used in the dynamical kinetic model (Lee <i>et al.</i> , 2021; Na <i>et al.</i> , 2019b; Velts, 2011).....	87
Table 4-1: Classification of gas-liquid contactors (Charpentier, 1981; Dutta, 2009; Gruenewald and Radnjanski, 2016a; Gunjal and Ranade, 2016; Kohl and Nielsen, 1997; Vinu, 2017; Wardhaugh <i>et al.</i> , 2017).....	100
Table 4-2: Summary of input parameters for the simulation	118
Table 4-3: Mixtures of air and input gas.....	118
Table 4-4: Average values of the gas mass transfer coefficient	125
Table 4-5: Summary of calculations for $k_L a_{CO_2}$	126
Table 5-1: Details of experimental conditions and hydrodynamic process variables (Pourmahdavi <i>et al.</i> , 2022)	145
Table 5-2: Mass flow rates of CO ₂ added to inlet air for each set point in each experiment (Pourmahdavi <i>et al.</i> , 2022).....	147
Table 5-3: Predicted initial and final addition rates of CO ₂ in the Baby HAC control volumes for experiment set points D.5 and D.6.....	160

Table 5-4: Summary of input parameters for the simulation	166
Table 5-5: Summary of calculations for $k_L a_{CO_2}$	169
Table 6-1: The performance table of the PVDF584 model of Mazzei injector	191
Table 6-2: Experimental measured values	192
Table 6-3: The pump performance table provided by the pump manufacturer	194
Table 6-4: The performance of the system (injector and pump)	201
Table 7-1: Details of experimental conditions and principal results	211
Table 7-2: The value of CO ₂ consumed in each experiment	224
Table 7-3: Concentrations of Ca ²⁺ and mass of recovered solid CaCO ₃	225
Table 8-1: Summary of input parameters for the simulation of selected experiments	237
Table 8-2: Summary of input parameters for the simulation	239
Table 8-3: The estimated values of $k_L a_{CO_2}$ according to the outlet pressure.....	239
Table 8-4: Summary of calculation for E and $k_L a_{CO_2}$	240
Table 8-5: The comparison between the experimental results and model predictions	252
Table 8-6: The results of sensitivity analysis of experiment E2	257
Table 9-1: Summary of input parameters for the simulation	265
Table 9-2: Mixtures of air and input gas.....	265

List of Appendices

Appendix A: Experimental data.....	308
Appendix B: Time series of experimental observations of CO ₂ concentrations for experiments A and B	313
Appendix C: Sample MATLAB Code.....	315

Nomenclature

a	specific interfacial area, m
A	interfacial area, m ²
A_s	total surface area of the Ca(OH) ₂ solid particles
C	concentration of species in liquid, mol/L
D	mass diffusivity of species in liquid
d	diameter, m
E	enhancement factor
E_i	Absorption or removal rate, kg/s
E_{CO_2}	carbonation efficiency
f	activity coefficient
I	ionic strength
K	Overall mass transfer coefficient
K_H	Henry solubility constant, mol/L bar
K_i	equilibrium constant
k_{ii}	reaction rate constant
k_L	liquid phase mass transfer coefficient, m/s
k_g	gas phase mass transfer coefficient, m/s
k_{La}	volumetric mass transfer coefficient, s ⁻¹
k_s	solid phase mass transfer coefficient
K_w	water solubility product
L	length of a downcomer segment, m
LHS	Left hand side
m	Mass of liquid, kg
\dot{m}	mass flow rate, kg/s
M	molar mass
MW	molecular weight
n	Number of moles of a given substance, mol

\dot{n}	molar flow rate, mol/s
P	Pressure, Pa
Q	volumetric flow rate
R_X	Reaction efficiency of mineral rock
R_{real}	Mass ratio
RHS	Right hand side
\mathcal{R}	universal gas constant, 8.314 J /K mol
s	Surface renewal rate, s ⁻¹
T	temperature, K
t_e	time of exposure of the gas and liquid, s
TH_{CO_2}	Theoretical mass fraction of CO ₂
v	velocity, m/s
V	volume, m ³
\dot{V}	volumetric flow rate, m ³ /s
W_{com}	work utilized on the gas compression
X_i	Liquid-phase mass fraction, kg/kg
X_{CO_2}	CO ₂ concentration in the solid products in weight percent
Y	Gas-phase mole fraction, mol/mol
Z_i	ion charge
$Z_{Ca(OH)_2}$	Initial weight of calcium hydroxide, g/L

Greek Letters

α	activity
$\beta(Ca(OH)_2)_S$	Solubility of calcium hydroxide, g/L
ε_A	Percent of weight
η	efficiency
f	activity coefficient
θ	Celsius temperature, °C
λ	frictional losses coefficient

μ	viscosity, Pa s
π	dimensionless mathematical constant, 3.14159
ρ	density
∂	Relative fraction of carbon species

1. Introduction

1.1 Mitigating global CO₂ emissions

Human activities have increased the concentrations of greenhouse gases such as CO₂, methane (CH₄), nitrous oxide (N₂O), and halocarbon gases in the atmosphere (IPCC, 2007). It is estimated that the current average atmospheric CO₂ concentration increased from a pre-industrial value of 280 ppm to 419 ppm in 2022, the highest level value in at least 2 million years. (US Department of Commerce, 2022). Emissions of greenhouse gases are expected to increase, reinforcing the greenhouse effect, which is predicted to increase the average temperature by 1–6 °C in the next century. A few visible impacts of climate change include the global average sea level rise, increase in the intensity and frequency of extreme weather events, disruption of ice shelves, and changes in rainfall patterns (IPCC, 2001). Reducing CO₂ emissions requires different strategies, such as switching to renewable energy, carbon capture and sequestration (CCS), reducing global energy consumption, and switching to less carbon-intensive fuels.

One of the primary sources of CO₂ emissions is the use of fossil fuels for electricity generation, particularly in developing countries. The combustion of fossil fuels, such as coal, oil, and natural gas, in power plants for generating electricity contributes over 70% of the total global CO₂ emissions. Coal-fired power plants alone account for approximately one-third of the CO₂ emissions from power generation. Fossil fuels are widely used for power generation because they are inexpensive, abundantly available, widely distributed geographically, and easily exploitable using existing technologies.

Although alternative energy sources, such as renewable energy, low-carbon energy, nuclear power, and clean-energy technology, have shown great potential to replace fossil fuels, they are not yet perceived as fully reliable and cannot effectively compete economically with cheap fossil fuels in some jurisdictions. Despite the efforts to fully replace fossil fuels with renewable sources, fossil fuels may remain the largest global energy source over the next several decades (IEA, 2016; IPCC, 2005a).

1.2 Carbon capture and sequestration

According to the IEA¹ (2016), carbon capture and sequestration (CCS) technologies are the most effective approaches for reducing CO₂ emissions from existing power plants because they can be retrofitted to existing generation infrastructure with minimal disruption (Blomen *et al.*, 2009; Yadav and Mehra, 2021). The deployment of CCS is important for reducing CO₂ emissions from power plants and other emitting industries such as iron and steel smelting, cement production, natural gas processing and petrochemical refining (O'Connor *et al.*, 2001b; Wiley *et al.*, 2011; Yi *et al.*, 2012), so that the climatic impact of these emissions is reduced.

The term ‘carbon capture and sequestration’ refers to technologies in which CO₂ is first captured from industrial or energy-related emissions sources (CO₂ capture) and then isolated from the carbon cycle through transfer to some form of storage site (CO₂ sequestration) (IPCC, 2007).

The aim of the capture of CO₂ is to remove or separate CO₂ from mixtures of exhaust gases in the flue streams of fossil fuel-based electricity-generating plants or other industrial processes

¹ International Energy Agency

that combust fossil fuels (Chai *et al.*, 2022). The process of capturing CO₂ can be grouped into three broad categories, such as capturing CO₂ before fuel combustion (pre-combustion capture), after combustion (post-combustion capture), and combustion in a pure stream of O₂ (oxy-fuel capture). A comparison of these technologies is presented in Table 1-1. For further information, please refer to Carpenter *et al.* (2017), Leung *et al.* (2014), Sethi and Dutta (2018) and Y. Wang *et al.* (2017).

Table 1-1: Advantages and disadvantages of CO₂ capture technologies modified (Leung *et al.*, 2014; Rao, 2010; T. Wang *et al.*, 2017; Y. Wang *et al.*, 2017; Woodall *et al.*, 2019)

Capture process	Application area	Advantages	Disadvantages
Pre-combustion	Coal-gasification plants	High CO ₂ concentration enhances sorption efficiency; fully developed technology, commercially deployed at the required scale in some industrial sectors; opportunity for retrofit to existing plant; For coal plants, efficiency, and cost penalties are generally lower than for post-combustion capture; CO ₂ is generated under pressure thus less compression is needed for transport	High parasitic power requirement for sorbent regeneration; Inadequate experience due to few gasification plants currently operated in the market; High capital and operating costs for current sorption systems; Efficiency loss in water gas shift section; Cooling and cleaning of syngas before capturing the CO ₂ is necessary
Post-combustion	Coal-fired and gas-fired plants	Technology is more mature than other alternatives; Can easily retrofit into existing plants; Applicable to the majority of existing coal-fired plants. Existing power plant can be retrofitted with minor modifications; The energy demand of the power plant can be controlled by-passing or adjusting the CO ₂ capture step during peak load.	Low CO ₂ concentration affects the capture efficiency; The high capital and operating costs; The high energy requirement of solution regeneration; Due to the high temperature, the gas needs to be cooled before the CO ₂ capture step; Energy penalty due to solvent regeneration; Degradation and loss of solvent
Oxyfuel combustion	Coal-fired and gas-fired plants	Very high CO ₂ concentration that enhances absorption efficiency; mature air separation technologies available; reduced volume of gas to be treated, hence required smaller boiler and other equipment; Combustors would be fairly conventional; Potential for advanced oxygen separation membranes with lower energy consumption	High efficiency drop and energy penalty; cryogenic O ₂ production is costly; corrosion problem may arise; Need to recycle large quantities of flue gas to avoid excessively high combustion temperatures; Power consumption of a cryogenic separation until may be cost prohibitive; Materials of construction have to resist to the high temperature of operation; Retrofit is an issue due to the high combustion temperature

To date, post-combustion carbon capture (PCC) has been the only industrial CO₂ capture technology demonstrated on a fully commercial scale. The Technology Centre Mongstad (TCM) in Norway (i.e., CO₂ capture by the Monoethanolamine (MEA) absorption process) and SaskPower's Boundary Dam 3 CCS Facility (BD3) (CO₂/SO₂ capture and H₂SO₄ production by the MEA absorption process) are two large-scale demonstrations of this technology. (Liang *et al.*, 2015; Zhang *et al.*, 2020).

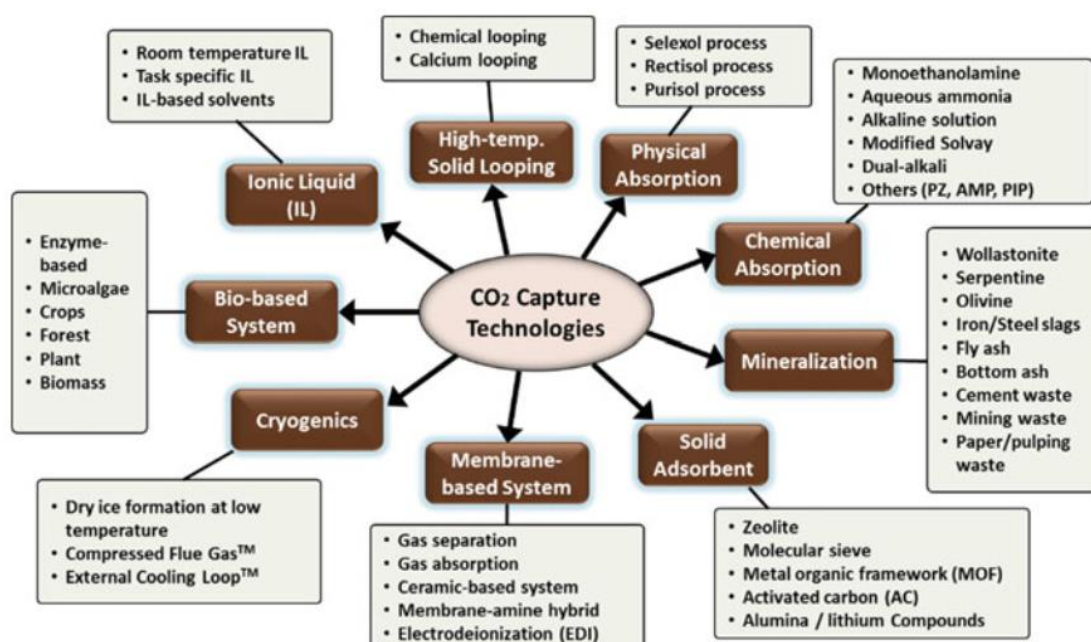


Figure 1-1: Different approaches to post-combustion CO₂ capture technologies (Chiang and Pan, 2017a)

The method which is described in this thesis is based on post-combustion carbon capture and sequestration process. Figure 1-1 illustrates the many of the technological options that have been developed and investigated for post-combustion CO₂ capture methods, motivated by the need to mitigate the climatic impact of anthropomorphic CO₂ emissions.

This work investigates a carbon capture method that is conceptually similar to those illustrated in Figure 1-1, but is not completely represented by any of those options. That novel concept is capture by pressurisation of a combustion flue gas stream with water so that the CO₂ becomes preferentially and dissolved in the water. In general, this is a feasible route because CO₂ is approximately ten times more soluble in water than the remaining gaseous constituents of the combustion flue gases (water vapor in the combustion gas condenses and becomes chemically indistinguishable from the water solvent).

The closest process to that proposed in this thesis, illustrated in Figure 1-1 is “Room temperature IL” because the compression process proposed for the flue gas is an isothermal compression process. Additionally, the “Compressed Flue Gas” process is also close for obvious reasons. However, compressing a flue gas alone will not separate the CO₂ from the other species in the flue gas without additional measures (i.e., dissolution in water). The overall CCS solution investigated in this thesis includes alkaline solutions. However, the alkaline solution is shown principally to be concerned with the sequestration method after capture rather than the capture mechanism itself

The straightforward dissolution of CO₂ is the mechanism investigated in this study, distinguishing it from other studies involving dissolution and reactions, such as the MEA method. However, the CO₂ capture concept relationship is also clearly close. Moreover, if another discriminant is required to distinguish the CO₂ capture process proposed in this study, it will be possible to distinguish it from the MEA dissolution of CO₂ in flue gas streams in the manner of capture solvent regeneration.

In the MEA process, the captured dissolved CO₂ is driven out of MEA solution by heating, which takes advantage of one of the general properties of gases in that they are less soluble in any solvent when the solvent temperature is higher. Although heat regenerates the solvent in the MEA process, the quantities of heat required to regenerate the solvent in practice at scale (e.g., the Boundary Dam coal-fired electricity-generating plant in Saskatchewan) have proven to be high enough to stall interest in this former leading capture technology (Kolawole, 2019).

However, the solvent regeneration method proposed in this thesis involves the precipitation of the CO₂ as an alkaline-earth metal oxide, such as calcium carbonate, CaCO₃(s). The precipitation process occurs under ambient temperature conditions and is accelerated by the high pressure at which the capture process occurs. The CCS methods proposed in this study involve mineral carbonation. However, they are applied in the CO₂ sequestration route, rather than in the CO₂ capture operation. In Chiang and Pan, (2017a) illustration of capture methods, mineral carbonation can be conceived as a capture process alone. It is applied to separate CO₂ from mixtures of atmospheric gas or combustion gas streams by fixing the gas to mineral substrates as gas streams pass over them. However, this is not an efficient process compared to the concepts investigated and developed in this thesis.

Following the capture, a separated or concentrated stream of CO₂ can be directed into the sequestration route. For CCS to be a useful option for reducing the total emissions of CO₂ to the atmosphere, the sequestration option for the captured CO₂ must ensure that the CO₂ is stored in a place and in a form that is isolated from the atmosphere (or other liberating environmental drivers) for a long period of time - measured on Earth's surface process timescales or possibly geological timescales (IPCC, 2005a; Sanna *et al.*, 2012).

Figure 1-2 shows the main sequestration routes following post-combustion CO₂ capture. There are four main CO₂ sequestration methods with different characteristics, including limitations, longevity, and costs involved (Neeraj and Yadav, 2020). These methods are classified as mineral, biological, geological and ocean sequestration methods. The advantages and disadvantages of these methods are summarized in Table 1-2.

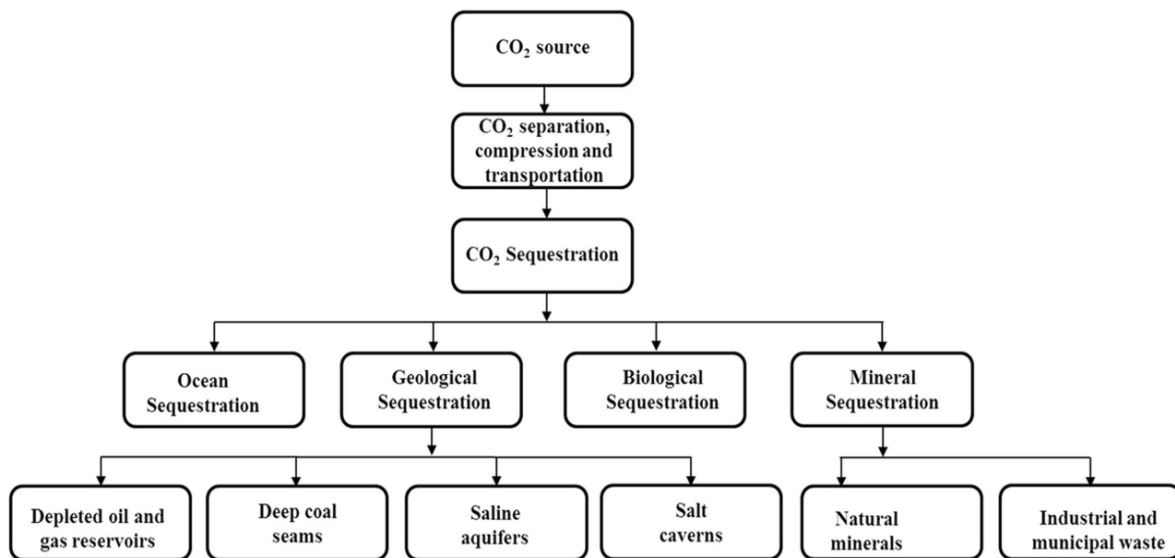


Figure 1-2: Different methods of post-combustion CO₂ sequestration

The CCS literature sometimes confuses the climate impact mitigation objective of CO₂ sequestration with the downstream use of captured CO₂, whatever form it takes, as economic feedstock for ongoing industrial processes (Teir, 2008). Therefore, the cost of the capture process is subsidized by revenues from CO₂ sales. However, the sequestration objective becomes confounded in these instances because CO₂ may be subsequently released back into the carbon cycle. Although end uses for CO₂ or its derived products, other than permanent storage, are allowed in this study on economic grounds, they are not considered CO₂ sequestration.

Table 1-2: Summary of different CO₂ sequestration methods (Bobicki *et al.*, 2012a; Chiang and Pan, 2017a; IPCC, 2005a; Neeraj and Yadav, 2020; Park *et al.*, 2016; Sipilä *et al.*, 2008)

Sequestration types	Mechanisms	Advantages	Disadvantages	Cost (US\$/t CO₂ stored)
Geological	It is also called enhanced reservoir recovery, which is the process of storing CO ₂ in underground geologic formations. The CO ₂ is usually pressurized until it becomes a liquid, and then it is injected into porous rock formations in geologic basins.	<ul style="list-style-type: none"> • Feasible on a large scale • Substantial storage capacity is known. • More extensive experience • Low cost and economical • Public acceptance 	<ul style="list-style-type: none"> • High threat of leakage • Requires constant monitoring. • Shortage of suitable sites 	0.5-8.0 (storage) 0.1-0.3 (monitoring)
Ocean	It involves injecting CO ₂ into the ocean at sufficient depth (>500 m). Below 500 m depth, CO ₂ can exist in the ocean as a liquid. Liquid CO ₂ is less dense than water and poorly miscible with water	<ul style="list-style-type: none"> • Large storage capacity • Universal availability • No monitoring 	<ul style="list-style-type: none"> • Temporary storage • Potential harmful effects on aquatic microbes and biota • Expensive than geo-storage 	6-31 (storage) 12-16 (tanker transfer)
Biological	It refers to the assimilation and storage of atmospheric carbon in vegetation, soils, woody products, and aquatic environments	<ul style="list-style-type: none"> • Low cost • Less environmental issues • High potential 	<ul style="list-style-type: none"> • Monocultures plantations can imbalance the ecosystem • Insufficient capacity • Risk of disruption of the food chain 	3–10
Mineral carbonation	It is based on the reaction of CO ₂ with metal oxide bearing materials to form insoluble carbonates, with calcium and magnesium being the most attractive metals.	<ul style="list-style-type: none"> • The only known form of permanent storage • Minerals required are available in quantities capable of binding all fossil-fuel bound carbon. • Carbonation products are environmentally benign 	<ul style="list-style-type: none"> • Energy-intensive and high cost • Slow reaction kinetics • Pre-treatment of feedstock and poor recovery of additive chemicals • The problem of storage or use of the process product if implemented on a large scale. • Mining of feedstock creates environmental issues 	50–100

Currently, one of the most common uses for captured CO₂ is to inject it into oil and gas reservoirs in a process known as enhanced reservoir recovery. In this process, although CO₂ is potentially permanently stored in the subsurface, the purpose of injecting CO₂ into the reservoir is to drive more oil or gas from that reservoir. Obviously, the combustion of that oil and gas in electricity generation and other industrial processes will exacerbate the climate impact of CO₂ rather than improve it. It should be noted that this use of captured CO₂ is represented in Figure 1-2 as a depleted oil and gas reservoir. The oil and gas reservoir sequestration option depicted is where the captured CO₂ is simply stored in depleted reservoirs without releasing more fossil fuel.

Routing to sequestration frequently necessitates CO₂ compression and pipeline transportation, both of which are energy-intensive processes requiring significant power and energy consumption (Lackner, 2003). Moreover, if a fossil-fuel electricity-generating plant supplies this power/energy, this consumption will also exacerbate rather than improve the climatic impact of CO₂. Similarly, sequestration through injection into depleted oil and gas reservoirs, or saline aquifers, or deep coal seams, or salt caverns, requires compression of the captured CO₂ to 40-50 bar, which requires considerable energy and power input and specialist compression equipment (IPCC, 2005a).

In contrast, mineral carbonation avoids the consumption of appreciable amounts of compression energy in the sequestration process. It can be deployed at any location, rather than requiring the opportunistic adjacency of a depleted oil and gas reservoir or a saline aquifer at depth, or geology that supports salt formations or coal seams, if the parasitic energy in the transportation of the captured CO₂ is to be avoided. Mineral carbonation requires the availability of large masses of alkaline earth metal oxides and hydroxide mineral feedstocks, exemplified by mineral-based wastes such as mine tailings and slags produced in iron/steel/nickel pyrometallurgy. Most of the

geological CO₂ sequestration options presented in Figure 1-1. remain energized to some extent, at least after sequestration. Therefore, these options must be associated with the potential that causes the CO₂ to become de-sequestered. For example, without appropriate engineering measures, pressurized gas in a confining cavern can cause fracture, breach, and escape of previously sequestered CO₂ (Yadav and Mehra, 2021). In contrast, mineral carbonation sequestration leaves CO₂ in a much lower energy state, and in a far more immobile form than geological sequestration options. Sequestered carbonates can be released through contact with acidic materials. However, the processes involved are much closer to those that operate in natural carbon cycles. It is for these reasons that the sequestration option/mechanism considered in this study is mineral carbonation.

Following CO₂ capture in a flue gas stream by continuous (not batch) pressure driven dissolution in water, with a co-current continuous dissolution of alkaline earth oxides and hydroxides in the same water body, the CO₂ is sequestered through chemical transformation to a CaCO₃ precipitate which removes the CO₂ from the water and regenerates the water as its solvent.

In the above discussions of the distinctions between the work of others, and the CCS concept explored in this thesis, reference has been made to a pressure-driven isothermal compression of combustion flue gases containing CO₂, which is captured and sequestered. In addition to the novelty of this CCS concept compared to mainstream alternatives, the compression device considered in this work is a further novel aspect of this work. The device considered is a hydraulic air compressor (HAC). HAC systems, which have been historically proven to be reliable machines at industrial scales and over decades of use, provide a practical, industrial-scale, isothermal gas compression process. An isothermal compression process is the most energy efficient conceivable over any specified pressure ratio (Hutchison, 2018a). In comparison to prior work with co-

investigators, the innovative conceptual pivot explored in this thesis is that the HAC should not simply be considered as a gas compressor, but that it is more appropriate to conceive of it as a pressurized, continuous chemical reactor. Thus, it resembles an autoclave in that the reactions occur at pressure. However, the HAC can also handle continuous flows of reactants and products. The analyses and experimental work presented in this thesis demonstrate the use of the HAC as a 2-phase continuous pressurized reactor (when gases are captured via pressure driven dissolution in water alone) and a 3-phase pressurized reactor. $\text{CO}_2(\text{g})$ and $\text{Ca}(\text{OH})_2(\text{s})$ are continuously supplied to the HAC and reacted as dissolved CO_2 and a suspension solution of $\text{Ca}(\text{OH})_2(\text{s})$ at saturation to continuously produce $\text{CaCO}_3(\text{s})$ precipitates. The economic by-product produced by the HAC during this process is pneumatic power; the gases that remain in the flue gas mixture after the CO_2 is removed from it are isothermally, maximally efficiently, compressed.

1.3 Thesis aim and objectives.

In recent years, the reduction in capital and operating costs of CO_2 capture, and its energy penalty have gained considerable attention. The high capital costs are due to the large reactor sizes that result from the significant mass transfer resistances that need to be overcome in conventional CCS methods. Heat and mass transfer improvements are achievable by creating better contact between the phases and fast mixing.

In this study, the technical feasibility of the CCS process using the HAC is investigated. The experiments conducted on the HAC prove that this system is a suitable technology for the intensification of carbon capture and sequestration due to its higher mass transfer performance compared to other mass transfer devices such as conventional bubble columns or spray towers. However, following the general Millar (2014a) design paradigm, the size of the HAC unit is

consistently large, implying that the capital cost of HAC construction is considerable in all the variations investigated thus far. Moreover, a system that can provide comparable performance with reduced height would render the concept more accessible to capital-restricted projects. Therefore, a horizontal injector loop is introduced as a new apparatus to increase the mass transfer rates between the phases and achieve better mixing. Thus, the objectives of this study are as follows:

- Provide an up-to-date review of potential raw materials that can be used as feedstocks for the capture and sequestration of CO₂
- Provide a literature review to assess how variables such as temperatures, pressure, rate of CO₂, partial pressure of CO₂, alkaline solutions and pH affect mineral carbonation yield.
- Develop a mathematical dynamic kinetic model to simulate the kinetic of absorption of CO₂ into an alkaline solution in a high pressure reactor. The significance of the evaluated model is that it can be used to predict the absorption rate under operating conditions beyond those of experimental tests. The model can also guide the design calculations for new reactors and future experiments.
- Perform the experiments to investigate the potential of the HAC as a post-combustion CO₂ capture system and to verify of a one-dimensional steady-state model for two-phase bubbly flow.
- Perform hydrodynamic and mass transfer comparison of HAC downcomers and upward co-current flow bubble column reactors using the verified bubbly flow model.
- Determine the effects of pressure and Ca(OH)₂ solution concentration on the CO₂ capture efficiency and gas-phase mass transfer.

- Design and fabricate a horizontal injector loop as a new high pressure reactor and perform experiments to demonstrate the carbon capture and sequestration applications of this system.
- Simulate the CO₂ capture and sequestration experiments in the horizontal injector loop with a dynamic kinetic model to verify the experimental work within a sound conceptual framework.

1.4 Thesis Structure

Chapter 1 introduces the challenge of global warming and climate change, CCS and the approaches to CO₂ capture and a description of post-combustion carbon capture and sequestration processes.

Chapter 2 presents a review of the relevant literature sources on post-combustion CO₂ capture and sequestration (PCC) processes, mineral carbonation as a promising method for reducing CO₂ emissions, and potential feedstocks for this method.

Chapter 3 describes the principles and mechanisms of carbonation using a Ca(OH)₂ aqueous solution. The kinetics of the three major carbonation steps, CO₂ dissolution in an alkaline solution, metal ion leaching, and carbonate precipitation, are illustrated. A model for CO₂ absorption and CaCO₃ precipitation in a reactor is also presented to aid in interpreting the experimental results.

Chapter 4 describes the hydraulic air compressor as a gas-liquid contactor accelerating the mass transfer rate between gaseous CO₂ and the liquid solution phase. Young *et al.* (2022) developed a one-dimensional model for estimating gas absorption during the compression process in a HAC

downcomer that couples the hydrodynamics, solubility kinetics and psychrometric aspects of the system. The experimental conditions and their results are discussed in detail in Chapter 5.

Chapter 6 introduces a horizontal injector loop, which is a variation of the previously presented HAC systems. The primary design objective of this system is to capture and sequester CO₂. The experimental results of CO₂ capture and sequestration are presented in Chapter 7, which aims to demonstrate the proof-of-concept of the designed system and constructed prototype. A dynamic kinetic model is also introduced to determine the yield of the CO₂ capture and sequestration processes. The results of this model are discussed in Chapter 8.

Chapter 9 presents a comparison of the hydrodynamic and mass transfers of HAC downcomers and upward co-current flow bubble column reactors using the verified bubbly flow model. A comparison between the HAC and the new experimental apparatus, the horizontal injector loop, is also presented.

Chapter 10 summarizes the major outcomes of this work and suggests potential future work.

2. A review of mineral carbonation as a post-combustion carbon capture and sequestration

In this chapter, different approaches for post-combustion CO₂ capture from flue gas or air are introduced, and the advantages and disadvantages of each method are discussed. Mineral carbonation is a post-combustion CO₂ capture and sequestration (PCC) process, and the aspects of this process that render it a promising method for reducing CO₂ emissions are explored.

2.1 Post-combustion CO₂ capture and sequestration

Carbon Capture and sequestration (CCS) is a range of technologies being developed to assist in mitigating climate change by isolating a significant fraction of CO₂ produced during fuel combustion (e.g., coal, gas, and biomass) from the atmosphere. Among CCS technologies, post-combustion CO₂ capture (PCC) is considered the most common process for CO₂ capture from industrial flue gases.

When separating CO₂ from industrial gas streams and/or conventional power plants, CO₂ content and pressure in the exhaust gas can determine the capture process (Fara, 2018; Thonemann *et al.*, 2022). Table 2-1 shows the relative proportions of the gas composition that can be used in a capture process. The combustion gas stream discharged from power stations or other industrial plants usually contains material concentrations of problematic species, particularly NO_x, and SO_x.

Table 2-1: Summary of emission gas characteristics from post carbon capture CO₂ source (“Boiler Combustion,” 2022; Ho *et al.*, 2019; Ho and Wiley, 2016; IPCC, 2005a; Last and Schmick, 2011; Padurean *et al.*, 2012; Pavri and Moore, 2007; Pellegrini *et al.*, 2020; Romano *et al.*, 2013; Song *et al.*, 2004)

Sources	CO ₂ concentration (% vol. (dry))	Major impurities	Minor impurities	Pressure of gas stream (MPa)	References
Power station					
Natural gas fired power station	7-10	H ₂ O, N ₂ , O ₂	CO, NO _x , SO ₂ , CH ₄ , VOC ¹ , TOC ²	0.1	("Boiler Combustion," 2022; <i>Fuel Oil Combustion</i> , 2010; Ho <i>et al.</i> , 2019; IPCC, 2005a; Padurean <i>et al.</i> , 2012; Pavri and Moore, 2007, 2007; Song <i>et al.</i> , 2004; Zhu and Frey, 2012)
Gas turbines	3-4	H ₂ O, N ₂ , O ₂	CO, NO _x , SO ₂ , UHC ³	0.1	
Coal-fired power station	12-14	H ₂ O, N ₂	CO, NO _x , SO ₂	0.1	
Oil fired boilers	11-13	H ₂ O, N ₂ O, O ₂ , CH ₄	CO, NO _x , SO _x , HC ⁴ , VOC	0.1	
Coal fired boilers	12-15	H ₂ O, N ₂	CO, NO _x , SO _x , O ₂	0.1	
IGCC ⁵ after combustion	12-14	N ₂ , O ₂ , H ₂	H ₂ O, NO _x , SO _x , H ₂ S, CH ₄ , NH ₃	0.1	
IGCC, synthesis gas after gasification	8-20	N ₂ , O ₂ , H ₂	H ₂ O, NO _x , SO _x , H ₂ S, CH ₄ , NH ₃	2-7	
Cement industry					
Cement kiln flow gas	14-33	CO, N ₂ +Ar, SO ₂	NO _x , HCL	0.1	(IPCC, 2005a; Last and Schmick, 2011)
Refineries					
Process heaters	8-9	H ₂ O, N ₂ +Ar	NO _x , SO _x	0.1	(Ho and Wiley, 2016; Straelen <i>et al.</i> , 2009)
Fluid catalytic cracker	12-13.5	H ₂ O, N ₂ + Ar	CO, NO _x , SO _x , Catalyst dust	0.1	
Hydrogen production					
Steam methane reforming emission	4-8	H ₂ O, N ₂ +Ar, O ₂ ,	NO _x , SO _x	0.1	(Ho and Wiley, 2016; IEAGHG, 2017; Pellegrini <i>et al.</i> , 2020)
Pressure-swing absorption tail gas	44.5-45.1	CO, CH ₄	N ₂ , H ₂ , H ₂ O, C ₂ H ₆	0.13	
Shifted syngas to PSA purification	14-15	H ₂ , CH ₄	N ₂ , H ₂ O, CO,	2.5-30	
An integrated iron and steel mill					
Coke oven gas	2-5	CO, C _n H _m	NO _x , SO _x , HCL	0.1	(Romano <i>et al.</i> , 2013; Wiley <i>et al.</i> , 2011)
Blast furnace gas	20-25	H ₂ O, N ₂ , H ₂	NO _x , SO _x , dust	0.1	
Sinter plant	5-8	H ₂ O, N ₂	SO ₂ , NO _x , Dioxins, Heavy metals	0.1	
Lime kiln	20-30	H ₂ O, N ₂ , O ₂	NO _x , SO _x	0.1	
Basic oxygen furnace	10-18	CO, N ₂	H ₂ , dust	0.1	
Hot strip mill	7-10	CO, N ₂	NO _x , SO _x	0.1	

¹ Volatile organic compound

² Total organic carbon

³ Unburned hydrocarbons

⁴ Hydrocarbon

⁵ Integrated gasification combined cycle, after combustion

The levels of CO₂ in the discharge gas stream depend on the type of fuel and the extent of excess air used in the combustion process. In most cases, flue gases from the power plant are delivered at atmospheric pressure (Hendriks *et al.*, 2009), so the partial pressure of CO₂ in the gas stream is low. When the concentration of CO₂ in the gas stream is low, the times associated with sequestration processes are longer (Chiang and Pan, 2017b). The reaction time is inversely proportional to CO₂ concentration in the off gas flow; the lower the gas CO₂ content is, the longer the duration of the sequestration.

In principle, post-combustion capture systems can be applied to stack gases produced from the combustion of any type of fuel. However, the impurities in the fuel are very important for the design and costing of the complete plant (IPCC, 2005a). The most common technologies used for post-combustion CO₂ capture are shown in Figure 1-2. Table 2-2 briefly compares the advantages and limitations of these carbon capture technologies.

In Table 2-2, five processes mentioned as capture technologies can concentrate the dilute CO₂ in flue gas to nearly pure CO₂. After that, the sequential storage or utilization should be considered (Chiang and Pan, 2017a). However, mineral carbonation and biological methods are related to the direct conversion and utilization of CO₂ because the physico-chemical property of CO₂ undergoes a change after the capture process. Therefore, no additional CO₂ storage site is required with the capture plant (Pan *et al.*, 2018c).

Table 2-2: General advantages and disadvantages of post-combustion CO₂ capture and sequestration (Chiang and Pan, 2017a; Kolawole, 2019; Singh and Dhar, 2019)

Technology	Mechanisms	Pros	Cons	
		Capture		
Absorption	Physical <ul style="list-style-type: none"> • Selexol process • Rectisol process • Purisol process 	The solubility of CO ₂ in a solvent	<ul style="list-style-type: none"> • High capacity at low temperature & high pressure • Cheaper solvent • Mature technology • Low vapor pressure and toxicity (Selexol) • Low corrosion (Rectisol) • Low energy consumption (Purisol) 	<ul style="list-style-type: none"> • Low selectivity • High energy consumption • Low capacity at high temperatures and low pressure • Absorbent loss • High capital and operation costs
	Chemical <ul style="list-style-type: none"> • Alkanolamine solution; MEA¹, DEA², MDEA³ • Aqueous ammonia • Alkaline solution • Modified solvay • Dual-alkali • Sterically hindered amine Promoter; PZ⁴, PIP⁵ 	Chemical reaction between a solvent and CO ₂	<ul style="list-style-type: none"> • High capacity at low CO₂ pressure • Mature technology 	<ul style="list-style-type: none"> • Energy-intensive regeneration • Low absorption-desorption rate • Corrosion and absorbent degradation • High operation cost • Large absorber volume required • Amine degradation by SO₂, NO₂, O₂ • The high cost of manufacturing the solvent (e.g. MEA ~ USD 1250 / tonne)
	Ionic liquid <ul style="list-style-type: none"> • Room temperature IL • Task specific IL • IL-based solvent 		<ul style="list-style-type: none"> • Low vapor pressure • Non-toxicity • Good thermal stability • High polarity 	<ul style="list-style-type: none"> • High viscosity • High energy requirement for regeneration • High unit costs
Adsorption	Physical (Solid) <ul style="list-style-type: none"> • Activated carbon (AC) • Zeolite • Mesoporous silica (MS) • Metal-organic frameworks (MOFs) • Activated carbon (AC) 	Molecular sieve confinement effect of solid materials, normally with micropores	<ul style="list-style-type: none"> • Wide availability and low cost • High thermal stability (AC) • Low sensitivity to moisture (AC) • High pore size and tunable pore size (MS & MOFs) 	<ul style="list-style-type: none"> • Low CO₂ adsorption capacity • Low CO₂ selectivity • Slow adsorption kinetics • Thermal, chemical, and mechanical stability in cycling

¹ Monoethanolamine
² Diethanolamine
³ Methyl diethanolamine
⁴ Piperazine
⁵ Piperidine

Technology	Mechanisms	Pros	Cons
High-temp. Solid looping	<ul style="list-style-type: none"> • Chemical looping • Calcium looping 	Based on a reversible reaction between CaO and CO ₂	<ul style="list-style-type: none"> • High capture efficiency • High energy requirement • Low efficiency
Membrane separation	<ul style="list-style-type: none"> • Gas separation • Gas absorption • Ceramic-based system • Membrane-amine hybrid • Electrodeionization (EDI) 	Different gas permeability	<ul style="list-style-type: none"> • Relatively low operation cost • Easy handling and operation • High manufacturing cost • Relatively low separation selectivity • Permeability still low • Negative effect of moisture
Cryogenic techniques	<ul style="list-style-type: none"> • Dry ice formation at low temperature • Compressed flue gases • External cooling loop 	Different condensation temperature	<ul style="list-style-type: none"> • High capture efficiency (up to 99.9%) • High energy requirement • Low efficiency • Moisture pre-removal is required • Solidified CO₂ may be accumulated on the surface of the heat exchanger
High-temp. Solid looping	<ul style="list-style-type: none"> • Chemical looping • Calcium looping 	Based on a reversible reaction between CaO and CO ₂	<ul style="list-style-type: none"> • High capture efficiency • High energy requirement • Low efficiency
Capture and sequestration			
Bio-based system	<ul style="list-style-type: none"> • Enzyme-based • Microalgae • Crops • Forest • Plant • Biomass 	Captured and utilized through photosynthesis in plants	<ul style="list-style-type: none"> • No hazards of chemicals • Long time requirement • Large area requirement • May affect biological diversity
Mineral carbonation	<ul style="list-style-type: none"> • Natural ores • Solid wastes 		<ul style="list-style-type: none"> • Environmentally safe • Exothermic reactions • Abundance of feedstock • Permanent • No monitoring • Utilization of industrial waste • High costs • Slow reaction kinetics • Pre-treatment of feedstock • Energy intensive • Unsecure future potential • Poor recovery of additive chemicals • Problem of storage or use of process product if implemented on large scale • Mining of feedstock creates environmental issues

2.2 A review of mineral carbonation routes and feedstocks

This work focuses on the capture and simultaneous sequestration of CO₂ by Ca(OH)₂ aqueous mineral carbonation in a pressurized continuous reactor. It constitutes a preliminary study of the feasibility of sequestering CO₂ with solid wastes containing CaO/Ca(OH)₂ using a horizontal injector loop. Calcium oxide/Calcium hydroxide (CaO/Ca(OH)₂) is adopted for clarity and the focus of investigations, however, mineral carbonation using additional metal oxide/hydroxide species is anticipated too. Calcium oxide is hygroscopic; the free CaO present in a solid rapidly converts to Ca(OH)₂ upon exposure to air, due to its absorption of airborne moisture. Therefore, Ca(OH)₂ constitutes the major reactive component in solid waste containing CaO/Ca(OH)₂ (Yan *et al.*, 2015a).

An aqueous solution of Ca(OH)₂ can be used as an effective solvent for absorbing CO₂ due to its various advantageous features:

- i) Ca is inexpensive, abundant, and non-hazardous. Calcium carbonate precipitation resulting from the carbonation of Ca(OH)₂ aqueous solutions or slurries containing calcium is a well-known and classic reaction, commonly observed in nature as a weathering process (Han *et al.*, 2011a).
- ii) Recovery and regeneration (via calcium looping technology) are available to dispose of the precipitated CaCO₃ (Wang *et al.*, 2017). The regenerative calcium cycle is a more efficient, less toxic alternative to current post-combustion capture processes, such as amine scrubbing. It is also more economic than traditional CO₂ sequestration due to the absence of any additional costs for CO₂ liquefaction and transportation (Dean *et al.*, 2011).

- iii) The precipitated CaCO_3 can be used as the raw materials in different industries such as construction, papermaking, rubber, and plastics (Liendo *et al.*, 2022).

Despite these advantages, the Ca(OH)_2 aqueous solution has not received much attention as a source for CO_2 capture. This is because the source of Ca(OH)_2 or CaO has mostly been considered to be natural limestone, where the extraction process is energy-intensive (Pan *et al.*, 2018a; Teir, 2008) and can lead to considerable CO_2 emissions as well.

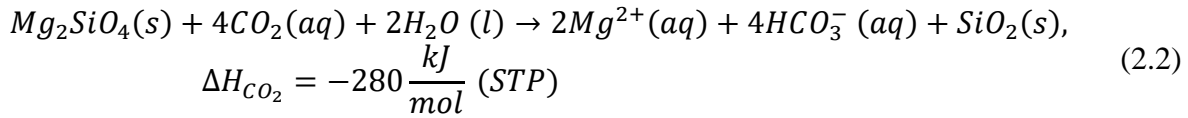
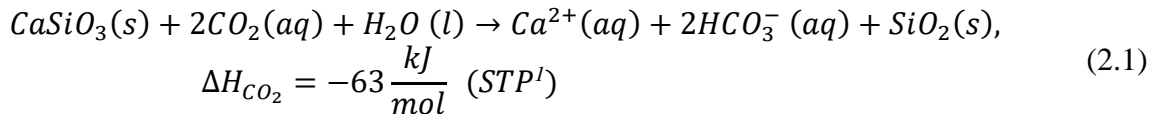
Recently, investigations into mineral carbonation have been reported to address these issues. (Azdarpour *et al.*, 2015; Hariharan *et al.*, 2017; Li and Hitch, 2017; Yadav and Mehra, 2021). Mineral carbonation uses alternative Ca sources, including Ca extraction from natural silicate minerals such as wollastonite (CaSiO_3) or alkaline solid wastes like iron and steel slags, cement wastes, air pollution ash, and gold mine tailings. (Andrade and Sanjuán, 2018; Chakraborty and Jo, 2018; Chen *et al.*, 2020a; Ji and Yu, 2018a; Kornmüller, 1995; Mokhtari, 2016; Pakzad *et al.*, 2021; Pan *et al.*, 2015a).

In the following sections, a literature review of mineral carbonation methods and feedstocks (alternative Ca sources) is presented in detail.

2.2.1 Process routes of mineral carbonation

The concept of mineral carbonation was initially introduced by (Seifritz, 1990) as a method for carbon capture and storage (CCS). In this approach, CO_2 is chemically reacted with alkaline earth-metal-bearing minerals or waste materials to form stable solid inorganic carbonates. In nature, calcium and magnesium carbonates are formed by the weathering process of rocks. In this natural process, which occurs over geological time scales, calcium and magnesium ions are leached out

of silicate rocks by rivers and rainfall. These ions then react with atmospheric CO₂ to form solid calcium and magnesium carbonates. Eqs. (2.1) and (2.2) show the reactions between natural alkaline silicate minerals and atmospheric CO₂ (Pan *et al.*, 2012).



Mineral carbonation can occur either below ground (*in-situ*) or above (*ex-situ*) ground. *In-situ* mineral carbonation involves injecting CO₂ into a geological formation to facilitate the reaction between CO₂ and alkaline earth metal minerals, leading to the formation of carbonates (Romanov *et al.*, 2015). *Ex-situ* mineral carbonation takes place above ground and utilizes natural ores or industrial waste products (Sanna *et al.*, 2014a). Figure 2-1 shows the *ex-situ* mineral carbonation process. In this thesis, the primary focus is on *ex-situ* mineral carbonation.

¹ Standard temperature and pressure

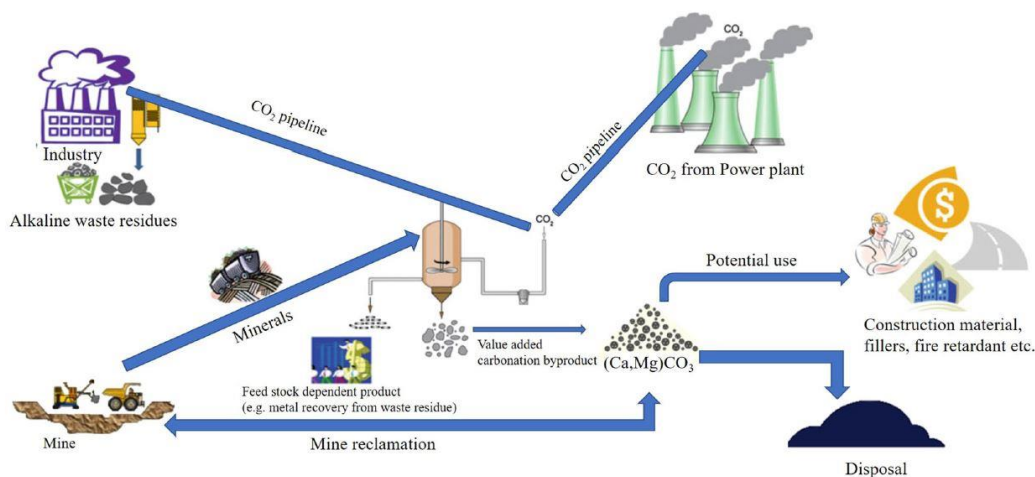


Figure 2-1: The ex-situ mineral carbonation process (Veetil and Hitch, 2020a)

In terms of technological concepts, mineral carbonation is relatively new compared to geological storage. This technology offers certain fundamental advantages that are not present in more established sequestration methods. Mineral carbonation products are thermodynamically stable, ensuring that CO₂ is permanently trapped in a solid state, as long as it is not exposed to an acidic environment. The resultant products of mineral carbonation can be managed through stockpiling in mines or repurposed for construction purposes. (IPCC, 2005b). There is no need for after storage surveillance and it is environmentally benign (Sanna *et al.*, 2014b).

In addition to offering substantial and secure storage, the exothermic nature of the overall carbonation reaction provides another advantage of mineral carbonation. This characteristic could potentially result in reduced energy consumption and costs compared to more established alternatives. (Pan *et al.*, 2012). In the case of industrial residues, there are additional potential benefits, such as: (a) the carbonation process can be more efficient since the residues generally exhibit higher reactivity than primary minerals, (b) the alkalinity of the residues is reduced, and (c) the residues can continue to be utilized in recycling processes after carbonation, for instance,

as aggregates in construction applications. However, this technology is still at the experimental stage, with only limited commercial applications (Zhang *et al.*, 2020).

The main barriers to the large-scale application of mineral carbonation remain high energy intensity, low carbonation efficiency, and slow reaction kinetics (Ji and Yu, 2018b). To overcome the slow reaction kinetics, researchers have focused their efforts on carefully selecting the process chemistry routes, feedstock, and pre-treatment options, as demonstrated in Bobicki *et al.* (2012a). *Ex-situ* mineral carbonation can be classified into two main methods: direct carbonation and indirect carbonation, both of which are summarized in the subsequent sections.

- ***Direct mineral carbonation***

Direct mineral carbonation is a single step reaction mechanism in which CO₂ reacts with the reactive compounds (minerals or alkaline solid wastes) to form carbonates. It can occur through two routes: (I) dry (gas–solid) carbonation, (II) aqueous carbonation.

- *Dry (gas–solid) mineral carbonation*

Carbon dioxide and a mineral are the only reactants in a direct gas-solid carbonation process. This approach was initially studied by Lackner *et al.* (1995). In general, this carbonation process has slower reaction kinetics compared to alternative mineral carbonation processes. It also demands a significant amount of energy due to the absence of a moist medium that would facilitate better interaction between the reactants (Chiang and Pan, 2017a). High CO₂ pressure (100-150 bar) is required to achieve reasonable reaction rates (Sanna *et al.*, 2014b). These factors contribute to a relatively low capture efficiency for dry carbonation. As a result, most of the published works primarily focus on evaluating the performance of aqueous carbonation.

Table 2-3: Summary of mineral carbonation process routes (Bobicki *et al.*, 2012b; Chiang and Pan, 2017b; Wouter, Huijgen and Comans, 2005)

		Characteristic	Challenges
Direct carbonation	Dry	CO ₂ is reacted with mineral carbonate in a gas-solid reaction; The simplest method of mineral carbonation; Not possible for silicate minerals	Slow rate of mass transfer between gas CO ₂ and liquid solution phase; Losses of material and energy (i.e., heat of reaction); Influence of impurity in flue gas, such as sulfur dioxide (SO ₂) and particulate matter (PM), on carbonation efficiency; High energy consumption of overall processes due to feedstock/material processing and reactor use (e.g., high temperature and pressure); Product separation and its subsequent utilization.
	Aqueous	CO ₂ is reacted with minerals in aqueous suspension; Pre-treatment is required; Needs higher pressure of CO ₂ to compare with other carbonation routes; Most promising technique	
Indirect carbonation	pH swing process	A multistep process consisting of metal ions extraction from the feedstock in acidic conditions in the first step and carbonate precipitation under high pH conditions in the following steps; Produce high purity products; The large amount of water that needs to be separated from the salts during the regeneration step;	The high energy consumption for evaporation of the aqueous solution.; The large variations in free energy resulting from the necessary formation of intermediate products; Other elements, such as heavy metals, may also leach out during the extraction step, thus leading to impure carbonate precipitate.
	HCl extraction	Metal ions extracted from mineral using HCl; Metal ions are precipitated as a hydroxide for carbonation; HCl recovered	
	Molten salt	Molten magnesium chloride salt is used to extract metal ions from silicate minerals; Metal ions precipitated as a hydroxide for carbonation; Molten salt is highly corrosive; Makeup chemical cost is prohibitive	
	Acid extraction	Acids used to extract metal ions from minerals; Extracted metal carbonated aqueously; Various acids used; High carbonate conversions achieved; Multiple process steps allow contaminants to be separated, resulting in a pure carbonation product; Chemically intensive; Energy intensive if acid recovered	
	Bioleaching	Chemolithotrophic bacteria combined with acid-generating substances and silicate minerals to extract metal ions for aqueous carbonation; Passive and inexpensive	
	Ammonia extraction	Ammonia salts used to extract metal ions from silicate rock for carbonation; Selective leaching of alkaline earth metals; Reagent recovery possible; Reasonable carbonate conversions achieved	
	Caustic extraction	Caustic soda (NaOH) used to extract metal ions from silicate rock for carbonation; Not a promising technique	

- *Aqueous mineral carbonation*

Direct aqueous mineral carbonation is a process in which CO₂ reacts with minerals in an aqueous suspension to produce solid carbonates that permanently fix the CO₂. The aqueous mineral carbonation process follows the carbonic acid processing route. This process comprises three simultaneous reactions. First, CO₂ is dissolved in water, producing carbonate and bicarbonate ions and protons (H⁺) that slightly reduce the pH of the reaction medium. The protons help to dissociate the mineral feedstock into metal cations (Chakraborty and Jo, 2018; Fara, 2018). The product is separated into a liquid solution and a carbonated solid following carbonation. Although no excessive heat is required in aqueous carbonation, the liquid solution (or slurry) can be heated to about 60–80 °C to achieve a higher carbonation conversion than at ambient temperature. (Chang *et al.*, 2012; Chen *et al.*, 2020b).

Direct aqueous carbonation can achieve high carbonate conversions and acceptable reaction rates by optimizing the reaction conditions, modifying the solution chemistry, and using pre-treatment techniques such as comminution to obtain small particle sizes (typically sub 75 μm) and liberation of alkaline earth metal oxides. Although no direct aqueous mineral carbonation scheme has yet been proven economical, many researchers consider it a promising CO₂ mineralization technique (Bobicki *et al.* 2012a; Kemache *et al.* 2017; Pan, Ling, *et al.* 2018). Researchers have concentrated on reaction kinetics modeling (Chang *et al.* 2013; Zhang and Jiang 2019), process evaluation and optimization by varying the conditions and contents of the aqueous phase (Na *et al.* 2019; Teir 2008), developing improved pre-treatment techniques (Rackley 2017; Tove Anette 2010) to study the applicability of different types of waste products as feedstock materials (Xiao *et al.* 2014), and developing novel reactor designs (Pan *et al.* 2015; Y. G. Zhang *et al.* 2013).

The process chemistry and kinetics of direct aqueous mineral carbonation are detailed in Chapter 3. The key factors necessary for effective direct aqueous carbonation are summarized in Table 2-4.

Table 2-4: The essential factors for effective direct aqueous carbonation (Chiang and Pan, 2017a)

Phases	Physical properties	Chemical properties
Solid phase (Silicate mineral, industrial alkaline residues)	<ul style="list-style-type: none"> • Particle size • Mineralogy • Specific surface area • Porosity/Permeability • Surface activities • Microstructure 	<ul style="list-style-type: none"> • Compositions (e.g., Ca and f-CaO content, Ca/Si ratio, Ferrite/C₃A ratio) • Metals (e.g., Pb, Cd, Ni, Cr) • Free water content • Permeability
Liquid phase	<ul style="list-style-type: none"> • Temperature • Liquid-to-solid ratio 	<ul style="list-style-type: none"> • Organics/Inorganic • Anions/Cations • pH (or alkalinity) • Permeability
Gas phase	<ul style="list-style-type: none"> • Partial pressure • Flow rate • Relative humidity • Temperature 	<ul style="list-style-type: none"> • CO₂ concentration • Organics/Inorganic • Particulate matter content • Other air pollutants (e.g., SO₂)

- ***Indirect mineral carbonation***

Indirect mineral carbonation follows a multi-step reaction process. Initially, the reactive magnesium or calcium compounds are extracted from the mineral using acids or other solvents. Subsequently, the extracted components undergo reactions with CO₂ either in the gaseous or aqueous phase (Sanna *et al.*, 2014b).

The result of indirect carbonation is the formation of pure metal carbonates, with impurities such as silica and iron being removed before carbonate precipitation (Pan *et al.*, 2015a). The process can also become complex due to the co-leaching of other impurities (such as iron and nickel) associated with the candidate metal. Additionally, complexities arise from the regeneration

and recycling of chemicals employed for metal extraction, the limited pH range for effective operation, and the fluctuations in free energy during the creation of intermediate reactive species (Annan and Gooda, 2018; Azadi *et al.*, 2019; Maroto-Valer *et al.*, 2005; Teir, 2008; Veetil *et al.*, 2015).

Direct carbonation typically allows for achieving a higher CO₂ removal capacity and rate in comparison to indirect carbonation. However, the CaCO₃ precipitate produced through indirect carbonation tends to possess a higher purity than that obtained via direct carbonation. This quality advantage could result in a more valuable product for utilization, should that be the intention (Pan *et al.*, 2018b).

Several technologies (Table 2-3) are available for indirect mineral carbonation, including a pH swing process, HCl extraction, the molten salt process, other acid extraction, bioleaching, ammonia extraction, and caustic extraction (Bobicki *et al.*, 2012a).

2.3 Natural mineral feedstock for mineral carbonation

Both natural mineral silicate rocks and industrial alkaline residues are potential feedstocks for sequestration through mineral carbonation. (Saran *et al.*, 2018). A brief description of both types of material is presented in the following sections. The raw materials that can be used for carbonation must be abundant, ideally already pre-processed, and cheap. This section focuses on natural mineral feedstocks.

From a chemical element perspective and a thermodynamic point of view, both alkali metals (i.e., Na, K, etc.) and alkaline earth metals (i.e., Ca, Mg, etc.) can be carbonated (Pan *et al.*, 2012; Teir, 2008). However, alkali metals are unsuitable for the long-term storage of CO₂ as their

carbonates or bicarbonates are soluble in water. Their dissolution would result in CO₂ being released back into the atmosphere. Additionally, minerals containing several other metals (e.g., Mn, Fe, Co, Ni, Cu, and Zn) could potentially be carbonated, but most of these elements are either too rare or too valuable to be used for the sequestration of CO₂ (Pan *et al.*, 2012; Teir, 2008). Magnesium and calcium are by far the most common in nature. The Earth's crust consists of roughly 2 mol-% magnesium and 2 mol-% calcium, primarily bound as carbonates and silicate minerals (Teir, 2008). Table 2-5 presents some of the natural minerals that are suitable feedstock for mineral carbonation.

The majority of research on mineral CO₂ sequestration is focused on the carbonation of natural silicate mineral materials, as exemplified in Daval *et al.* (2009), Haque *et al.* (2019), Krevor and Lackner, (2011a), and Power *et al.* (2013).

Table 2-5: Potential mineral rocks for mineral carbonation (King, 2022; Lackner *et al.*, 1995; Sanna *et al.*, 2014; Yadav and Mehra, 2021)

Rock	Minerals	Chemical formula	Mg (%)	Ca (%)	Fe ²⁺ (%)	R _{real} ¹	R _x ² (%)
Serpentine	Antigorite	Based on a rock formation it can be $X_{2-3}Y_2O_5(OH)_4^3$	26.1	0.019	2.61	2.1	92
	Lizardite		23.9	0.314	2.4	2.5	40
Olivine	Fayalite	Based on a rock formation it can be $A_2SiO_4^4$	0.3	0.6	44.3	2.8	66
	Forsterite		27.9	0.1	6.1	1.8	81
Feldspar	Anorthite	$CaAl_2Si_2O_8$	4.8	10.3	3.1	4.4	9
Pyroxene	Augite	(Ca, Na) (Mg, Fe, Al) (Si, Al) ₂ O ₆	6.9	15.6	9.6	2.7	33
Basalt		Based on a rock formation	4.3	6.7	6.7	4.9	15
Ultramafic	Talc	$Mg_3Si_4O_{10}(OH)_2$	15.7	2.2	9.2	2.8	15
Ultramafic	Wollastonite	$CaSiO_3$	0.3	31.6	0.5	2.8	82
Ultramafic	Harzburgite	$CaMgSi_2O_6+(Fe, Al)$	46.4	0.5	7.8	7.3	-

2.3.1 Carbonation potential and efficiency of natural silicate rocks

Carbonation potential is a theoretical parameter that represents the value of a specific mineral reactant in mineral carbonation. Goff *et al.* (2000) initially described this parameter regarding the hydrated magnesium silicate serpentine [$Mg_3Si_2O_5(OH)_4$]. Goff used the molar concentration of Mg^{2+} in a serpentine sample to calculate the theoretical number of moles of CO_2 , which reacts with the serpentine and converts it to magnesite ($MgCO_3$) (Goff *et al.*, 2000). This method was modified by O'Connor *et al.* (2005) to include the cations Ca^{2+} and Fe^{2+} in the calculation because all three cations can potentially form stable carbonate compounds.

¹ Ratio of ore mass that must be processed to carbonate 1-unit mass of CO_2 , assuming 100% carbonation of all Ca, Mg, and Fe^{2+} .

² Reaction efficiency

³ Where X could be Mg, Fe^{2+} , Fe^{3+} , Ni, Al, Zn, or Mn and Y could be Si, Al, and Fe. For example, the Antigorite can be presented as $(Mg, Fe)_3Si_2O_5(OH)_4$

⁴ Where A could be Mg or Fe. For example, the Fayalite can be presented as Fe_2SiO_4 and pure Forsterite can be expressed by Mg_2SiO_4

The carbonation potential, R_{real} is defined as the mass ratio of rock or mineral necessary to convert a unit mass of CO_2 to the solid carbonate (Eq. 2.3). By this definition, a low R_{real} is preferable to a high R_{real} (O'Connor *et al.*, 2005).

$$R_{\text{real}} = \frac{100}{(\sum[\text{Ca}^{2+}] + [\text{Fe}^{2+}] + [\text{Mg}^{2+}]) \times MW_{\text{CO}_2}} \quad (2.3)$$

where \sum is the sum of the molar concentrations for the specified cations. MW_{CO_2} is the molecular weight of CO_2 .

While the R_{real} is a property of a rock or mineral, based on its chemical composition (O'Connor *et al.*, 2005), the carbonation reaction efficiency of that rock or mineral is also dependent on numerous additional factors, including the mineral composition, pretreatment methods, and solubility at the specific carbonation conditions of time, temperature, pressure, and pH. The reaction efficiency of mineral rock, R_x , is the percent stoichiometric conversion of the Ca^{2+} , Fe^{2+} , and Mg^{2+} in silicate feed to their carbonate counterparts.

$$R_x = \frac{X_{\text{CO}_2}}{\varepsilon_A \times (1 - X_{\text{CO}_2})} \quad (2.4)$$

where X_{CO_2} is CO_2 concentration in the solid products in weight percent. ε_A is percent weight gain assuming 100% stoichiometric conversion of the available cations to the carbonates (O'Connor *et al.*, 2005).

2.3.2 Studies of mineral carbonation by neutral silicate materials

A summary of the significant studies of mineral carbonation is presented in Table 2-6. The most common natural silicate minerals used in mineral carbonation are wollastonite, serpentine, and

olivine. According to Table 2-6, all samples are pretreated. The purpose of the pre-treatment step is to promote and accelerate carbonation reaction rates and the efficiency of the process (Sanna *et al.*, 2014a).

- ***Pre-treatment of feedstock***

Numerous options exist for pre-treating the feedstock to enhance the carbonation rate. Mechanical activation, heat activation, chemical activation techniques, ultrasonic, and microwave activation are detailed below:

Mechanical activation: In this pre-treatment process, mechanical force is used to accelerate the reaction rate by making changes to the surface properties and crystal structures of minerals. (Li and Hitch, 2016). The mineral feedstock is ground because the reaction rate increases with the specific surface area. Wet grinding creates smaller particles, but the dry grinding process is more effective in disrupting the lattice structure and generating a more reactive product. The feedstock particles are typically reduced to an average diameter of 100-150 μm , with further reduction to less than 38 μm being a trade-off between additional energy costs and increased mineral conversion. (Li and Hitch, 2018; Rackley, 2017).

Chemical activation techniques: There is a wide range of organic and inorganic acids, bases, and salts available as options to improve feedstock reactivity. A possible disadvantage of this method is the reduction in alkaline metal content in the feedstock, leading to increased sequestration costs. (Huijgen and Comans, 2005)

Heat (thermal) activation: Heat activation is a common pre-treatment method for natural minerals, used to remove chemically bound water from the ores. For instance, heating serpentine to temperatures around 600-650 °C changes its crystalline characteristics, transforming it from crystalline to amorphous as hydroxyl groups decompose. After heat treatment, the materials experience an increase in porosity and surface area, leading to an unstable structure that subsequently promotes the rate of carbonation (Jie Li *et al.*, 2018; Park and Fan, 2004a). The energy required for heat pre-treatment is considerable and can exceed the energy released from carbon combustion, which generates the volume of CO₂ captured as carbonate. Therefore, achieving a net-negative heat treatment sequestration efficiency seems viable only when waste process heat is available through integration with another industrial process (Rackley, 2017).

Ultrasonic and microwave activation: Early works on mineral activation through ultrasonic or microwave pre-treatment do not yield higher reactivity (Rackley, 2017).

Conventional grinding remains the sole viable pre-treatment option that has demonstrated both energetic and economic feasibility. Heat treatment, due to its high energy consumption, appears to be a candidate for avoidance. However, if waste process heat is accessible through integration with another industrial process, this pre-treatment approach could be considered (Huijgen and Comans, 2005). The benefits of all pre-treatment options should be weighed against their additional costs and energy consumption.

In most studies, process heating and pre-treatment (thermal and mechanical) are the most energy-intensive processes (Huijgen *et al.*, 2007). Among the natural silicates used, wollastonite does not necessitate thermal feedstock activation due to the absence of hydroxyl groups in its crystal structure (Veetil and Hitch, 2020b).

Table 2-6: Summary of the significant studies of mineral carbonation using natural minerals (DAC = direct aqueous carbonation, DC = direct carbonation, IC = indirect carbonation, CEA= Chemical extraction agent used for metal leaching)

Resource	Metal Oxide (%)	Particle size	Additives	CO ₂ % in gas	Pre-treatment	Reaction conditions	Efficiency/ Amount	Cost US\$/ tCO ₂	Reference
Wollastonite	CaO: 30	< 38 μm	No	~ 100	Mech. grinding	DAC, T = 200 °C, P = 20 atm, L/S=2 kg/kg, t=15 min	69	102	(Huijgen <i>et al.</i> , 2007, 2006)
Wollastonite	CaO: 22	< 38 μm	No	~ 100	Mech. grinding	DAC, T = 200 °C, P= 20 atm, L/S=2 kg/kg, t= 15 min	67	77	(Huijgen <i>et al.</i> , 2007, 2006)
Wollastonite	CaO: 42.05	< 75 μm	No	~ 100	Mech. grinding	DAC, T = 150 °C, P = 40 atm, t= 1 hour	83.5	-	(Yan <i>et al.</i> , 2015b)
Wollastonite	-	< 75 μm	No	~ 100	Mech. grinding	DAC, T = 100 °C, P= 40 atm, t=1 hour	70	112	(Gerdemann <i>et al.</i> , 2007a)
Wollastonite	CaO: 32.4	15.6 μm	0.02 % NaCl	~ 100	-	DAC, T=150 °C, P= 4 MPa, stir, L/S=13 kg/kg, t=2 hour	90	-	(Zevenhoven <i>et al.</i> , 2010)
Wollastonite	-	38 μm	No	~ 100	Mech. grinding	DC, T=100 °C, P= 40 bar, t=1 hour	80	-	(O'Connor <i>et al.</i> , 2000)
Wollastonite	-	NA	succinic acid	~ 100	-	IC, T=80 °C, P= 30 bar	-	-	(Baldyga <i>et al.</i> , 2010)
Wollastonite	CaO: 46.6	NA	NH ₄ OH	~ 99.9	-	IC, CEA: 6 M HCl, Dissolution T = 80 °C, t = 3 h Carbonation T = 30 °C, P = 1 atm, t= 1 h	93	120	(Ding <i>et al.</i> , 2016)
Serpentine	-	< 75 μm	0.64 M NaHCO ₃ & 1 M NaCl	~ 100	Heat treatment: 630 °C, Mech. Grinding	DAC, T = 155 °C, P = 115 atm	65	300-500	(Gerdemann <i>et al.</i> , 2007a)
Serpentine	MgO: 45.7	< 37 μm	0.64 M NaHCO ₃ & 1 M NaCl	~ 100	Heat treatment: 630 °C, Mech. Grinding	DAC, T = 155 °C, P = 185 atm	78	-	(O'Connor <i>et al.</i> , 2001a)
Serpentine	-	150–200 μm	NaHCO ₃	15	Heat treatment: 650 °C, Mech. Grinding	DC, T = 140 °C, P = 30-40 bar	-	-	(Sanna <i>et al.</i> , 2014; Verduyn <i>et al.</i> , 2011)
Serpentine	-	100 μm	Acid/NH ₃	~ 100	Mech. Grinding	DC, T = 550 °C, P = 50 bar	90	-	(Wee, 2013)
Serpentine	MgO: 44.82	75 μm	NH ₄ OH	~ 100	Mech. Grinding	IC; CEA: 1 vol % H ₃ PO ₄ , 0.9 wt. % C ₂ H ₂ O ₄ , and 0.1 wt. % EDTA; Dissolution T = 70 °C, time = 1 h; Carbonation T = 25 °C, P = 1 atm, L/S=2.5 g/80 mL, t = 10 min	65	-	(Park and Fan, 2004b)
Serpentine	-	75 μm	NH ₄ HCO ₃ / NH ₃	~ 100	Mech. Grinding	IC; CEA: NH ₄ SO ₄ and NH ₃ ; Dissolution T = 100 °C, t= 2 h; Carbonation T = 85 °C, P = 1 atm, t = 30 min	95.9	-	(Wang and Maroto-Valer, 2011)

Resource	Metal Oxide (%)	Particle size	Additives	CO ₂ % in gas	Pre-treatment	Reaction conditions	Efficiency/ Amount	Cost US\$/ tCO ₂	Reference
Serpentine	MgO: 40.72	10-56 µm	1 M Na ₂ CO ₃	~ 100	Mech. Grinding	IC; CEA: Leaching 1 M HCl Purification 1 M NaOH; Dissolution T = 80 °C, t = 6 h; Carbonation T = 50 °C, P = 1 atm, t = 1 h	82.5	-	(Hemmati <i>et al.</i> , 2014b, 2014a)
Serpentine	MgO: 40.1	75–150 µm	NH ₄ HCO ₃	~ 100	Mech. Grinding	IC; CEA: Leaching 1.4 M NH ₄ HSO ₄ Purification NH ₄ OH; Dissolution T = 100 °C, P = 1 atm, t = 3 h; Carbonation T = 80 °C, P = 1 atm, t = 1 h	93.5	-	(Sanna <i>et al.</i> , 2013)
Serpentine	-	75 µm	-	~ 100	Mech. Grinding	IC; CEA: 0.1 M citrate, EDTA; T = 120 °C, P = 2 atm, t = 2 h	60	-	(Krevor and Lackner, 2011b)
Serpentine	-	425 µm	(NH ₄) ₂ SO ₄ / NH ₃	~ 100	Heat treatment: 250 °C, Mech. Grinding	IC; T = 500-550 °C, P = 2 atm, t = 30 min	60	-	(Nduagu <i>et al.</i> , 2012)
Olivine	MgO: 46.8	37 µm	0.50 M NaHCO ₃ & 1 M NaCl	~ 100	Mech. Grinding	DAC; T = 185 °C, P = 115 atm, t = 6 h	80	-	(O'Connor <i>et al.</i> , 2001a)
Olivine	-	75 µm	0.64 M NaHCO ₃ & 1 M NaCl	~ 100	Mech. Grinding	DAC; T = 185 °C, P = 150 atm, t = 6 h	80	80	(Gerdemann <i>et al.</i> , 2007a)
Olivine	MgO: 46.4	100 µm	No	~ 100	Heat treatment: 1000 °C, Mech. Grinding	DAC; T = 180 °C, P = 20 atm, t = 24 h	78.8	-	(Julcour <i>et al.</i> , 2015)
Olivine	MgO: 50.9	38 µm	2.5 M NaHCO ₃ & 1 M NaCl	~ 100	Mech. Grinding	DAC; T = 185 °C, P = 65 atm, t = 6 h	84.4	-	(Li <i>et al.</i> , 2019)
Olivine	MgO: 48.1	75-100 µm	NH ₄ HCO ₃	~ 100	Mech. Grinding	IC; Dissolution T = 100 °C, t = 3 h; Carbonation T = 90 °C, pCO ₂ = 1 atm, t = 1 h	90	-	(Sanna <i>et al.</i> , 2014a)
Olivine	-	75 µm	NaHCO ₃	~ 100	Heat treatment: 630 °C, Mech. Grinding	DAC, T = 185 °C, P = 150 atm, t = 1-2 h	80	-	(Gerdemann <i>et al.</i> , 2007a)
Olivine	MgO: 49.3	10 µm	-	20	Mech. Grinding	DC, T = 150-200 °C, P = 0.37 atm, t = 14 min	25	-	(Kwon <i>et al.</i> , 2011)
Olivine	-	65 µm	-	10	Mech. Grinding	IC; Leaching, NH ₄ HSO ₄ ; Dissolution T = 61 °C, t = 2 h; Carbonation T = room temp, P = 1 atm, t = 2 h	43	-	(Reynes <i>et al.</i> , 2021)
Dunite	MgO: 45.3	20–45 µm	0.64 M NaHCO ₃	~ 100	Mech. Grinding	T = 180 °C, P = 130 atm, t = 8 h	62.3	-	(Rashid <i>et al.</i> , 2019)

- ***Challenges in utilizing natural materials as feedstock for mineral carbonation***

Although the natural silicate minerals have sufficient capacity for CO₂ storage, using them as feedstock for mineral carbonation presents certain challenges. Mining operations are required to extract the raw materials for mineral carbonation. Furthermore, mineral carbonation demands substantial energy input, making it an energy-intensive process to facilitate the carbonation reaction. (Chiang and Pan, 2017a). For example, a considerable amount of energy is needed for several aspects, such as:

- Preparation of the solid minerals, involving mining, transportation, grinding, and activation when required
- Processing, including the energy associated with recycling and possible losses of additives or catalysts
- Separation of valuable metals (e.g., iron oxide) from the feedstock before undergoing accelerated carbonation or accelerated weathering, and disposing of carbonates and by-products (Gerdemann *et al.*, 2007b; IPCC, 2005a)

Pure calcium or magnesium oxides are rare in natural minerals due to their high reactivity. As illustrated in Table 2-6, calcium or magnesium are present in various oxides within a silicate matrix. The conversion of silicate to carbonate does not occur in the solid state; rather, it necessitates the dissolution of minerals in the aqueous phase. (O'Connor, Dahlin, Rush, *et al.* 2001). In general, the dissolution of the mineral constitutes the rate-limiting step in the aqueous mineral carbonation process.

The mineral carbonation reaction is limited by mass transfer phenomena resulting from slow reaction kinetics, which necessitates the use of large reactor sizes. An estimated reactor volume of approximately 60 m³ could potentially achieve a 20% reduction in the CO₂ emissions from a typical 500-MW coal-fired power plant (Rau *et al.* 2007).

2.4 Alkaline waste materials

Alkaline waste residues have some distinct advantages over natural mineral feedstocks. There is not any requirement for mining activities when an industrial alkaline waste material is used as feedstock. Moreover, these wastes are relatively cheap and are frequently close to CO₂ emission points (e.g., power plants and industries), where the cost of transportation can be reduced considerably. Table 2-7 shows examples of industrial alkaline wastes that have been tested as feedstock for mineral carbonation.

Alkaline waste residues are highly reactive and may not require pre-treatment to achieve high carbonate conversions. Furthermore, the carbonation of alkaline waste residues can improve their environmental qualities and allow them to be stored more safely, reused, or sold as value-added by-products (Sanna *et al.*, 2014a; Veetil and Hitch, 2020a; Woodall *et al.*, 2019).

Table 2-7: The examples of alkaline wastes used as feedstock for mineral carbonation collated from Chiang and Pan (2017a), Doucet (2010a), Li (2016), Sánchez-Cotte *et al.* (2020) and, Sanna *et al.* (2012)

Waste Group	Types of wastes	MgO (%)	CaO (%)
Iron and steel slags	Blast furnace slag (BFS)	6-11	15-41
	Basic oxygen furnace slag (BOFS)	1.5-10	34-55
	Electric arc furnace slag (EAFS)	1.9-17.6	25-47
	Ladle furnace slag (LFS)	7.5-11.9	50.5-57.5
	Argon oxygen decarburization slag (AODS)	8.0-9.0	54.5-58.8
	Electric arc furnace reducing slag (EAFRS)	6.2-9.8	40.8-49.4
Cement wastes	Cement kiln dust (CKD)	1.5-2.1	34.5-46.2
	Cement bypass dust (CBD)	0.8	68.0
	Recycled concrete aggregate (RCA)	1.0-5.11	6.5-22.8
Air pollution control (APC) residues	Municipal solid waste incinerator (MSWI) fly ash	1.9-2.1	16.4-21.1
	Air pollution control (APC)	8	50-60
	Coal fly ash	2.4-3.9	5.9-9.2
	Cyclone dust	-	-
	Cloth-bag dust	-	-
Bottom ash (from furnace or incinerator)	MSWI bottom ash	2.8	32-53
	Boiler ash (BA)	-	-
	Coal slag	-	-
	Oil shale ash	42-50	5-6.5
	Wood ash (WA)	8-9	24-46
Mining and mineral processing wastes	Red mud (RM)	0.27-2.06	2.99-42.2
	Asbestos tailings	39.4	0.16
	Nickel tailings (Nickel-copper-tailing)	0.04-1.2	32.83
Paper mill wastes	Lime kiln residues (calcium mud or lime mud)	-	-
	Green liquor dreg	-	-
	Paper sludge	1.3-5.3	45-69

2.4.1 Carbonation capacity and efficiency of alkaline waste residues

The carbonation capacity, or the CO₂ uptake capacity, can be deemed as the net uptake of CO₂ as a proportion of the mass of the original material before carbonation. The determination of the CO₂ uptake capacity can be measured by different methods, such as the mass gain method, the mass curve method, and the thermogravimetric analysis.

$$CO_{2-uptake} = \frac{M_{CO_2}}{M_c} \times 100 \quad (2.5)$$

where M_{CO_2} is the mass of CO_2 that has been successfully sequestered in carbonation treatment and M_c is the original mass of the material before carbonation treatment.

The other key parameter to quantify the carbonation effect of materials is the carbonation efficiency (or degree of carbonation). The carbonation efficiency (E_{CO_2}) is estimated by comparing the successfully captured mass of CO_2 (M_{CO_2}) by a material under a given condition, with the calculated theoretical extent of carbonation based on the composition of the pre-carbonated waste. (Eq. (2.6))

$$E_{CO_2} = \frac{M_{CO_2}}{M_c \times Th_{CO_2}} \times 100 \quad (2.6)$$

where Th_{CO_2} is the theoretical mass fraction of CO_2 sequestration achievable based on stoichiometry and the reactive-oxide content of the waste and it is determined based on Steinour's formula (Andrade and Sanjuán, 2018) or Huntzinger's formula (Huntzinger *et al.*, 2009).

$$\begin{aligned} Th_{CO_2} = & 0.785 \times (\%CaO - 0.53 \times \%CaCO_3 - 0.7 \times \%SO_3) \\ & + 1.091 \times \%MgO + 0.71 \times \%Na_2O \\ & + 0.468 \times (\%K_2O - 0.632 \times \%KCL) \end{aligned} \quad (2-7)$$

This method is based on the assumption that the total amount of Ca^{2+} and Mg^{2+} can be fully extracted from the waste, and subsequently, carbonated (Sun, 2010). The experimental CO_2 uptake (ECO_2 uptake) expressed in wt.% is also presented in Table 2-7.

The storage of CO₂ can be maximized by optimizing the operating conditions including pressure, temperature, liquid-to-solid ratio, gas humidity, the gas flow rate, the liquid flow rate, particle size, and solid pre-treatment (Sanna *et al.*, 2014a).

2.4.2 Studies of mineral carbonation by alkaline waste materials

Table 2-8 presents some of the studies of mineral carbonation by alkaline waste materials. The direct comparison of the performance of mineral carbonation for different alkaline wastes is difficult because each waste has its own unique set of advantages and disadvantages (Pan *et al.* 2015). For example, industrial alkaline wastes such as air pollution control wastes and ashes from solid fuel combustion often contain a considerable amount of free lime (Sanna *et al.* 2014). However, the steelmaking slag may contain a significant fraction of CaO and MgO.

The alkaline-earth metal oxides are primarily locked into silicate, aluminate, or ferrite phases (Lekakh *et al.* 2008). Notably, the mineralogical compositions of the steel slags are generally more complex than other types of waste materials, such as air pollution control ashes (Pan *et al.* 2015).

Table 2-8: Main properties and carbonation conversions of waste materials (DC – direct carbonation, DAC – direct aqueous carbonation, IAC – indirect aqueous carbonation, NW – natural weathering, CRW – cold rolling wastewater, DI – deionized water)(Bobicki *et al.*, 2012b; Reddy *et al.*, 2019; Sanna *et al.*, 2014a)

Waste	Composition		Th _{CO2} (%)	Particle size (µm)	CO ₂ % in gas	Reaction conditions	ECO ₂ (%)	Advantage	Disadvantage
	CaO (%)	MgO (%)							
Iron and Steelmaking slags									
BFS	15-42	5-11	20-44	10	-	IAC: (1) step (T = 70 °C, CH ₃ COOH); (2) step (T = 30 °C, P = 1 bar, NaOH)	22.7	<ul style="list-style-type: none"> • High CO₂ sequestration capacity • Generated in large quantities • Generated near CO₂ source • Possible applications: PCC • Carbonation improves mech. char. of slag 	<ul style="list-style-type: none"> • Must undergo milling, except AODS and LFS • High T&P or additives are needed for acceptable conversion • Currently expensive to achieve high carbonate conversion • High energy consuming
				-	100	DAC: P = 5 bar; L/S = 0.15; t = 2 h	7		
	38.3	10.2	98	75-150	-	DAC: T = 100 °C; P = 1 bar; t = 30 min	-		
BOFS	34-56	2-6	29-52	38	100	DAC: T = 100 °C; P = 19 bar, L(DI)/S = 2; t = 30 min	25		
				-	100	DAC: T = 70 °C; P = 1 bar; L(DI)/S = 10; t = 2 h	22.9		
				-	100	DAC: T = 60 °C; P = 1.47 bar; L(DI)/S = 20; t = 30 min	28.9		
				44	-	DAC: T = 25 °C; P = 1 bar; L(CRW)/S = 20; t = 125 min	28.3		
				2000	13	IAC: (1) step (T = 80 °C P= 1 bar, NH ₄ Cl); (2) step (T= 80 °C, t= 2h)	16.2		
EAFS	25-47	4-9	24-48	-	100	IAC: (1) step (T = 30 °C; CH ₃ COOH); (2) step (T = 30 °C; P = 1 bar; NaOH)	9		
				38-106	15	DAC: T = 20 °C; P = 1 bar; L(DI)/S = 10; t = 40 h;	1.74		
				100	15	DAC: T = 20 °C; P = 1 bar; L(DI)/S = 10; t = 65 min	1.9-8.7		
				-	100	DAC: P = 5 bar; L/S = 0.15; t = 2 h	12		
				150	100	DAC: T = 50 °C; P = 3 bar; L/S = 0.4; t= 1-4 h	18		
AODS	41-61	4-7.5	31-54	63-200	100	DAC: T = 50 °C; L(DI)/S = 10; t = 4 h;	15.1		
				-	10	DAC: T = 50 °C; L (16.6 g L ⁻¹ MgCl)/S = 10; t = 240 min	27		
				-	-	DAC: T = 90 °C; P = 9 bar; L/S = 16; t = 120 min	26.4		

Waste	Composition		Th _{CO2} (%)	Particle size (µm)	CO ₂ % in gas	Reaction conditions	ECO ₂ (%)	Advantage	Disadvantage
	CaO (%)	MgO (%)							
Cement wastes									
CKD	34-48	1-1.5	10-30	-	5 -15	DAC: ambient T&P; L/S = 0.33; t= 8 h	8-18	<ul style="list-style-type: none"> Generated in large quantities Generated near CO₂ source (CKD, CBD) Carbonated product can be reused in cement manufacturing, aggregates, to produce PCC etc.; CKD, CBD has fine particle size; 	<ul style="list-style-type: none"> Waste cement needs to be ground Low carbon sequestration capacities (CKD); cost: IAC with PCC production: \$136 - 323 per t-CaCO₃
				-	100	DAC: ambient T, P = 2 bar; H ₂ O to form paste; t = 72 h	10		
CBD	66	1	50	-	100	DAC: ambient T, P = 2 bar; H ₂ O to form paste; t = 72 h	25		
				1.8	0.03-100	DAC: T = 20 °C; P = 1-4 bar; L/S = 0.25-0.5; t = 0.8-100 h;	1.6-16.5		
RCA	25-63	0.3-2	20	-	20	DAC: T = 20 °C; L(DI)/cement = 0.26; t = 60 min	8.9		
MSWI ashes									
MSWI				710	100	DAC: P = 3 bar; L/S = 0.3-034; RH =65%; t = 2.5 h	3.2	<ul style="list-style-type: none"> Produced in large quantities (MSWI BA) Produced near CO₂ source Carbonation reduces pH and leaching of hazardous elements for safer landfill Grinding not required 	<ul style="list-style-type: none"> Low carbon sequestration capacity (MSWI BA)
BA	22-53	2.8	25	-	100	DAC: ambient T, P = 2 bar; H ₂ O to form paste; t = 72 h	4		
				212	100	DAC: P = 3 bar; L/S = 0.2-0.3; RH = 65%; t = 2.5 h	7.3		
APC residue	36-60	1-2.5	50-58	66	20	DAC: T = 20-30 °C; L/S = 0.3; t = 50-150 min	8-12		
				-	10-50	DC: T = 650-500 °C; P = 1 bar	25		
				-	100	T = 30-50 °C; P = 1-10 bar; L/S = 0-0.6	25		
Alkaline paper mill wastes									
APMWA	45-82	1-5	45-55	15	-	DAC: T = 30 1C; P = 10 bar; L(DI)/S = 20; t = 2 h	21.8	<ul style="list-style-type: none"> High carbon sequestration capacity Grinding not required 	<ul style="list-style-type: none"> Generated in small quantities
				-	100	DAC: ambient T& P = 2 bar; H ₂ O to form paste; t = 72 h	10-26		

Waste	Composition		Th _{CO2} (%)	Particle size (μm)	CO ₂ % in gas	Reaction conditions	ECO ₂ (%)	Advantage	Disadvantage
	CaO (%)	MgO (%)							
Fuel combustion ashes (FA)									
Coal FA	1.3-10	1-3	6-9	40	100	DAC: T = 20–60 °C; P = 10–40 bar; L/S = 10; t=18 h	2.6	<ul style="list-style-type: none"> Produced in large quantities (coal FA) Produced near CO₂ source Grinding usually not required High CO₂ sequestration capacity (OS FA) 	<ul style="list-style-type: none"> Low CO₂ sequestration capacity (coal FA) Waste available in few areas (OS FA); cost: \$11-21 per tCO₂ at mineralization capacity of 0.1-0.2 tCO₂ per t-FA.
				20-150	100	DAC: T = 30 °C; 90 1C; P = 10–40 bar;L/S= 1–10	3.6-7.2		
				-	-	DAC: T = 90 °C; P = 40 bar; L/S = 1; bulk ash; t = 2 h	6.5		
				-	-	NW: ambient T&P; wet deposited ash; t= 20 years	6.8		
Lignite FA	27.5	6.5	43	<250	10	DAC: T = 75 °C, P = 1 bar; L/S = 20; 4.5 h	23	<ul style="list-style-type: none"> Carbonation destroys the asbestos nature (asbestos tailings, Ni tailings if chrysotile present) Grinding not required (asbestos and Ni tailings) Large quantities produced in localized areas 	<ul style="list-style-type: none"> Low carbon sequestration ECO₂ Too expensive to achieve high carbonate conversion (asbestos and Ni tailings) Bicarbonates generated instead of carbonates (RM); cost: \$147 per tCO₂ for DAC of RM;162 IAC of Ni tailings with hydromagnesite production US\$600- 1600 per tCO₂ for chemicals only
				30-125	100	DAC: T = 30–80 °C; L/S = 40–80; NaCl 1–25 g L-1; pH = 5–9; t = 10–50 min	7.1		
Oil shale FA	38-50	5-12	26-49	15	-	DAC: ambient T&P; L/S = 10; t = 65 min	29		
				-	-	NW: ambient T&P; wet deposited ash; t = 8 w	2.2		
Wood Ashe	24-46	8-9	50	-	100	DAC: ambient T& P = 2 bar; H ₂ O to form paste; t = 72 h	8		
Mine tailings									
Asbestos tailings	0.2	39	43	37-75	56	DC: T = 375 °C; P = 1 bar; 10% H ₂ O; t = 5 h	0.5	<ul style="list-style-type: none"> High carbon sequestration capacity Grinding not required 	<ul style="list-style-type: none"> Generated in small quantities
Nickel tailings	3.4	21-40	43	<0.5	100	IAC: (1) step (T = 70 1C; L (4 M HCl, HNO ₃)/S = 10; t = 2 h); (2) step (T = 30 °C; NaOH; t = 0.5 h)	29		
Red mud	2-7	<1	7-19	30	-	DAC: T = 20 °C; P = 3.5 bar; L/S = 0.2-0.6; t = 12 h	5.3		
				0.1-160	100	DAC: ambient T&P; 3 carbonation cycles, (each 5h)	7.2		
				<1000	15	DAC: ambient T&P; L/S = 10; t = 24 h	4.15		
APMWA	45-82	1-5	45-55	15	-	DAC: T = 30 1C; P = 10 bar; L(DI)/S = 20; t = 2 h	21.8		
				-	100	DAC: ambient T& P = 2 bar; H ₂ O to form paste; t = 72 h	10-26		

- **Iron and Steelmaking slags**

The iron and steel industry produces 2.6 Gt CO₂ annually and it consumes 7% of the global energy (“Iron and Steel Technology Roadmap Analysis,” 2022). Steel slag is an inevitable by-product of the manufacture of steel from pig iron (blast furnace) and metal scrap (electric arc furnace). During steel production, 2 to 4 tons of solid wastes are generated per one ton of steel produced. The main types of iron and steelmaking slags are classified as blast-furnace slag (BFS), basic oxygen furnace (BOFS), electric arc furnace (EAFS), and ladle furnace (LFS) slags each named for the processes where they are produced (Sanna *et al.*, 2012; Yildirim and Prezzi, 2011).

The chemical composition of slags can change widely due to the production process, the type of furnaces from which they are produced, and the raw materials and their particle sizes. However, their composition, especially in the form of Ca and Mg silicates, is like natural sand, gravel, and crushed stones (Chiang and Pan 2017a; Sanna *et al.* 2014). The mineralogical compositions of the steel slags are generally more complex than other types of industrial waste like air pollution control ashes. They are a consolidated mix of many compounds, e.g., primarily calcium, iron, silicon, aluminum, magnesium, and manganese oxides, presented in different phases (Pan, Chiang, *et al.* 2018).

USA, Japan, Germany and France utilize most of the produced steel slag. The iron and steel slags can be utilized in the following fields: (a) aggregate in concrete or asphalt, (b) cement industry, (c) road construction, (d) glassmaking, (e) ceramic tiles, (f) soil conditioner for agriculture, (g) aquaculture, and (h) land amendments (Yi *et al.* 2012). However, conventional

uses of untreated iron and steel slags in civil engineering have faced several technological barriers, such as heavy metal leaching and low cementitious property of slag (Chiang and Pan 2017b).

The iron and steel industries are one of the highest CO₂ emitters. For every single tonne of iron / steel manufactured, 0.28 to 1.0 tonnes of CO₂ is released into the atmosphere (Yadav and Mehra 2021). The recent studies on the steel slag as a feedstock for the CCS process (Table 2-8) show that the different types of steel slag have a considerable reactivity with CO₂, allowing achievement, for specific process routes and operating conditions, high CO₂ uptake (Bobicki *et al.* 2012b; Baciocchi *et al.* 2016; Huijgen and Comans 2006). Eloneva *et al.* (Eloneva *et al.* 2008) show the steelmaking slag can sequester up to 171 million tonnes of CO₂ per year globally which amounts to storing 0.6% of the global CO₂ emissions annually

- **Cement waste**

Waste cement is a by-product obtained from the aggregate recycling process. The CO₂ emissions of cement manufacturing are significantly high and are responsible for approximately 5-8% of global CO₂ emissions annually (de Lorena Diniz Chaves *et al.* 2021). The cement-type wastes are mainly composed of SiO₂, CaO, Al₂O₃, and Fe₂O₃, along with several trace elements such as SO₃, TiO₂, and Na₂O. The chemical composition of metal oxides with an alkaline character of cement-type wastes could be considered a suitable material for CO₂ mineralization (Chiang and Pan 2017b)

Annually, cement industries produce large amounts of cement waste in the form of cement kiln dust (CKD) and cement bypass dust (CBD). Cement kiln dust (CKD) is a fine powdery material that is the by-product of Portland cement and lime high-temperature rotary kiln

production. CKD is categorized as potentially hazardous waste because of its caustic nature and potential as a skin, eye, and respiratory irritant (Sanna *et al.* 2012). The cement industry generates 0.150 to 0.20 tonnes of CKD per tonne of cement (world output 2.8 Gt) (Sanna *et al.* 2014). The CDK ECO_2 uptake achieved is 8-25 wt.% (i.e., 0.08-0.25 t- CO_2 per t-CDK) (Dri 2014). Cement bypass dust (CBD), which is removed after kiln firing, has a much lower carbonate content than CKD, and therefore much higher potential to capture CO_2 (0.5 t- CO_2 per t-CBD) (Gunning, Hills, and Carey 2009).

Recycled concrete aggregate (RCA) is another type of cement waste. It is produced during the processing of inorganic material previously used in construction and principally comprises crushed concrete (Dri 2014). It consists of a series of calcium silicate hydrate, calcium aluminate hydrate, and calcium hydroxide compounds, which are all highly alkaline. Because of the high variability in CaO content, RCA ECO_2 uptake is also very variable, 6–22wt%.

Waste cement can be considered a significant source of mineral carbonation feedstock. The annual waste concrete production of EU, USA, and China is 1100 million tonnes which has the potential to capture up to 61 million tonnes CO_2 (Bobicki *et al.* 2012b). Considering the highest waste cement ECO_2 uptake as 16.5 CO_2 capture wt.% and taking the waste concrete produced in the above-mentioned countries, waste cement could collectively sequester a maximum of 60 million tonnes of CO_2 /year, accounting for 0.2% of global CO_2 emissions from fuel combustion.

- **Municipal solid waste incinerator (MSWI) fly ash**

Incineration is a popular waste management option for municipal solid waste processing. It produces a solid residual containing approximately 12% vol/vol CO_2 . The solid residues are rich

in calcium oxide. Mineral carbonation can be used to stabilize the MSWI ash before re-use or landfilling as it limits heavy metal mobility and aids in CO₂ sequestration. The small particle size of MSWI ash, high CaO concentration, and proximity to CO₂ sources are other factors that make MSWI ash favorable for CO₂ sequestration (Yadav and Mehra, 2021). The amount of municipal solid waste (MSW) was estimated at 1.3 billion tons per year worldwide in 2012 and is expected to rise to 2.2 billion tons in 2025 (Sanna *et al.*, 2012).

- **Fuel combustion ashes**

Coal fired power plants produce annually 12000 Mt CO₂ and 600 Mt fly ash. The combustion of fossil fuels such as coal, oil, and natural gas in power plants for generating electricity contributes over 70% of the total global CO₂ emissions (Ho *et al.*, 2019; Romano *et al.*, 2013). The bituminous fly ash contains 5-10% CaO and 1-3% MgO. The CO₂ sequestration potential of bituminous coal FA is relatively low ~ 9wt% but it could reach 43-49% for Ca-rich lignite type coal or oil shale ashes (Sanna *et al.*, 2014).

- **Mine tailings and alkaline paper mill waste**

The carbonation of these residues not only sequesters CO₂ but also improves the properties of these wastes materials before final storage: safely stored or used for secondary purposes. Mine tailings produced in asbestos, serpentine, dunite, and serpentinite sites can be used as a feedstock for mineral carbonation. In addition, residues such as red mud and bauxite from aluminum manufacturing sites can be used in carbon sequestration to improve their properties and make them suitable for reuse and safe landfilling (Bobicki *et al.*, 2012a; Yadav and Mehra, 2017). Due to the hazards involved in working with asbestos tailings, very little study has been undertaken on this

material (Azadi *et al.* 2019; McCutcheon *et al.* 2017). However, the carbonation process can fix and immobilize hazardous elements and mineral groups in carbonation forms to create environmentally benign products which can be used for mine site rehabilitation. (Bobicki *et al.*, 2012a; Pan *et al.*, 2015b; Sanna *et al.*, 2014b)

The cost involved in using nickel tailings as a CO₂ sequestration feedstock is high, but nickel tailings are often very rich in magnesium (40%). The use of new technologies to integrate the mining process with CCS could make nickel tailings a valuable raw material for feasible mineral carbonation (Bodor *et al.* 2013).

Red mud, an alumina manufacturing residue, is produced from the digestion of bauxite ores with caustic soda (i.e., Bayer process) under elevated heat and high pressure. It is a highly alkaline process (pH > 13) (Azadi *et al.*, 2019; Bobicki *et al.*, 2012a). For every tonne of alumina produced, approximately 1 to 1.5 tonnes of red mud are also generated. Annual production of alumina in 2020 was over 133 million tons resulting in the generation of over 175 million tons of red mud. ('Alumina Production' 2022). Mineral carbonation can be used to reduce and neutralize the alkalinity and contaminations in red mud. Carbonated red mud can be used for various applications like fertilizers, brick and tile industry, cement production, and wastewater treatment (Azadi *et al.*, 2019)

Production of cellulose pulp from paper manufacturing produces alkaline paper mill wastes (APMWs) which typically contain 42-82% free CaO. These materials are suitable sorbents for mineral carbonation. CO₂ is also a by-product of pulp production which can be used to carbonate the APMW. The resulting CaCO₃ from the carbonation process can be used in the pulp and paper industry or sold as a by-product (Yadav and Mehra 2021).

2.5 Summary

In this chapter, the post-combustion CO₂ capture and sequestration methods and options for mineral carbonation process routes have been detailed. An up-to-date review of the potential raw materials that can be used as the feedstocks for the sequestration of CO₂ has also been presented. Generally, mineral carbonation is a very promising option in terms of resources available and enhanced security, but the technology is still in its infancy and transport and storage costs are still higher than geological storage in sedimentary basins (\$17 instead of \$8 per tCO₂) (Sanna *et al.*, 2014b)

In the following chapter, the process chemistry and kinetics of direct aqueous mineral carbonation are described in detail.

3. The direct aqueous mineral carbonation chemical process

Direct aqueous mineral carbonation follows a complex reaction mechanism, which has been modeled in various ways (Gopinath and Mehra, 2018). Typically, three steps are involved:

- i) Dissolving CO₂ in water via gas-liquid interfaces (bubbles, contactor materials)
- ii) Mobilizing cations for CO₂ capture by dissolving calcium- and magnesium-bearing solids (dissolution of the minerals), and;
- iii) Formation of carbonate precipitates suspended in the liquid phase or at the liquid-solid interface (Pan *et al.*, 2012).

The work herein exemplifies the mineral carbonation process using a simplified system that starts with aqueous Ca(OH)₂ and the dissolution of the atmospheric CO₂ in water. Aqueous calcium hydroxide is a good choice of exemplar for the following reasons. First, as shown in Chapter 2, Ca is abundantly available in mineral and waste feedstocks, is relatively non-hazardous, and thus may be expected to be relatively inexpensive to obtain or procure for carbonation. Calcium carbonate precipitation from the carbonation of Ca(OH)₂ aqueous solution is a very familiar and classic reaction commonly observed in nature. Second, mineral carbonates such as CaCO₃ are thermodynamically one of the most stable forms of carbon. Therefore, long-term storage of CO₂ can be achieved once it is converted into carbonate form, and the product of this reaction is environmentally benign (Chang *et al.*, 2017; Han *et al.*, 2011a).

In this chapter, the process chemistry and kinetics of the reactions for CO₂ capture and sequestration using aqueous Ca(OH)₂ solutions are reviewed. Based on this review, a mathematical

model for the reaction set is formulated and subjected to verification tests to check that the model captures the necessary behaviors.

3.1 Reaction equilibria

3.1.1 Carbon species arising when CO₂ is dissolved in water

Carbon dioxide is a colorless, odorless, and non-flammable gas with a slightly sour taste that is essential to life on Earth. Its critical temperature, pressure, and density are 304.13 K (31.0° C), 73.8 bar (1070 psi), and 469 kg/m³, respectively. At standard temperature and pressure, the density of CO₂ is around 1.98 kg/m³, about 1.67 times that of air (Chiang and Pan, 2017a). The diffusion of CO₂ through water is approximately 10,000 times slower than through air (Gough, 2016).

The solubility of gases in water depends on temperature, pressure, liquid properties, the ratio of liquid to gas by volume or mass, and numerous additional factors. When the temperature rises, the solubility of CO₂ decreases due to increased kinetic energy. Higher kinetic energy leads to greater molecular motion, breaking intermolecular bonds and causing CO₂ to escape from the solution. (Dodds *et al.*, 1956). The solubility of CO₂ in water is directly proportional to the pressure. When the pressure is increased, the CO₂ molecules are forced into the solution (Mokhtari, 2016). Dodds *et al.* (1956) provide a CO₂ water solubility chart showing solubility as a function of pressure and temperature. Using the chart permits a more precise estimation of CO₂ solubility in water, and this is shown in Figure 3-1.

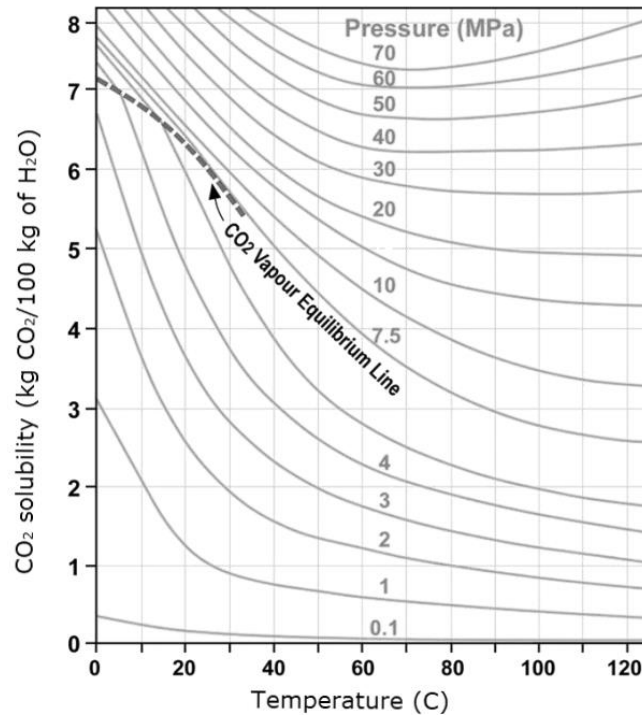


Figure 3-1: Solubility of carbon dioxide in water (temperature, pressure effects)(Dodds *et al.*, 1956)

The dissolution of the CO₂ in water can be considered a mass transfer process, the controlling factors of which are described in detail in Section 3.2.1 with more details. Here, the process is initially described in simpler terms. In a batch reactor (rather than an open reactor), the three major techniques available to increase the CO₂ transfer rate from the gas stream to the solution are (Jiajie Li *et al.*, 2018; Nasser, 2010; Park, 2005):

- Increasing the stirrer speed of the reactor (when there is a stirrer)
- Increasing the CO₂ concentration (partial pressure) in the input gas mixture
- Increasing the reaction pressure involving the gas

Increasing the stirrer speed increases the CO₂ transfer rate from the gas stream to the solution in the cited work, but the fundamental reason for high CO₂ transfer when stirred is because the

time that the gas bubbles are in contact with the liquid increases, an idea shared by (Hu *et al.*, 2011) and that the potential for gas transfer remains high because the liquid solution concentration becomes more homogenous. Agitation also breaks down the gas bubbles into smaller ones, increasing the surface area in contact with the liquid (Nasser, 2010). By Stoke's law, smaller bubbles will be suspended or entrained in liquid flows for longer periods (Dey *et al.*, 2019)

The physical dissolution of gaseous CO₂ in the solution is denoted in Eq. (3.1). Henry's constant controls the amount of CO₂ dissolution. According to Henry's law, up to a point, there is a linear relationship between the partial pressure of a gas and its concentration in a dilute solution (Rasi, 2009). As expressed in Eq. (3.2), Henry's law presents that the solubility of the gas in pure water is proportional to its partial pressure above the water. It is strictly valid only for gases that can be infinitely diluted in solution (Chiang and Pan, 2017a). At high pressures (more than 5 bar), Henry's law is no longer valid in its simple form, and temperature becomes a more critical factor than pressure for gas solubility (Rasi, 2009).



$$C_{CO_2} = K_H \times P_{CO_2} \quad (3.2)$$

In Eq. (3.2) C_{CO_2} is the concentration of CO₂ dissolved in aqueous solution (mol/L), K_H is Henry's solubility constant for CO₂, and P_{CO_2} is the partial pressure of CO₂ in the gas phase. The value of Henry's solubility constant (expressed in mol/L bar) is a function of temperature and can be expressed by Eq. (3.3).

$$\log K_H = 9.1229 - 5.9044 \times 10^{-2}T + 7.8857 \times 10^{-5}T^2 \quad (3.3)$$

where T is the temperature (K) (Velts, 2011). The dissolution of CO_2 (g) into an aqueous solution is described in more detail in Section 3.2.1.

When CO_2 is dissolved in water, the carbon in the CO_2 will exist in various chemical forms. The specific chemical form that arises depends on the pH of the solution in which the CO_2 dissolves. The possible forms are i) aqueous carbon dioxide, CO_2 (aq) ii) true carbonic acid, H_2CO_3 , iii) bicarbonate ions HCO_3^- (aq), and iv) carbonate ions, CO_3^{2-} (aq). Mineral carbonation becomes possible when there is sufficient availability of these carbon species in closed or open systems (Chiang and Pan, 2017a).

A closed system refers to one system where the total quantity of carbon species within the system remains constant, there is no exchange of carbon species with atmospheric CO_2 (g) or solid phases produced like CaCO_3 (Pankow, 1991). A system is considered open when the addition or removal of CO_2 with the environment occurs; for example a fixed volume of water in equilibrium with the atmosphere is characterized by a constant partial pressure of CO_2 (Pankow, 1991; Stumm and Morgan, 1995). The direct air CO_2 capture and mineralization of mine tailings materials discussed by Liu *et al.* (2021) is another example of an open system.

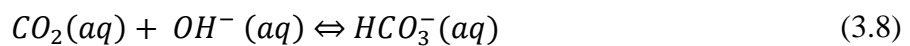
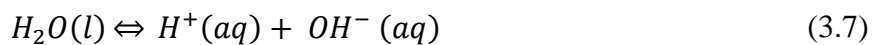
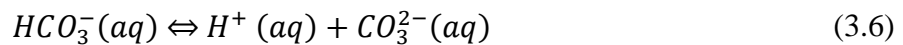
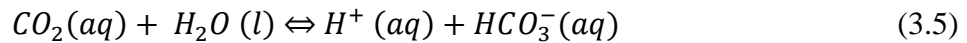
In an aqueous solution, less than 0.3% of the CO_2 is hydrated to H_2CO_3 (true carbonic acid) (Fioravante *et al.*, 2019). As it is difficult to distinguish between the un-ionized species CO_2 (aq) and the pure acid, H_2CO_3 , in consideration of dissolution processes, both quantities are frequently ‘lumped together’ to one single component in calculations, H_2CO_3^* :

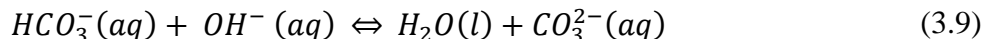
$$[\text{H}_2\text{CO}_3^*] = [\text{CO}_2 \text{ (aq)}] + [\text{H}_2\text{CO}_3] \quad (3.4)$$

where brackets represent total concentrations. $H_2CO_3^*$ is named *apparent* carbonic acid and is the carbonic acid that is generally accepted to be carbonic acid in the literature (Zeebe and Wolf-Gladrow, 2001a)

The relative concentrations of $CO_2(aq)$ and H_2CO_3 , and the deprotonated forms of bicarbonate $HCO_3^-(aq)$ and carbonate $CO_3^{2-}(aq)$, depend on the pH of the solution (Figure 3-2). At $pH < 6.5$, $H_2CO_3^*$ is the main constituent. At the pH ranging $6.5 < pH < 10.5$, the production of $HCO_3^-(aq)$ dominates. When the pH is more than 10.5, carbon species exist in the form of carbonate ions, $CO_3^{2-}(aq)$ (Han *et al.*, 2011a).

H_2CO_3 has a strong tendency for dissociation and rapidly breaks down into bicarbonate plus hydrogen ions. Thus, the concentrations of the H_2CO_3 specifically can be negligible (Khodayari, 2010). For these reasons, when the chemical reaction equations are written down as a complete set across the pH range, $H_2CO_3^*$ does not appear as a distinct species, but HCO_3^- and CO_3^{2-} feature instead as presented in Eqs (3.1) and (3.5) to (3.9):





These equations govern the dynamic equilibrium of the solution condition that is created when CO₂ is dissolved in water. If CO₂(g) cannot be introduced into the water by (3.1), then the following reactions to (3.9) are inhibited. When some CO₂(g) is dissolved to aqueous form, the system of equations brings about transformations of the concentrations of species, with a state of completion that depends on the so-called *equilibrium constants* with a pace which depends upon the so-called *kinetic constants*.

A large value of the equilibrium constant will reflect a reaction that has the potential to proceed to completion in the sense that the reactants shown on the LHS of the equilibrium sign are consumed virtually completely to produce the products that are shown on the RHS of the equilibrium sign.

The pH connected with the condition of the resulting solution, depends upon the extent to which the reaction kinetics and equilibrium constants permit the production of protons (3.7) and (3.8), as well as the availability of protons (or the consumption of protons) arising from external / additional reactions operating co-currently with CO₂ dissolution. An example of the latter would be the dissolution of NaOH in water at the same time as the dissolution of the CO₂ in water as in (Covington *et al.*, 1985). If the system is modelled, it must also accommodate kinetic rate constants depending upon the species actually present within the mix (and indirectly the equilibrium constants) which, in turn, depend on the pH. Such systems are complex and sets of coupled differential equations are required to represent the interactions.

Reaction (3.5) can be the rate controlling reaction of the dissolution of CO₂ in water as it is relatively slow (the kinetic constants are numerically small), except at high pH. Reaction (3.6) is faster than reaction (3.5) (Han *et al.*, 2011b). The kinetic rate constants of the reactions, which are described in much more detail in section 3.2, determine reaction speed.

When the reaction proceeds in pH > 10 (the pH of the solution is high), direct reaction with OH⁻ predominates and reactions (3.8) and (3.9) are most active in this range. Reaction (3.9) is faster than reaction (3.8). Thus, reaction (3.8) is the rate controlling reaction in this pH range (Han *et al.*, 2015). The two reactions (3.8) and (3.9) are also active across 7 < pH < 10 range. However, reaction (3.8) is faster than reaction (3.9) in this range, leading to a higher concentration of HCO₃⁻ than CO₃²⁻ in solution.

When CO₂ is dissolved in water, equilibrium is established between hydrogen H⁺, carbonate CO₃²⁻(aq) and bicarbonate HCO₃⁻(aq) ions. The corresponding stoichiometric equilibrium constants for (3.5), (3.5), and (3.7) are defined in equations (3.10), (3.11), and (3.12) respectively from (Stumm and Morgan, 1995):

$$K_1 = \frac{[HCO_3^-][H^+]}{[CO_2(aq)]} \quad (3.10)$$

$$K_2 = \frac{[CO_3^{2-}][H^+]}{[HCO_3^-]} \quad (3.11)$$

$$K_W = [H^+][OH^-] \quad (3.12)$$

The corresponding stoichiometric equilibrium constants for (3.9), and (3.10) are defined in equations (3.13), and (3.14) respectively:

$$K_a = \frac{K_1}{K_W} = \frac{[HCO_3^-]}{[CO_2(aq)][OH^-]} \quad (3.13)$$

$$K_b = \frac{K_2}{K_W} = \frac{[CO_3^{2-}]}{[HCO_3^-][OH^-]} \quad (3.14)$$

In contrast to other authors (Mokhtari, 2016; Stumm and Morgan, 1995; Zeebe and Wolf-Gladrow, 2001a) in this work, K_a and K_b are introduced distinctly as it is clear that they represent slightly different reactions in the reaction set (compare K_1 with K_a and K_2 with K_b). Introducing this distinction applies focus on knowing exactly which reactions of the reaction set are in play, and thus which values of kinetic constants should be applied to match. Overall, this makes tracking of the chemical system dynamics less ambiguous and thus, less prone to error. When $Ca(OH)_2$ is introduced into the system as a pH influencing species in addition to, or instead of, $NaOH$, because the former also contains the alkaline earth metal cations, one needs to account for additional interactions / couplings. Section 3.2, illustrates these issues and explains the coupling steps in detail.

Stoichiometric equilibrium constants have a weak temperature dependence due to low enthalpies of reaction. The mole balances of the carbonic acid system at equilibrium can be expressed as:

$$C_T = [CO_2(aq)] + [HCO_3^-(aq)] + [CO_3^{2-}(aq)] \quad (3.15)$$

where C_T is the total inorganic carbon (TIC) concentration (mol/L), and this can change dynamically depending on the pH of the solution and the partial pressure of CO_2 gas, among other factors. By substitution of Eqs. (3.10) and (3.11) into Eq. (3.15), an explicit formula for $[CO_2(aq)]$, $[HCO_3^-(aq)]$, and $[CO_3^{2-}(aq)]$ can be obtained as is done in (Chiang and Pan, 2017a):

$$[CO_2(aq)] = \partial_0 C_T, \quad \partial_0 = \frac{[H^+]^2}{[H^+]^2 + K_1[H^+] + K_1K_2} \quad (3.16)$$

$$[HCO_3^-(aq)] = \partial_1 C_T, \quad \partial_1 = \frac{K_1[H^+]}{[H^+]^2 + K_1[H^+] + K_1K_2} \quad (3.17)$$

$$[CO_3^{2-}(aq)] = \partial_2 C_T, \quad \partial_2 = \frac{K_1K_2}{[H^+]^2 + K_1[H^+] + K_1K_2} \quad (3.18)$$

Figure 3-2 shows the fraction (∂_i) of each carbon species present as these vary with the pH of the solution. When CO_2 is dissolved in water, equilibrium is established between hydrogen $[H^+]$, bicarbonate $[HCO_3^-(aq)]$, and carbonate $[CO_3^{2-}(aq)]$ ions. Due to the presence of protons, the solution becomes acidic and its pH decreases. The pH of a saturated solution of carbon dioxide solution varies from 3.7 at 1 atm to 3.2 at 23.4 atm as the pressure of the gas over the water varies (Dodds *et al.*, 1956). The pH of the solution is a direct function of carbon dioxide solubility, which varies with temperature and pressure (Park, 2005).

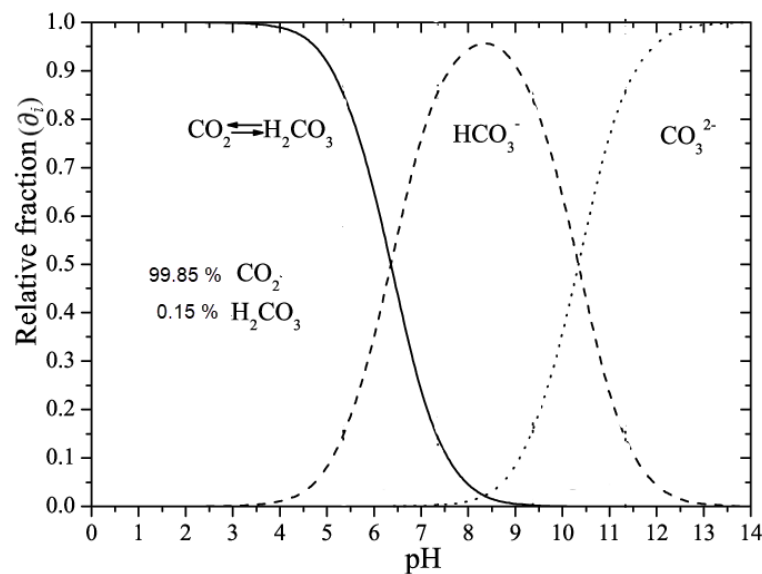


Figure 3-2: Distribution of carbon species as a function of pH (in the presence of P_{CO_2} of 1 atm, and at ambient temperature of 25 °C) (Fioravante *et al.*, 2019)

At atmospheric pressure (1 atm) and ambient temperature (20–25 °C), carbon dioxide is scarcely soluble in water (0.0384 mol/L at 20 °C), although this can be an order of magnitude higher than the solubility of other atmospheric gases in water. The dissolution of CO₂ in water can be enhanced by increasing the alkalinity of the solution. The pH modifies the amount of ionic species present in the aqueous solution. Therefore, specific carbonate concentrations can be achieved by controlling the pH of water for carbon dioxide dissolution, as in Aghajanian and Koiranen (2020).

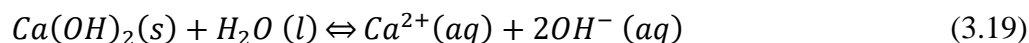
One of the challenges in the CO₂ capture process is the relatively low rate of mass transfer between gaseous CO₂ and the liquid solution phase (Chiang and Pan, 2017b) depicted in equation (3.1). As will be seen subsequently, this thesis proposes alternative means to accelerate the mass transfer between these two phases by elevating the gas pressure with the HAC. In Chapters 5 and 6, the applications of i) a HAC and ii) a horizontal injector loop as a generalization of the HAC process, are proposed as means of CO₂ mass transfer and mixing devices and are described in detail.

3.1.2 Dissolution of the minerals into solution

Mineral dissolution, to mobilize cations for CO₂ (or other species associated to CO₂ through the equilibria in Section 3.1.1) to react with as part of the sequestration process via mineral carbonation, may also turn out to be the rate-limiting step in the overall aqueous mineral carbonation process. Mineral dissolution also depends on the pH, temperature, and the solid material properties (particle size, porosity and surface area, and mineralogy) (Ji and Yu, 2018b). The intent is that alkaline cations will be leached from the natural mineral feedstock of section 2.3

and the alkaline waste materials of section 2.3. However, for simplicity in explaining the chemistry of direct aqueous mineral carbonation here, the system is set out using calcium hydroxide as an example.

The chemical equilibrium equation for the dissolution of Ca(OH)_2 in water is:



If Ca^{2+} (aq) is the only calcium species in the solution, the equilibrium constant of Ca(OH)_2 can be considered as:

$$K_{\text{Ca(OH)}_2} = \alpha_{\text{Ca}^{2+}} \times \alpha_{\text{OH}^-}^{-2} \quad (3.20)$$

where α refers to the activity of either calcium and hydroxide ions (Greenberg and Copeland, 1960). The solubility of metals through the formation of aqueous complexes can be influenced by activity and the effective concentration (Vanderzee, 2016). Activity (α) is a measure of the “effective concentration” of a species in a mixture and is defined as the product of concentration, C , and an activity coefficient, f .

The activity coefficient represents the deviation of the behavior of a real solution from that of an ideal solution and takes into account the effects of intermolecular interactions between solute and solvent molecules. By considering both the concentration and activity coefficient, the activity provides a more accurate measure of the true behavior of a species in a mixture, which can be used in the reaction kinetics modeling (Atkins *et al.*, 2014). For many complex dynamical descriptions of chemical equilibria and reaction kinetics, where species concentrations are shown, they may be replaced by activities to better reflect experimental reality.

To avoid doubt, in the immediately following involving algebraic manipulation, the variable C is used to denote the concentration of a species of a reaction, but it should be noted elsewhere in the thesis the concentration of a species is denoted adopting the convention that the species is surrounded by square brackets e.g. $[\text{CO}_2]$.

$$\alpha = f \times C \quad (3.21)$$

The activity coefficients can be calculated if the ionic strength is known (Vanderzee, 2016). As will be seen subsequently, such a procedure, as implemented by Lee *et al.* (2021) and Na *et al.*, (2019a) have been applied when the dissolution of $\text{Ca}(\text{OH})_2$ in water has been computed. However other reaction systems presented herein adopt species concentrations rather than [the superior] activities. The reason for this is that data drawn from the literature to complete mathematical descriptions of reaction chemistry must be consistent and complete. It has not proved possible to draw a complete set of activity-based values of equilibrium constants and kinetic rates from the literature to populate the dynamic equations for mineral carbonation. Consistent and exclusive data from the literature for that system has only been found when expressed with species concentrations.

In electrolyte solutions, each ion will exert an electrostatic force on every other ion, and this force increases as the distance between ions is reduced. The extent of these electrostatic forces is determined by ionic strength, I . Generally, ionic strength measures the concentration of ions in a solution, considering both the number of ions present and their charges. It is calculated by summing the products of the concentrations of each ion species in the solution, raised to the power of the absolute value of their respective charges (Bockris and Reddy, 1972; David Glasstone,

1962). Mathematically, the ionic strength, I , can be expressed by Eq (3.22) in units of molality (moles solute/kg solvent) or molarity (mol/L)

$$I = \frac{1}{2} \sum_j C_j Z_j^2 \quad (3.22)$$

where C_i and Z_i denote the concentration and charge number of the i th ion species in the solution, respectively. The ionic strength is influenced by concentration, because higher concentrations reduce the distance between ions, and by the ion charge, Z (Johannsen and Rademacher, 1999; Lee *et al.*, 2021).

When the ionic strength is known, activity coefficients can be calculated as (Johannsen and Rademacher, 1999).

$$\log_{10} f = \frac{(-0.5\sqrt{I})}{(1 + 1.4\sqrt{I})} \quad (3.23)$$

The above equation is an approximation used by the Debye-Hückel equation to calculate activity coefficients. The extended Debye-Hückel theory describes the behavior of electrolyte solutions at relatively low concentrations. Its equation accounts for the interactions between the different ions, which are the primary cause of differences between the properties of dilute electrolyte solutions and those of so-called ideal solutions (Drew *et al.*, 1981).

The value of 1.4 in the Eq. (3.23) is an empirical correction factor. It is used to account for the fact that real ionic solutions deviate from ideal behavior, especially at higher ionic strengths. The 1.4 factor helps improve the accuracy of the extended Debye-Hückel theory's predictions over a wider range of concentrations. However, it's important to note that this factor is empirical and

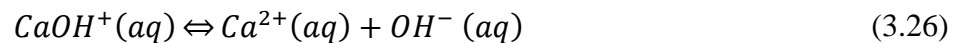
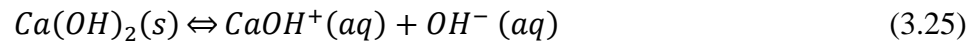
may not be valid for all systems. It is often used as a simplification in practice. Ionic strength can decrease the activity coefficient and therefore increase the solubility of Ca(OH)_2 by decreasing activity (Harris and Lucy, 2020).

The equation (3.20) can be expressed in the form of

$$K_{\text{Ca(OH)}_2} = C_{\text{Ca}^{2+}} \times C_{\text{OH}^-}{}^2 f^3 \quad (3.24)$$

where C is species concentration and f is the activity coefficient (Greenberg and Copeland, 1960).

In order to calculate the concentrations $C_{\text{Ca}^{2+}}$ and C_{OH^-} during the dissolution process the total calcium species concentration is required. However, there is no agreement in the literature regarding the identity of water soluble calcium species in equilibrium with $\text{Ca(OH)}_2(\text{s})$ (Johannsen and Rademacher, 1999; Kutus *et al.*, 2016; Lito *et al.*, 1998a). Some researchers considered $\text{Ca}^{2+}(\text{aq})$ is the only calcium species in the solution (Vanderzee, 2016). However other literature sources, suggest, that in alkaline solutions, beside $\text{Ca}^{2+}(\text{aq})$, the formation of $\text{CaOH}^+(\text{aq})$ is also significant (Pallagi *et al.*, 2012a). In systems containing Ca(OH)_2 as the initial solid phase the following chemical equilibria can be considered (Baes and Mesmer, 1977; Pallagi *et al.*, 2012b).



The corresponding equilibrium constant of Eq. (3.26) is:

$$K_{\text{CaOH}^+} = \frac{C_{\text{Ca}^{2+}} \times C_{\text{OH}^-}}{C_{\text{CaOH}^+}} f^4 \quad (3.27)$$

The total calcium species concentration of calcium ions can be calculated as (Wiechers and Sturrock, 1975)

$$(C_{Ca^{2+}})_T = C_{Ca^{2+}} + C_{CaOH^+} \quad (3.28)$$

In this work, the activity coefficient is only considered in the kinetic model of dissolution of $Ca(OH)_2$ particles in the solution (see section 3.2.2).

However, activity coefficients (of one form or another) also affect the pH of the solution. The pH of the standard saturated $Ca(OH)_2$ solution is 12.45 at 25° C (Bates *et al.*, 1956; Lito *et al.*, 1998b). In theory, the concentration of hydroxide ions determines the pOH and then pH of the $Ca(OH)_2$ solution. Later in this work, it will become evident that the value of the calculated pH is found to be higher than the pH measured. It is suspected that the reason for this is because activity coefficients are not able to be considered in the pH calculation.

The solubility of $Ca(OH)_2$ in water is known to be temperature-dependent. There are varying reports on the effect of temperature on the solubility of $Ca(OH)_2$ in water. For instance, Johannsen and Rademacher (1999) proposed an equation to calculate the solubility of $Ca(OH)_2$ in water that suggests that the solubility of $Ca(OH)_2$ decreases with increasing temperature. However, other authors have reported that the solubility of $Ca(OH)_2$ increases with increasing temperature (Hassanpour *et al.*, 2016; Lemus-Ruiz *et al.*, 2012; Sazonov *et al.*, 2014). Notably, Johannsen and Rademacher (1999) is a widely used reference for modeling the dissolution of $Ca(OH)_2$ in water, and many researchers have utilized the assumptions and equations in that work to model the behavior of $Ca(OH)_2$ in aqueous solutions (Lee *et al.*, 2021; Na *et al.*, 2019b; Velts *et al.*, 2011a). This work has followed suit for the present study. Eq. (3.29) shows the solubility of $Ca(OH)_2$ as a

function of the temperature and the size of Ca(OH)_2 particles being dissolved, and becomes important when the diameter of the Ca(OH)_2 particles are less than $0.5 \mu\text{m}$:

$$\beta(\text{Ca(OH)}_2)_S = \sqrt{K_{\text{Ca(OH)}_2}} = (5.214 - 0.0124 T) \exp(0.0313/d) \quad (3.29)$$

where $\beta(\text{Ca(OH)}_2)_S$ is solubility of calcium hydroxide, $K_{\text{Ca(OH)}_2}$ is the equilibrium constant of Ca(OH)_2 in water, T is the temperature (K), and d is diameter of the Ca(OH)_2 particles (μm). The theoretical solubility at 25°C for a particle size of $1 \mu\text{m}$ is 1.57 mg/L (Johannsen and Rademacher, 1999; Lee *et al.*, 2021).

Lee *et al.* (2021) also present the equilibrium constant of CaOH^+ in water (K_{CaOH^+}) as:

$$\log_{10} K_{\text{CaOH}^+} = -1.299 + 260.388 \left(\frac{1}{298.15} - \frac{1}{T} \right) \quad (3.30)$$

where T is the temperature (K).

A challenge of mineral carbonation using alkaline solid wastes is that the dissolution of calcium species in alkaline residues of the mineral feedstocks reviewed in Chapter 2 is favored at low pH, while low pH is not favorable for the subsequent precipitation of calcium carbonate. As will be seen subsequently, the balance between dissolution and precipitation depends on the kinetics and solubility of the feedstock present and the possible products (Chakraborty and Jo, 2018), and dissolution of Ca(OH)_2 at high pH is a characteristic of the carbonation process in the reactor designed and tested.

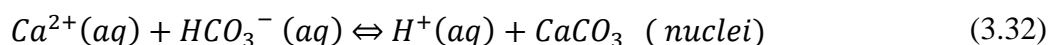
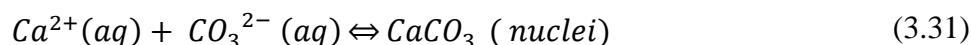
The mechanical or other properties of the calcium (or magnesium) solids may change considerably by the leaching of the solid particles (Chiang and Pan, 2017b). McCabe *et al.* (2005)

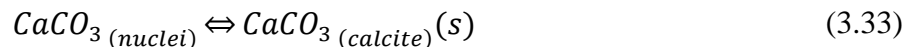
observed that coarse, hard, or granular feed solids may disintegrate into pulp or mush when their soluble content is removed, and this may present potential challenges in residue storage. The rate and extent of calcium or magnesium leaching from solid particles are inversely related to particle size and pH. The factors that might affect the rate and extent of leaching of metal ions of the potential feedstocks for mineral carbonation and lead to a lowering of mass-transfer rate are:

- Lack of porosity or permeability in solid wastes and their particles,
- Formation of isolating layer of precipitate on the surface of alkaline metal earth hydroxide particles suspended in solution,
- Insufficient stirring and mixing between solid and liquid phases, and;
- Severe agglomeration of (fine) particles in the solution (Chiang and Pan, 2017a)

3.1.3 Formation of calcium carbonate precipitates: nucleation and growth

Calcium carbonate is formed by reactions between i) calcium ions and carbonate ions (3.31) and ii) calcium ions and bicarbonate ions (3.32) (Ji and Yu, 2018c). The first reaction is known to be fast and leads to thermodynamically stable (Figure 3-3) precipitate products (3.33) (Han *et al.*, 2011c). The energy of formation for gaseous CO₂ is approximately -400 kJ/mol, and that of solid CaCO₃ precipitate is considerably lower at -1100 kJ/mol, according to Pan *et al.* (2015a), which is the main reason the mineral carbonation process is favourable.





As is evident from Figure 3-2, and as stated by Chiang and Pan, (2017b), when the pH is more than 10.5, the predominant carbon containing species are carbonate ions (CO_3^{2-}) and thus CaCO_3 would be formed principally according to (3.33). During the formation of CaCO_3 , the pH value would decrease gradually.

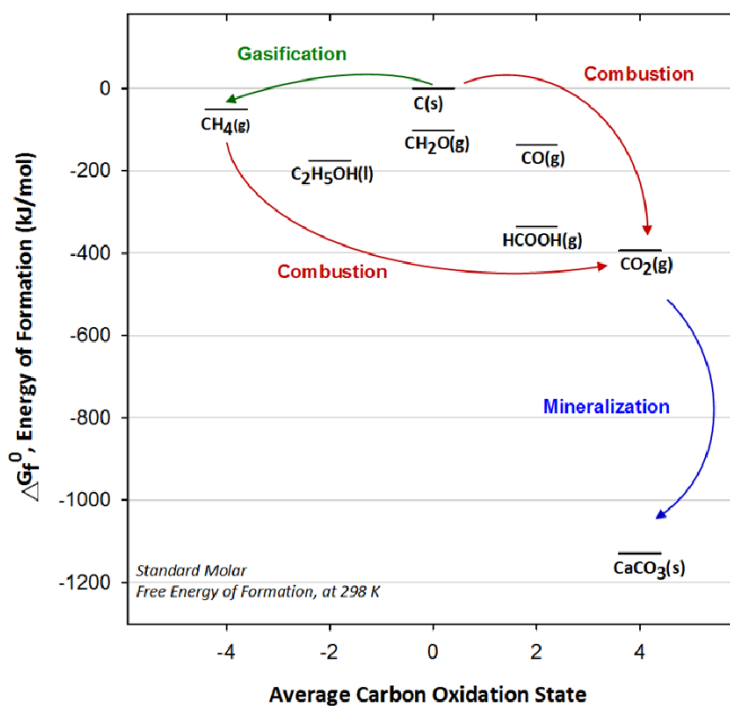


Figure 3-3: Standard molar free energy of formation for several carbon-related substance at 298 K (Pan *et al.*, 2015a)

At $\text{pH} < 9$, the bicarbonate ions (HCO_3^-) react with Ca^{2+} (Chiang and Pan, 2017b). Energetically, the precipitation of CaCO_3 from carbonate ions (CO_3^{2-}) is more straightforward than its formation from bicarbonate ions (HCO_3^-), because the bicarbonate ion requires deprotonation before forming CaCO_3 (Allen, 2019). The growth of the CaCO_3 crystals, (3.33) is not considered

in the dynamical kinetic model of the mineral carbonation kinetics formulated subsequently. The omission of crystal growth from the dynamical kinetic model represents a simplification that can be improved upon with further work that is beyond the scope of the current thesis.

The equilibrium constant, K_{sp} , for the formation of calcium carbonate (Eq. (3.31)) can be expressed as:

$$K_{sp} = \alpha_{Ca^{2+}} \times \alpha_{CO_3^{2-}} = C_{Ca^{2+}} \times C_{CO_3^{2-}} f^2 \quad (3.34)$$

where α refers to the activities of the calcium and carbonate ions, C is the concentration of the calcium and carbonate ions, and f is the activity coefficient (Duggirala, 2005). To simplify the calcium carbonate precipitation model, it is assumed $f \approx 1$, so $\alpha \approx C$.

The value of solubility constant of $CaCO_3$ depends on the temperature and empirically given by (Plummer and Busenberg, 1982):

$$\log(K_{sp}) = -171.9773 - 0.077993T + \frac{2903.393}{T} + 71.595 \log(T) \quad (3.35)$$

The pH of the solution has no direct impact on K_{sp} , although it does affect solubility by controlling the level of CO_3^{2-} present in solution (Duggirala, 2005).

This author has not been able to recover values for the equilibrium constant associated with (3.32). However, values for the kinetic rate constants for this reaction are presented in Velts, (2011).

3.2 Kinetics of the reactions

Chemical kinetics deals with the change of chemical properties through time and considers the details of the transitions of one chemical species to another on a molecular level. At chemical equilibrium predicted by the reaction equilibria, reactions take place continuously, with the rates of the forward reactions equaling the backward reaction rates (Zeebe and Wolf-Gladrow, 2001b). According to Levenspiel (1999), reactor design needs to consider both the equilibria (of the prior section) and the kinetics (presented in this section). The mineral carbonation process is limited by the kinetics of one of three possible steps:

- i. the dissolution of CO₂ into an aqueous solution,
- ii. the dissolution of Ca-bearing solid compounds, or,
- iii. the formation of solid products under diffusion control.

The kinetics of calcium carbonate dissolution and the inverse process of precipitation in an aqueous solution have been the subject of numerous investigations (Arakaki and Mucci, 1995; Liu, 1997; Pan *et al.*, 2018e; Plummer *et al.*, 1978; Ragipani *et al.*, 2019; Zeebe and Wolf-Gladrow, 2001a). Various models and sets of associated equations have been proposed based on either homogeneous or heterogeneous systems (Montes-Hernandez *et al.*, 2006; Pan *et al.*, 2018e; Vacassy *et al.*, 2000; Wiechert and Sturrock, 1975) to describe the dissolution/precipitation kinetics of calcium carbonate.

The first empirical equation for the dissolution/precipitation of calcium carbonate was reported by Dorange and Guetchidjan (1978). They investigated the dissolution of marble chips as a function of the initial calcium concentration and the partial pressure of CO₂. They deduced that

the rate of reaction was governed by the degree of undersaturation in the system (Compton and Daly, 1987; Kornmüller, 1995). However, their model does not give a general description of the dissolution kinetics of calcium carbonate. Plummer *et al.* (1978) presented a model to predict the net rate of the dissolution of calcium carbonate in terms of the activities of the reacting species. Their model gives an excellent fit to the experimental data produced by Compton and Daly (1987) and many other researchers have used Plummer's model in their work (Arakaki and Mucci, 1995; Mitchell *et al.*, 2010; Na *et al.*, 2019c; Velts *et al.*, 2011b; Zeebe *et al.*, 1999), and parts of it are deployed in the system developed in this work.

Mitchell *et al.* (2010), Na *et al.* (2019), Velts *et al.* (2011) modified the kinetic model of Plummer. They used it to describe the kinetics of direct aqueous mineral carbonation (the reactions for CO₂ capture using Ca(OH)₂ aqueous solution). These models are of great relevance to the work herein. However, one of their deficiencies is that the particle size of the CaCO₃ produced does not feature. In each of these models, the system is considered homogeneous in that the kinetics of the nucleation and growth of calcium carbonate particles are not considered. When the system is heterogeneous, the focus is retained on the dynamics of solid particle growth. When mineral wastes are considered the feedstock, several theoretical models have been put forward, such as the random pore model (Morales-Flórez *et al.*, 2015), the overlapping grain model (Liu *et al.*, 2012) the shrinking core model (for dissolution of, e.g. Ca(OH)₂, mineral silicates) (Johnsen *et al.*, 2006), and the surface coverage model (Pan *et al.*, 2014). These can be applied to simulate the performance of the direct aqueous mineral carbonation using a CaO-based / silicate-based material, where the time evolution of CaCO₃ crystal growth, and feedstock substrate coating mechanisms, are important.

Another significant challenge in the mineral carbonation process is the relatively slow rate of mass transfer of gaseous CO₂ to the liquid solution phase (Chiang and Pan, 2017a). Most of the studies of mineral carbonation kinetics focus on the kinetics of the dissolution of feedstocks, such as Ca(OH)₂ and the precipitation of calcium carbonate. An accurate representation of the kinetics of CO₂ absorption in the system is a critical step for building reliable numerical models to quantitatively characterize the process of CO₂ capture and sequestration.

To improve on this situation, part of the thesis work, involved experimental verification (Pourmahdavi *et al.*, 2022) of a detailed representation of the mass transfer kinetics of CO₂ absorption in a HAC (Young *et al.*, 2022). In the model of reaction kinetics presented in this section, the HAC is conceptualized as a pressurized, continuous chemical reactor into which the CO₂(g) is continuously supplied to the HAC to dissolve in a suspension solution of Ca(OH)₂(s), so that a CaCO₃(s) precipitate is continuously produced. Consequently, the kinetic model, which is presented in the following, is divided into two parts:

- I. The gas absorption in the HAC system
- II. The dissolution of Ca(OH)₂ and precipitation of CaCO₃

Young *et al.* (2022) developed a one-dimensional model for estimating the gas absorption in the compression process in a HAC downcomer, which couples the hydrodynamics, solubility kinetics, and psychrometric aspects of the system. This model can be used to predict the mass transfers between the gas and liquid phases and can consider the impacts of raising the liquid temperature and the addition of inorganic co-solutes to examine changing aqueous systems (Young *et al.*, 2022).

In order to verify the bubbly flow model developed by Young *et al.* (2022), some experiments have been conducted. The conditions of the experiments and their results are discussed in detail in Chapter 5. After verifying the bubbly flow model, the $\text{CO}_2(\text{g})$ absorption rate into the alkaline solution is predicted with this model.

Part two of the kinetic model uses the rate constants with results from the bubbly flow model to calculate the amount of precipitated CaCO_3 obtained for conditions subsequently used experimentally with $\text{Ca}(\text{OH})_2$ solution (Chapter 5).

The dissolution of calcium oxide or calcium hydroxide in water generates the Ca^{2+} in the solution. The rapid and strong increase in pH ($\text{pH} \approx 12.5$) observed is due to this leaching step (Dijkstra *et al.*, 2004). CO_2 is injected continuously into the solution rich in Ca^{2+} ions at a designated pressure and a constant flow rate.

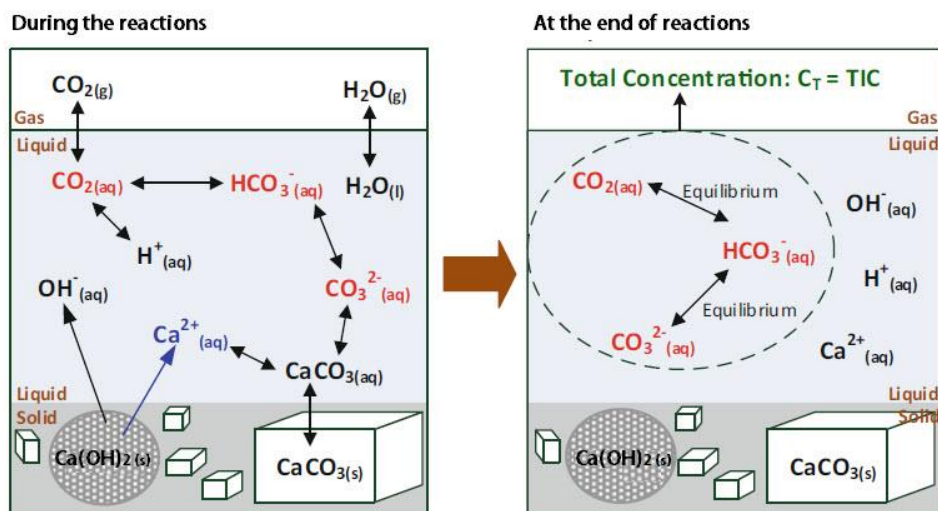


Figure 3-4: Schematic of the direct aqueous mineral carbonation mechanism ($\text{Ca}(\text{OH})_2$ aqueous solution), modified from (Chiang and Pan, 2017b)

The mechanisms of the direct aqueous mineral carbonation in a batch reactor are illustrated in Figure 3-4. The kinetic reactions involved in the carbonation process can be categorized into three groups: first, the mass transfer of carbon dioxide gas into the alkaline solution. Second, the dissolution of calcium hydroxide solid particles into a reactant. Last, ionic reactions between the dissolved ions derived from the gas and solid reactants cause the CaCO_3 to precipitate. Generally, the ionic and precipitation reactions are fast. In contrast, the gas–liquid mass transfer and solid dissolutions are slow and regarded as rate-limiting steps because of the resistance between two phases.

The following section briefly describes the gas mass transfer model used by Young *et al.* (2022). Then, the reaction kinetics for the dissolution of $\text{Ca}(\text{OH})_2$, ionic reactions between the dissolved ions, and precipitation of CaCO_3 are explained.

The model articulated by Cents *et al.* (2005) for the reaction of dissolved CO_2 with aqueous solutions of hydroxides is extended based on the theoretical considerations of Velts *et al.* (2011), Na *et al.* (2019b), and Zeebe and Wolf-Gladrow (2001a) to permit all the reactions occurring in the reactor to be modelled.

3.2.1 Mass transfer of CO_2 gas into the alkaline solution

CO_2 absorption in the alkaline solution involves physical mass transfer and chemical reaction. Several theories exist that model the gas absorption process as a chemical reaction. The penetration theory (Higbie, 1935), the surface renewal theory (Danckwerts, 1955) and the two-film theory (Whitman, 1962) have been extensively used to describe the interphase gas-liquid mass transfer mechanism in different systems. It has been shown that these theories give almost identical

quantitative predictions (Danckwerts and Sharma, 1966; Khodayari, 2010). All of these theories assume that the rate of mass transfer is determined by a mass transfer coefficient and a driving force arising from a concentration or pressure gradient (Amaral *et al.*, 2019).

The bubbly flow model has employed the two-film theory for description of the mass transfer between the gas and the liquid phases (Young, 2017). The two-film theory assumes that the flux (rate) of molar transfer across a gas liquid interface is a function of the rate at which it travels to the interface from the bulk gas phase and from the interface into the bulk liquid (Figure 3-5) (Young, 2017).

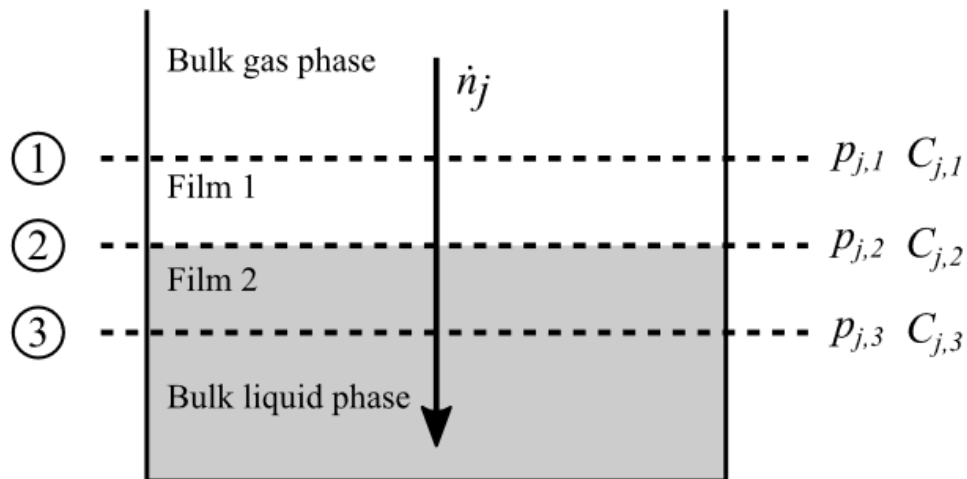


Figure 3-5: Two film theory. $P_{j,k}$ and $C_{j,k}$ are the partial pressure and molar concentration gas species j at position k respectively (Young, 2017)

The two-film theory affords the mass transfer process a gas-side resistance and a liquid-side resistance and leads to the following equation for the rate of absorption of the gas species into a liquid:

$$\dot{n}_j = k_g A (P_{j,1} - P_{j,2}) = k_L A (C_{j,2} - C_{j,3}) \quad (3.36)$$

where 1 is the bulk gas phase, 2 is the gas-liquid interface, 3 is the bulk liquid phase, $P_{j,k}$ is the partial pressure of species j at a given location k in Pa, $C_{j,k}$ is the concentration of species j at a given location k in mol/m³, k_g is the gas phase mass transfer coefficient (m/s), k_L is the liquid phase mass transfer coefficient (m/s) and A is the interfacial area (m²). The driving potential for gas absorption in the gas phase is shown by $(P_{j,1} - P_{j,2})$ and the driving potential for gas absorption in the liquid phase is represented by $(C_{j,2} - C_{j,3})$ (Wang *et al.*, 2018; Young, 2017).

When the limiting resistance is on the gas side, the overall mass transfer rate can be calculated using the gas phase parameters of the equation (3.36, middle term) only. When the limiting resistance is on the liquid side, the overall mass transfer can be described using the liquid phase parameters of equation (3.36, RHS) only (Young, 2017).

In the systems considered in this study (HAC, Chapters 4 and 5 and horizontal injector loop, Chapter 6), the gas phase comprises small (1mm to 1cm) bubbles. Therefore, the rate at which the gas solutes diffuse within the bubbles can be neglected. The gas absorption rate would be limited by the rate of the gas diffuses from the gas-liquid interface to the bulk fluid (Young, 2017).

It is assumed that there is no resistance to molecular diffusion at the gas-liquid interface. Therefore, the gas solute concentration in the liquid at the gas liquid interface is always at equilibrium with the partial pressure of the gas in the gas phase. Henry's law can be used to convert the partial pressure of the species in the gas phase to its concentration in the liquid phase at the interface (Young, 2017). Therefore, $C_{j,2}$ which is the gas-liquid interface concentration for gas species j (here CO₂) is expressed as:

$$C_{CO_2,2} = K_H \times P_{CO_2} \quad (3.37)$$

where K_H is the Henry's solubility constant defined by concentration and pressure in mol/L bar, and P_{CO_2} is the partial pressure of CO₂ in the gas phase (Pa).

In the bubbly flow model, the liquid phase mass transfer coefficient is based on the work of Higbie (1935), which investigated the liquid film resistance in simulated industrial conditions and was formulated as:

$$k_L = 2 \sqrt{\frac{D}{\pi t_e}} \quad (3.38)$$

where D is the diffusion constant for a given gas species in the liquid phase in m²/s and t_e is the time of exposure of the gas and liquid in s (Young, 2017). k_L is a measure of the rate of mass transfer between gas and liquid at the interface between the two phases.

The liquid mass transfer coefficient together with the available interfacial area can be referred to as a single parameter known as $k_L a$, also known as, the overall volumetric mass transfer coefficient (s⁻¹) (Kimweri, 2001). Mathematically, it is defined as the product of the specific interfacial area (a) and the gas-liquid mass transfer coefficient (k_L), which can be represented as:

$$k_L a = k_L \times a \quad (3.39)$$

where a is the specific interfacial area and it represents the amount of interface available for mass transfer per unit volume of the liquid phase. It is expressed as:

$$a = \frac{A}{V} \quad (3.40)$$

where A is the interfacial area (m^2) and V is the volume of the liquid phase (m^3) (Kimweri, 2001; Whitman, 1962). The value of $k_L a$ dictates the gas transfer process (Galán Sánchez *et al.*, 2011; Na *et al.*, 2019b). The larger it is, the greater the mass of a gas species is transferred to the liquid phase.

With the above simplifications, the CO_2 gas mass transfer rate into the liquid can be written:

$$\dot{n}_{\text{CO}_2} = k_L a_{\text{CO}_2} (K_H P_{\text{CO}_2} - [\text{CO}_2(aq)]) \quad (3.41)$$

where $[\text{CO}_2(aq)]$ is the CO_2 bulk liquid concentration.

Young's bubbly flow model can be used to estimate $k_L a$ accounting for the increase in pressure as the gas is inducted into the reactor. That such an increase of pressure of the gas phase occurs in the flow direction should be recognized as one potentially leading to significant improvements in the mineral carbonation process compared to conventional contactors (where the gas pressure falls) because the CO_2 mass transfers are elevated and accelerated.

An overview description of the bubbly flow model is presented in Chapter 4. However, for more information about the formulation of this model for the hydrodynamics, solubility kinetics, and psychrometrics of the gas compression, please refer to (Young *et al.*, 2022).

- ***The effect of precipitation reaction on the rate of CO_2 mass transfer***

The reaction of the CO_2 with $\text{Ca}(\text{OH})_2$ solution increases the rate of absorption and increases the capacity of the liquid solution to dissolve CO_2 (Velts *et al.*, 2011b). Kimweri (2001); Lee *et al.*

(2021), Na *et al.* (2019b), and Velts, 2011a) introduce a so-called ‘enhancement factor’, E , to represent the effect of the chemical reaction driven phenomenon on the mass transfer process performance. The mass transfer enhancement is generally expressed as the ratio of the volumetric mass transfer coefficient with chemical reaction ($k_L a_{CO_2}^R$) to that without chemical reactions ($k_L a_{CO_2}$) (Velts *et al.*, 2011d; Wang *et al.*, 2018).

$$E = \frac{k_L a_{CO_2}^R}{k_L a_{CO_2}} \quad (3.42)$$

Various methods can be used to calculate the enhancement factor. For example, Velts *et al.* (2011e) were not able to estimate the bubble interfacial area in their models that simulated their experimental results, so they back-calculated $k_L a_{CO_2}$ and E directly as a lumped value from their model. In contrast, Na *et al.* (2019a) and Lee *et al.* (2021) utilized correlations and models to predict $k_L a_{CO_2}$ and E by considering various system parameters, such as flow rate, geometry, and physical properties of the phases involved.

As mentioned earlier, Young’s bubbly flow model is used in this study to estimate the $k_L a$. The value of E can be estimated by comparing this model’s results with experimental data.

An enhancement factor greater than 1 indicates that the presence of a chemical reaction has increased a mass transfer rate compared to the case without a reaction. Conversely, an enhancement factor less than 1 indicates that the presence of a reaction has decreased the mass transfer rate. The enhancement factor is a useful tool for quantifying the impact of chemical

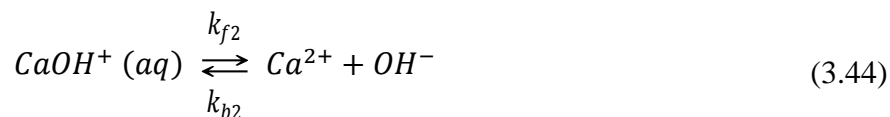
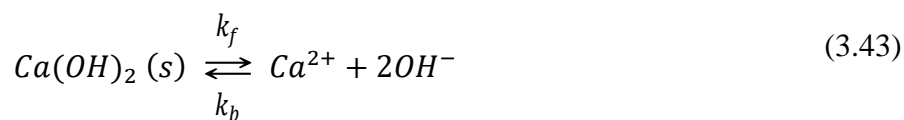
reactions on mass transfer performance and for optimizing the design of chemical reactors and other mass transfer systems (Haynes, 2011).

CO₂ transfers from a gas into the liquid phase in a gas-liquid contactor device. The gas-liquid contactor is the equipment that brings a gas and a liquid phase together to facilitate the mass transfer process. Contactors provides a large interfacial area of contact between the phases to achieve a high mass transfer rate (Gruenewald and Radnjanski, 2016a). In Chapters 4 and 6, the hydraulic air compressor (HAC) and horizontal injector loop as the gas-liquid contactor are described in more detail. These devices can provide CO₂ (aq) at high concentrations.

3.2.2 Calcium hydroxide dissolution in water

The equations for a solution of calcium hydroxide in water including forward and backward reactions are:

Dissolutions of Ca(OH)₂:



The k_f , k_{f2} , k_b , and k_{b2} denote the rate constants of the forward and backward reactions, which follow the elementary reaction rate equation (Na *et al.*, 2019b).

The values of the rate constants of the forward and backward reaction (3.43) are estimated as a function of temperature with the following relations:

$$k_f = 2.2 \times 10^{-8} \exp\left(\frac{0.0297(T - 298.15)}{298.15RT}\right) \left(\frac{\text{mol}}{\text{L s cm}^2}\right) \quad (3.45)$$

$$k_b = 1.9 \times 10^{-3} \exp\left(\frac{0.0528(T - 298.15)}{298.15RT}\right) \left(\frac{\text{L}^2}{\text{mol}^2 \text{ s cm}^2}\right) \quad (3.46)$$

where T is the temperature (K) and R is the gas constant, (J/mol K) (Na *et al.*, 2019d). It should be noted that k_f and k_b are dependent on total surface area of the solid to reflect the decrease in dissolution rate owing to the shrinkage of the solid particles as the reaction proceeds (Na *et al.*, 2019b).

This author has not been able to recover values for the rate constants of the forward and backward reactions (3.43). However, Lee *et al.* (2021) set the k_{f2} to $1.958 \times 10^2 \text{ s}^{-1}$ and defined the value of k_{b2} with the value of the equilibrium constant for this reaction ($k_{b2} = \frac{k_{f2}}{K_{\text{CaOH}^+}}$). Lee *et al.* (2021) and Na *et al.* (2019a) showed that variations in k_{f2} and k_{b2} do not significantly affect the reaction rate.

The overall dissolution rate of calcium hydroxide particles is expressed as

$$\dot{n} = A_s \left(k_f - k_b ([\text{Ca}^{2+}] f^4 [\text{OH}^-] f^2) \right) + k_{f2} [\text{CaOH}^+] - k_{b2} ([\text{Ca}^{2+}] [\text{OH}^-]) \quad (3.47)$$

where A_s is the total surface area of the $\text{Ca}(\text{OH})_2$ solid particles in water, and f is the activity coefficient (Johannsen and Rademacher, 1999; Na *et al.*, 2019b).

During the reaction, the shrinkage of the solid particles causes the dissolution rate of calcium hydroxide to decrease in proportion to the total surface area of the solid. The activity coefficient f is calculated from the ionic strength, I , according to (3.23).

In order to calculate the dissolution rate, \dot{n} , the total surface A_s of the Ca(OH)_2 particles is required. During the dissolution, the surface area decreases, and this has to be taken into consideration. The required calculation can be simplified by assuming that all particles have the same diameter and are spherical in shape. In this case, the total number of particles remains constant, and the volume of one Ca(OH)_2 particle of diameter d is:

$$V_{particle} = \frac{4}{3}\pi \left(\frac{d}{2}\right)^3 \quad (3.48)$$

The total number of particles per volume of solution, n_s , is given by the total volume of the dosed amount of calcium hydroxide and the particle volume.

$$n_s = \frac{Z_{Ca(OH)_2}}{\rho_{Ca(OH)_2} \times V_{particle}} \quad (3.49)$$

where $Z_{Ca(OH)_2}$ refers to the initial weight of calcium hydroxide and $\rho_{Ca(OH)_2}$ is its density. Due to the dissolution, the total volume of Ca(OH)_2 , $V_{Ca(OH)_2}$, decreases. Simultaneously the total concentration of calcium species in solution increases.

$$V_{Ca(OH)_2} = \frac{1}{\rho_{Ca(OH)_2}} \left(Z_{Ca(OH)_2} - ([Ca^{2+}] - [CaCO_3]) MW_{Ca(OH)_2} V_R \right) \quad (3.50)$$

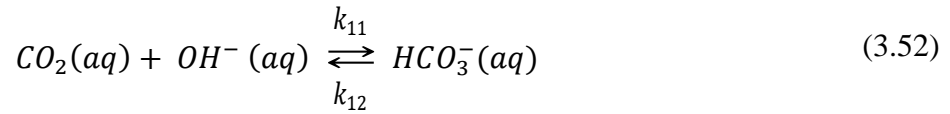
where $MW_{Ca(OH)_2}$ is molecular weight of Ca(OH)_2 and V_R is the volume of the reactor. The total surface area A_s of the Ca(OH)_2 particles is calculated as follows:

$$A_s = (\pi \times n_s)^{1/3} (6V_{Ca(OH)_2})^{2/3} \quad (3.51)$$

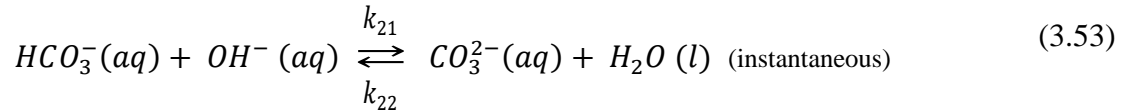
3.2.3 Ionic reactions and precipitation of CaCO₃

When CO₂ is dissolved into strong alkaline solutions like Ca(OH)₂ solution, the following reactions become applicable. As before, any existence of H₂CO₃ is negligible because of its strong tendency for dissociation (Na *et al.*, 2019b).

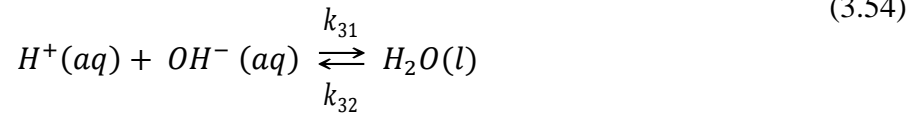
Formation of bicarbonate:



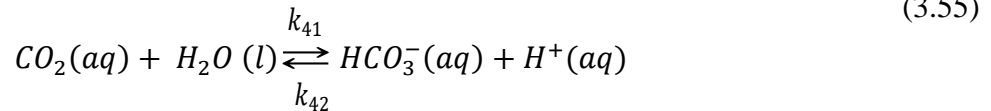
Dissociation of bicarbonate:



Ionization of water:



CO₂ hydration



The values of the equilibrium constants of above reactions are denoted as K_a , K_b , K_w , and K_1 respectively are presented in the section 3.1.1 as Eq. (3.13), (3.14), (3.12), and (3.10).

The forward and backward reaction rates follow the elementary reaction rate equations. The forward rate constant k_{11} of reaction (3.51), has been correlated as a function of temperature and ionic strength by Pohorecki and Moniuk (1988). However, considering the infinite dilution ionic strength of Ca(OH)₂ solution, the value of the second-order rate k_{11} (L/mol s) can be calculated only as a function of temperature from the following relationship (Velts, 2011).

$$\log k_{11} = 11.916 - \frac{2382}{T} \quad (3.56)$$

The backward reaction rate of reaction (3.53) k_{12} is defined with the value of the equilibrium constant for this reaction ($k_{12} = \frac{k_{11}K_W}{K_a}$). The value of the solubility product K_W (mol^2/m^6) is given by Tsonopoulos *et al.* (1976)

$$\log\left(\frac{K_W}{\rho_W^2}\right) = -\frac{5839.5}{T} - 22.4773 \log(T) + 61.062 \quad (3.57)$$

The value of the equilibrium constant K_a (mol/m^3) is given as a function of temperature by Edwards *et al.* (1978):

$$K_a = \exp\left(-\frac{12092.1}{T} - 36.786 \ln T + 235.482\right)\rho_W \quad (3.58)$$

where ρ_w is the density of water (kg/m^3).

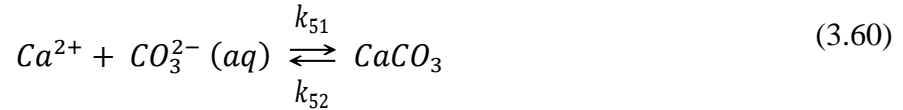
The forward rate constant k_{21} of reaction (3.53) was reported as 6×10^9 L/mol s by Eigen (1963). The equilibrium constant K_b (m^3/mol) at infinite dilution determines the value of the backward reaction rate ($k_{22} = \frac{k_{21}}{K_b}$) as given by Hikita *et al.* (1976).

$$\log(K_b) = -\frac{1568.9}{T} - 2.5866 - 6.737 \times 10^{-3}T \quad (3.59)$$

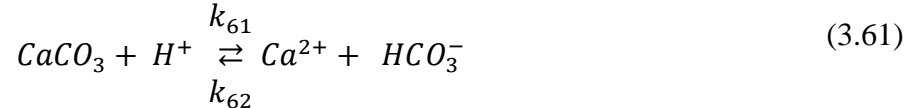
The neutralization rate constant, k_{31} , is 1.4×10^{11} L/mol s (Eigen, 1954). The rate constant k_{41} for the reaction between CO_2 and water is 0.024 s⁻¹ (Eigen, 1954). The values of the backward reaction rate constants k_{32} , and k_{42} may be calculated from the equilibrium constants and are equal to $\frac{k_{31}}{K_W}$ and $\frac{k_{41}}{K_a}$ (Cents *et al.*, 2005).

Two reactions lead to production of calcium carbonate.

Formation of CaCO₃ crystals:



Back-dissolution of CaCO₃ crystals at lower pH:



Neither of these reactions becomes a rate-limiting step because they are fast ionic reactions producing thermodynamically stable product.

The backward rate constant k_{52} of the reaction (3.60) was estimated to be $9 \times 10^{-3} \text{ s}^{-1}$ by Velts *et al.* (2011c). The value of the forward reaction rate constant k_{51} is calculated from the solubility constants and is equal to $\frac{k_{52}}{K_{sp}}$. The average values of the reaction rate constants k_{61} and k_{62} are given by Velts (2011) as $0.1 \times 10^7 \text{ s}^{-1}$ and $4 \times 10^2 \text{ L/mol s}$.

3.3 Formulation of a dynamical kinetic model of the reactions

3.3.1 The differential equations

A set of ordinary differential equations (ODEs) based on the reaction equilibria and kinetics described in the prior sections is presented here. Together, they form a model that accounts for absorption and reaction kinetics in the liquid phase, including the formation of the solid product and the hydrodynamic conditions within the system. The concentration time series of all species participating in the precipitation process can be predicted with this system of equations, given appropriate initial conditions and values of equilibria parameters and kinetic constants. The formulation is based on those of Na *et al.*, (2019b) and Velts *et al.* (2011f).

$$\frac{d[CO_2(g)]}{dt} = \left(\frac{Q_G([CO_2(g)]_{IN} - [CO_2(g)])}{V_G} \right) - \frac{(k_L a_{CO_2} E (K_H P_{CO_2} - [CO_2(aq)])(V_L + V_G))}{V_G} \quad (3.64)$$

$$\begin{aligned} \frac{d[CO_2(aq)]}{dt} = & \frac{(k_L a_{CO_2} E (K_H P_{CO_2} - [CO_2(aq)])(V_L + V_G))}{V_L} - k_{11}[CO_2(aq)][OH^-] \\ & + k_{12}[HCO_3^-] - k_{41}[CO_2(aq)] + k_{42}[HCO_3^-][H^+] \end{aligned} \quad (3.65)$$

$$\frac{d[CO_2(g)]_{out}}{dt} = \left(\frac{Q_G([CO_2(g)]_{IN} - [CO_2(g)]_{out})}{V_{G2}} \right) \quad (3.66)$$

$$\begin{aligned} \frac{d[HCO_3^-]}{dt} = & -k_{11}[CO_2(aq)][OH^-] + k_{12}[HCO_3^-] - k_{21}[HCO_3^-][OH^-] + k_{22}[CO_3^{2-}] \\ & - k_{41}[CO_2(aq)] + k_{42}[HCO_3^-][H^+] - k_{61}[Ca^{2+}][HCO_3^-] + k_{62}[H^+] \end{aligned} \quad (3.67)$$

$$\frac{d[CO_3^{2-}]}{dt} = k_{21}[HCO_3^-][OH^-] + k_{22}[CO_3^{2-}] - k_{51}[Ca^{2+}][CO_3^{2-}] + k_{52}[CaCO_3] \quad (3.68)$$

$$\begin{aligned} \frac{d[H^+]}{dt} = & -k_{31}[H^+][OH^-] + k_{32} - k_{42}[HCO_3^-][H^+] + k_{41}[CO_2(aq)] + k_{42}[HCO_3^-][H^+] \\ & + k_{61}[Ca^{2+}][HCO_3^-] - k_{62}[H^+] \end{aligned} \quad (3.69)$$

$$\begin{aligned} \frac{d[OH^-]}{dt} = & -k_{11}[CO_2(aq)][OH^-] + k_{12}[HCO_3^-] - k_{21}[HCO_3^-][OH^-] + k_{22}[CO_3^{2-}] \\ & - k_{31}[H^+][OH^-] + k_{32} + 2A_s (k_f - k_b ([Ca^{2+}]f^4[OH^-]f^2)) \\ & + k_{f2}[CaOH^+] - k_{b2}([Ca^{2+}][OH^-]) \end{aligned} \quad (3.70)$$

$$\begin{aligned} \frac{d[Ca^{2+}]}{dt} = & -k_{51}[Ca^{2+}][CO_3^{2-}] + k_{52}[CaCO_3] - k_{61}[Ca^{2+}][HCO_3^-] + k_{62}[H^+] \\ & - A_s (k_f - k_b ([Ca^{2+}]f^4[OH^-]f^2)) + k_{f2}[CaOH^+] - k_{b2}([Ca^{2+}][OH^-]) \end{aligned} \quad (3.71)$$

$$\frac{d[CaOH^+]}{dt} = -k_{f2}[CaOH^+] + k_{b2}([Ca^{2+}][OH^-]) \quad (3.72)$$

$$\frac{d[CaCO_3]}{dt} = +k_{61}[Ca^{2+}][HCO_3^-] - k_{62}[H^+] + k_{51}[Ca^{2+}][CO_3^{2-}] - k_{52}[CaCO_3] \quad (3.73)$$

In Eqs (3.64) to (3.73) concentrations are expressed in molar units (mol/L), Q_G is the gas mass flow rate (L/s), $[CO_2(g)]_{IN}$ is the inlet CO_2 gas concentration, $k_L a_{CO_2}$ is the volumetric mass transfer coefficient of CO_2 in the absence of chemical reaction (s^{-1}), E is the enhancement factor, K_H is the Henry's law constant in (mol/L bar), P_{CO_2} is the the partial pressure of CO_2 in the gas phase (Pa), V_L is the solution volume (L) , V_G is the volume of gas in the gas–liquid mixture (L). V_{G2} is the gas volume in the empty space above the reaction mixture (L), A_s is the total surface area of the $Ca(OH)_2$ particles (m^2).

When the alkaline solution is saturated or below saturation concentration, there are no $Ca(OH)_2$ particles in the solution and thus A_s is zero. The reaction rate constants used in Eqs. (3.64) to (3.73) and other parameters used in this model ($T = 295.1 K$) are summarized in Table 3-1. The 'kinetic model' constitutes this system of ordinary differential equations with time as the independent variable and can be solved by using the MATLAB ODE solver (Lee *et al.*, 2021; Na *et al.*, 2019c; Velts, 2011a).

Table 3-1: Parameters and constants used in the dynamical kinetic model (Lee *et al.*, 2021; Na *et al.*, 2019b; Velts, 2011).

Parameter	Value	Parameter	Value
k_{11} (L/mol s)	8.4×10^3	k_{51} (L/mol s)	1.9×10^6
k_{12} (s^{-1})	2.0×10^{-4}	k_{52} (mol/L s)	9.0×10^{-3}
k_{21} (L/mol s)	6.0×10^9	k_{61} (s^{-1})	0.1×10^7
k_{22} (s^{-1})	1.2×10^6	k_{62} (L/mol s)	0.4×10^3
k_{31} (L/mol s)	1.4×10^{11}	k_f (mol/L s cm^2)	2.2×10^{-8}
k_{32} (mol/L s)	1.3×10^{-3}	k_b ($L^2 / mol^2 s cm^2$)	1.9×10^{-3}
k_{41} (s^{-1})	2.4×10^{-2}	k_{f2} (s^{-1})	1.95×10^3
k_{42} (L/mol s)	5.7×10^4	k_{b2} (s^{-1})	1.99×10^3

The resulting system of differential equations exhibits a so-called ‘stiff’ behavior. Any model of ordinary differential equations is said to exhibit such behavior if the solution being sought varies slowly. However, their nearby solutions change rapidly, so that the numerical method must take small time steps to obtain satisfactory results, perhaps requiring millions of evaluations without special measures. The ODE solvers of MATLAB that are designed for stiff ODEs, known as stiff solvers, deploy measures so that they are able to take much larger time steps and have improved numerical stability compared to the non-stiff solvers. The stiff ODE solvers available within MATLAB and include: ode15s, ode23s, ode23t, ode23tb, and ode15i (Moler, 2022). In this work, ode23tb is used to solve the system for varying initial and boundary conditions.

3.3.2 Verification 1: CO₂ absorption in NaOH solution

Velts *et al.* (2011c) conducted comprehensive experiments with lime-containing oil shale waste ash. They experimentally investigated the mechanism of ash leachate carbonation in a stirred semi-batch reactor by changing the CO₂ partial pressure, gas flow rate, and agitation intensity. They also provided consistent model equations and physical–chemical parameters to describe the CaCO₃ precipitation process. The results of Velts *et al.* (2011c) experiments are employed to validate the functionality of the MATLAB model applied in this study.

All the experiments were performed in a semi-batch reactor equipped with a turbine-type impeller. The volume of the reactor was 15 L. Operating variables that were varied during the experiments included air-CO₂ gas mixture flow rate, CO₂ concentration in the inlet gas, and stirring rate of impeller. Experiments were conducted until the solution pH reached a value of 7 (Velts *et al.*, 2011d).

These experimental trials aimed to identify the key factors influencing the CO₂ absorption process in alkaline solutions. By analyzing the experimental data alongside a CO₂ mass transfer model, the volumetric mass transfer coefficients of CO₂ for the system in the absence of chemical reaction with Ca(OH)₂ are estimated under different conditions of gas flow rate, stirrer rotation speed, CO₂ concentration in the inlet gas and its partial pressure. When the experimental conditions were applied, it was found that the $k_L a_{CO_2}$ was 0.0194 s⁻¹ (Velts *et al.*, 2011d).

The volume of the NaOH solution, concentration, and pH were fixed at 10 L, 0.01 mol/L, and 12, respectively. The air-CO₂ gas mixture flow rate (Q_L), CO₂ concentration in the inlet gas, and stirring rate of the impeller were 1000 L/h, 15 (%), and 400 rpm, respectively (Velts *et al.*, 2011d). When CO₂ gas is bubbled into a solution containing a strong base such as NaOH, the electro-neutrality balance in terms of molar concentration units can be expressed as follows:

$$[H^+] + [Na^+] = [HCO_3^-] + 2[CO_3^{2-}] + [OH^-] \quad (3.69)$$

The Na⁺ ions do participate in reactions with carbon species and are therefore not included in the kinetic model being verified. The reaction rate constants and other parameters used are summarized in Table 3-1. The change of the experimental and MATLAB simulated concentrations of the reactive species (CO₂(g), HCO₃⁻(aq), CO₃²⁻(aq)) and pH of the solution over time are shown in Figure 3-6 and Figure 3-7.

In Figure 3-7, the pH values predicted by the model show good agreement with the experimental data. The values of CO₂ concentration in the discharge gas predicted by the model are slightly higher than the results of the experiment. However, the shape of the modeled curve aligns with the sequence of discrete experimental observations, including their complexity.

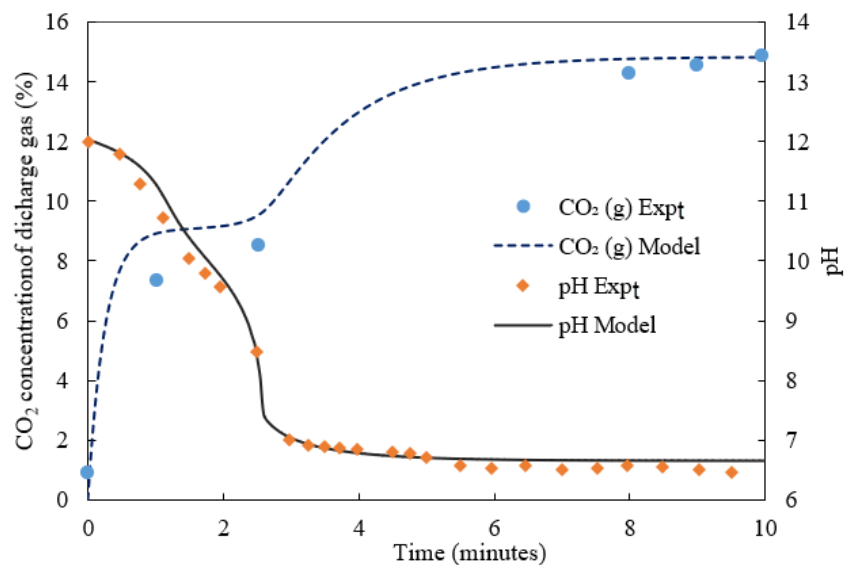


Figure 3-6: The variations of CO₂ concentration of the discharge gas and pH

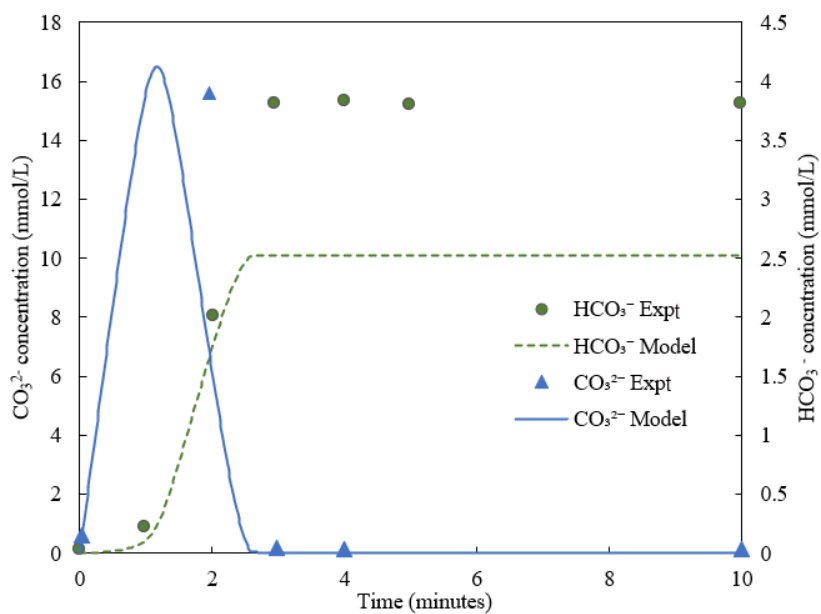


Figure 3-7: The variations of CO₃²⁻ and HCO₃⁻ concentrations

In Figure 3-7, the experimental values of HCO_3^- concentrations are higher than the values predicted by the MATLAB model. However, the presence of the plateau evident in the modeled curve aligns with the discrete sequence of experimental observations.

According to Figure 3-2, when the pH is 6.5, the dominant carbon species in solution are HCO_3^- and $\text{CO}_2(\text{aq})$. Velts *et al.* (2011c) did not measure the concentration of $\text{CO}_2(\text{aq})$ during the experiment. They only measured the off-gas concentrations. It is assumed that the model correctly predicts the concentration of the $\text{CO}_2(\text{aq})$. When the model predicts more $\text{CO}_2(\text{g})$ in the discharge gas of the reactor, it implies that less $\text{CO}_2(\text{aq})$ must be dissolved in the solution and converted to the HCO_3^- ions. Therefore, there are the differences between the measured and model prediction of $\text{CO}_2(\text{g})$ discharge concentration and HCO_3^- .

3.3.3 Verification 2: CO_2 absorption into alkaline solution (lime-containing oil shale waste ash)

Oil shale combustion ash (containing approximately 8.0% free CaO) was dispersed in distilled water at a liquid-to-solid ratio of 10:1 (w/w). The resulting alkaline suspension solution was filtered to remove all solid particles. The volume of the alkaline solution, initial concentration of Ca^{2+} ions, and pH value were 10 L, 0.028 mol/L and 12.65, respectively. The air- CO_2 gas mixture flow rate (Q_L), CO_2 concentration in the inlet gas and stirring rate of impeller were 1000 L/h, 15 (%), and 1000 rpm, respectively. In previous experiments, the value of the $k_L a_{\text{CO}_2}$ was determined to be 0.0194 s^{-1} . The reaction between CO_2 and $\text{Ca}(\text{OH})_2$ solution enhances the rate of absorption and increases the capacity of the solution to dissolve more CO_2 . The $k_L a_{\text{CO}_2}^R$ value for this

experiment was found to be $0.035 \text{ (s}^{-1}\text{)}$ (Velts *et al.*, 2011d) and the enhancement factor (E) was 1.8.

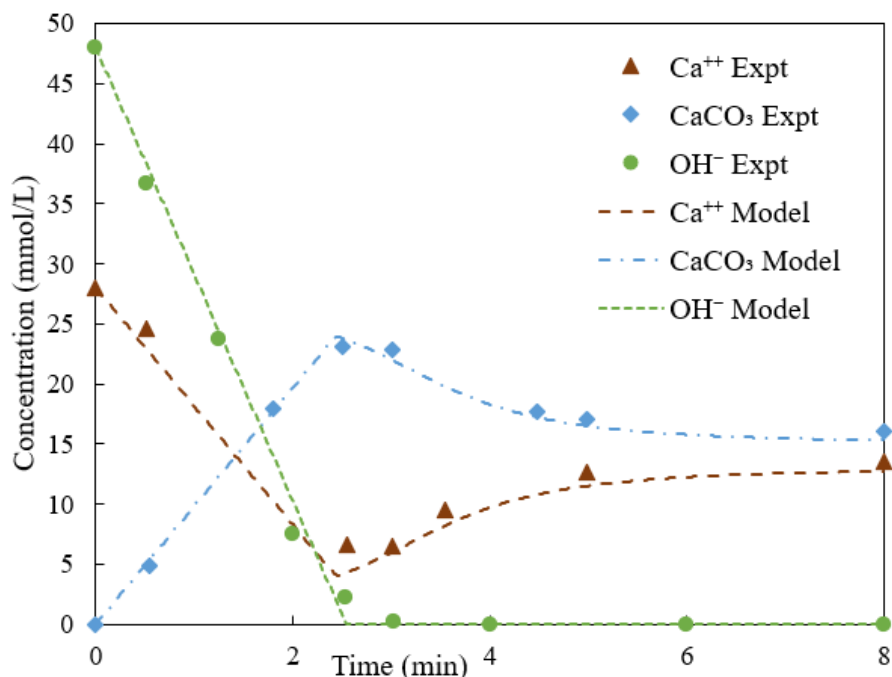


Figure 3-8: The variation of Ca^{2+} , CaCO_3 , and OH^- concentrations according to the time

Figure 3-8 shows the concentrations of Ca^{2+} , CaCO_3 , and OH^- at different times during the experiment. The discrete points represent the experimental observations from Velts *et al.* (2011c) and the continuous lines represent the predictions from the initial conditions obtained from the MATLAB model prepared for this work.

This experiment indicated that that an alkaline solution reacts with a CO_2 -containing gas, leading to a decrease in the content of Ca^{2+} ions. The reaction between Ca^{2+} ions and dissolved CO_2 resulted in the formation of CaCO_3 , which is practically insoluble in water when the pH exceeds 9. As the pH decreased, H^+ concentrations triggered the re-dissolution of CaCO_3 , releasing calcium ions back into the solution. The relatively small differences between the measured and

predicted data confirm the ability of the MATLAB model of this study to accurately represent the process course, including re-dissolution of precipitated calcium carbonate at lower pH.

3.3.4 Verification 3: CaCO₃ precipitation through direct mixing of Ca(OH)₂ and a solution of dissolved CO₂

Relative to the rates of the chemical reactions that lead to CaCO₃ formation, the rate of gas-liquid mass transfer is slow because of the resistance between two different phases. Consequently, the rate of CO₂ mass transfer will determine the overall CO₂ removal efficiency in a mineral carbonation reactor. To illustrate the reaction kinetics without such a constraining step, a simple experiment was conducted. A solution of Ca(OH)₂ and water containing dissolved CO₂ were mixed together. The system (3-68) to (3-73) was used to predict the response, applying initial and boundary conditions to (3-68) that effectively omitted the gas mass transfer mechanism from the system model.

A 0.5 L saturated aqueous solution Ca(OH)₂ was prepared by dissolving Ca(OH)₂ to its maximum solubility of 0.7383 g in 500 g of D.I water at 25°C. The solution was filtered through a 5-micron filter, resulting in no undissolved particles. The initial measured pH of the solution was 12.35.

Carbon dioxide gas from a cylinder was bubbled through 0.5 L of D.I. water for 2 minutes. The concentration of dissolved CO₂ in water was not measured directly. However, the measured pH of the water was 4.5 at 25°C and atmospheric pressure.

In the next step, 0.015 liters of 0.036 mol/L Ca(OH)₂ aqueous solution were added to a beaker containing 0.015 liter of D.I. water containing the dissolved CO₂. The resulting liquid in

the beaker became cloudy after mixing the two solutions, indicating precipitation of $\text{CaCO}_3(\text{s})$. The final pH of this mixture was measured at 10.8 (Figure 3-9).

Figure 3-10 shows the results of the kinetic model of this reaction, undertaken within MATLAB. The concentration of $\text{Ca}(\text{OH})_2$ is considered as 0.036 (mol/L) as the initial condition of the model. The initial concentration of total inorganic carbon (TIC) is assumed to be the same as that of $\text{Ca}(\text{OH})_2$. The pH of D.I. water is 4.5, so $\text{CO}_2(\text{aq})$ is the dominant form of carbon species. The $\text{CO}_2(\text{aq})$ converts to CO_3^{2-} and the produced CO_3^{2-} ions react with Ca^{2+} . In Figure 3-10, the $\text{CO}_2(\text{aq})$ converts to CO_3^{2-} and the produced CO_3^{2-} ions react with Ca^{2+} .

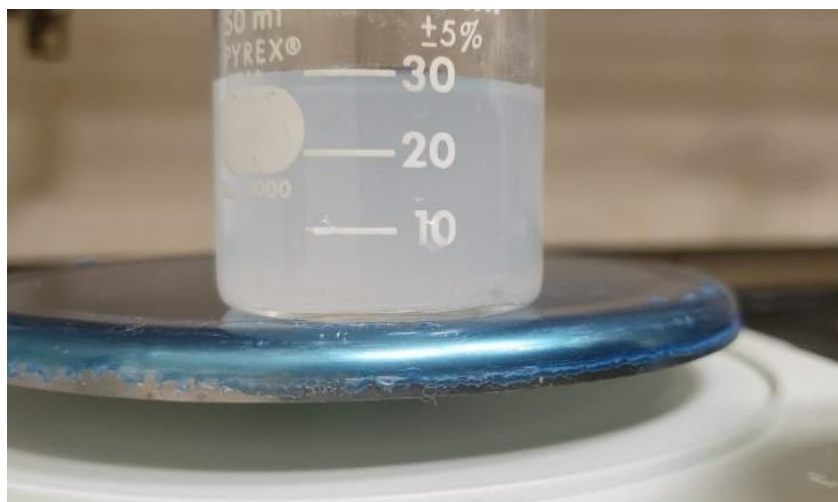


Figure 3-9: The slurry of calcium carbonate

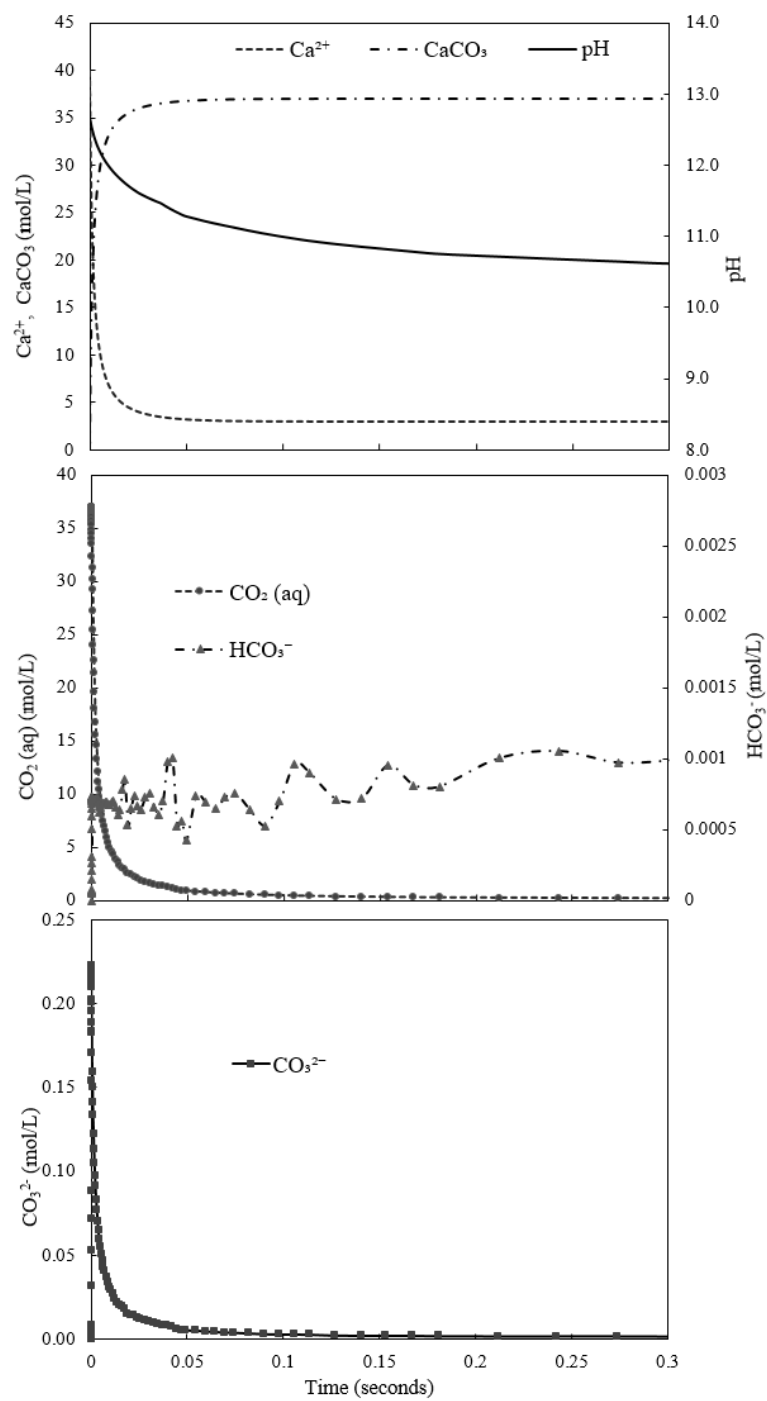


Figure 3-10: The predicted changes in the concentrations of various species over time.

Precipitated CaCO_3 is the product of these reactions. The model illustrates that the reaction between the dissolved ions (derived from the gas and solid reactants) to precipitate CaCO_3 occurs rapidly with the reactions essentially completing within a period of 0.2 seconds.

In contrast, the time scales to completion for the simulations and experiments presented in Figure 3-7 and Figure 3-8, where the gas mass transfer logic is utilized are on the order of 10 minutes. The comparison of those curves and Figure 3-10 confirms that the gas–liquid mass transfer process, as well as the dissolution of $\text{Ca}(\text{OH})_2$ in water, will be rate-limiting steps of the mineral carbonation process.

3.4 Summary

The literature review of the equilibria and kinetics of reactions relevant to the mineral carbonation process led to the collection of relevant equilibrium, solubility, and kinetic constants, which were then used to formulate a mathematical model of the chemical systems. The model formulation's efficacy was confirmed by comparing its results to experimental data reported in the literature, and it was found to be accurate.

The carbonation reaction rate is controlled by the gas–liquid mass transfer rate, the availability of $\text{CO}_2(\text{aq})$ species, and the rate of dissolution of solid $\text{Ca}(\text{OH})_2$ under varying pH conditions. Dissolving $\text{CO}_2(\text{g})$ to $\text{CO}_2(\text{aq})$ is a relatively slow process because of the resistance between the two different phases.

Increasing pressure is one of the key factors to consider accelerating the carbonation reaction rate. According to Henry's law, the solubility of CO_2 in the liquid increases with enhancing the pressures (Carroll *et al.*, 1991). In the next chapters, the models of mass transfer processes in the

HAC systems will be introduced and verified to demonstrate their ability to achieve high rates of CO₂ dissolution from flue gas streams and accumulate high concentrations of CO₂(aq).

Without a simultaneous high rate of Ca(OH)₂ solution to maintain high pH, higher rates of CO₂ dissolution into the liquid phase will tend to lower pH and favor the production of soluble bicarbonate species. Carbonate precipitation is favored to realize the intended sequestration mechanism if a high pH can be maintained. For a reaction sequence using Ca(OH)₂, the rate of CaCO₃ production, or equivalently, the rate of CO₂ sequestration, will then depend on the rate of solution of alkaline earth metal oxides and hydroxides. Whether the latter process can keep up with an accelerated rate of CO₂(g) mass transfer will be tested experimentally in Chapter 7.

4. Hydraulic air compressor as a gas-liquid contactor

Many industrial processes such as mineral carbonation involve the flow and contact of multiple phases. One phase can be finely dispersed into another to increase the interfacial contact area and create high turbulence in the continuous phase. It is desirable to promote intense mixing between immiscible phases to increase mass, momentum, and energy transfer. According to Tatterson (1991), 25% of all chemical reactions occur between gases and liquids. A major class of gas-liquid flows is one in which the liquid phase is continuous, and the gas phase is dispersed in the form of bubbles (Fara, 2018). Generally, the term bubbly flow refers to the flow of a gas or a mixture of gases in a continuous liquid as a dispersed phase of bubbles.

One of the challenges in the CO₂ capture process is the relatively low mass transfer rate between gaseous CO₂ and the liquid solution phase. CO₂ enters the liquid phase through a gas-liquid contactor. These devices play an important role in the capture efficiency of mineral carbonation. Gas-liquid contactors can be categorized into three main groups depending on the relative flow of the phases (co-current, counter-current, and cross-current) and the nature of the gas and liquid phases. The different contactor types are as follows:

1. The liquid is present as discrete drops that are distributed within a continuous gas phase. Examples of this system are spray towers and atomizer units.
2. Both the liquid and gas exist as separate continuous phases with a single contact boundary surface. An example of this system is a wetted wall column.

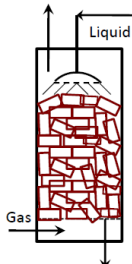
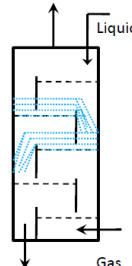
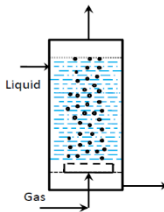
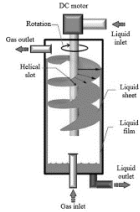
3. The gas is dispersed as bubbles in a continuous liquid phase. Examples of such systems include mechanically agitated reactor vessels and bubble columns (Charpentier, 1981; Majumder, 2016a).

Table 4-1 provides a classification of the different characteristics of the gas-liquid contactors. The sources referred to in this table use qualitative descriptors such as “small,” “low,” and “high” to describe discriminating variables, and the author follows suit. However, it will be preferable if discriminating parameters are provided more quantitatively. The principal message of Table 4-1 is that specific types of gas–liquid contactor are suited for specific types of services. According to Majumder, (2016a), selecting an appropriate gas-liquid contactor in process design requires the following considerations

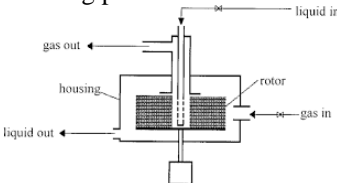
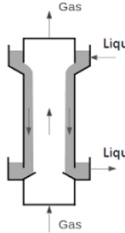
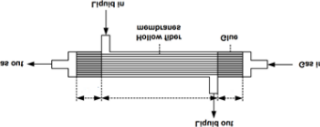
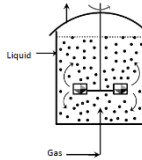
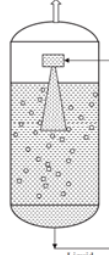
- greatest selectivity for desired products
- maximum conversion of reactants
- minimum environmental impacts
- ease of process automation and process control
- simple to construct, scale-up and easy to operate
- low capital and operating cost

Although each of the gas–liquid contactors listed in Table 4-1 is suited to specific applications, bubble column devices have become increasingly popular for conducting gas-liquid or gas-liquid-solid mass transfer reactions in numerous industrial processes (e.g., oxidation, hydrogenation, aqueous mineral carbonation) (Majumder, 2016a; Zheng Chao *et al.*, 2020).

Table 4-1: Classification of gas-liquid contactors (Charpentier, 1981; Dutta, 2009; Gruenewald and Radnjanski, 2016a; Gunjal and Ranade, 2016; Kohl and Nielsen, 1997; Vinu, 2017; Wardhaugh *et al.*, 2017)

Gas-liquid contactor type	Advantages	Disadvantages
Packed column 	<ul style="list-style-type: none"> • Able to manage fouling liquids; • Low gas-side pressure drops; • Small diameters possible; • Can handle foaming systems; • Low capital, operating, and maintenance cost; • Simple construction; • Can handle corrosive materials with corrosion-resistant packing; • Reduces back mixing¹ in comparison to spray columns; • Better mass transfer than in spray columns; 	<ul style="list-style-type: none"> • Not appropriate for liquids with solid particles • Channeling, which must be controlled by redistributing liquid. • Cannot handle extremely high or low flow rates. • Cannot handle liquids with high viscosities. • Need to be preferentially wetted to avoid reduction of the interfacial area to volume ratio.
Tray column 	<ul style="list-style-type: none"> • Wide operational gas/liquid range; • High mass transfer coefficients; • The liquid/vapor contact in the crossflow of plate columns is more effective than the countercurrent flow in packed columns; • Can handle solids; • Easily customized to specific requirements such as operations requiring much heat; 	<ul style="list-style-type: none"> • Less applicable for foaming and corrosive liquids; • High costs • Higher pressure drops than packed columns. • Slow reaction rate processes. • Plugging and fouling may occur.
Bubble column 	<ul style="list-style-type: none"> • Low capital and maintenance cost; • Simple construction • High thermal stability. • Uniform distribution because of high liquid circulation. • Low energy input requirements. • No moving parts and minimum maintenance • Reasonable interfacial mass transfer area 	<ul style="list-style-type: none"> • Low contact efficiency. • Considerable degree of back mixing in the liquid and gas • Short gas residence time. • High gas pressure drops.
Rotating liquid sheet contactor 	<ul style="list-style-type: none"> • Reducing the column size; • Achievement of higher gas velocities not restricted by flooding limits; • High mass transfer coefficients; • The potential to use higher viscosity liquid absorbents 	<ul style="list-style-type: none"> • Complex technology • High capital and operating cost; • Unstable liquid sheet; • High gas pressure drop

¹ is the tendency of reacted chemicals to intermingle with unreacted feed in a reactor (Abu Reesh, 2021)

Gas-liquid contactor type	Advantages	Disadvantages
<p>Rotating packed bed</p> 	<ul style="list-style-type: none"> • High mass transfer rate; • Low energy consumption; • Significant reductions in equipment volume 	<ul style="list-style-type: none"> • Complex technology; • Under development technology; • Low angular slip velocity of gas
<p>Wetted wall column</p> 	<ul style="list-style-type: none"> • Can also recover waste heat; • Can handle flammable feeds and dust; • Can neutralize corrosive gas; • Can minimize odors from waste; • Can be used in a multi-staged configuration; • No secondary dust sources; • Relatively small space requirements; • Can handle high-temperature, high humidity gas streams; • Low capital cost 	<ul style="list-style-type: none"> • Complex design; • High maintenance costs; • Corrosion problems with interior metal
<p>Membrane contactors</p> 	<ul style="list-style-type: none"> • Flexible modular; • Easy scale-up; • Enables the two phases to be independently controlled 	<ul style="list-style-type: none"> • The membrane itself provides additional mass-transfer resistance; • Prone to fouling
<p>Stirred tank reactor</p> 	<ul style="list-style-type: none"> • Most effective with viscous liquids or slurries • Can handle low gas flow rates and large liquid volumes 	<ul style="list-style-type: none"> • Back mixing. • High maintenance costs;
<p>Jet reactor (high-velocity gas-liquid contactors)</p> 	<ul style="list-style-type: none"> • Relatively low maintenance • High removal yield • Simple and compact construction • No mechanical components • Gaseous components are absorbed • Able to deal with fluctuating gas flows • No ventilator required 	<ul style="list-style-type: none"> • Large pressure drops • Signs of erosion when scrubbing abrasive mediums

Due to this trend, this chapter first describes bubble column contactors and then discusses the effects of specific variables on the mass transfer coefficient in a bubble flow column.

Subsequently, a HAC, which is a type of co-current downward bubble column, is introduced as a new gas-liquid contactor system.

4.1 Bubble column devices and the mass transfer coefficient

The simplest form of a bubble column reactor is a device with a cylindrical vessel in which the compressed gas enters the bottom of the cylinder through a gas distributor, which may vary in design. The liquid phase may be supplied in batch form, or it may move with or against the gas flow (Figure 4-1). Liquids can contain suspended, fluidized, reactive, or catalytic solids. Accordingly, the device is called a two- or three-phase (slurry) bubble column.

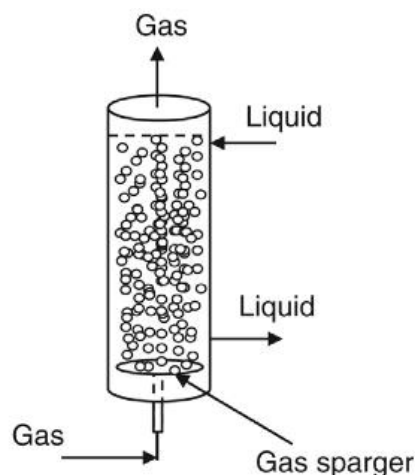


Figure 4-1: A simplest form of the bubble column (Majumder, 2016a)

Based on the phase flow, bubbly flow devices are classified as horizontal flow, vertical up- or down-flow, co-current, and countercurrent (Andreussi *et al.*, 1999). Many different bubble column designs have been used over the years based on specific practical requirements. Figure 4-2 shows a few frequently used vertical bubble columns (Jakobsen, 2014).

When additional perforated plates are incorporated into a simple bubble-column reactor (Figure 4-1), a cascade bubble column is formed (Figure 4-2 (a)) and the gas is redistributed over the perforated plates. This redistribution of gas over perforated plates intensifies mass transfer, reduces the fraction of large bubbles, and prevents back-mixing in both phases (Jakobsen, 2014). Back-mixing can also be reduced by filling the bubble column with an inert packing material (Figure 4-2 (b)) or using static mixers (Figure 4-2 (d)) (Bai, 2010).

Multishift bubble column reactors (Figure 4-2 (c)) prevent bulk circulation such that a uniform distribution of gas bubbles can be achieved throughout the reactor. In addition, circulation can be increased via either an internal or an external loop, as shown in Figure 4-2 (e) – 4-2 (f). When solid particles are suspended in a liquid, a slurry phase is formed, and the bubble column is referred to as the slurry bubble column reactor (Figure 4-2 (g)) (Bai, 2010; Jakobsen, 2014).

In recent years, co-current down flow bubble columns (Figure 4-2 (h)) have attracted significant attention, particularly when the interfacial mass transfer area is the rate-controlling step of the process. In these devices, the gas is first introduced into the liquid medium at the top of the reactor and then allowed to move against its buoyancy by the downward liquid momentum in the column.

The principal advantage of this type of reactor is that the relatively short gas residence times obtained in up-flow reactors can be increased because the residence time is determined by the bubble rise velocity. In other words, by selecting the appropriate liquid and gas throughput rates, the gas residence times can be adjusted to the maximum gas content within certain limits (Jakobsen, 2014; Majumder, 2016a).

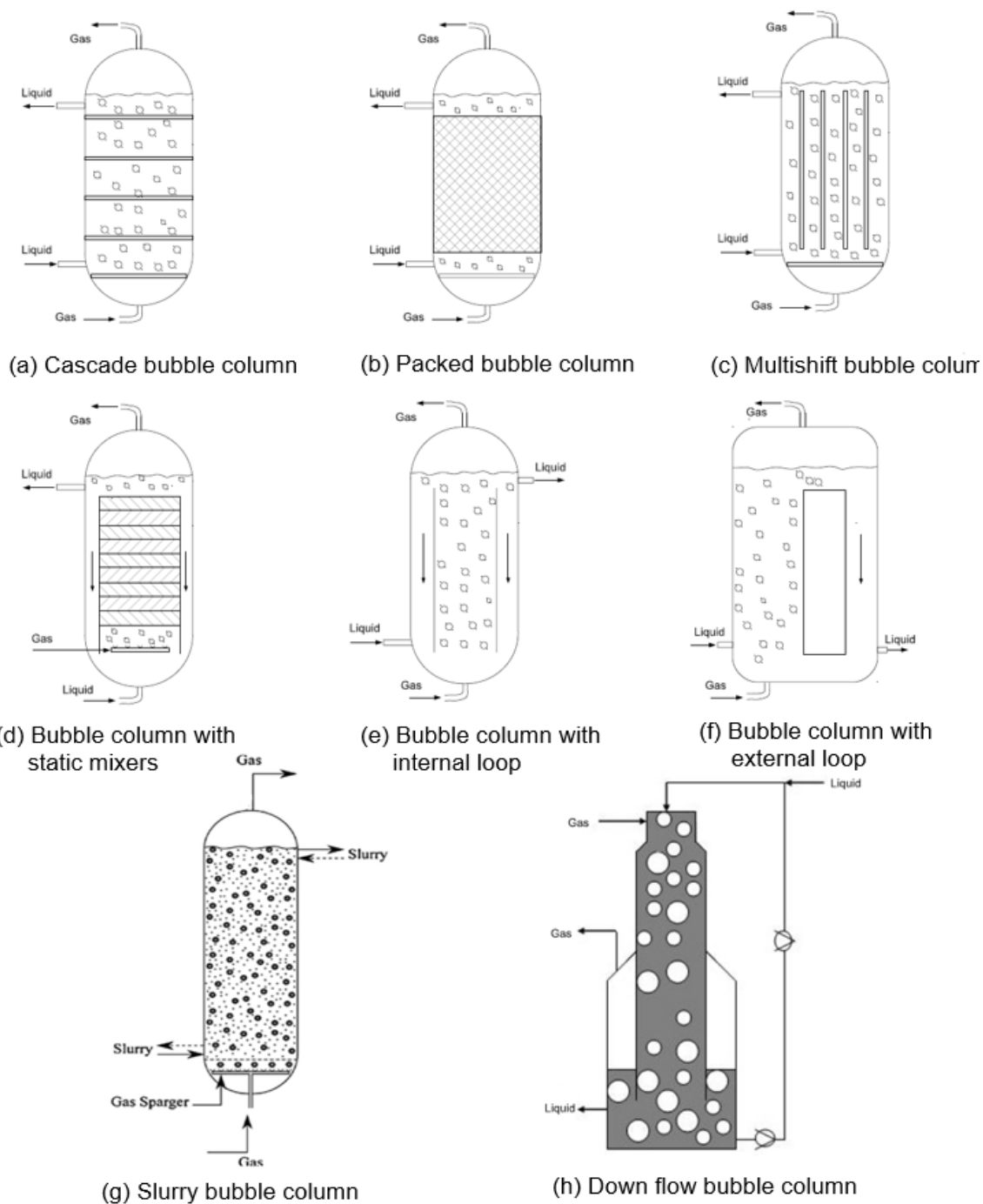


Figure 4-2: Types of bubble column contactors / reactors (Abdul Majeed Saed, 2003; Bai, 2010; Jakobsen, 2014)

The key parameter in designing a gas-liquid contactor, particularly a bubble column device, is the volumetric mass transfer coefficient ($k_L a$) of the liquid (Besagni *et al.*, 2018). This factor depends on the gas-liquid mass transfer coefficient (k_L) and specific interfacial area a (Majumder, 2016a). It was introduced in Section 3.2.1 in the context of the kinetics of carbonation reactions, and it is a term in the differential equations that model those reactions in Section 3.3.1. Because this is a key parameter, some variables that influence the values of the volumetric mass transfer coefficient in gas-liquid contactors are described in detail in the forthcoming subsections.

4.1.1 Effect of temperature on $k_L a$

An increase in the system temperature may increase $k_L a$ significantly (Majumder, 2016b; Rakymkul, 2011). As the temperature increases, the liquid viscosity and surface tension decrease, whereas the diffusivity of the gas in the liquid increases. A lower viscosity and surface tension together results in the formation of smaller bubbles and a decrease in bubble velocity. Therefore, the specific interfacial area, a , increases with increasing temperature. Moreover, because k_L is inversely proportional to the liquid viscosity, a decrease in viscosity will increase k_L . An increase in gas diffusivity into the liquid increases k_L because k_L is proportional to the diffusivity to the power 0.5 or 1.0. In the case of gases undergoing mass transfer to liquids, the general negative characteristic of gas solubility is that it is inversely proportional to temperature (Kwon *et al.*, 2008).

4.1.2 Effect of gas and liquid velocity on $k_L a$

The gas and liquid velocity profiles and their variations with the mass transfer coefficient depend on the type of bubble column device. In co-current up-flow bubble columns, the high rising velocity of the bubbles leads to a decrease in the bubble residence time, which in turn leads to a

low gas holdup¹ of approximately 30%. The interfacial area and mass transfer rate also decrease (Mandal, 2010).

As the gas is forced to move downward against its natural tendency to rise, co-current downflow bubble columns have a higher slip velocity² than up-flow systems (Mandal *et al.*, 2005). Thus, bubbles can have a higher residence time, which leads to higher gas holdups for given gas injection rates. This increase in the residence time of the bubbles and the high gas holdup also leads to an increase in the interfacial area and enhanced mass transfer rates (Walke and Sathe, 2011).

The volumetric mass transfer coefficient increases with superficial gas velocity (Majumder *et al.*, 2006) and systematically induces an increase in the specific interfacial area. At a low liquid-phase flow rate, an increase in the superficial gas velocity causes an increase in the mass transfer coefficient owing to higher turbulence in the liquid phase (Majumder *et al.*, 2006).

At high liquid flow rates, the effect of the superficial gas velocity is negligible because the influence of the liquid flow rate on the mass transfer behavior is higher than that of the gas flow rate. However, the ratio of the gas to liquid velocities depends on the type of gas-liquid contactor (Majumder, 2016c). A suitable choice of the liquid and gas throughput rates permits the gas

¹ is a dimensionless parameter defined as the volume occupied by the gas phase in the form of bubbles to the total volume of the bubble column. It plays an important role in the design and analysis of bubble columns. The gas holdup increases with increasing gas velocity and operating pressure, and it decreases with increasing liquid viscosity and solid concentration (Walke and Sathe, 2011)

² Slip velocity is the relative velocity between two phases (e.g., gas and liquid) within a flowing mixture (Walke and Sathe, 2011)

residence times to be adjusted to the maximum gas content within certain limits (Majumder, 2016a).

4.1.3 Effect of bubble size on k_La

Bubble size distribution determines the interfacial area per unit volume of the gas phase. Therefore, it has a considerable influence on the volumetric mass transfer coefficient. The bubble size distribution at any point in a column is determined by i) the initial bubble size at the point where the gas and liquid meet, ii) bubble coalescence during column transit, and iii) break-up during column transit (Majumder, 2016b; Zahradník and Fialová, 1996). According to Chen *et al.* (2021), the bubble coalescence and break-up rates are principally affected by the turbulent energy dissipation rate in a given system. Decreasing the bubble size can effectively increase the volumetric mass transfer coefficient (k_La), particularly when the bubble size decreases to several micrometers (Majumder, 2016a; Zahradník and Fialová, 1996).

However, the bubble size has opposite effects on the gas holdup, depending on whether the flow is upward or downward in the bubble column. The slip velocity of the bubble increases with its size. In the up-flow bubble column, an increase in bubble size, and thus slip velocity, leads to a lower gas holdup because the bubbles will then exit the column more quickly. In the downflow bubble column, large bubbles will spend more time in the column, thus increasing the gas holdup (Briens *et al.*, 1992).

4.1.4 Effect of pressure on k_La

Another parameter that plays a significant role in characterizing and designing a bubble flow column is the operating pressure. It is commonly accepted that increased pressure results in a

higher gas holdup (Zahradník and Fialová, 1996). The change in pressure in a system governs the flow energy required to transport multiphase fluids in a certain flow system. Many studies on bubble columns have been published in the literature (Majumder, 2016b). However, most of them used laboratory-scale columns, in which consideration of the falling pressure along the length of the bubble column (for upward flows) was not necessary. Laboratory-scale bubble columns are typically up to 2 m high. Therefore, it is possible to assume a simple mass transfer modeling with perfect mixing in the liquid phase and no pressure variation along the column height. However, tall bubble columns with a high height-to-diameter ratio (aspect ratio > 10) and good gas dispersion systems provide a large interfacial area and long contact times between the phases (Biń *et al.*, 2001; Deckwer *et al.*, 1978; Liu *et al.*, 2020; Zahradník and Fialová, 1996).

However, most of these investigators agree that the effect of pressure on k_La is related to the liquid-phase physicochemical properties, leading to a general increase in gas solubility with pressure. This can also lead to a decrease in the viscosity and surface tension of the liquid phase (Rakymkul, 2011).

4.1.5 Effect of solid concentration on k_La

The addition of solid particles to a liquid phase can have varying effects on k_La . Low concentrations of small particles have a limited impact on the slurry viscosity. They can inhibit the coalescence tendency or promote the breakup of gas bubbles by interacting directly at the gas-liquid interface, resulting in a small increase in k_La values. However, high solid concentrations are more likely to increase the slurry viscosity, promoting gas bubble coalescence and decreasing the gas-liquid interfacial area. However, increasing the bubble size can increase the mass transfer

coefficient k_L . As a result, $k_L a$ might increase, decrease, or remain unaffected by the solid concentration, depending on the resultant effect on both k_L and a . (Rakymkul, 2011).

4.1.6 Challenges in estimating mass transfer coefficient in bubble columns

Several difficulties are associated with estimating the mass transfer and volumetric mass transfer coefficients in a bubble column. Some of the most significant challenges are as follows:

- **Complex flow dynamics:** Although the bubble column reactor has a simple geometry, complex hydrodynamics and their influence on the mass transport characteristics make it difficult to achieve a reliable design and scale-up of bubble column contactors (Abdul Majeed Saed, 2003). It can be challenging to model and predict the mass transfer characteristics accurately.
- **Non-uniform bubble size distribution:** The bubbles generated in a bubble column are typically not uniform in size, making it difficult to estimate the interfacial area and mass transfer coefficient accurately (Krishna and van Baten, 2003).
- **Gas-liquid interfacial area:** Measuring the interfacial area between gas and liquid phases can be challenging and requires advanced experimental techniques. Accurate parameter estimation is essential for calculating the mass transfer coefficient (Doran, 2013).
- **Chemical reactions:** In many industrial applications, mass transfer occurs in conjunction with chemical reactions, which can further complicate the estimation of the mass transfer coefficient (Jakobsen, 2014). This effect is clearly illustrated in Section 3.3.

- Limited experimental data: The experimental data required to estimate the mass transfer coefficient may be limited, particularly for complex systems or conditions outside the range of typical operating parameters (Pinto *et al.*, 2016).

Overall, accurately estimating the mass transfer coefficient in a bubble column can be challenging because of the complex flow dynamics and numerous variables that can influence the mass transfer rates of each phase. A combination of advanced experimental techniques and sophisticated modeling approaches is required to obtain accurate results.

Young *et al.* (2022) have presented a model that estimates gas absorption during the compression process in a HAC downcomer by incorporating the hydrodynamics, solubility kinetics (for varying aqueous, non-reacting systems), and psychrometric aspects of the system. Although it is principally developed to predict the gas mass transfer behavior of co-current downward gas-liquid bubble column contactor systems (as present in a HAC), this model can also be applied to co-current bubbly flows in any orientation, including upward flows (as present in a conventional bubble column contactor). The following sections describe the HAC as a co-current downward bubble column and then summarize the hydrodynamic and mass transfer behavior of the HAC downcomer using the Young *et al.* (2022) bubbly flow model in Section 4.4.3.

4.2 Hydraulic air compressor (HAC) developments

A hydraulic air compressor (HAC) is a no-moving-parts gas compression technology that uses hydropower to compress air. Original commercial development of this technology is attributed to Charles H. Taylor in the 1890s whereby a run-of-river hydropower resource was utilized to induct and compress atmospheric air (Schulze, 1954).

The modern HAC systems investigated by Millar (2014b) do not rely on natural watercourses, but instead use pumps to circulate the liquid (Figure 4-3) while taking advantage of near-isothermal gas compression (Hutchison, 2018b). A HAC system can be arranged in two different configurations: open loop, or closed loop as depicted in Figure 4-3.

In a closed loop system, the forebay tank is removed and replaced by a pipe loop to connect the pump directly to the downcomer pipe (Hutchison, 2018a). Its process begins with water entering the forebay from the pump discharge. Water flows through a mixing head and atmospheric air is entrained in the water and produce a liquid-dominated two-phase bubbly flow at the air–water mixing horizon (AWMH). As the bubbly flow continues vertically downwards in the downcomer duct, the static pressure of the water increases, which is subsequently transmitted to the gas, compressing the bubbles. At the lower elevation end of the compression process, the high-pressure air bubbles are separated from water by reducing the two-phase flow velocity in a duct of larger area and permitting buoyancy to lift the bubbles from the liquid phase to form a compressed air plenum above the separator operating water level (SOWL).

When the water stream passes up the riser it recovers its potential energy. Then the water enters a tailrace tank open to atmospheric pressure at the tailrace operating water level (TOWL). A pump lifts water from the tailrace tank to the AWMH, thereby completing the circuit.

The elevation difference between the mixing horizon (AWMH) and tailrace water level (TOWL) provides the driving head for the liquid flow in the system and the column of water between the tailrace (TOWL) and the water level in the liquid–gas separator (SOWL) determines the delivery pressure (Hutchison, 2018a; Young *et al.*, 2022).

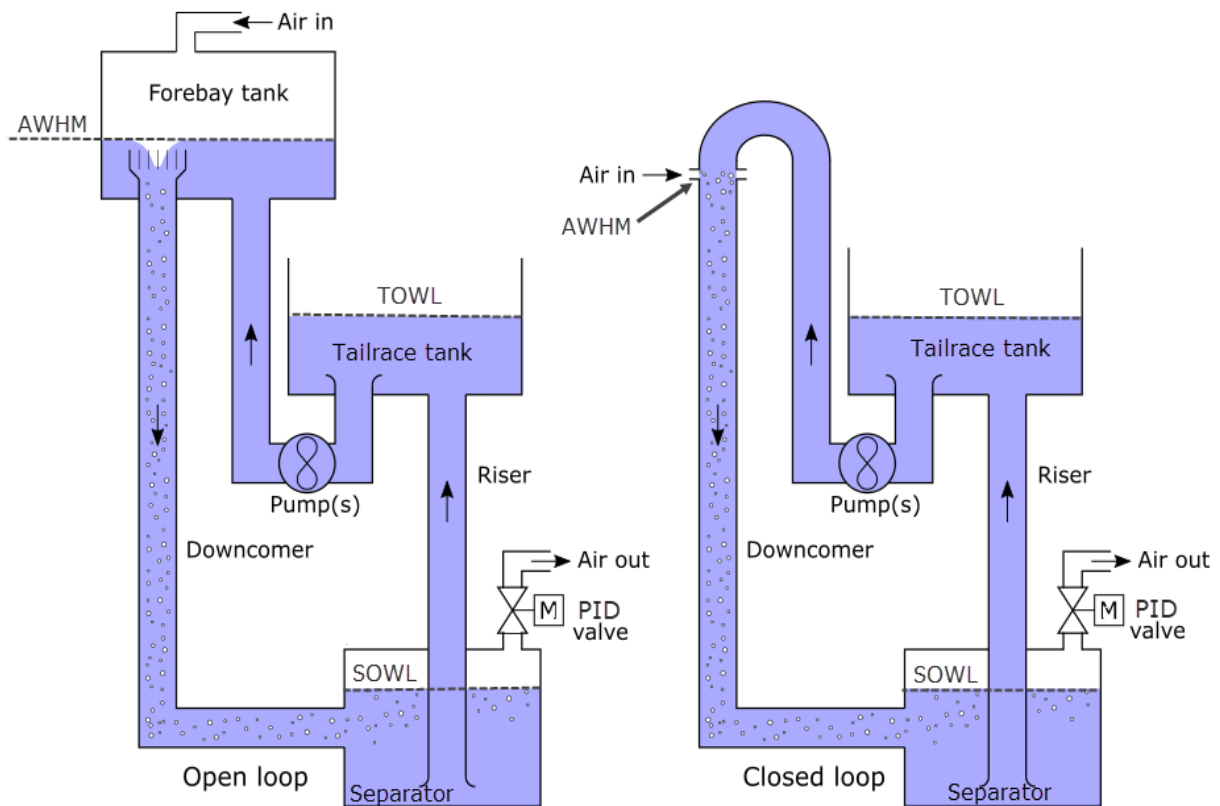


Figure 4-3: Schematic of the open and closed looped systems of the HAC (Hutchison, 2018a)

The water flow rate can be controlled by either a throttling valve, a variable speed drive, or the operating configurations of multiple parallel pumps as explored by Millar and Pourmahdavi, (2021). The gas is passively inducted by the HAC and the amount of gas inducted is essentially determined by the amount of input hydropower remaining after the frictional losses of the fluid flow circuit are overcome. The delivery of compressed air can be controlled by adjusting the water level in the separator with a motorized valve and a PID controller which enables the separator to double as a compressed air storage vessel (Young *et al.*, 2022).

In a closed loop HAC, there is a significant emphasis on the energy efficiency of the system because the source of the compression work is the mechanical shaft work of the pumping system

which provides the input hydropower. Unlike a run-of-river HAC, where the cost of power is effectively zero, electrical power is required to run the closed-loop HAC. The reduction of energy consumed to compress air is achieved when each source of wasted energy is appropriately addressed. Therefore, the target for the efficiency improvement of HACs is the reduction of irreversibility from all sources (Hutchison, 2018a; Millar and Pourmahdavi, 2021).

Currently, two prototypes of HACs have been constructed: an initial prototype (“Baby HAC”) and a larger pre-commercial demonstrator (“Dynamic Earth HAC” or “demonstrator”). Both of the systems were initially designed to operate as open loop as reported by Hutchison, (2018b), but have since been modified to operate in the closed loop configuration. The experimental work presented in Chapter 5 was completed on Baby HAC, and the system will be described in much greater detail therein.

As will be seen in Chapter 6, as part of this work, a further variant of HAC configuration has been developed to lab prototype stage, which removes the tailrace tank from the system and connects the riser directly to the suction side of the circulating pumps. As a consequence, this removes the possibility for mass transfer interactions with the atmosphere, and thus affords greater control of gas mass transfer behaviour and the opportunity for the greater degree of chemical control required for CO₂ capture and sequestration applications of HACs.

Whether they are open loop or closed loop, the downcomers of HACs clearly represent a type of gas-liquid contactor (Figure 4-2). An important distinguishing factor between the system illustrated in Figure 4-2(h) and a HAC illustrated in say, Figure 4-3, is that in a HAC, the mass flow rates of the phases are connected to one another as induction of the gas phase is passive,

whereas mass flow rates of the phases are taken to be independently controllable for devices of type Figure 4-2(h).

4.3 The hydrodynamic and mass transfer bubbly flow model of the HAC

In the HACs of Figure 4-3, water is circulated through the system, while being isolated from the natural environment everywhere with the exception of the tailrace tank. This feature allows the gases other than air to be inducted into the process at the AWMH and provides the means to manipulate the solubility kinetics and psychrometric aspects of the compression process by controlling (i) the circulating liquid temperature and, (ii) the circulating liquid chemistry (Young *et al.*, 2017).

Young *et al.* (2022) describes a model for estimating the absorption of gas in the compression process in a HAC downcomer which couples the hydrodynamics, solubility kinetics and psychrometric aspects to establish a novel capability. It upgrades the Millar (2014b) model by integrating the mass transfers between the gas and liquid phases with the hydrodynamic formulation, rather than leaving these respective aspects of behavior weakly coupled, and can account for the effects of increasing the liquid temperature and the addition of inorganic, non-reacting, co-solutes so that varying aqueous systems can be explored.

In the Young *et al.* (2022) model, the gas compression process in the downcomer of the HAC is modelled as a steady one-dimensional two-phase bubbly flow and it permits species to transfer between gas and liquid phases due to the solubility-driven gas species mass transfer and changing psychrometric conditions of the gas phase in the process. The state of the fluids through the process is defined by the pressure, temperature, liquid velocity, gas slip velocity, species molar

flows in the gas and liquid phases. The model also predicts the pressure, temperature, liquid velocity, gas slip velocity and the species molar flows in the gas and liquid phases at the outlet of the downcomer from which the composition of the compressed off-gas produced by a HAC at the separator and the concentrations of the same gas species dissolved in the water can be estimated. For full details of the HAC downcomer bubbly flow model formulation, please refer to (Young, 2017).

As reported in Young *et al.* (2022), this HAC downcomer model, originally reported with only minor formulation variations in Young (2017), improves upon the next best representation of mass transfer behavior of co-current upward and downward gas-liquid bubble column contactor systems due to Deckwer *et al.* (1978). Rzehak (2016), and Hissanga *et al.* (2020) have also made valuable contributions. While good agreement was obtained between the Young (2017, 2022) simulation predictions and the experimental data of Deckwer *et al.* (1978), similar experimental data was not available for downward co-current bubbly flow of a HAC. The results of the experiments presented in Chapter 5 aim to correct this gap. But more pertinently, before the simulation tool could be adopted in design of a carbon capture and sequestration system following the concepts of Chapter 3, the Young (2017, 2022) model needed to be experimentally verified.

4.4 HAC systems as mineral carbonation contactors

The application of HAC systems as a general gas compression devices has been discussed in detail by Schulze (1954), Chen and Rice (1982), and Millar (2014b) with more specific aspects being dealt with by Hutchison (2018b) (air-water mixing & separation), Millar and Pourmahdavi (2021) (pump manifolds), and Young (2017) (psychrometric and gas mass transfer aspects). From the

descriptions of HACs presented in section 4.2 compared alongside the bubble column devices reviewed in section 4.1, it may be readily appreciated that the HAC downcomer duct at least may be considered as a co-current downward flow bubble column reactor.

4.4.1 Isothermal compression

When viewed as a gas compressor only, one of the advantages of HACs over contemporary compressor technologies is the nearly isothermal gas compression process it embodies. In a HAC, air is compressed and simultaneously cooled as the heat generated from compression of the gas is simultaneously transferred to the water (Hutchison, 2018a). A typical HAC has a mass flow of water more than 1000 times that of air and the heat capacity of water is four times that of air. There is a large interfacial area available for heat transfer within the two-phase bubbly downward flow of the HAC downcomer, and the resulting temperature rise of the gas is small (Pavese *et al.*, 2017). Therefore, this compression process approaches one of isothermal compression, the theoretically minimum work compression process. Gas-phase compression heat must enter the liquid phase and thus the gas temperature must rise a little to drive the heat transfer process between the phases. Consequently, the gas compression process of the HAC is termed nearly-isothermal.

4.4.2 Pressure gradient varies with the sense of interphase mass transfers

The pressure gradient increases with the direction of the downward co-current flow which is thought to lead to greater mass transfer in comparison to the upward co-current flow bubble columns which currently prevail. The pressure boundary condition at the terminal of the process in an upward co-current flow is atmospheric. In a downward co-current flow contactor, the terminal pressure boundary condition can be any pressure desired, depending on bubble column

(downcomer) length. Such characteristics could enhance the mass transfer characteristics and provide greater options in the design of CO₂ capture systems.

4.4.3 Hydrodynamic and mass transfer of HAC downcomer

In Young *et al.* (2022) bubbly flow model (all the graphs presented in this section have been prepared on this basis), the gas species are permitted to transfer between the gas and liquid phases because of the solubility-driven gas species mass transfer and the changing psychrometric conditions of the gas phase in the process. The pressure, temperature, liquid velocity, gas slip velocity, and species molar flow in the gas phase define the state of the fluid during the mass transfer process.

In this model, the bubbly flow is discretized into a series of conduit segments with different inlet and outlet diameters and nonvertical flow directions. The conservation equations for energy, momentum, mass, and gas species are applied, assuming a terminal slip velocity condition to solve the state of the fluids at the outlet of each segment (Young *et al.*, 2022).

This section presents the simulation results of the hydrodynamics and mass transfer of the HAC downcomer designed for a Dynamic Earth HAC demonstrator. The model input parameters obtained from the design configuration and performance testing of the demonstrator system are listed in Table 4-2.

The number of conduit segments in which the downcomer is discretized in the model is 60. The mixtures of dry air and input gas used in the model are listed in Table 4-3. These are not experimentally tested concentrations obtained from Dynamic Earth trials but are instead assumed

to illustrate the probable performance of the demonstrator system in stripping CO₂ from an input gas stream to simulate the expected behavior with an exhaust gas stream.

Table 4-2: Summary of input parameters for the simulation

Input parameter	HAC Downcomer
Input water mass flow rate (kg/s)	401.27
Input air mass flow rate (kg/s)	0.109
Input pressure (Pa)	101325
Input temperature (K)	293.15
Diameter (m)	0.368
Length (m)	21.94
Flow direction (°)	-90
Absolute roughness (m)	5.8×10^{-3}
Input gas relative humidity (%)	100

The initial CO₂ concentration in the water at HAC intake is assumed to be zero. The initial concentrations of the other species are calculated using Henry's law and assumed to be at approximate equilibrium with the atmospheric concentrations of the same species.

Table 4-3: Mixtures of air and input gas

Mixture	N₂	O₂	Ar	CO₂
Atmospheric dry mol fractions	0.7808	0.2095	0.0093	0.0004
Input gas dry mol fractions	0.75	0.05	0.01	0.19

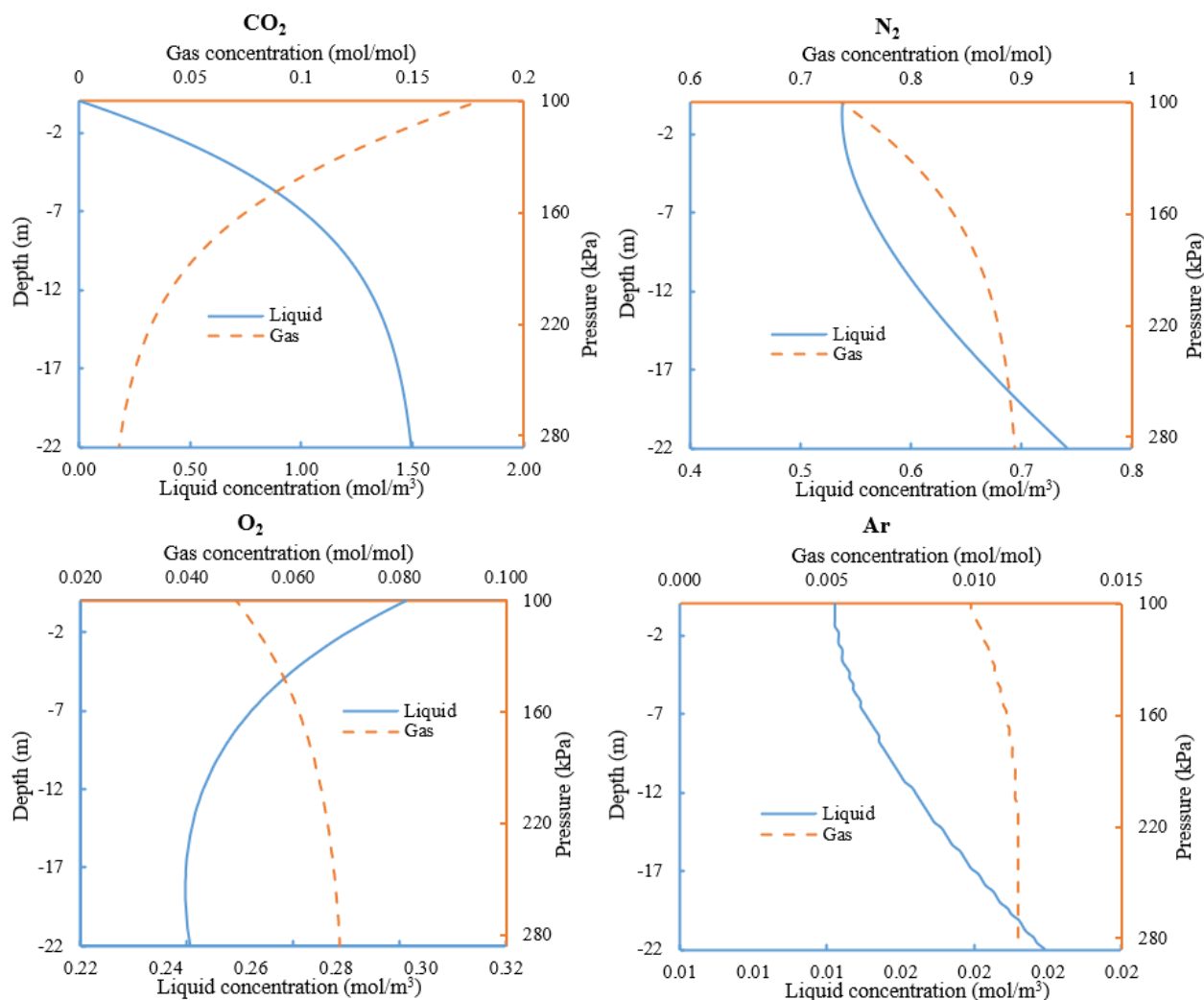


Figure 4-4: Concentration profiles of the gas and liquid in the HAC downcomer predicted by the model

The input pressure of the HAC downcomer is defined to be 101.325 kPa. Figure 4-4 shows the model prediction of the concentration profiles of each gas in the gas and liquid phases of the HAC downcomer. The delivery pressure of the downcomer is found to be 285.96 kPa.

The concentrations of dissolved CO_2 (aq), N_2 (aq), and Ar (aq) in the water increase as the depth of the HAC downcomer increases. However, the concentration profile of dissolved O_2 (aq) shows an interesting behavior. Figure 4-4 shows that the initial concentration of dissolved O_2 (aq)

is 0.30 mol/m^3 . Water is initially saturated with oxygen relative to the atmospheric O_2 concentration. However, it is in contact with a gas that has significantly less oxygen than the atmosphere. Therefore, water is initially supersaturated with oxygen at the top of the HAC downcomer. Some dissolved O_2 (aq) exited the solution through the HAC downcomer, causing an increase in the concentration of the remaining oxygen gas. The minimum value of dissolved O_2 is 0.244 mol/m^3 at -18.29 m of HAC downcomer.

As previously mentioned, the initial concentration of dissolved CO_2 (aq) is considered zero. The concentration of dissolved CO_2 in the water increases as the water transits the HAC downcomer. The concentration of remaining CO_2 in the gas phase decreases as more CO_2 dissolves in water. The concentrations of dissolved CO_2 (aq) and gaseous CO_2 (g) at the length of 21.95 m of the HAC downcomer are 1.50 mol/m^3 and 0.0082 mol/mol , respectively. These results show that most of the inlet CO_2 gas is dissolved in the water.

Figure 4-4 shows that the concentration of the remaining N_2 (g) increased more than that of the other gases. This is because the other species dissolved faster due to their different solubilities. The concentration of the remaining Ar (g) does not change significantly.

The model also calculated the liquid concentration of the gas species at the gas-liquid interface in each section of the downcomer (Figure 4-5). According to the two-film theory implemented in the Young (2022) model (refer to Figure 3-5), the liquid-phase concentrations at the bubble interfaces are considered to be at pressure-dependent saturation conditions determined through Henry's law.

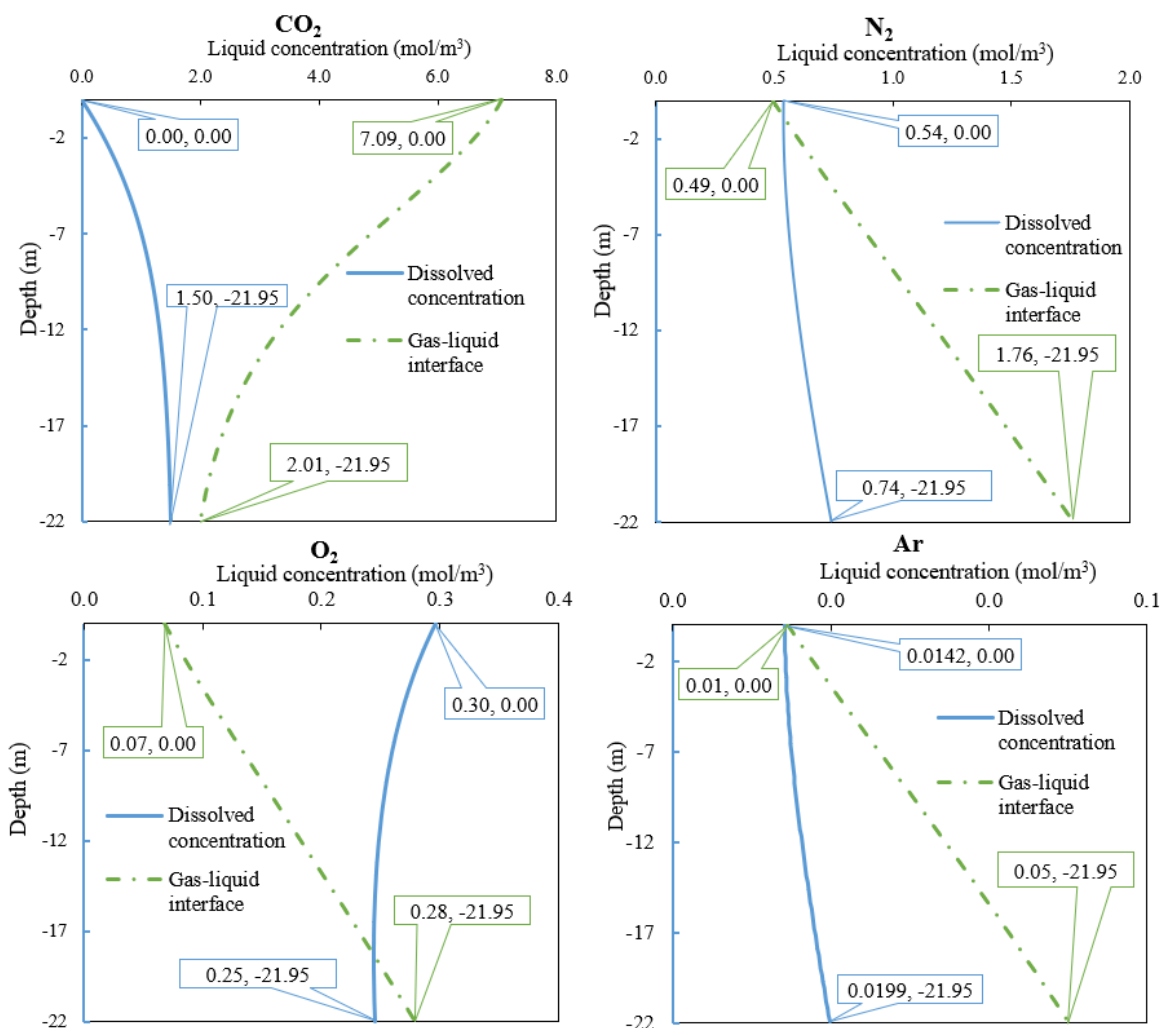


Figure 4-5: Liquid concentration profile of the gas species at the gas-liquid interface in each section of the downcomer

According to Figure 4-6, along the entire length of the HAC downcomer, the concentration of CO₂ at the gas-liquid interfacial area is higher than the bulk liquid-phase concentration of dissolved CO₂ at the same HAC downcomer depth. This is because the concentration of CO₂ at the gas-liquid interfacial area is calculated based on the local gas compositions. The difference

between the interfacial and bulk concentrations provides the potential to drive the gas into the solution.

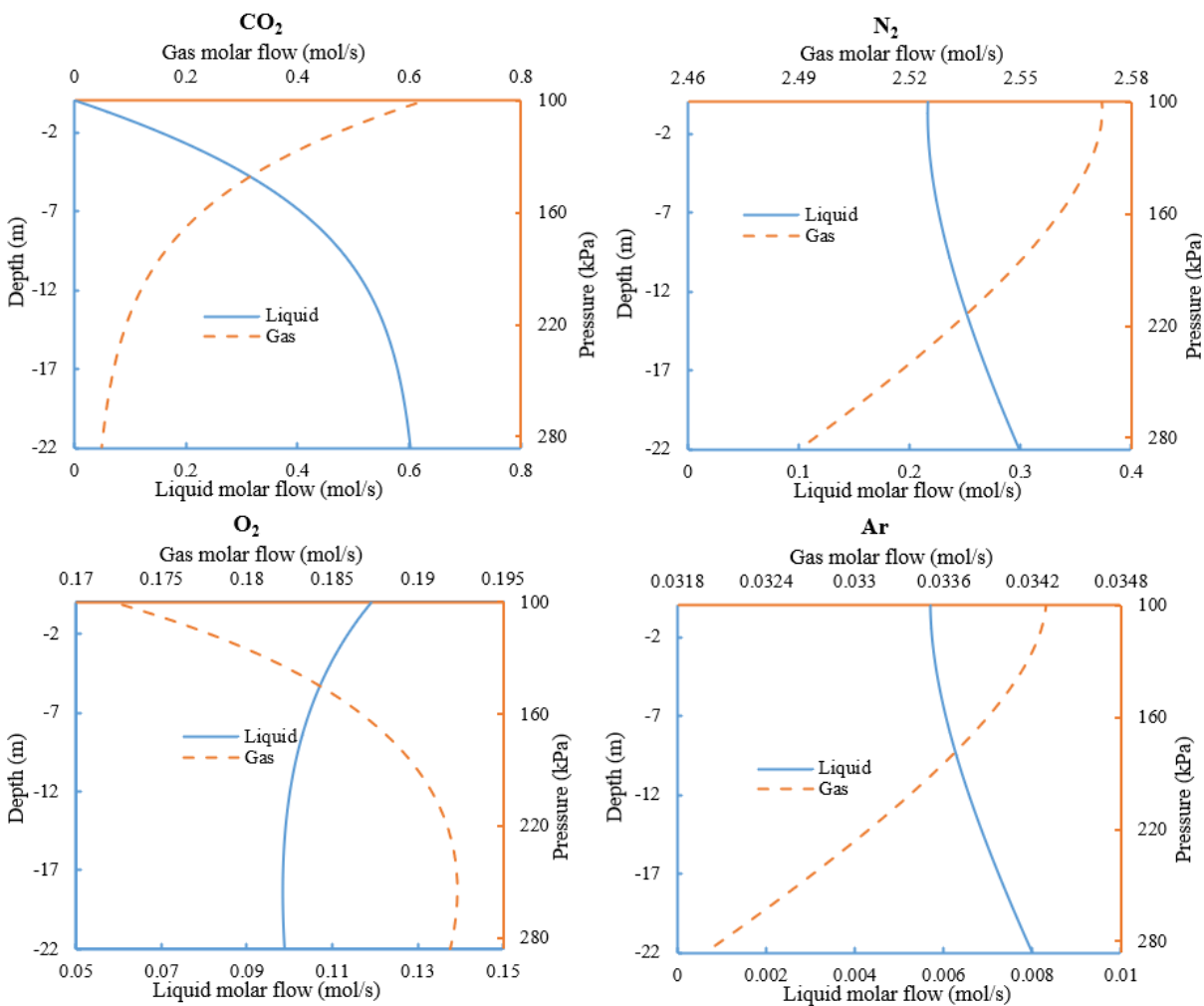


Figure 4-6: Variations of gas and liquid molar flow rates in HAC downcomer predicted by the model

The concentration of CO₂ in the gas phase is 0.19 mol/mol at the inlet of the HAC downcomer. Since CO₂ dissolves in water as the flow progresses downward, the concentration of the remaining CO₂ in the gas phase decreases, which reduces the potential to drive CO₂ into the solution. Consequently, despite the higher pressure of the bulk gas in the bubbles with increasing

depth, the concentration of CO_2 at the gas-liquid interfacial area also decreases. However, the O_2 concentration profile exhibits a different behavior. The water is initially supersaturated with O_2 . The concentration of dissolved O_2 is higher than that of O_2 in the gas-liquid interfacial area. The O_2 comes out of the solution through the HAC downcomer process.

In Figure 4-6, significant variations can be observed in the molar flow rates of the CO_2 gas and liquid in the HAC downcomer. However, no considerable changes are observed in the molar flow rates of the other species in either phase.

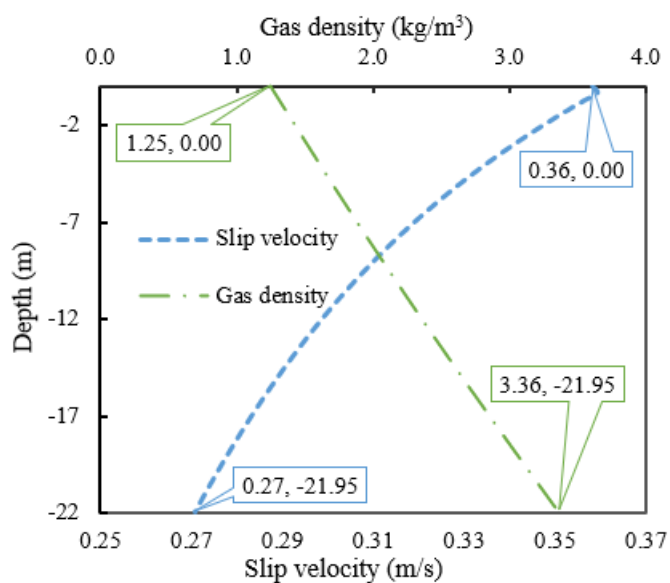


Figure 4-7: The variation of slip velocity and gas density

4.4.4 Back-calculation of k_{La} for HAC downcomer

Figure 4-7 shows that the gas density increases in the HAC downcomer (as the gas is compressed, as expected in a HAC) while the slip velocity decreases. The mean bubble diameter decreases as the gas bubbles move down the column after accounting for inter-phase mass transfers (Figure

4-8). The Young *et al.* (2022) model conserves the number of gas bubbles (bubble coalescence and bubble breakup are not considered). Thus, the interfacial area between the gas and liquid phases decreases as the flow progresses downward.

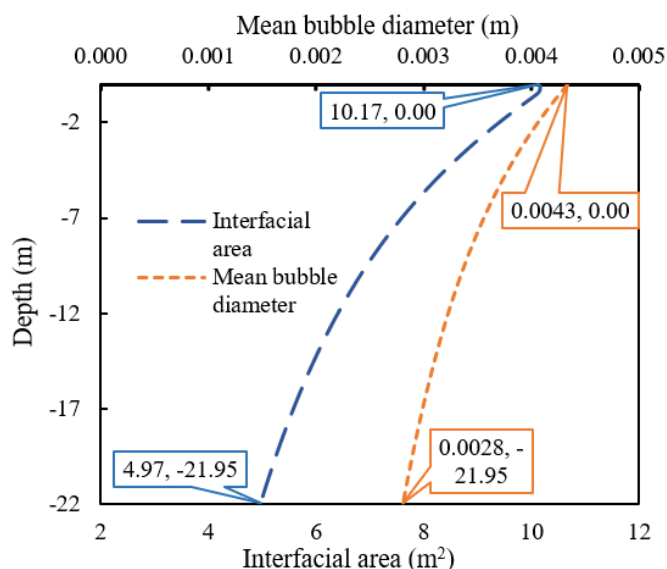


Figure 4-8: The variation of mean bubble diameter and interfacial area available for the gas mass transfer.

For the case presented in Table 4-2 and Table 4-3, by integrating the interfacial area present in each of the 60 ‘slices’ of the HAC downcomer model, the total interfacial area available is 414.35 m². Normalizing this by the 2.334 m³ volume of the downcomer, the average value of the specific interfacial area in the HAC downcomer, a , is 177 m²/m³.

Internally, the Young *et al.* (2022) bubbly flow model computes the gas mass transfer coefficient for each gas species at each ‘slice’ of the HAC downcomer. These values for the simulation case presented are plotted in Figure 4-9 for CO₂ (g). The variation in values is as expected based on the model formulation, but it is also worth noting that it is relatively small and does not vary significantly. The average values of the mass transfer coefficient are presented for

each gaseous species in Table 4-4 which may be taken to be representative of the HAC downcomer geometry and the given flow conditions.

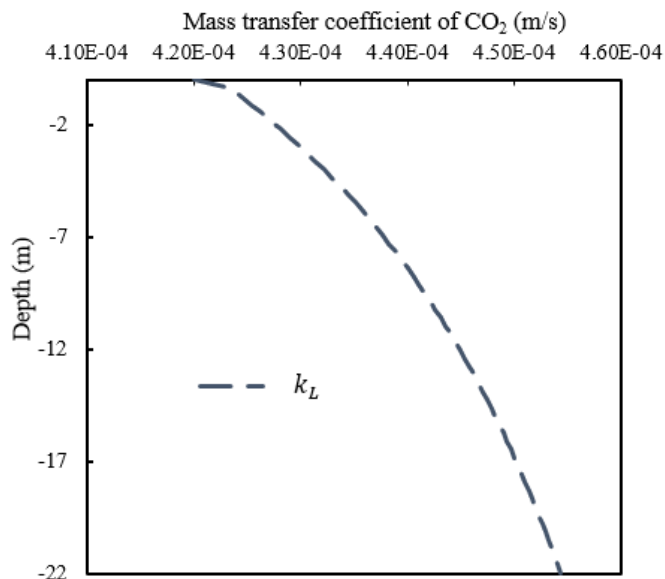


Figure 4-9: Variation of the mass transfer coefficient of CO₂ in the HAC downcomer

Table 4-4: Average values of the gas mass transfer coefficient

$k_L \text{ (m/s)} \times 10^{-3}$			
N ₂	O ₂	Ar	CO ₂
0.44	0.50	0.38	0.44

From the Young *et al.* (2022) model, system values of $k_L a$ can be back-calculated from the simulation results according to:

$$k_L a = \frac{\dot{n}}{V \times \Delta C} \quad (4.1)$$

where \dot{n} is the overall addition rate of CO₂ to the liquid phase (mol/s) in the downcomer (shown in Figure 4-6), V is the total downcomer volume (m³), and ΔC is a log mean concentration difference between the inlet and the outlet of the downcomer, (mol/m³) that may be calculated

from the plots of Figure 4-4. For convenience, example calculations for $k_L a_{CO_2}$ are presented in Table 4-5.

Table 4-5: Summary of calculations for $k_L a_{CO_2}$

Parameter	Value	Unit
Volume of downcomer, V	2.33	m^3
Interfacial area, A	414.35	m^2
Specific interfacial area, $a = A / V$	177.48	m
Mass transfer coefficient, k_{LCO_2}	4.42×10^{-4}	m/s
$k_L a_{CO_2} = k_{LCO_2} \times a$	0.0784	s^{-1}

Equation (4.1) showed that $k_L a$ could be considered a type of ‘volume normalized’ mass transfer co-efficient, permitting comparison of values derived from results of bubbly flow systems of different types and scales. For example, in Section 3.3.2, $k_L a_{CO_2} = 0.0194 \text{ s}^{-1}$ was reported for the experimental systems of Velts *et al.* (2011c), which comprised a batch reactor in which the liquid was stirred and gas was bubbled into the stirred liquid. In this study, the bubbly flow model of Young *et al.* (2022) was used to estimate the CO_2 gas mass transfer coefficient ($k_L a_{CO_2}$) for the dynamic kinetic model of mineral carbonation. For the demonstrator conditions modelled, $k_L a_{CO_2}$ was 0.0784 s^{-1} , approximately 4 times higher than that of Velts *et al.* (2011c).

4.5 Summary

In this chapter, various types of gas-liquid contactors were briefly introduced. Subsequently, the bubble column contactors were described in more detail, and the effect of different variables on the volumetric gas mass transfer coefficient in a bubble column was discussed. HACs were then presented as gas-liquid contactor systems that utilized a co-current downward bubble column, and

the model developed by Young *et al.* (2022) to simulate such systems was outlined. Finally, simulation results from the downcomer model were used to illustrate how the values of $k_L a$ could be back-calculated so that they could be used in the reaction kinetics model presented in Section 3.3.1. The exemplar value produced by the back-analysis process was comparable to the values of $k_L a$ cited by other workers. The latter was based on the results of experimental observations of gas mass transfer and thus were empirically derived. In contrast, those from the Young *et al.* (2022) bubbly flow model emerged from a synthesis of the process, physics of 2-phase flow, and assumed flow conditions. Although the latter process produced back-calculated $k_L a$ values comparable to those from empirical sources, the source of the variance between them was unknown. It was concluded that experimental verification of the Young *et al.* (2022) bubbly flow model would be necessary so that the values derived from it could be used with confidence.

5. The Experimental verification of bubbly flow model of the HAC¹

This chapter presents the experimental verification of a one-dimensional steady-state bubbly flow model. Young (2017, 2022) can simulate the hydrodynamics and interphase mass transfer of two-phase bubbly flow during the compression process in the downcomer of the HAC. In addition to its application in this context, the model is also proposed to estimate the CO₂ volumetric mass transfer coefficient of the dynamic model for the mineral carbonation chemical process discussed in Chapter 3, using a back-calculation process based on simulation, as described in Chapter 4. The overall approach to verification aims to establish a reliable digital twin (Grieves, 2019) of the HAC process.

In the following sections, after a more detailed explanation of the approach to experimental verification of the bubbly flow model, the experimental set-up and procedures employed to verify the Young *et al.* (2022) model are described. Results from the experimental procedures are presented and the experimental results are compared with the results of simulation using the Young *et al.* (2022) model. The discussion of the results, along with a summary of the presented material are provided in the concluding sections of this chapter.

¹ Some of the contents of this chapter have been adapted from the papers published at:

- M. Pourmahdavi, S.M. Young, A. Hutchison, C. Noula, D.L. Millar, *Gas absorption in a hydraulic air compressor. Part II: Experimental verification*, *Chemical Engineering Science*, Volume 261, 2022, 117870.
- S.M. Young, M. Pourmahdavi, A. Hutchison, D.L. Millar, *Gas absorption in a hydraulic air compressor. Part I: Simultaneous hydrodynamic and mass transfer bubbly flow model*, *Chemical Engineering Science*, Volume 260, 2022, 117871

5.1.1 Approach for model verification

A series of practical experiments were designed and conducted on the Baby HAC (Figure 5-1) pilot testing system such that the initial and boundary conditions prescribed for the model could be matched to the physical reality of the experiment. If the bubbly flow model produced simulation results that agreed with the hydrodynamic variable observations for these same conditions and this recurs for different operating conditions, this presents strong evidence that the model is verified – in one respect.

But during HAC operation, the system not only maintains a hydrodynamic energy balance across all HAC components at all times, a species mass balance between the phases is maintained too. If the input gas-phase species concentrations, off-gas species concentrations, dissolved gas concentrations at the AWMH and dissolved gas concentrations at the separator confirm a mass balance in both model and experiment, and those mass balances agree between model and experiment, this exhibits further evidence of verification of the Young (2017, 2022) downcomer model.

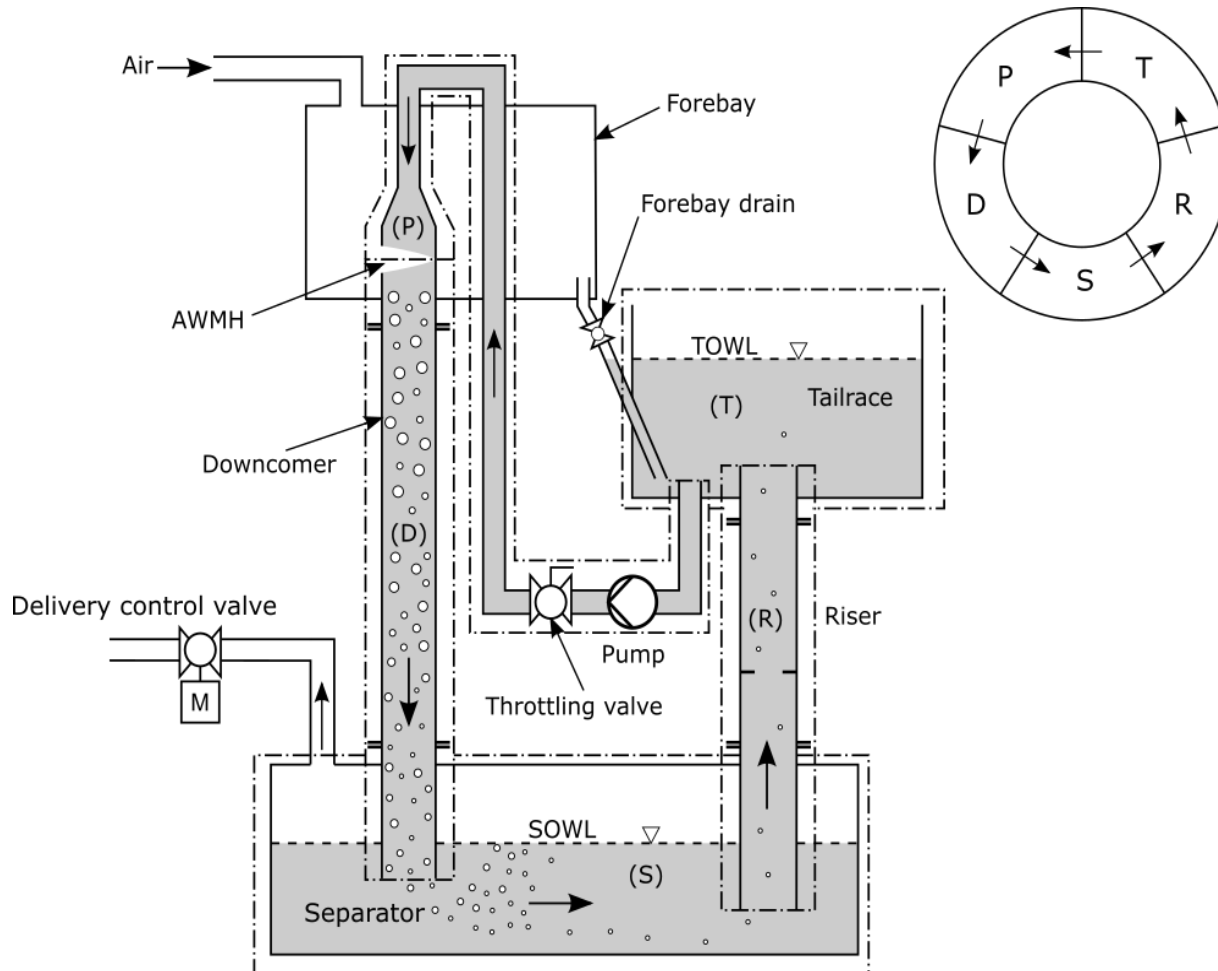


Figure 5-1: Schematic of the modern style of the hydraulic air compressor and its control volumes, AWMH: air–water mixing horizon, SOWL: separator operating water level, TOWL: tailrace operating water level

The predictions of the composition of the compressed gas product and liquid-phase concentrations of gas species by using the Young *et al.* (2022) bubbly flow model are strongly dependent on the liquid phase concentrations of gas species defined at the AWMH. Essentially, for the same hydrodynamic operating conditions, identical flow rates of liquid and gas, and identical composition of inlet gas mixture, the simulation tool revealed multiplicities of gas mass transfer behaviour, with significant variations in resulting off-gas compositions, depending on the

dissolved gas concentrations at the AWMH at the start of each experimental phase. Initialization of the liquid-phase dissolved gas concentrations at the AWMH in the model thus required careful consideration. When a run-of-river style HAC is being considered, the water in the HAC passes through the process only once and initialization of the liquid-phase concentrations is straightforward: the liquid phase concentrations of the gas species are initialized assuming equilibrium with atmospheric air at atmospheric pressure.

However, modern HAC systems such as the Baby HAC pilot utilize pumps to continuously circulate the water. Simulation of mass transfers as well as hydrodynamic performance using the bubbly flow model, required much more sophisticated definition of the boundary conditions for dissolved gas concentrations in the circulating liquid in these cases, particularly at the AWMH. As the water recirculates continuously in the Baby HAC pilot, the liquid-phase concentrations of gas species reflect the history of admissions and removals of dissolved gas species within the downcomer and the remaining components of the HAC (i.e., separator, riser, tailrace, pump). Consequently, as a part of the experimental verification efforts, an auxiliary model for the time-evolution of dissolved gas species within the ducts and vessels of HAC systems had to be developed to provide a basis for the appropriate definition of the dissolved gas concentrations in the liquid phase at the AWMH in simulations of each stage of the experiment. An outline of this auxiliary model is presented in Section 5.1.3. The experimental methods also had to be designed to ensure that the time evolution of dissolved gas concentrations predicted by this dynamic model in each of the HAC system compartments (P, D, S, R, T, Figure 5-1) matched the actual dissolved gas concentrations at these locations, and that the latter were confirmed through direct observation.

Overall, verification of the Young (2017, 2022) model involved obtaining consistency between sets of i) hydrodynamic operating variables, ii) species concentrations at the AWMH in both the gas phase and the liquid phase as well as iii) species concentrations in separated compressed offgas and separator liquid, for varying system set ups and operating conditions.

5.1.2 Experimental control

During the experiments, some of the variables which were subject to control processes were measured and recorded continuously. These process variables included the liquid mass flow rate (by means of a regulating valve) and liquid temperature (by means of a cooling loop installed in the tailrace with adjustable water flow rate) and the level of water in the separator (SOWL) and tailrace (TOWL) tanks (controlled by means of actuation of a servo-controlled compressed off-gas delivery valve). Keeping the SOWL and TOWL steady also provided steady off-gas delivery pressure. The Author designed a servo-controlled delivery valve that operated with a PID control loop using the SOWL as the control variable. This afforded excellent control over the SOWL and the system delivery pressure at all times during testing.

The Baby HAC operates within a temperature-controlled space however, the input gas temperature and relative humidity fluctuate diurnally. These variables are also monitored throughout. During the experiment, the gas and liquid phase concentrations of atmospheric gas species are measured continuously at multiple locations around the Baby HAC. The only experimental parameter that is systematically varied during the experiment is the input gas composition at the AWMH. During the experiment, the input gas mixtures change by mixing ambient air with progressively higher and then progressively lower controlled mass flows of pure CO₂ gas. Carbon dioxide is three orders of magnitude more soluble than nitrogen, and two orders

of magnitude more soluble than oxygen and argon (Sander, 2015). A series of set points of the experimental conditions are formed by gas mixtures admitted to the AWMH dosed with higher mass flows of CO₂. They would also provide readily measurable changes in the composition of the gas inducted and delivered by the Baby HAC.

5.1.3 Details of the auxiliary model for the time evolution of dissolved gas species within HAC systems.

In order to characterise the time-evolution of liquid phase concentrations resulting from the absorption history of continued operation of a HAC with water recirculation, a formulation to provide a framework for this time-varying aspect of the performance of recirculated HAC systems was developed. This model permits the general natures (constant, increasing, reducing) of additions and removals of dissolved gases in the liquid phase, within different components of the HAC system, to be represented and permits the expected gas species concentrations in the liquid phase in different parts of the HAC system to be computed.

For a liquid mass flow \dot{m}_l (kg/s) passing through a control volume, i , containing mass m_i (kg) of liquid, from a control volume $i-1$ subject to gas dissolution or exsolution E_i (kg/s) from or to a gas phase, the time evolution of concentration C_i of that dissolved gas (kg/kg) is given by Ekberg, (1994):

$$m_i \frac{dX}{dt} = E_i + \dot{m}_l X_{i-1} - \dot{m}_l X_i \quad (5.1)$$

For the purposes of this formulation, a HAC with water recirculation is divided into 5 control volumes (as shown in Figure 5-1) where: $i = \{D; S; R; T; P\}$, D is the downcomer which starts at the AWMH and ends at the downcomer outlet in the separator, S is the separator which

encompasses the liquid in the separator vessel, R is the riser pipe from the separator to the tailrace, T is the tailrace tank and P is the liquid in the pump circuit which brings water from the tailrace back to the AWMH. For steady input concentration, $X_{i-1} = \text{constant}$, the analytical solution of (5.1) is:

$$X_i(t) = X_{i-1}(t) + \frac{E_i}{\dot{m}_i} + \left[X_i(0) + \frac{E_i}{\dot{m}_i} - X_{i-1}(t) \right] e^{-\frac{\dot{m}_i t}{m_i}} \quad (5.2)$$

For $i=D$, the downcomer, $X_{i-1} = X_P$ which is not steady during Baby HAC start-up and transient periods between set points. If the input gas concentrations are unsteady, a finite difference solution of (5.1) at the $n+1^{\text{th}}$ period, each of duration Δt seconds, can be used instead:

$$X_i^{n+1} = \left(\frac{E_i^n + \dot{m}_i X_{i-1}^n - \dot{m}_i X_i^n}{m_i} \right) \Delta t + X_i^n \quad (5.3)$$

For the system of 5 consecutive control volumes comprising a HAC, the system of equations is:

$$\begin{aligned} X_D^{n+1} &= (E_D^n + \dot{m}_l X_P^n - \dot{m}_l X_D^n) \Delta T_D + X_D^n \\ X_S^{n+1} &= (E_S^n + \dot{m}_l X_D^n - \dot{m}_l X_S^n) \Delta T_S + X_S^n \\ X_R^{n+1} &= (E_R^n + \dot{m}_l X_S^n - \dot{m}_l X_R^n) \Delta T_R + X_R^n \\ X_T^{n+1} &= (E_T^n + \dot{m}_l X_R^n - \dot{m}_l X_T^n) \Delta T_T + X_T^n \\ X_P^{n+1} &= (E_P^n + \dot{m}_l X_T^n - \dot{m}_l X_P^n) \Delta T_P + X_P^n \end{aligned} \quad (5.4)$$

where $\Delta T_i = \Delta t / m_i$.

In the HAC, the control volumes that contain a gas–liquid interface are the downcomer, separator, riser, and tailrace control volumes and therefore it is assumed that dissolution or exsolution can only occur in these control volumes. The gas–liquid interface in the riser control volume depends upon the gas–liquid separator’s effectiveness at separating the compressed gas from the liquid. Supposing that no gas entering the separator reports to the riser, as was observed in the Baby HAC pilot, the system (5.4) can be simplified:

$$\begin{aligned}
 X_D^{n+1} &= (E_D^n + \dot{m}_l X_P^n - \dot{m}_l X_D^n) \Delta T_D + X_D^n \\
 X_S^{n+1} &= (E_S^n + \dot{m}_l X_D^n - \dot{m}_l X_S^n) \Delta T_S + X_S^n \\
 X_R^{n+1} &= (\dot{m}_l X_S^n - \dot{m}_l X_R^n) \Delta T_R + X_R^n \\
 X_T^{n+1} &= (E_T^n + \dot{m}_l X_R^n - \dot{m}_l X_T^n) \Delta T_T + X_T^n \\
 X_P^{n+1} &= (\dot{m}_l X_T^n - \dot{m}_l X_P^n) \Delta T_P + X_P^n
 \end{aligned} \tag{5.5}$$

E_D^n , E_S^n and E_T^n can seen to drive the system evolution as a whole, depending on their nature, that is, whether they are values that are steady, increase or decline in time. In order that a fully predictive scheme can be established, mechanistic models of the addition rates of species in the downcomer, separator and tailrace control volumes are required. E_D^n is evaluated with the Young *et al.* (2022) bubbly flow model while the models for E_S^n and E_T^n are presented in the following.

The addition or removal rate of gas species in the separator and tailrace need to respond to the changes in the bulk and interfacial concentrations at the operating liquid level. The addition rate of species to the liquid in the separator and tailrace control volumes can be evaluated by:

$$E_i^n = MK(C_i^n - C_i^n)A_i \quad (5.6)$$

where $i = \{S; T\}$, M is the molar mass of species, K is the mass transfer coefficient, C_i^n is the molar concentration of species at the SOWL or TOWL and A_i is the gross plane area available for mass transfer inside the separator or tailrace.

The mass transfer coefficient for the flow conditions in the separator and tailrace tanks (5.7) is estimated using surface renewal theory (Knudsen *et al.*, 1999):

$$k = \sqrt{Ds} \quad (5.7)$$

$$s = \frac{m}{\dot{m}_l} \quad (5.8)$$

where D is the mass diffusivity of the species and s is the surface renewal rate estimated by the mass exchange rate of the tank.

The concentration of species at the gas–liquid interface, C_i^n are evaluated using Henry's law while the mass fraction of the species in the bulk liquid is converted to a molar concentration, C_i^n .

$$C_i^n = K_H P Y^n \quad (5.9)$$

$$C_i^n = \frac{\rho_l}{M} X_i^n \quad (5.10)$$

where K_H is the Henry's constant for the species, P is the operating pressure of the tank, Y^n is the gas-phase mole fraction of the species and ρ_l is the density of the liquid solution. During HAC operation, the operating pressures of the separator and tailrace are steady with the tailrace operating

at atmospheric pressure and the separator operating at the delivery pressure determined by the elevation differences between the TOWL and SOWL.

5.2 Principal dimensions and process flow diagram

A schematic diagram of the experiment apparatus developed to verify the bubbly flow model of the compression process in the downcomer of the HAC is shown in Figure 5-2.

The Baby HAC is constructed of transparent PVC plastic and its total height is 5 m. As mentioned before, the delivery pressure of a HAC depends on the elevation difference between the TOWL and SOWL so this system typically generates a gauge delivery pressure of around 30 kPa (Hutchison, 2018a). In the Baby HAC, the water flow rate through the system can be controlled by a throttling valve. The downcomer section of the Baby HAC is a 4 in (102 mm) schedule 40 PVC pipe, and its internal diameter is 0.102 m. The length of the downcomer is 4.225 m, and its roughness is 1.5×10^{-5} m. Further details of the Baby HAC test configuration and instrument calibration are explained in (Hutchison, 2018a).

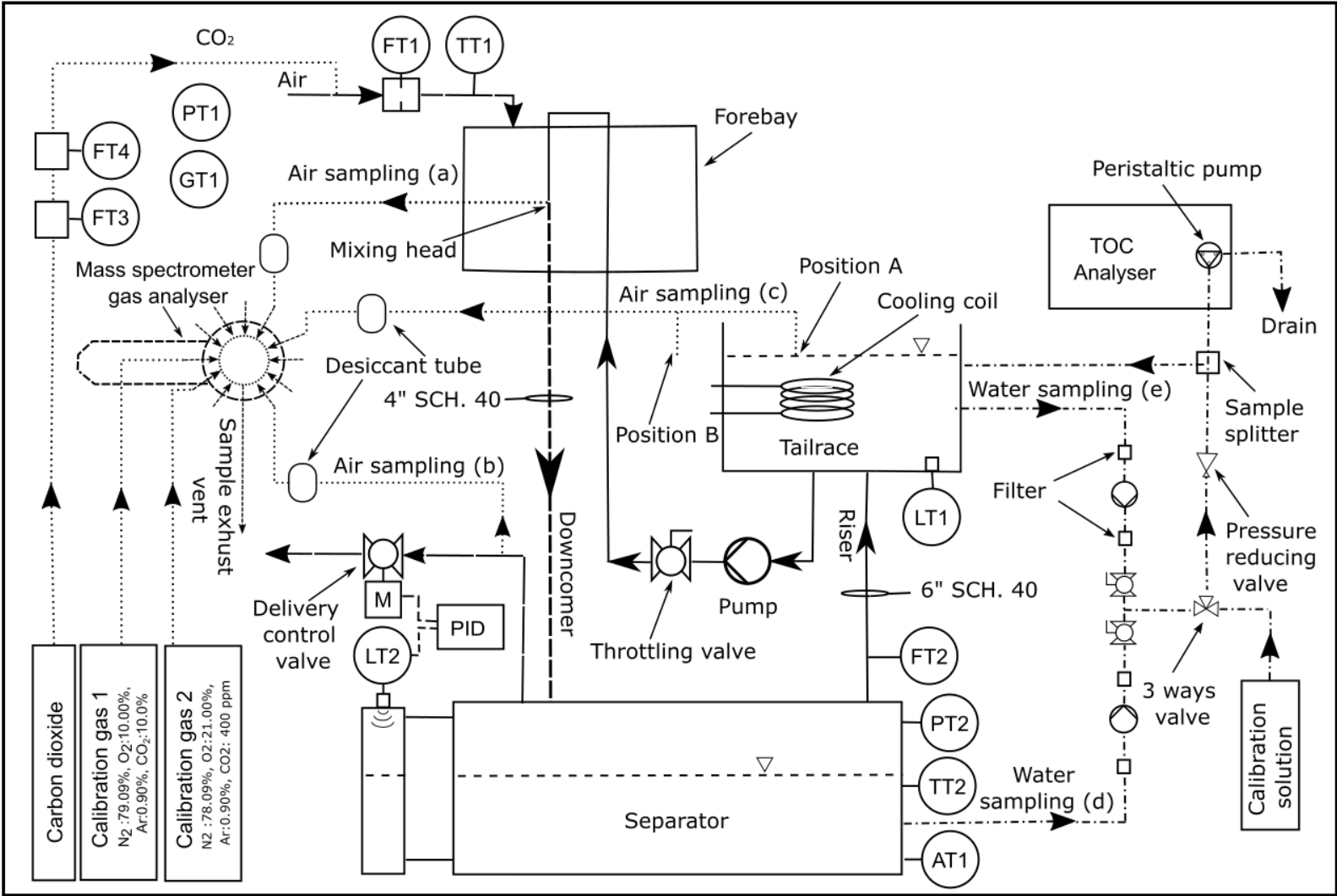


Figure 5-2: Schematic diagram of the experimental set-up.

5.3 Instrumentation

For the safe operation of the BabyHAC, several process parameters are monitored and recorded continuously by different instruments. These parameters also provide input to the model being verified. The main features of the measuring instruments are described in the following.

5.3.1 Temperature

Two U.S. Sensor USP10978 thermistors are used to measure the temperature of the air in the gas inlet (TT1) and the temperature of the water in the separator (TT2). The Baby HAC is located indoors in a temperature-controlled laboratory, so the air temperature range is limited. During the experiments, if the Baby HAC is not actively cooled, the temperature of the water increases over time because of the continuous addition of gas isothermal compression heat and heat added due to the efficiency of the pump. A cooling coil is thus used for regulation of water temperature. It is located in the tailrace tank. The strength of the PVC materials reduces after 35°C. Therefore, 35°C is the maximum limit of liquid operating temperature.

5.3.2 Pressure

Two Freescale Semiconductor MPX4250AP pressure transmitters (PT1 and PT2 in Figure 5-2) are used to measure pressure. PT1 at the top of the Baby HAC measures the atmospheric pressure while PT2 measures the absolute delivery pressure inside the separator of the Baby HAC.

5.3.3 Water level

The level of water in the tailrace tank (LT1) is measured by an Impress Sensors IMSL IP86 submersible level transmitter. LECFreaks HC-SR04 ultrasonic ranging module is utilized as a water level sensor (LT2) and is installed in a stilling-well-connected in parallel with the separator to measure the water level of the separator. An Arduino Uno Rev3 A000066 is programmed as a proportional-integral-derivative (PID) controller and is integrated with LT2 and the motorized control valve (MCV-1) to maintain the SOWL at the desired set point (typically 0.230 m).

5.3.4 Water flow rate

The water flow rate was independently determined using a ‘bucket and stopwatch’ method utilizing the water depth sensor in the tailrace (LT1) while water was discharged through the pump from the tailrace to the AWMH as during experimental trials and the riser was plugged so that the tailrace would be drained. The throttling valve is used to modulate the water mass flow rate. During the experiments, the position of the throttling valve was not changed and so the water flow rate of the Baby HAC is assumed constant. During operation, and as a redundancy, the water flow rate is also measured by the orifice flow meter on the riser pipe (FT2). The readings from this flow meter were highly variable but consistent with the mean flow established with ‘bucket and stopwatch’ flow rate fixed with throttling valve.

5.3.5 Gas flow rate

The gas mass flow rate inducted by the Baby HAC is measured by the orifice flow meter with an Allsensors 1 INCH-D differential pressure transducer (DPT) on the air inlet pipe (FT1). A ProStar

HRF 1425–580 rotameter (FT3) and an Omega FMA-A2308 digital mass flow meter (FT4) are used to measure the CO₂ flow rate which is added to the inlet air.

5.3.6 Gas composition

In order to continuously monitor and record the concentration of the inlet and discharge gases of the Baby HAC, Hiden Analytical HPR-20 QIC mass spectrometer gas analyzer is used. This system is a multi-stream gas composition analyzer, and it is suited to a range of applications where multi-component, multi-stream gas analysis is required in real-time (Hiden Analytical, 2021). Water vapour admitted into the mass spectrometer challenges mass spectrometer calibration procedures. Therefore, water vapour is removed from the sample lines by passing it through a drying tube containing calcium chloride and calcium sulfate desiccants. The mass spectrometer thus reports the dry composition of the gas. The humidity of the inlet air into the Baby HAC during the experiment is measured with a Kestrel 5400 handheld digital psychrometer (GT1).

5.3.7 Dissolved CO₂ concentration

The concentration of dissolved carbon dioxide (CO₂) in the circulating process water in the liquid sample streams from the Baby HAC is measured by a Sievers 800 series total organic carbon (TOC) analyzer. The pH of the sampled water of the Baby HAC separator is measured with a Dr.meter PH100-V (AT1) at specific times during experiments.

5.4 Experimental methodology

5.4.1 Gas sampling

The gas sampling lines to the mass spectrometer gas analyzer are shown in Figure 5-2. The input and discharge gas compositions are sampled at the AWMH in the forebay (a), gas discharge (b) and tailrace evolved gas (c). The instrument was set up to switch between the sampling streams every 25 seconds, and return a full set of concentrations of N₂, O₂, Ar and CO₂ for each reading. Calibration of the Hiden HPR-20 QIC is conducted with gas mixtures of known composition with gas species concentration magnitudes bracketing those expected to be measured. Two gas cylinders, (calibration gas 1 and 2 in Figure 5-2) are used to calibrate the mass spectrometer prior to any experimental run and the calibration is checked against these reference mixtures immediately after an experimental run. The instrument calibration spanned the expected CO₂ concentrations measured. The certificates of analysis for the first mixture provided 400 ppm CO₂ with analytical accuracy ± 4 ppm and that for the second mixture provided 10.00% CO₂ with analytical accuracy of $\pm 0.02\%$

5.4.2 Liquid sampling

According to the manual of the TOC analyzer (Ionics Instrument Business Group, 2004), under normal operation in this instrument, liquid sample is reacted with phosphoric acid to convert any dissolved inorganic carbon (e.g., HCO₃⁻, CO₃²⁻) to CO₂ (aq) and oxidizing agents after irradiation from UV light to convert any organic carbon to CO₂ (aq). In this work, the CO₂ (aq) is the process parameter that must be measured. Therefore, the TOC analyzer is operated with no phosphoric

acid or oxidizing agents and with the UV lamp turned off. Under these conditions, only the dissolved CO₂ in the liquid will be measured by the TOC analyzer.

Carbon concentrations reported by TOC analyzer are in parts per million or parts per billion by mass (kg/kg) and are converted to carbon dioxide concentrations by the ratio of their molecular weights. The instrument was calibrated by using a standard solution following procedures documented in the TOC analyzer manual. The concentration of carbon in the solution standard was 25.00 ppm and the observations from the instrument when analyzing the solution standard were 25.00 ppm, repeatedly and consistently.

Figure 5-2 shows the liquid sampling lines to the Sievers 800 TOC analyzer that each deliver 250 mL/min to PRV-1 (pressure reducing valve) during the operation. The concentration of CO₂ (aq) is measured at the separator (d) and tailrace (e). The design sample stream flow rate of the TOC analyzer is 0.35 mL/min dictated by the pressure reducing valve (PRV-1) upstream of the unit and a peristaltic pump within the unit.

During the experiment, the liquid sample streams are brought to PRV-1 using two pumps capable of delivering 3 m head with a flow rate of 250 mL/min to PRV-1. Sample streams from either the separator or tailrace can be analyzed by adjusting valves HV-2 and HV-3. There is a latency of around 6 min between the time sample arrives at the sample splitter and the time of the first reading from the TOC analyzer that is representative of that sample.

5.4.3 Experimental procedure

Tap water is used to fill the Baby plant HAC. The system operates for approximately 1 h until the water level in the separator and the temperature of the circulating water reach a steady state.

Throughout the whole experiment and across input CO₂ mass flow set points, observations are taken of input and discharge gas stream compositions using the mass spectrometer gas analyzer and dissolved CO₂ observations are taken using the TOC analyzer. The Baby HAC process/hydrodynamic variables are characterized by repeated 150 second sampling and logging periods of all instruments at 20 Hz. A cylinder of CO₂ gas is used to enrich the CO₂ concentrations in the gas inducted by the Baby HAC. CO₂ gas is added to the inducted air at a constant rate by adjusting the CO₂ gas cylinder regulator settings while monitoring the CO₂ gas mass flow meters (FT3 and FT4 in Figure 5-2 on the regulator). Thus, the only experimental parameter that is systematically varied during the experiment is the flow rate of CO₂ added to the inlet air stream, in order to explore a series of set points. At each specific CO₂ mass flow rate set point, the baby HAC plant is operated until measured concentrations of CO₂ reach asymptotic values both in liquid and gas phases. Experimental control is applied to ensure that all other processes and environmental parameters are held constant, at a steady state, as far as practicable.

5.5 Experimental results

The results of four replicate experiments are presented. These were conducted to verify the bubbly flow model of the compression process in the downcomer. Later these are compared with results from simulations of the same experimental conditions undertaken with the Young (2017) and Young *et al.*, (2022) model.

5.5.1 HAC process operating conditions

A summary of the process operating conditions of the four experiments conducted, labelled A, B, C, D, and any variation in experimental procedure undertaken are presented in Table 5-1.

Table 5-1: Details of experimental conditions and hydrodynamic process variables (Pourmahdavi *et al.*, 2022)

Experiment	A	B	C	D
Date	21 Mar 2020	13 Aug 2020	14 Aug 2021	18 Aug 2021
Time	3:00–22:00	10:55–22:50	10:10–20:30	10:20–20:45
Gas composition analysis at points (a) and (b)	*	*	*	*
Gas composition analysis at point (c)			*	*
Continuous measurement of carbon concentration in separator and tailrace water	*	*	*	*
Recording of lab temperature, atmospheric pressure, and relative humidity	*	*	*	*
Recording of pH of separator liquid samples				*
Number of set points of CO ₂ gas addition to intake air	5	8	8	7
Typical set point duration (minutes)	105	60	64	60
Maximum CO ₂ concentration added in inlet pipe (mol%)	10	10	10	10
Relative humidity of the lab (%)	21.9	52.9	47.4	50.6
Total mass of water in the HAC (kg)	324	325	294	318
Average water mass flow rate (kg/s)	7.5	7.3	7.4	9.2
Average circulating water temperature (K)	289.05	294.16	296.88	296.78
Average input gas mass flow rate (g/s)	1.652	1.578	1.805	2.110
Average tailrace water level (m)	0.21	0.23	0.23	0.18
Average atmospheric pressure (kPa)	100.057	99.078	99.087	98.791
Average delivery pressure (kPa, abs)	132.001	131.601	131.760	131.352
Average delivery pressure (kPa, gauge)	31.945	30.205	32.676	31.699

The experiment labels are ordered in the sequence in which they were undertaken. During each experimental trial learnings were gained to improve or refine experimental technique, or to expand the set of observations acquired. An important reason for the execution of multiple experimental trials was to establish the replicability of the core experimental procedure. Experiment D is the final replicate of the experiment and as such benefited from the learnings gained from the earlier experiments. It is the principal set displayed in this section during the explanation of the results gained but does include some observations taken that are absent in results for earlier trials. A full set of all experimental results is deferred to Appendix A.

5.5.2 CO₂ additions defining experimental set points

The measured mass flow rate of CO₂ added to the input gas of the Baby HAC at each set point is shown in Table 5-2. Gas composition monitoring shows that gas species concentrations in liquid gas phase reach steady state around 30 min after the set point is set. This time depends on the total mass of water circulating in the HAC. From the start of each experiment, the rate of CO₂ addition was stepped up for subsequent set points. Toward the end of each experiment the rate of CO₂ addition was stepped down, ultimately to zero. In order to better understand how the system responds to the change of CO₂ concentrations, during experiment C, the rate of CO₂ addition was increased to 142.4 mg/s at set point 5, then decreased to 32.2 mg/s (set point 6). The maximum CO₂ mass flow rate of this experiment is 195.0 mg/s at set point 7.

Table 5-2: Mass flow rates of CO₂ added to inlet air for each set point in each experiment (Pourmahdavi *et al.*, 2022)

Set point	Input CO ₂ mass flow for set point in experiment (mg/s)			
	Expt A	Expt B	Expt C	Expt D
1	0.0	0.0	0.0	0.0
2	59.1	33.2	32.2	32.1
3	74.1	95.2	95.9	95.6
4	143.4	140.3	128.0	142.0
5	0.0	184.7	142.5	253.1
6	-	65.0	32.2	105.4
7	-	43.1	195.0	0.0
8	-	0.0	0.0	-

5.5.3 Time series of experimental observations of CO₂ concentrations

The time series of experimental observations of CO₂ concentrations in both gas and liquid phases throughout experiment D and C are shown in Figure 5-3 and Figure 5-4 respectively. The time series of CO₂ concentrations of experiment A and B are presented in Appendix B.

In Figure 5-3 and Figure 5-4, the CO₂ (g) concentration in the gas inducted by the Baby HAC (location (a) in Figure 5-2) during the experiment D and C is shown with the dashed line. The solid line indicates the CO₂ (g) concentration in the compressed offgas delivered by the system (location (b) in Figure 5-2). These figures also show the CO₂ (g) concentration in the evolved gas of the tailrace tank with the dotted line. As the scale of the vertical RHS axis is principally set to follow changes in the intake and offgas concentrations, the time series of CO₂ concentration in the tailrace evolved gas is shown in Figure 5-5 with expanded scale, for experiment D. Discrete circular points on Figure 5-3 and Figure 5-4 show the liquid phase dissolved CO₂ (aq) concentrations. For experiment D only, the pH of the circulating water was also recorded at specific times throughout the experiment.

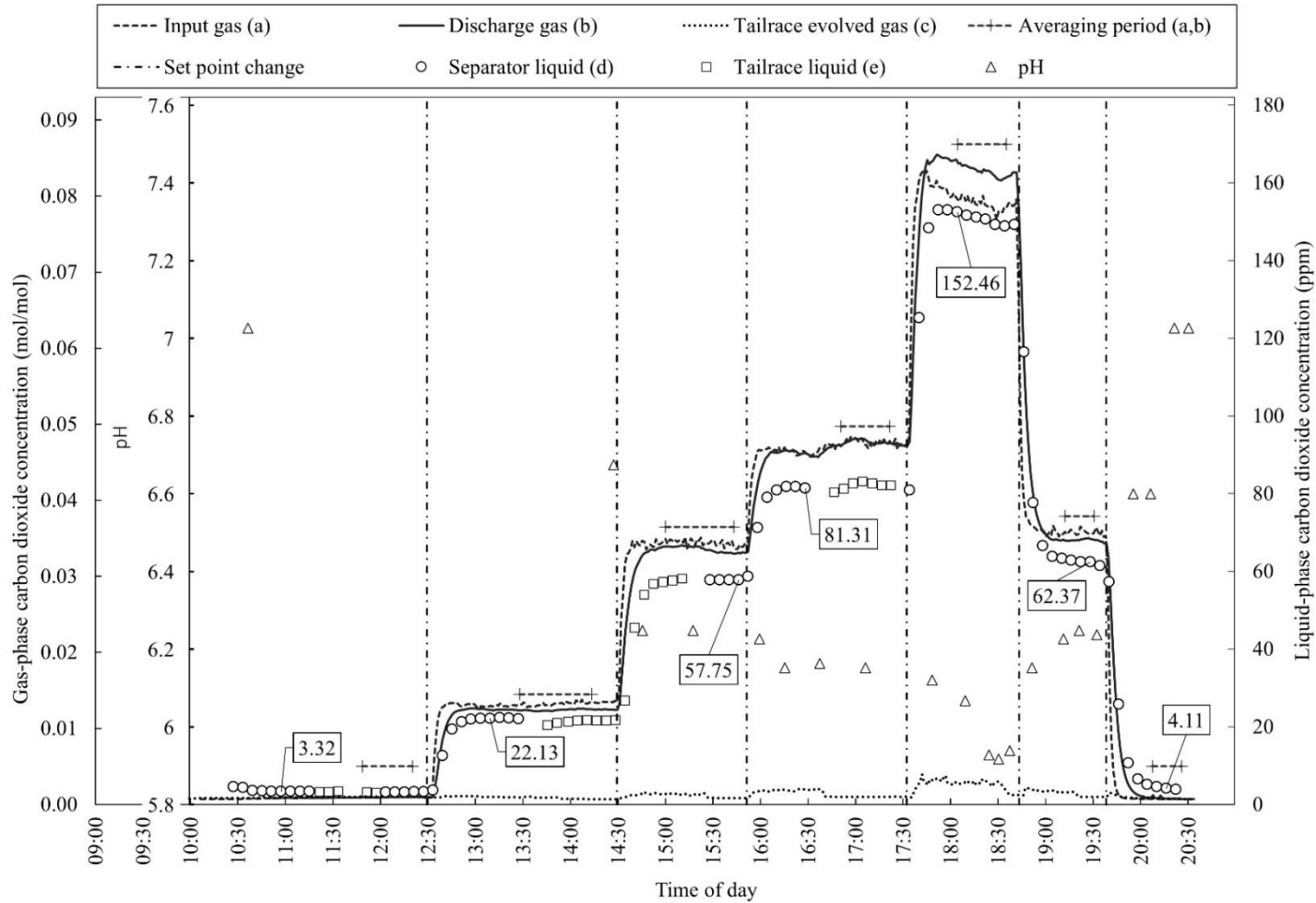


Figure 5-3: CO₂ concentration monitored in gas phase and liquid phase during experiment D. Mass flow rates of CO₂ added for each of the 7 set points are as consecutively listed in Table 5-2. For each set point, average steady state concentrations were computed over the time durations indicated by the horizontal dashed lines.

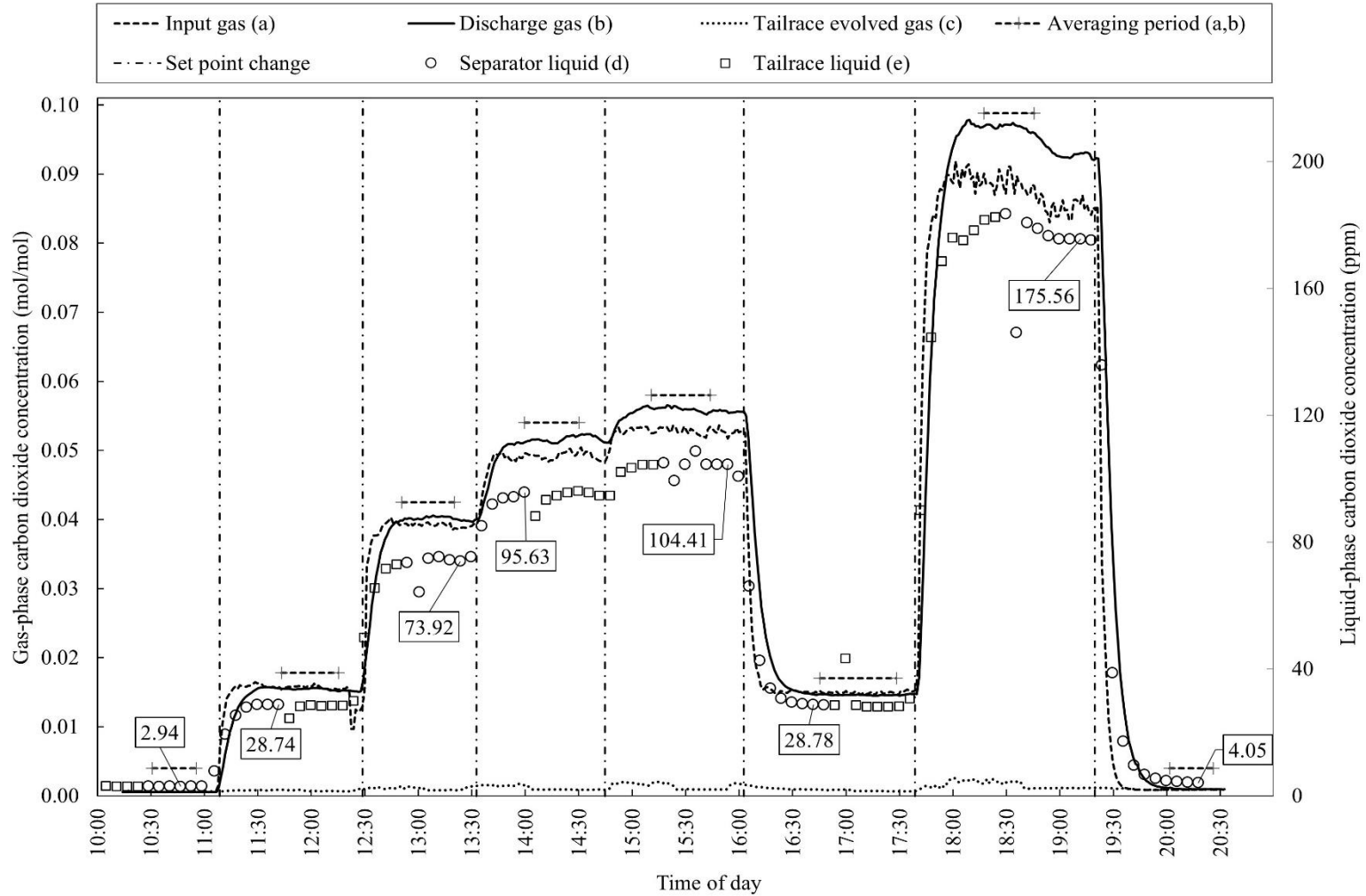


Figure 5-4: CO₂ concentration monitored in gas phase and liquid phase during experiment C. Mass flow rates of CO₂ added for each of the 7 set points are as consecutively listed in Table 5-2. For each set point, average steady state concentrations were computed over the time durations indicated by the horizontal dashed lines.

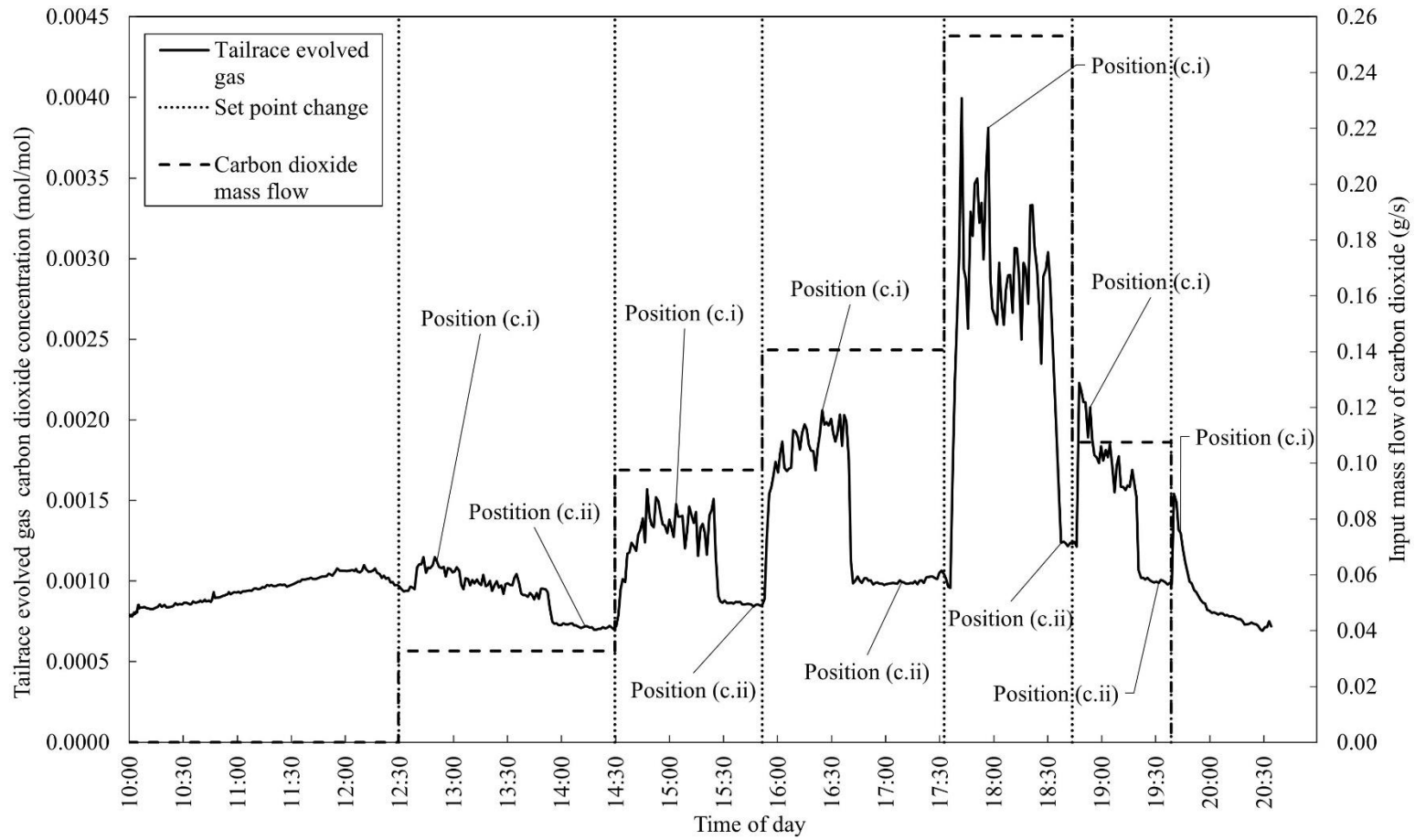


Figure 5-5: CO₂ concentration measured at location c (Figure 5-2) during experiment D. Mass flow rates of CO₂ added for each of the 7 set points are as consecutively listed in Table 5-2.

Figure 5-3 and Figure 5-4 show that the time-variation of the CO₂ concentrations (and other species) in gas and liquid phases is not steady and changes rapidly when the input CO₂ mass flow rate is changed at the start of a set point. After the input gas concentrations and other HAC operating conditions have been held steady for approximately 30 min, the measured gas species concentrations asymptotically converge to new steady state values associated with each set point. At these steady-state conditions, the time average of the concentrations of CO₂ in gas phase are calculated for each set point. The time intervals over which the steady state values were averaged for each set point are indicated in Figure 5-3 and Figure 5-4.

As illustrated in Figure 5-3 and Figure 5-4 for the early set points of the experiments, the concentration of CO₂ measured at the AWMH in the forebay tank (location (a) in Figure 5-2) is higher than CO₂ concentration measured at gas discharge (location (b) in Figure 5-2). As expected, when adding more CO₂ to the system, the concentration of dissolved CO₂ in the circulating water is increased, with the trends being broadly consistent whether their concentrations are measured from sampled liquid from the tailrace or from the separator vessels. Increasing dissolved CO₂(aq) would be expected to make the water more acidic and cause the pH of the system to become depressed. This was confirmed with the pH observations reported in Figure 5-3. As experiments progress, the concentrations measured in the gas discharge become slightly higher than those measured at the forebay.

In Figure 5-3 and Figure 5-4, the observations of the concentration of CO₂ in the separator and tailrace liquid are shown along with the gas phase observations. When the concentration of CO₂ is steady in the input and discharge gas of the Baby HAC, the concentrations of CO₂ in the

separator water samples (point (d) in Figure 5-2) are close to the concentration of CO₂ in tailrace water samples (point (e) Figure 5-2).

The water mass flow rate of experiment D is 9.2 kg/s, around 2 kg/s higher than in the prior experiments. When the Baby HAC circulates higher water mass flow rates, the system inducts more gas into the forebay tank, presenting this to the downcomer. Therefore, the CO₂ admitted is diluted with more humid air, when the same CO₂ mass flow rate is set. This is why the concentrations of CO₂ in the inducted gas mixture of the experiment D are lower than in experiments A, B and C for comparable CO₂ mass flows. This also explains why the concentration of dissolved CO₂ in the water in experiment D is generally lower than in the earlier experiments. As expected, Figure 5-3 and Figure 5-4 confirm that the CO₂ concentrations measured in the gas and liquid phase during experiment D are lower than those measured in experiment C.

In Figure 5-5, position (c.i) shows the CO₂ concentration in the evolved gas that leaves the circulating water across the free water surface in the tailrace tank. Position (c.ii) shows the CO₂ concentration in laboratory air outside the tailrace tank but immediately adjacent to it during experiment D. Indicator, i.e., approximate, concentrations of CO₂ in gas exsolving across the air–water interface of the tailrace tank are thus obtained by subtraction of the CO₂ concentrations of position (c.i) from position (c.ii).

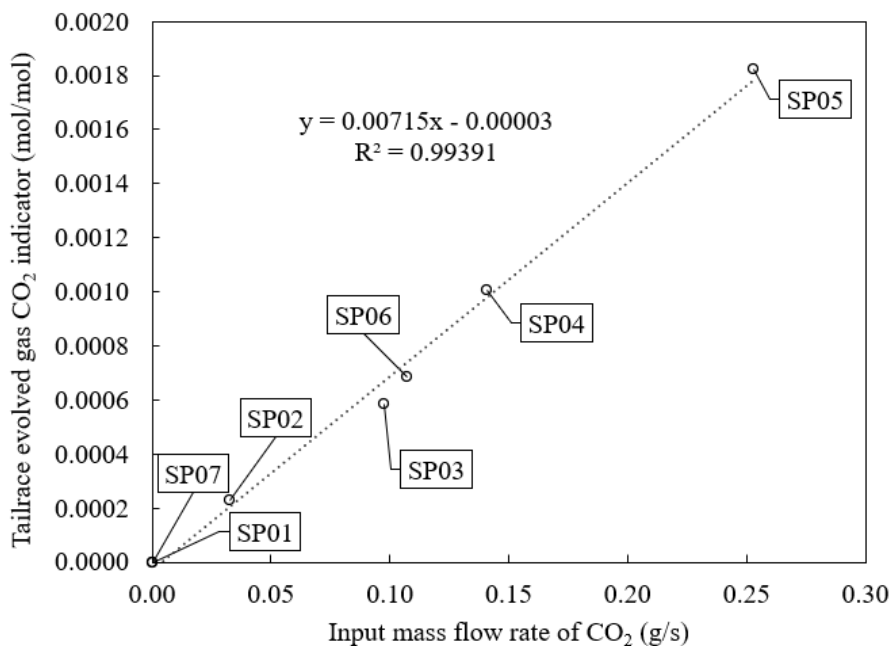


Figure 5-6: Added CO₂ mass flow rate to the inlet air versus absolute values of CO₂ concentration of the evolved gas of tailrace tank through experiment D.

Figure 5-6 shows the input CO₂ mass flow rate versus CO₂ concentration of the evolved gas of the tailrace tank throughout experiment D (from Figure 5-3). According to this figure the exsolution of CO₂ from the tailrace water is in direct proportion to input CO₂ mass flow. Although this is not at all counter-intuitive, to the best of the Author's knowledge, Figure 5-6 is the first direct experimental evidence presented confirming gas exsolution in the riser ducts and tailrace area of HACs.

5.6 Comparison of the experimental data with numerical results

To compare the numerical results of models for the Baby HAC with the experimental data, time-averaged values of observations are computed for (i) the dry mole fractions of the gas species at the AWMH (location (a) in Figure 5-2) and ii) the separator off-gas (location (b) in Figure 5-2)

(iii) atmospheric pressure, (iv) delivery pressure, (v) input gas temperature (vi) circulating liquid temperature (vii) input gas mass flow, (viii) the asymptotic values of liquid-phase CO₂ concentrations in the separator (location (d) in Figure 5-2) and ix) the tailrace (location (e) in Figure 5-2). This is done for each set point, over each experiment.

The time averaged values for each set point for each experiment can be provided as input to the Young *et al.* (2022) bubbly flow model in two distinct ways:

- I. a single downcomer simulation at the measured steady (average, asymptotic) operating conditions at each set point, and;
- II. a transient HAC simulation from measured operating conditions at the start of each set point.

The approach I is referred to as the ‘static downcomer’ scheme and uses the simulation procedure described in Young *et al.* (2022) while the second approach, II, is referred to as the ‘dynamic equilibrium’ scheme also incorporates the auxiliary model described in section 5.1.3 with the procedure shown in Figure 5-7.

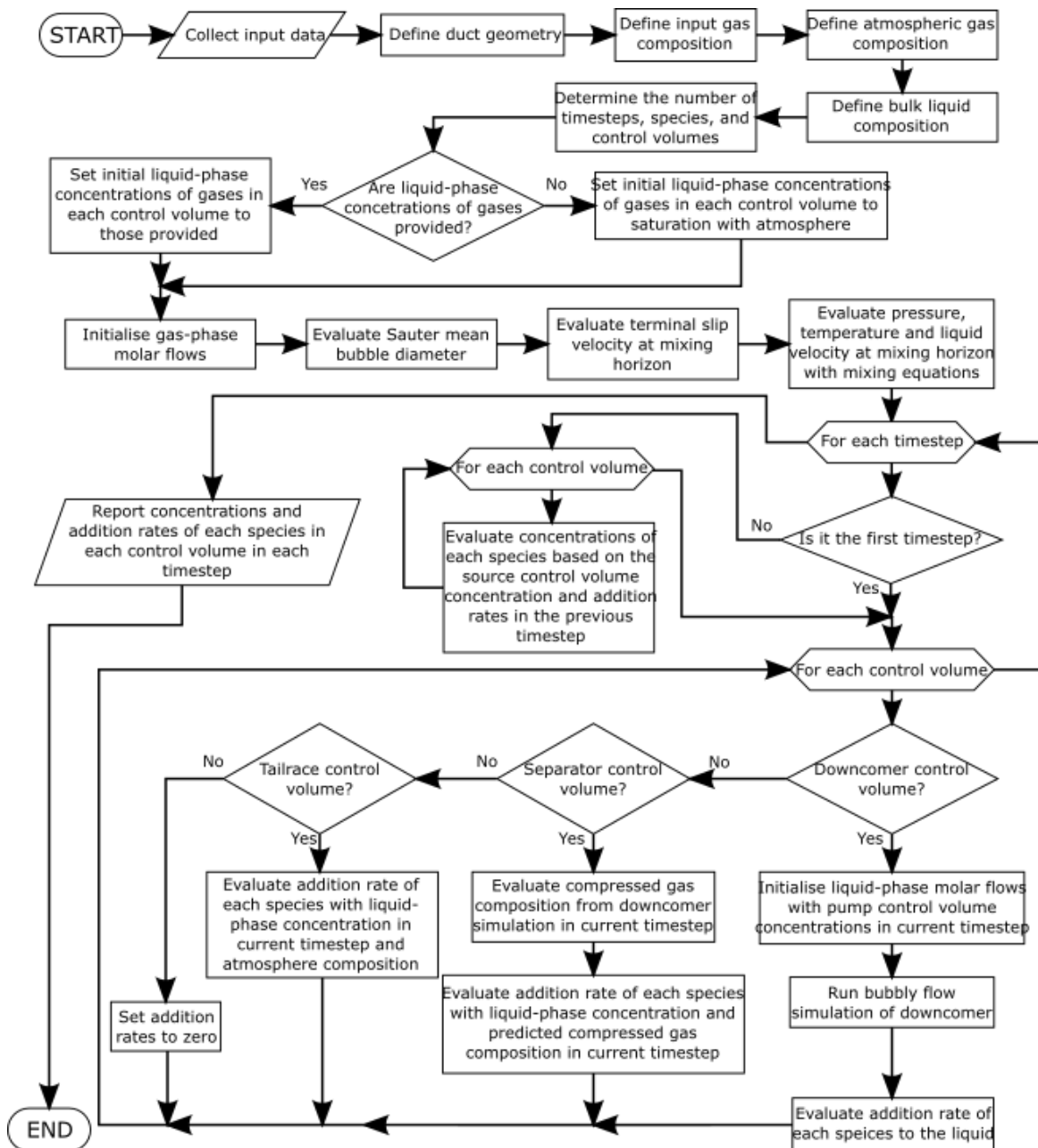


Figure 5-7: Flowchart of the dynamic scheme used to predict the steady-state concentrations of experiment set points

For the model, in either static or dynamic schemes, the liquid-phase concentrations of all gas species present need to be initialized to execute the simulation but the Baby HAC is equipped to

measure only the CO₂ liquid-phase concentration. An initialization scheme for the remaining gas species, specifically, nitrogen, oxygen, and argon, was required.

For the dynamic equilibrium scheme, the liquid-phase concentrations of each gas species considered in the simulation, including CO₂, are initialized at equilibrium with the lab air composition measured for the first set point of each experiment.

The liquid-phase concentrations in subsequent experimental set points are initialized with the measured value for CO₂ while the remaining gas species are initialized with the predicted final concentrations from the previous set point. For the static downcomer scheme, the liquid-phase concentration of CO₂ is initialized with the measured value and the remaining species are initialized at the saturation concentrations with the measured discharge gas composition at the measured delivery pressure.

Each experiment set point is simulated with the dynamic equilibrium scheme for 3600 s at 1 s intervals discretizing the downcomer into 5 segments. When the downcomer is discretized into 5 segments, an hour of simulated time requires approximately an hour to execute on a Dell XPS 9500 with a 2.60 GHz Intel i7-10750H CPU and 16 GB of RAM.

Figure 5-8 plots the experimentally measured CO₂ concentrations in the discharge gas of the Baby HAC against the experimentally measured CO₂ concentration in the liquid phase of the separator for each set point measured across experiment D, once steady operation has been established. The same two quantities are plotted on the same axes, using values arising from the numerical simulations.

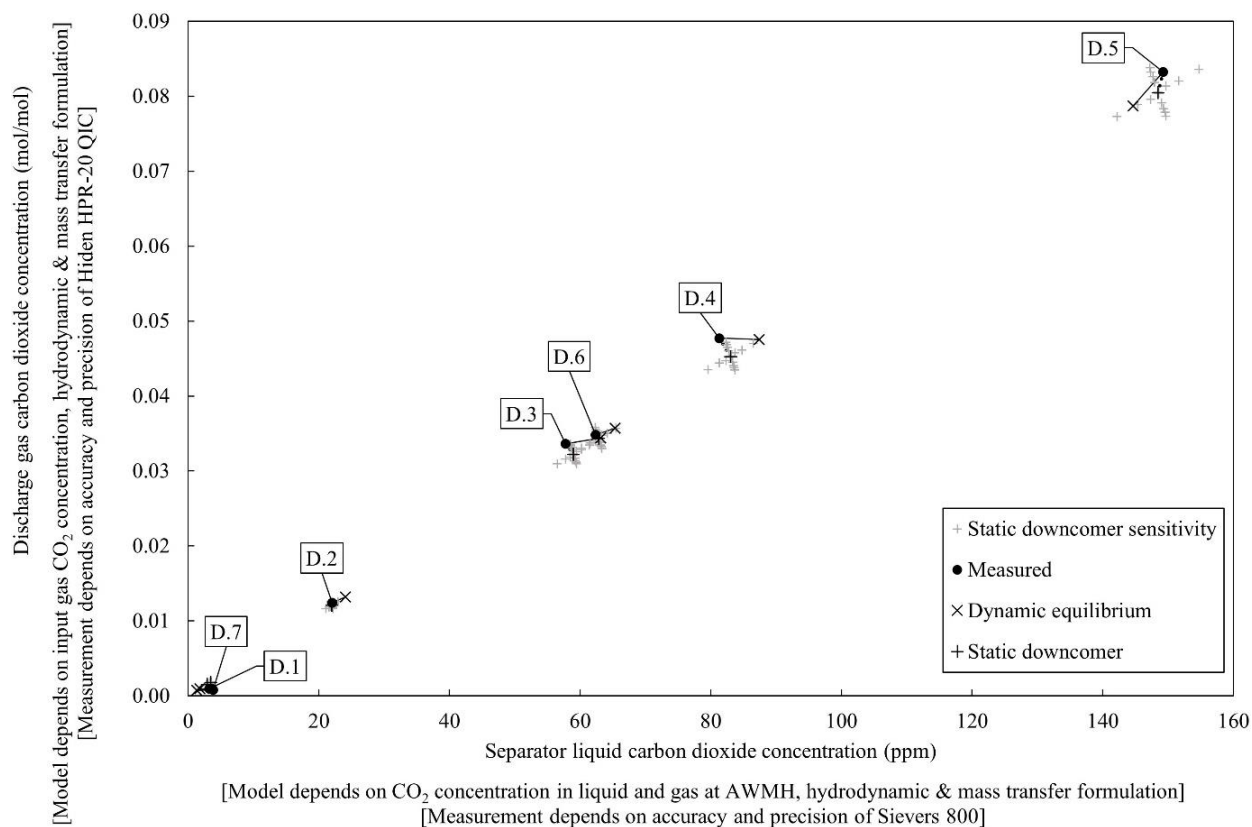


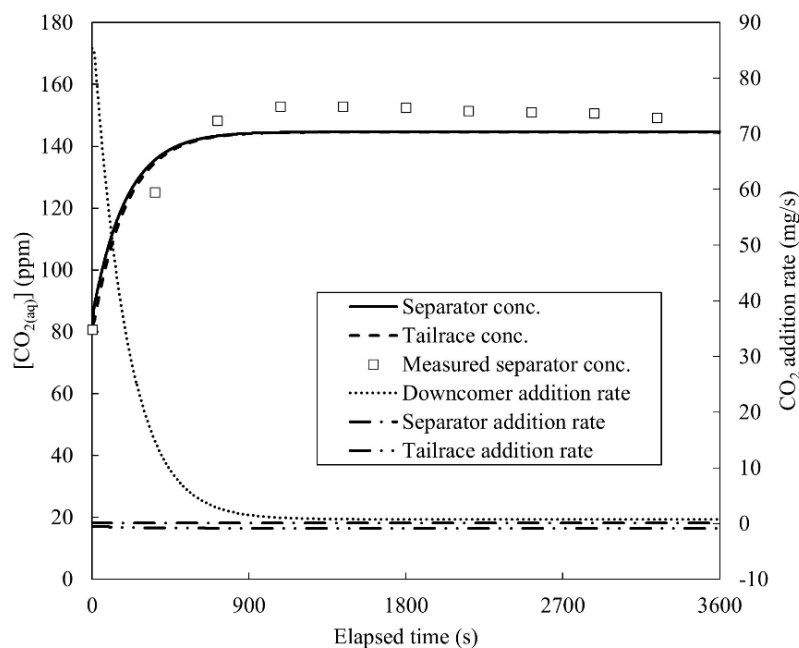
Figure 5-8: CO₂ concentration in the discharge gas of the Baby HAC versus CO₂ concentration in the liquid phase of the separator measured and modelled for experiment D. Dynamic equilibrium predictions of individual set points linked with corresponding measured points with solid line segments.

Predictions from the dynamic equilibrium (II) and static downcomer (I) schemes from the Young (2017,2022) model are also shown in Figure 5-8. Since the variables plotted on both axes are dependent variables of the process, the accuracy of the model is judged by the distance between measured and predicted marks for the same set point. Perfect agreement between experimental measurements and simulation results arises if the set point values from each source plot at the same location on the chart. While the predictions of the static downcomer (I) better match the observed values, the predictions of the dynamic equilibrium scheme (II) are fully predictive and do not rely

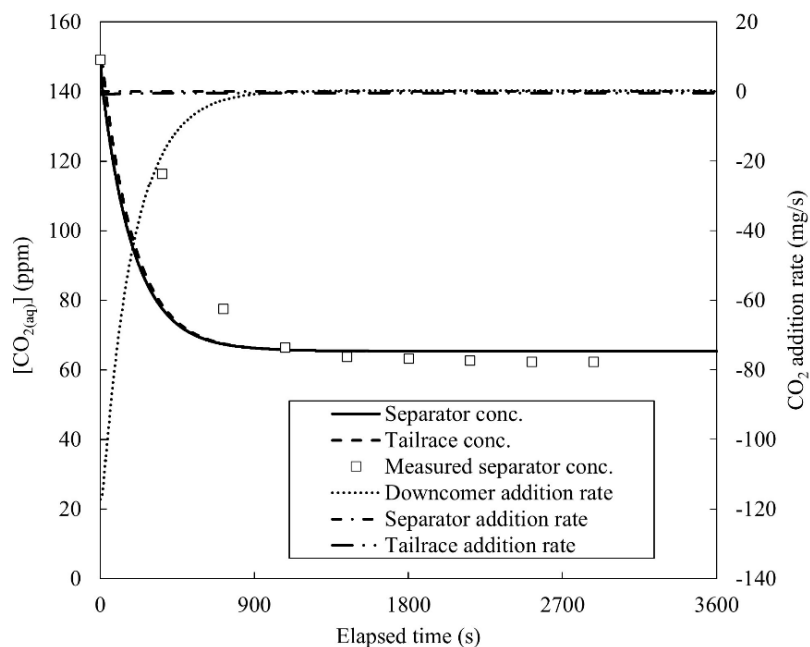
on prior knowledge of the new steady operating condition of the experimental set point. Both modelling schemes produce predictions within 10% of the observed values except for the extreme low end of the range (less than 5 ppm in the liquid phase and less than 0.1% in the gas phase).

Figure 5-8 also shows results from a sensitivity analysis of the static downcomer (I) simulations where eleven input model parameters were systematically varied individually: i) atmospheric pressure, ii) liquid mass flow rate, iii) input gas mass flow rate, iv) liquid temperature, v) input gas temperature, vi) input gas relative humidity, vii) input gas CO₂ concentration, viii) input liquid CO₂ concentration, ix) Henry's constant, x) Sauter mean bubble diameter and xi) mass diffusivity. Each parameter was varied over an interval of $\pm 20\%$ from the observed value at each set point at the experimental conditions or a base value, however the results in Figure 5-8 are limited to an interval of $\pm 5\%$. The results of this type of sensitivity analysis show that the measured and predicted values from both simulation schemes are all within an error ellipse produced by the predictions of all the $\pm 5\%$ variations of all selected flexed input parameters. This suggests that predictions from the Young *et al.* (2022) bubbly flow model are robust.

The predicted time series of liquid-phase CO₂ concentrations in the separator and tailrace liquid and addition rates in the downcomer, separator, and tailrace control volumes, according to scheme II, are shown in Figure 5-9 a and b for experiment set points 5 and 6 for experiment D, respectively.



(a) Transient simulation of experiment set point D.5



(b) Transient simulation of experiment set point D.6

Figure 5-9: Resulting time series of CO₂ concentrations in the separator and tailrace liquid and addition rates in the downcomer, separator and tailrace predicted by the dynamic equilibrium scheme with the time series of observed CO₂ liquid concentrations

The predicted initial and final addition rates of CO₂ in the Baby HAC control volumes for set points D.5 and D.6 are summarised in Table 5-3. The predicted addition rates of the tailrace are consistent with the elevated indicator CO₂ gas concentrations measured in the evolved tailrace gas. While the latency in the observation of the concentration of CO₂ (aq) impairs direct comparison of the observed and predicted time series, there does appear to be general agreement.

Table 5-3: Predicted initial and final addition rates of CO₂ in the Baby HAC control volumes for experiment set points D.5 and D.6.

Control volume	Initial addition rate of CO ₂ (mg/s)		Final addition rate of CO ₂ (mg/s)	
	D.5	D.6	D.5	D.6
Downcomer	85.32	-117.15	0.76	0.34
Separator	0.13	-0.05	0.07	0.03
Riser	0.00	0.00	0.00	0.00
Tailrace	-0.47	-0.87	-0.83	-0.37
Pump	0.00	0.00	0.00	0.00
Total	84.98	-118.07	0.00	0.00

Figure 5-10 aggregates the measured and predicted CO₂ concentration in the discharge gas of the Baby HAC against CO₂ concentration in the liquid phase of the separator for each set point across all experiments A to D, once steady, asymptotic, operation has been established. The measured points, marked with solid circles, are linked with a line segment to the corresponding model predicted point, marked with x's. Good agreement between measured and predicted values is obtained across all set points of all experiments and the model returns a similar linear behaviour as exhibited by the measured data.

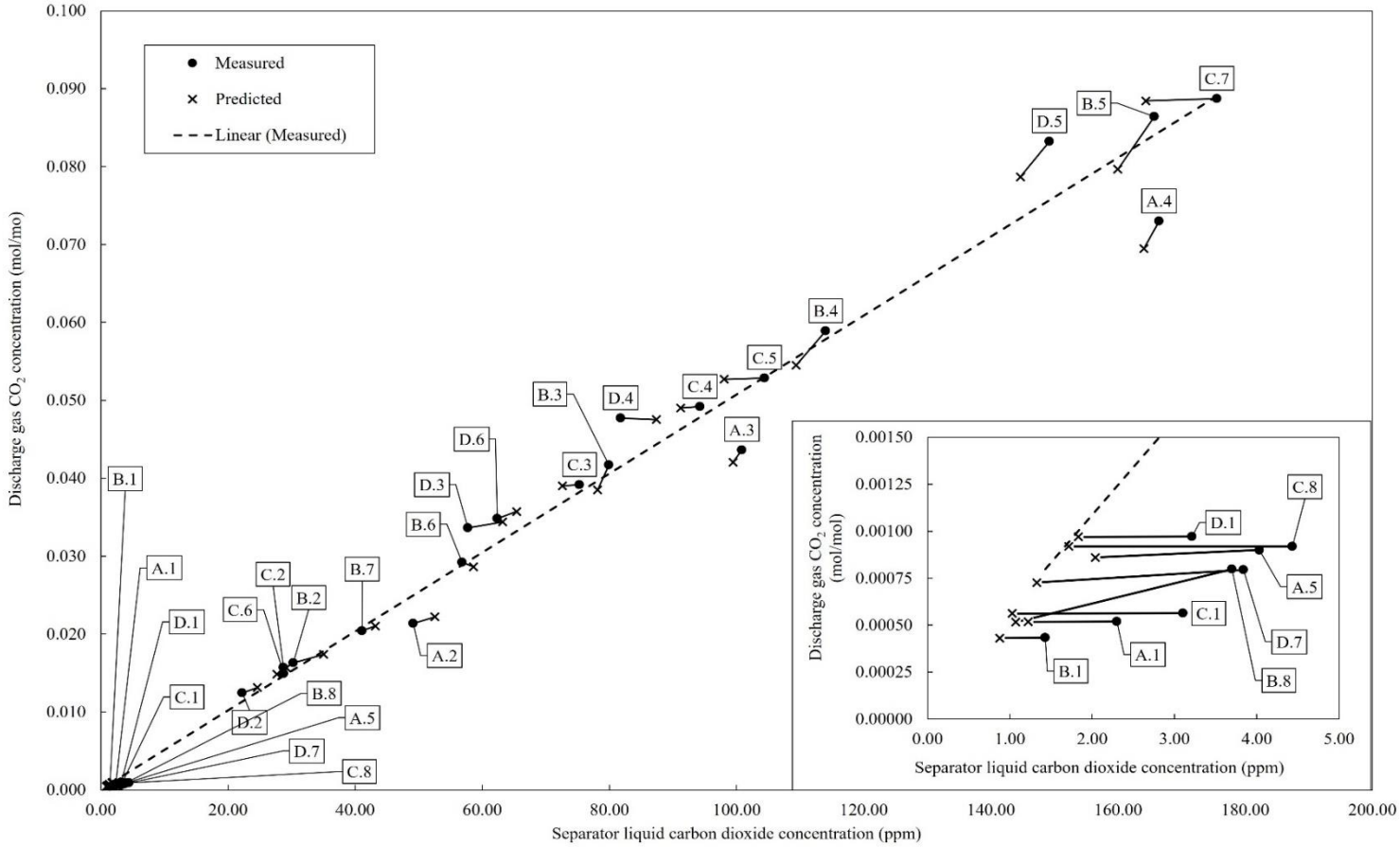


Figure 5-10:CO₂ concentration in the discharge gas of the Baby HAC versus CO₂ concentration in the liquid phase of the separator measured and modelled for experiment D. Dynamic equilibrium predictions of individual set points linked with corresponding measured points with solid line segments.

The inset axis in Figure 5-10 shows the set points with CO₂ gas concentrations below 0.15% and CO₂ liquid concentrations below 5 ppm. Predictions of the CO₂ concentration in the discharge gas in this concentration range produce results close to that measured but the predictions of the liquid phase concentrations of CO₂ in the separator liquid are different by as much as 2 ppm in 4 ppm (exhibited in the figure by the largely horizontal line segments). The TOC analyzer is calibrated at DIC > 25 ppm (91.67 ppm [CO₂(aq)]). When the instrument is used to determine values appreciably lower than this value for [CO₂ (aq)] < 5 ppm, this tests the limits of measurement precision of this instrument. Potential evidence of this is how, in the inset axis of Figure 5-10, the modelled values more closely follow the general linear trend of the measured data in this region and the measured values are largely offset horizontally from the modelled values.

Figure 5-10 shows the performance of the prediction of the steady concentrations of CO₂ in the gas and liquid phases with the dynamic equilibrium scheme (II). The model tends to over-predict the liquid-phase concentration of CO₂ until 100 ppm after which the model tends to under-predict the steady concentrations. A possible explanation for this trend may be attributed to acidification of the circulating water to produce CO₂ (aq) from the stock dissolved carbonates and bicarbonates in the mains water used to charge the HAC system, as the Young (2017), Young *et al.*, (2022) model does not consider the chemical equilibria of the carbonate species at all. However, the predictions of the model do remain within 10% of the observed values.

Figure 5-11 compares the delivery pressure measured and predicted for each set point of all experiments. No boundary conditions on the outlet of the downcomer are applied when evaluating the mass transfer rate of gas to the liquid phase in the downcomer control volume. The resulting

prediction of pressure at the outlet of the downcomer is the result of the initial conditions set at the downcomer inlet and the modelled hydrodynamics of the process.

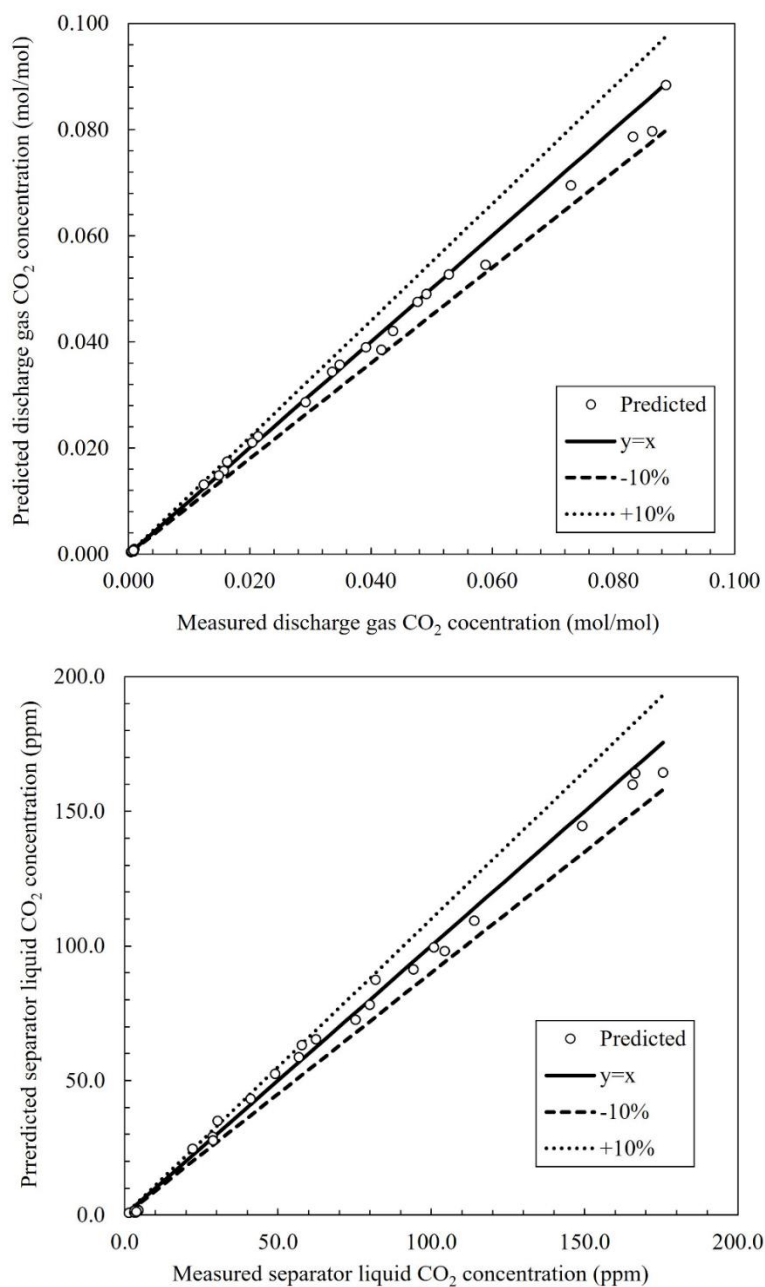


Figure 5-11: Performance of the dynamic equilibrium prediction of the pilot HAC

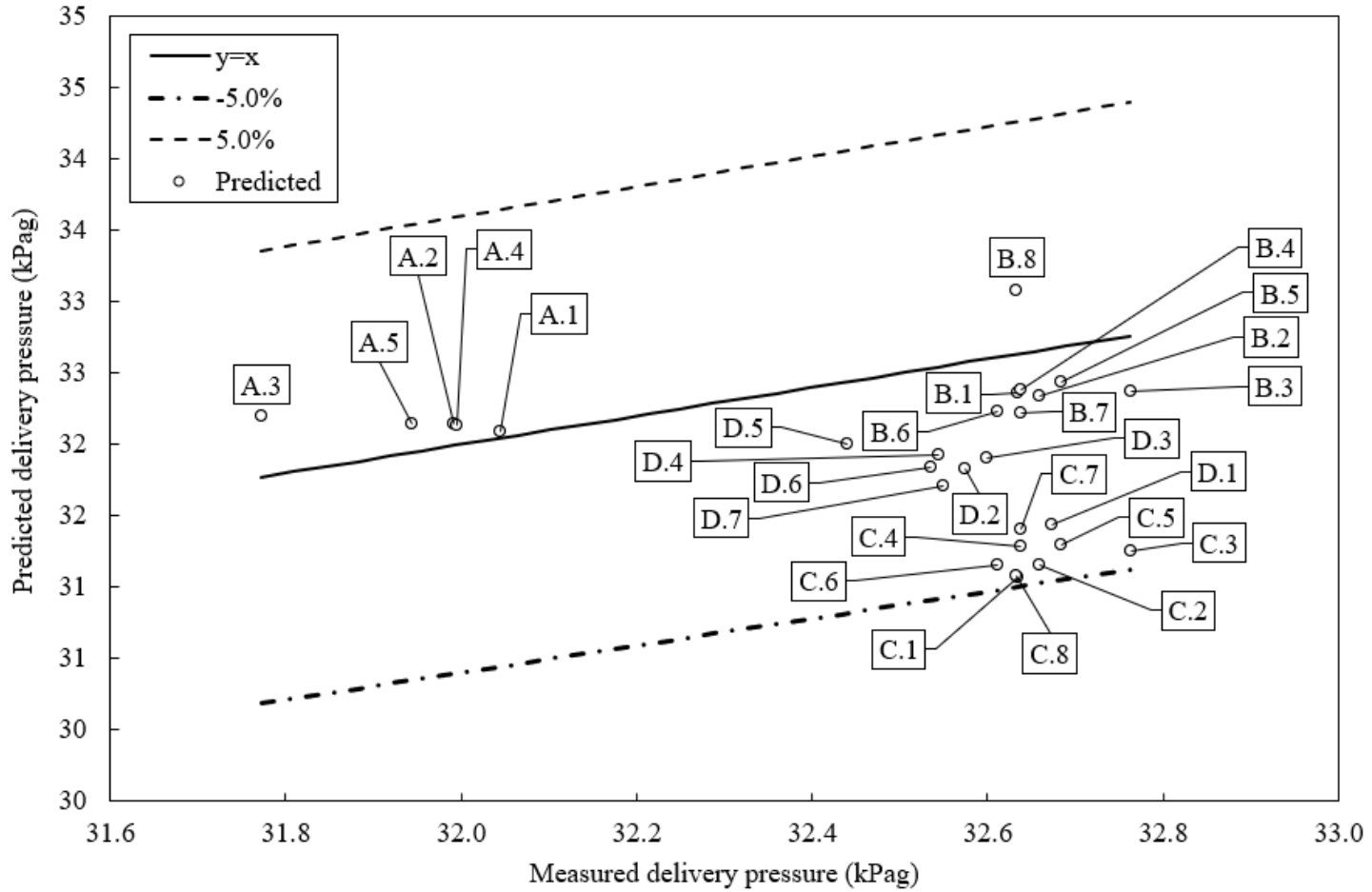


Figure 5-12: The performance of the Young *et al.* (2022) bubbly flow model predicting the gauge delivery pressure of the pilot HAC.

The prediction of the concentrations of CO₂ in the gas and liquid phase at the downcomer outlet are dependent on the prediction of the pressure due to the pressure-dependence of the absorption rate of gas by the liquid (Young *et al.*, 2022). Consequently, comparison of the predicted and measured delivery pressure is required to fully assess the agreement between experiment and model as agreement in the prediction of concentrations could be the result of the propagation of erroneous predictions of pressure in the downcomer instead of true agreement with experiment. From Figure 5-12 Figure 5-12, it can be seen that the model tends to under-predict the delivery pressure of the Baby HAC, but it is within 5% of the measured gauge pressure.

5.7 Discussion

Having established good agreement between observations and model predictions, reasons for the disparities that still remain are explored.

5.7.1 The effect of pH on the CO₂ concentration in liquid and gas phases

The pH of the system influences the concentration of dissolved inorganic carbon in water. As mentioned in Chapter 3, the reactions of carbonate species in water are reversible and fast. Once the CO₂ has dissolved into the water while the mass flow rate remains broadly the same, it can react with the water to form carbonic acid. H₂CO₃^{*} (aq) always occurs in very small concentration compared to CO₂ (aq) (< 0.3%) (Stumm and Morgan, 1995; Zeebe and Wolf-Gladrow, 2001a). Figure 3-2 shows the distribution of carbonate species as a function of pH at 25°C.

The bubbly flow model for the downcomer process does not consider those equilibria (Young *et al.*, 2022). In all of the experiments, mains tap water is used to fill the Baby HAC. The mains tap water typically has a pH from 7.2 to 7.8 (Health Canada, 2015) and contains some

bicarbonate and carbonate species. When the pH of the system drops to 6.18 or lower, these species are converted to aqueous carbon dioxide and CO_2 (aq) is the dominant form of DIC. Some of this CO_2 comes out of the solution in the separator. This explains why, as is evident in Figure 5-3, for low pH set points, the concentration of CO_2 measured at gas discharge is more than the CO_2 concentration measured at inlet gas when mass flows at inlet and outlet should be comparable at steady state, equilibrium operating conditions. It also would explain why the model, as can be seen in Figure 5-10 does not perform as well at the set points with the highest CO_2 (aq) concentrations. There is a mechanism for producing CO_2 (aq) in the experiment that is not considered by the model.

5.7.2 Estimating the values of k_La for Baby HAC downcomer

In this section, some of the simulation results of the hydrodynamics and mass transfer of the Baby HAC downcomer are presented. Table 5-4 presents the input parameters of the model.

Table 5-4: Summary of input parameters for the simulation

Input parameter	Downcomer of Baby HAC
Input water mass flow rate (kg/s)	7.3
Input air mass flow rate (g/s)	1.57
Input CO_2 mass flow rate (g/s)	0.23
Input pressure (kPa)	99.078
Input water temperature (K)	294.16
Input gas relative humidity (%)	100
Absolute roughness (m)	1.5×10^{-5}
No. segments	60
Diameter (m)	101.5×10^{-3}
Length (m)	4.225
Flow direction ($^\circ$)	-90

The initial concentration of CO₂ in the water at the inlet of the Baby HAC is assumed to be zero. The initial concentrations of the other species, which are calculated using Henry's law, are assumed to be at equilibrium with the atmospheric concentrations of the same species. The percentage of CO₂ concentration added in the inlet air of the Baby HAC is 14.57 mol% of the inlet air to simulate the combustion off-gas.

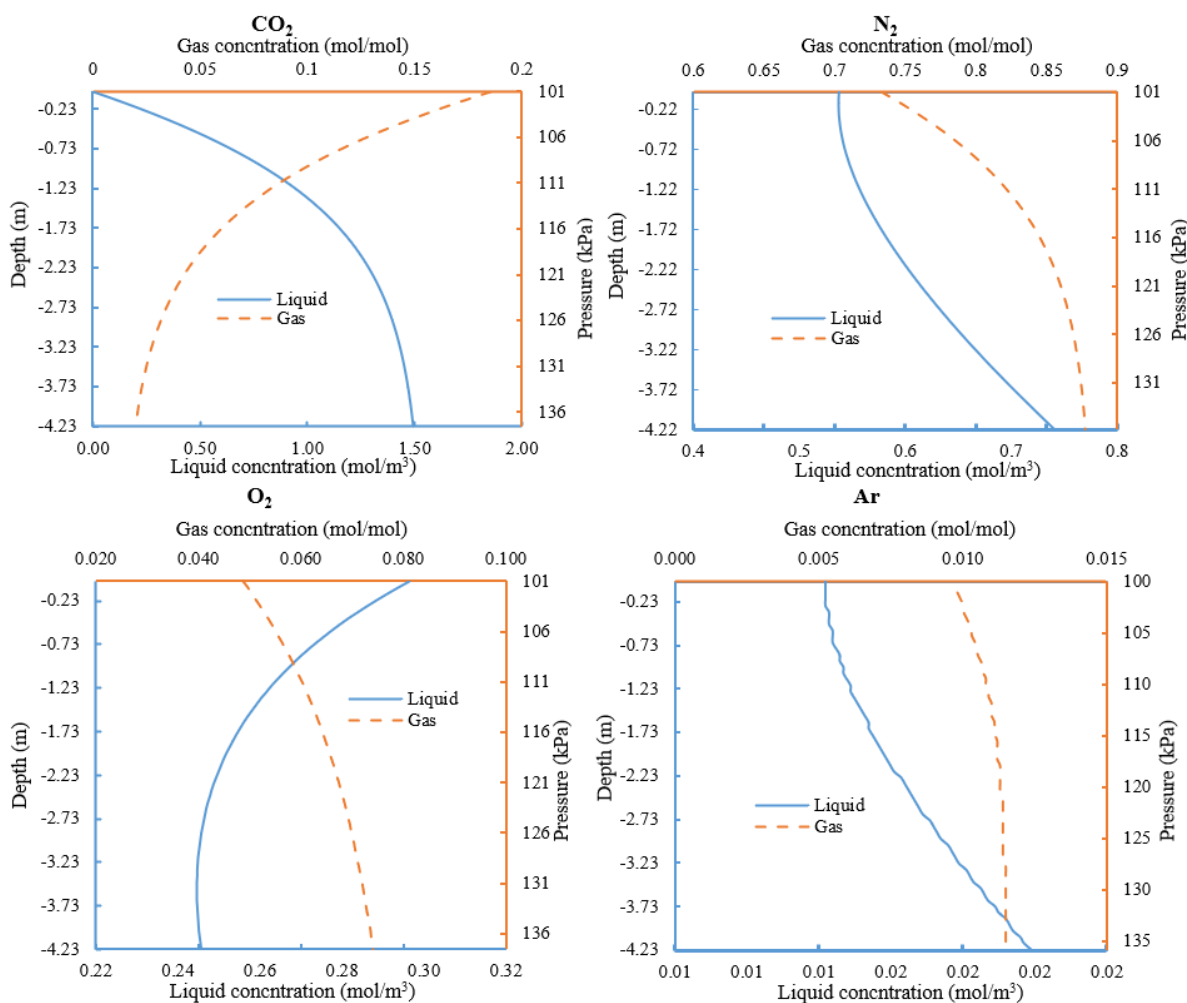


Figure 5-13: Concentration profiles of the gas and liquid in the Baby HAC downcomer predicted by the model

Figure 5-13 shows the model prediction of the concentration profiles of each gas in the gas and liquid phases of the Baby HAC downcomer. The delivery pressure is 137.75 kPa. The simulation results for the hydrodynamic and mass transfer of the Baby HAC downcomer simulating one of the experimental set points return qualitatively similar behavior to that of the Dynamic Earth HAC demonstrator downcomer presented in Section 4.4.3.

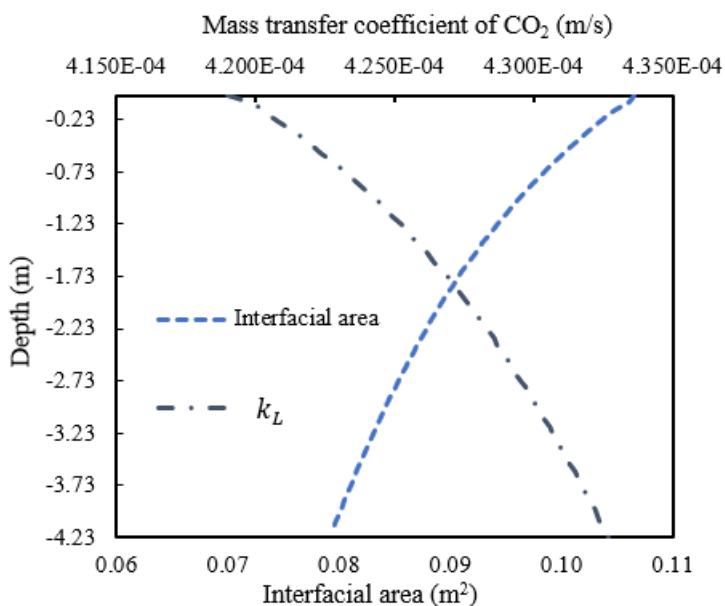


Figure 5-14: Variation of mass transfer coefficient of CO₂ and interfacial areas of the Baby HAC downcomer

Figure 5-14 shows that the CO₂ (g) mass transfer coefficient through the Baby HAC does not vary significantly. Table 5-5 shows that the average value of $k_L a_{CO_2}$ is 0.0674 s^{-1} , which is comparable to the value of 0.0784 s^{-1} for the Dynamic Earth HAC demonstrator, which is back-calculated using the same model but with a much larger scale and greater operating head and liquid and gas mass flow rates. This outcome provides confidence in adopting the model to back-calculate $k_L a_{CO_2}$ for design purposes.

Table 5-5: Summary of calculations for $k_L a_{CO_2}$

Parameter	Value	Unit
Volume of downcomer, V	3.424×10^{-2}	m^3
Interfacial area, A	5.407	m^2
Specific interfacial area, $a = A/V$	157.859	m
Mass transfer coefficient, k_{LCO_2}	4.47×10^{-4}	m/s
$k_L a_{CO_2} = k_{LCO_2} \times a$	6.74×10^{-2}	s^{-1}

5.7.3 HAC as a CO₂ capture system

The mineral carbonation process faces the challenge of achieving efficient mass transfer between gaseous CO₂ and the liquid solution phase (Chiang and Pan, 2017b). A gas–liquid contactor is used to transfer CO₂ from the gas phase to the liquid phase. The primary function of these devices is to increase the interfacial area between the two phases, thereby enhancing mass transfer (Gruenewald and Radnjanski, 2016b).

A HAC is a type of co-current downward bubble column. In this Chapter, the bubbly flow model of Young *et al.*, (2022) is used to predict the amount of dissolved carbon dioxide in the water of Baby HAC at different pressures, and varying flow rates, and varying input CO₂ mass flow rates. BabyHAC simulations are performed assuming an extended downcomer/riser height to estimate the HAC pressure (HAC height) required for almost complete CO₂ dissolution from the off-gas for the carbon capture and sequestration process. The input parameters of the model are listed in Table 5-4.

Figure 5-15 shows the results of the calculations that estimated the length of the revised downcomer/riser to provide the required pressure for practically complete CO₂ dissolution from the off-gas for the carbon capture and sequestration process. The CO₂ off-gas ‘yield’ of a HAC is calculated as the amount of CO₂ in the off-gas at the off-gas delivery pressure divided by the

amount of CO₂ in the inlet air. Lower yield values demonstrate that more CO₂ is dissolved in water (because the principal product of the HAC process is compressed gas).

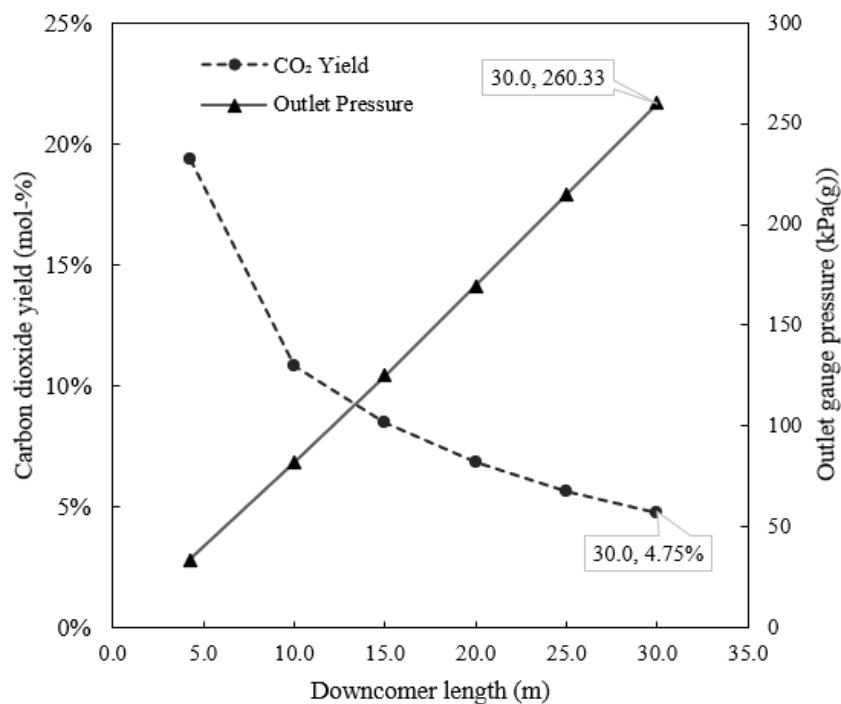


Figure 5-15: Variation of CO₂ yield and discharge gauge pressure according to the downcomer length

According to Figure 5-15, when the length of the downcomer is 15 m, the discharge gauge pressure of the downcomer is 125.151 kPa(g) (18.2 psi(g)). The CO₂ yield of this HAC would be 8.46% meaning that more than 90% of the injected CO₂ would become dissolved in circulating water. The HAC downcomer length has to be extended to 30 m / 260.3 kPa / 37.8 psi(g) to reduce CO₂ yield to below 5% while dissolving 95% of the injected CO₂. The HAC acting as a CO₂ capture device in this work means converting the CO₂ present in an inlet gas mixture to its aqueous form dissolved in HAC circulating water.

5.8 Summary

In this section, a formulation for modeling the time evolution of the gas species concentrations in a pumped HAC was presented. When coupled with the bubbly flow model described in Young *et al.*, (2022) and estimations of the mass transfer rates in the separator and tailrace vessels of a pumped HAC, the transient periods between steady-state operating points were understood to be driven by the nature and characteristics of the addition rates of the gas species in the downcomer and tailrace control volumes.

The instrumentation and procedures used to observe the absorption of CO₂ by the Baby HAC were described. The methods described ensured that experimental errors in observations were minimized as much as possible.

The results of four experiments conducted over two years and at different times of the year were presented. The observed behavior in the concentration-time evolution across all experiments was consistent and repeatable. The modeling results agreed well with the hydrodynamic and chemical process variables, and the model was considered sufficiently well-verified for engineering purposes. An effective digital twin of the pump-recirculated HAC was produced when coupled with the finite-difference transient concentration scheme described in this Chapter. The bubbly flow model predicted the delivery pressure of the Baby HAC within 5% of the measured gauge pressure. The elevated CO₂ concentrations measured in the gas above the TOWL agreed with the prediction of increased mass transfer rates of CO₂ from the tailrace liquid at higher liquid-phase concentrations of CO₂.

Furthermore, mechanisms not captured by the model at high CO₂ concentrations were identified. A sensitivity analysis of the static downcomer model showed that the concentrations of CO₂ in the separator liquid and discharge gas predicted in both static and dynamic schemes were within a $\pm 5\%$ flex of all relevant model input parameters of each other and the measured values.

6. Horizontal injector loop test rig

In the previous chapter, the application of the HAC as a gas-liquid contactor was described. A series of experiments was conducted to demonstrate how the HAC system can deliver dissolved CO₂ in the solution at controllable concentrations. Chapter 5 also confirmed the level of reliability with which the Young *et al.* (2022) downcomer model predicts the HAC operating conditions, both hydrodynamically and in accounting for the solubility/mass transfer behavior of gaseous species. Based on this knowledge, in this Chapter, a HAC configuration, which is a variation on the HAC systems presented previously, is introduced, with both the capture and sequestration of CO₂ as its primary design objective. Later, in Chapter 7, experimental results will be presented that aim to demonstrate proof of concept of the effectiveness of the system designed. In Chapter 8, simulation results from the dynamic kinetic model of the chemical kinetics of carbonation will show that a basis for the design of CO₂ capture and sequestration systems according to the concepts herein has been established.

The verification trials conducted on the HACs and presented in Chapter 5 strongly suggest that these systems are well suited to the intensification of carbon capture and sequestration processes. They present opportunities for higher mass transfer performance compared to other mass transfer devices such as conventional bubble columns or spray towers. Despite this, the height of HAC units, following the Millar (2014) design paradigm, is consistently extensive due to the mechanism employed to pressurize the system: a column of water. To produce service air pressure at 800 kPa(g), a HAC height of approximately 100 m is required. In detailed engineering studies, the capital cost of HAC construction is considerable in all variations that have been explored so far. Despite its capital intensity and despite the high flow rates of liquid circulated, as

a machine for producing pneumatic power, its lower energy consumption and lower operating cost have meant that it still offers adopters credible payback periods. However, a system that can offer comparable performance with reduced height would render the concept more accessible for projects that are capital constrained. If a HAC system could be designed that did not feature appreciable elevation differences while retaining the energy efficiency and mass transfer characteristics, such developments could be enabling.

As it turns out, such developments are exactly those that feature in the HAC system that was designed and fabricated specifically to explore at-pressure aqueous mineral carbonation that will be explained in the forthcoming sections of this chapter. The experimental apparatus so designed retains desirable characteristics of HACs as efficient providers of pneumatic power at constant elevation, and yet are short, and so it has been called a ‘horizontal injector loop’ (HIL). But before the design of the HIL is set out, a brief review of the alternatives is offered.

6.1 Review of alternative reactors for CO₂ capture and sequestration process

In recent years, different types of reactors, such as batch (autoclave) reactors, fluidized bed reactors, and rotating packed bed reactors have been developed to enhance the mass transfer of the carbonation process.

6.1.1 Batch reactor

Batch reactors (autoclave reactors) are widely proposed for direct carbonation processes (Figure 6-1). The carbon dioxide is injected continuously into the reactor at a design pressure and a constant flowrate (Han *et al.*, 2011d). In the batch reactor, the key operating factors include the

reaction time, liquid to solid (L/S) ratio, slurry volume, stirring rate, reaction temperature, gas flow rate, CO₂ pressure, mineral feedstocks and their initial pH (Chiang and Pan, 2017a).

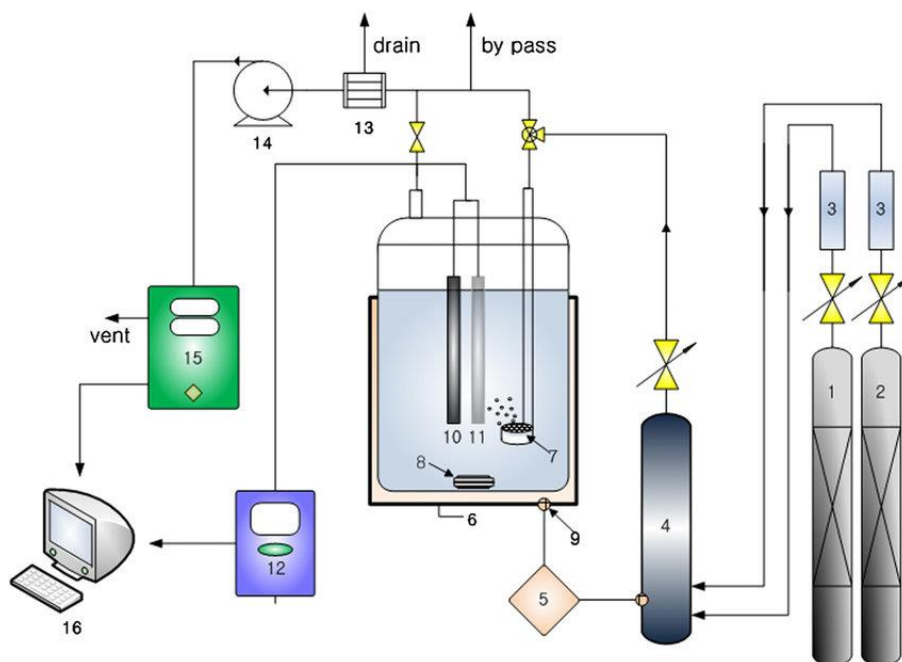


Figure 6-1: Schematic diagram of the experimental setup of batch reactor for the CO₂ capture using Ca(OH)₂ solution as the absorbent. (1) N₂ cylinder, (2) CO₂ cylinder, (3) Mass flow controller, (4) gas mixer, (5) temperature controller, (6) Pyrex reactor, (7) sparger, (8) magnetic stirrer, (9) thermometer, (10) pH sensor, (11) electrical conductivity (EC) sensor, (12) pH/EC meter, (13) dehumidifier, (14) sampling pump, (15) gas analyzer, and (16) computer for data acquisition (Han *et al.*, 2011d)

The carbonation reaction would become stable after some time because of the formation of carbonates on the surface of the feedstock particles. This would strongly reduce the reactive surface available for further carbonation and hinder the extraction of Ca/Mg ions from alkaline solid particles (Chiang and Pan, 2017a; Ji and Yu, 2018b). In a batch reactor, gaseous CO₂ dissolution can be accelerated by increasing the pressure of admitted CO₂ gas. Calcium leaching from alkaline solid matrix into solution can be enhanced by mechanical stirring. However, the

mass transfer is still low because of the small contacting surface of gas-liquid-particle three-phase system (Chiang and Pan, 2017a; Ji and Yu, 2018b).

6.1.2 Fluidized bed reactors

Figure 6-2 shows a schematic diagram of the fluidized bed reactor containing the fine alkaline solid wastes particles suspended in a liquid (Chang *et al.*, 2015). These kinds of reactors are frequently used in the chemical and/or biochemical industries because of their ability to increase mass transfer (Ji and Yu, 2018b). The fluidized bed can provide more contact area between the CO₂ and the feedstock in comparison to a batch reactor (Chang *et al.*, 2013).

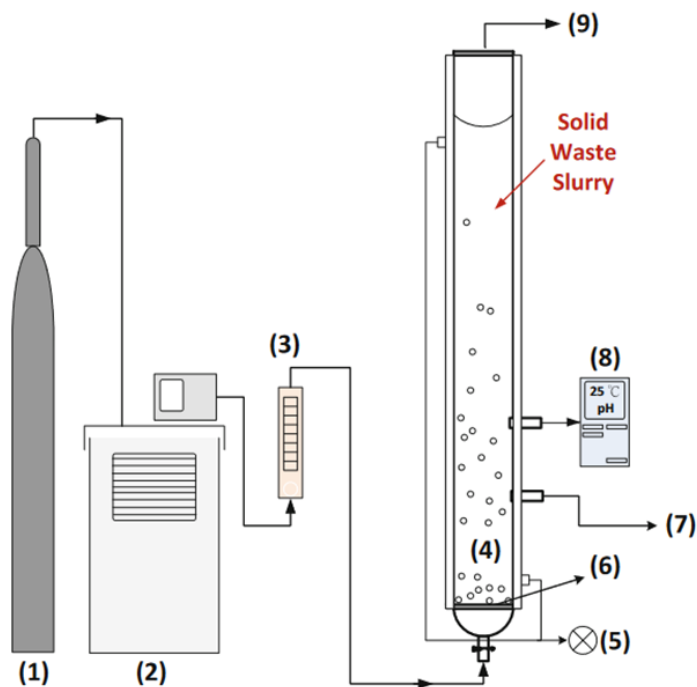


Figure 6-2: Schematic diagram of the experimental setup of fluidized bed reactor for mineral carbonation of alkaline solid wastes (1) gas cylinder; (2) circulating bath; (3) rotameter; (4) slurry reactor; (5) heating jacket; (6) gas distributor; (7) sampling; (8) thermos couple and pH analyzer; and (9) vent to hood (Chang *et al.*, 2015).

It can be operated at various conditions (Chang *et al.*, 2015). Normally, the CO₂ is injected into the slurry reactor continuously at 101.3 kPa (ambient) and a constant flow rate (Chang *et al.*, 2015). However, when examining the diagram in Figure 6-2, this appears unlikely as the gas pressure would have to be high enough to allow the gas to enter the bubble column at the bottom. By increasing the CO₂ flow rate, the mass transfer between the liquid and gas phases can be raised and the carbonation conversion can be improved. However, the carbonation conversion decreases moderately with further increases in the flow rate in a slurry reactor. The high flow rate of CO₂ in a fluidized bed results in a poor gas-liquid mass transfer rate and decreases the carbonation conversion. Furthermore, elevated CO₂ flow rates can accelerate a rapid pH decrease, which is detrimental to the carbonation reaction. Therefore, the CO₂ flow rate should be limited to a certain value (Chiang and Pan, 2017a; Ji and Yu, 2018b).

6.1.3 Rotating packed bed reactors

Figure 6-3 shows the rotating packed bed (RPB) reactor which is designed to improve the mass transfer among the gas-liquid-solid phases in the carbonation process (Pan *et al.*, 2013). This reactor is designed to enhance the mass transfer between gas and liquid phases via high centrifugal acceleration. It can provide a mean acceleration of up to 1000 times greater than the force of gravity, thereby leading to the formation of thin liquid films and tiny liquid droplets (microscale to nanoscale) (Pan *et al.*, 2018a). Therefore, the mass transfer between CO₂ gas and aqueous solution in an RPB reactor can be improved, resulting in high carbonation conversion within a short contact period (Chen *et al.*, 2020b; Pan *et al.*, 2018b; Pei *et al.*, 2017). The liquid velocity at the rotor tip of RPB is 50 m/s, which can develop appreciable energy penalties as a loss of kinetic energy. The main disadvantage is the rotating parts, including the rotor, bearings, and dynamic

seals, which result in long-term reliability concerns. This reactor also requires a liquid distributor (Cortes Garcia *et al.*, 2017; Hassan-Beck, 1997).

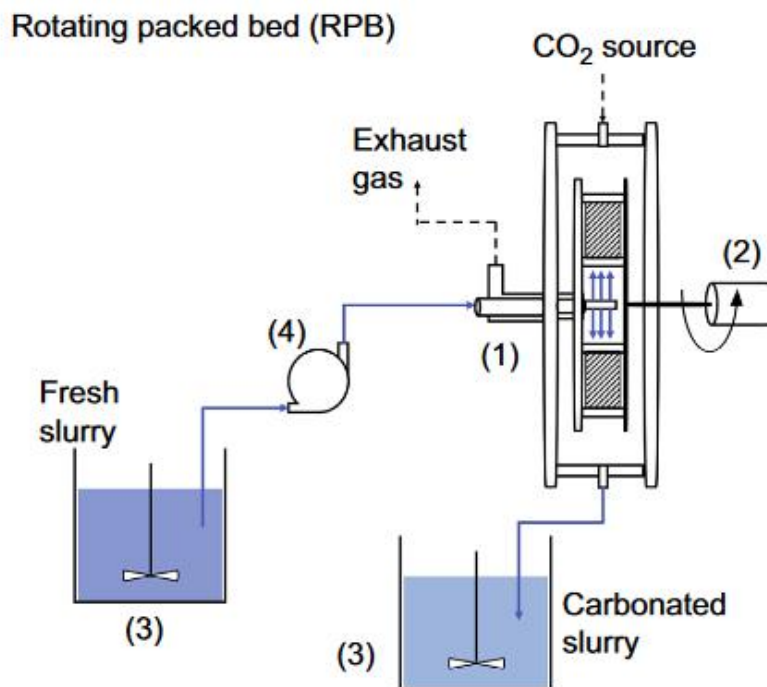


Figure 6-3: Schematic diagram of the experimental setup of rotating packed bed (RPB) for the carbonation of fly ash: (1) high-gravity RPB reactor; (2) stirring heating machine; (3) slurry storage tanks; and (4) pump (Pan *et al.*, 2013)

6.2 Horizontal injector loop

In this work, the production of calcium carbonate particles from calcium hydroxide solution by using a new experimental apparatus called the HIL, is investigated. Compared to a traditional batch reactor, the HIL is expected to provide operating conditions more favorable to carbonation conversion due to expected improvements in mass transfer from gas to liquid. It provides higher bubble contact area, agitation by means of circulation of solid, liquid and gas in the rig, higher

final pressure in the contactor, and does this with superior energy efficiency due to the HAC nearly isothermal compression process.

In this work, the reaction of Ca^{2+} ions with CO_2 (aq) to produce precipitated calcium carbonate particles is performed in an injector and separator, where flows are highly turbulent, and the bubbles created provide an appreciable mass transfer area for CO_2 to dissolve at the gas pressurises of the diffuser of the injector. Based on the literature review, there are only 2 studies found (Altiner *et al.*, 2019; Parivazh *et al.*, 2022) that use an injector as a gas distributor in a gas-liquid contactor for a carbonation process that may be regarded as comparable.

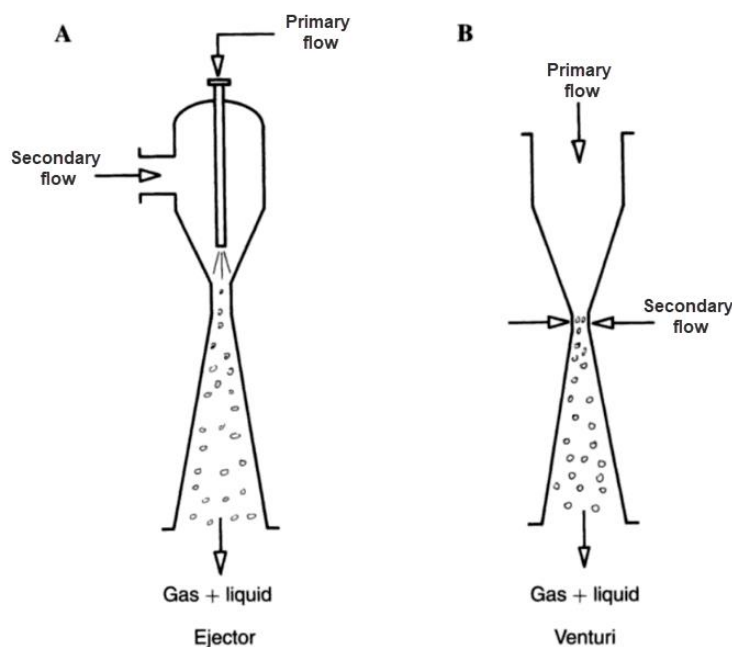


Figure 6-4: The ejector and venturi gas distributors (Trambouze, 2004)

Literature review (Majumder, 2016b; Mandal, 2010) also reveals that contactors or reactors belonging to the jet-mixing category, such as ejectors, venturi distributors, and other similar devices are a good alternative for achieving efficient dispersion of one fluid into another. These

are generally all co-current flow devices, where the kinetic energy of a fluid is used to achieve fine dispersion and mixing between the phases (Mandal *et al.*, 2005).

Figure 6-4 illustrates an ejector distributor and a venturi injector distributor. In the ejector, (Figure 6-4, A), the primary flow is introduced through one or more nozzles immediately before the throat of the ejector. The pressure energy of the primary fluid converts to a low-pressure, high-velocity flow in the nozzle, which draws in and entrains a secondary. In the venturi distributor (Figure 6-4, B), the primary flow passes through the converging part of the venturi and induces a secondary flow through the venturi wall and level with the throat of the venturi (Parmar and Majumder, 2013; Trambouze, 2004).

Based on the flow direction, three types of systems have been reported, vertical up-flow, vertical down-flow, and horizontal flow (Balamurugan *et al.*, 2007).

6.2.1 Description of process flow of the horizontal injector loop

The horizontal injector loop (HIL) was designed and constructed as a test reactor to confirm the expected performance of the system as a CO₂ capture and sequestration device.

Figure 6-5 shows the HIL apparatus that was designed and assembled. It is constructed of transparent PVC plastic and clear vinyl tubing. Thus, as well as being a platform for instrumented observations, the process is open to visual observation, which leads to better overall understanding of the rig operation. The major components of the system are a gas-liquid venturi injector, a gas-liquid separator, and a centrifugal pump.

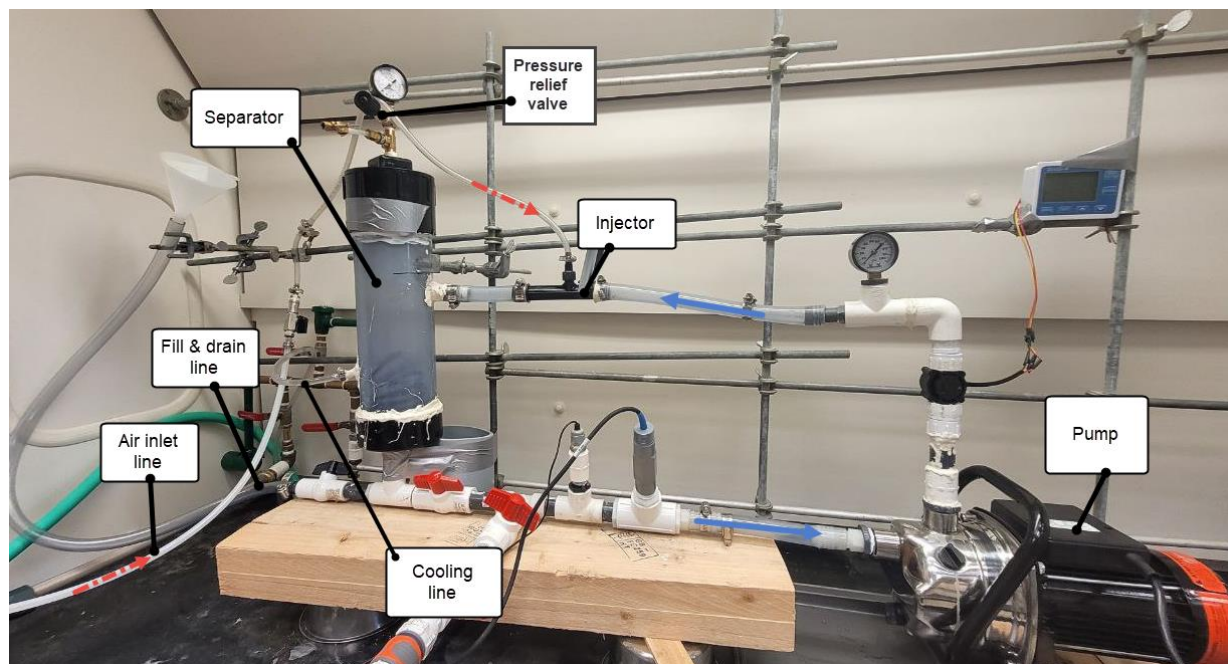


Figure 6-5: The horizontal injector loop

A venturi injector is used to distribute gas into the liquid circulating in the system and is installed horizontally, following the recommendations of the manufacturer (“Mazzei venturi Injectors,” 2022), and it is connected to the separator with a vinyl tubing which permits visual inspection of the nature of the flow before separation of the phases. The inside diameter of the tube is 1.27 cm (1/2”) and its length is 15.1 cm. A section of clear vinyl tubing is also used upstream of the venturi injector so that the nature of the flow entering can be visually confirmed too.

The pump forces the motive liquid through the injector. When pressurized liquid enters the injector inlet, it is constricted toward the injection chamber and changes into a high-velocity jet stream. The increase in velocity through the injection chamber results in a decrease in static pressure, creating a vacuum that draws a gas additive through the suction port and mixes it thoroughly into the liquid stream.

As the bubbly flow is diffused toward the injector outlet, its velocity is reduced, pressure is recovered (for the liquid) and flow proceeds in a thoroughly mixed state with slightly lower energy than when it entered the injector (“Mazzei venturi Injectors,” 2022). Bubbly flow commenced just downstream of the mixing throat and can be seen to occupy the whole section of the injector extension tube to the separator. When the bubbly flow reaches the separator, the flow velocity is reduced to permit the gas bubbles to separate from the liquid to form a compressed gas plenum at the top of the separator vessel.

A pressure relief valve with an adjustable setting is located at the top of the separator, which can be set to open at a predetermined pressure. When the set pressure is exceeded, the relief valve is forced open and allows the compressed gas to flow out of the system. Using this valve, it is possible to control the delivery pressure of the HIL as a compressor. This pressure is the separator pressure which is the same as the back-pressure faced by the injector. As the separator pressure increases, the extent of bubbly flow visible in the separator is reduced, and liquid and gas distribution visible in the transparent tubing can be seen to stratify. Separated liquid is drawn from the base of the separator and is recirculated back to the inlet of the injector via the pump.

6.2.2 Design characteristics of the HIL

The size of all fittings used in the rig is $\frac{3}{4}$ ". This dimension is not critical to the function of the HIL except that flow losses in the fittings consume energy that would otherwise be utilized for creating more suction in the injector. The $\frac{3}{4}$ " fittings are convenient because they are not expensive and readily available. This rig is designed to be low-cost and easy to construct and operate to provide rapid proof of concept. The pump circulates the liquid in the system. The model of the

injector (Mazzei PVDF584 - shown in Figure 6-6) was selected based on the performance curve of the pump (Figure 6-11) provided by the manufacturer (“Mastercraft 3/4 HP Stainless Steel Irrigation Jet Pump | Canadian Tire,” 2022). The size of the suction and discharge ports of the pump are 1” (2.5 cm) female national pipe thread (FNPT) and the maximum flow and pressure of the pump are 17 U.S. GPM (64 L/m) and 64 psi respectively.

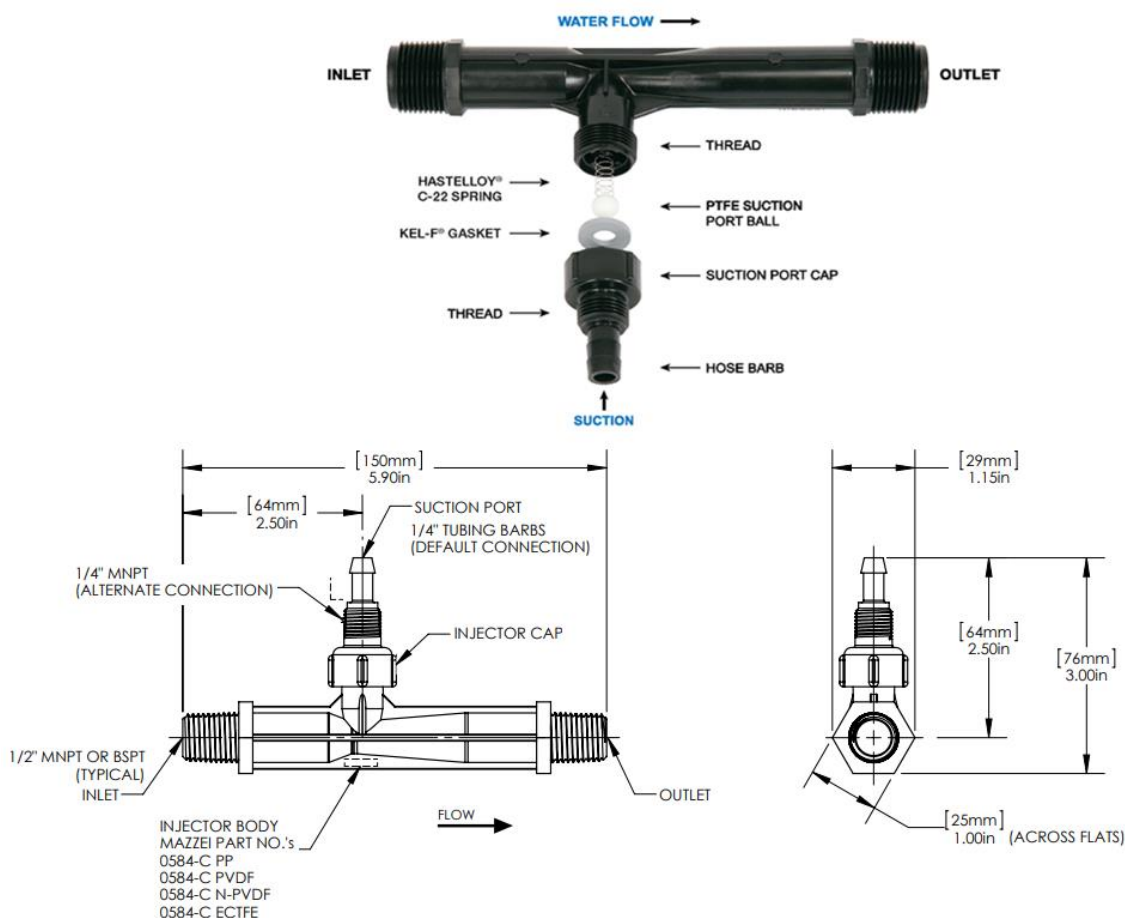


Figure 6-6: Mazzei injector (“Mazzei venturi Injectors,” 2022)

The material of this injector is polyvinylidene fluoride (PVDF) and the maximum operating temperature and pressure are 100° C and 8.44 bar(g) (at 20°C) respectively. There is a check valve in the suction inlet of the injector. However, if the system works at a pressure higher than

atmospheric pressure at the nozzle throat, this check valve does not prevent the flow of water into the air intake line.

A gas–liquid separator is an essential part of the apparatus, in which the phases of the gas–liquid mixture are separated from each other. The separator should be sufficiently large to provide a near-perfect gas–liquid separation at all flow rates. In the HIL, the separator is a 4 inch (10 cm) schedule 40 clear PVC pipe. The maximum pressure for this pipe is 110 psi (g) at 73.4°F (23°C).

As the rig harnesses bubbly flow, the hydrophobicity / hydrophilicity of the rig materials deserves some discussion. Hydrophobic materials are non-polar materials with a low affinity to water, which makes them water repelling. Hydrophobic surfaces can be self-cleaning to some extent. Water droplets tend to roll off hydrophobic materials, carrying dirt and contaminants away with them. PVC and PVDF are a characteristically hydrophobic materials, and consequently, these materials choices may present significant influence over bubble formation mechanisms in the injector, and bubble separation processes in the receiver, a topic of investigation beyond the scope of this thesis.

To design an effective separator with adequate size, separators of varying lengths and orientations have been designed and tested. Based on these experiments, the shortest length (height, for a vertically oriented separator) of the separator is 40 (cm). The design water level inside the separator is 26.4 cm at the design operating pressure of 24 psi and water flow rates of 24.5-28.5 L/min. When the system is filled to this level it contains 3.55 L of liquid. The water flow that enters the pump must be free of gas, otherwise, the gas bubbles enter the pump rotor chamber, and the cavitation-type behavior occurs in the pump. The separator was not designed to be able to separate particles of the precipitated calcium carbonate from water.

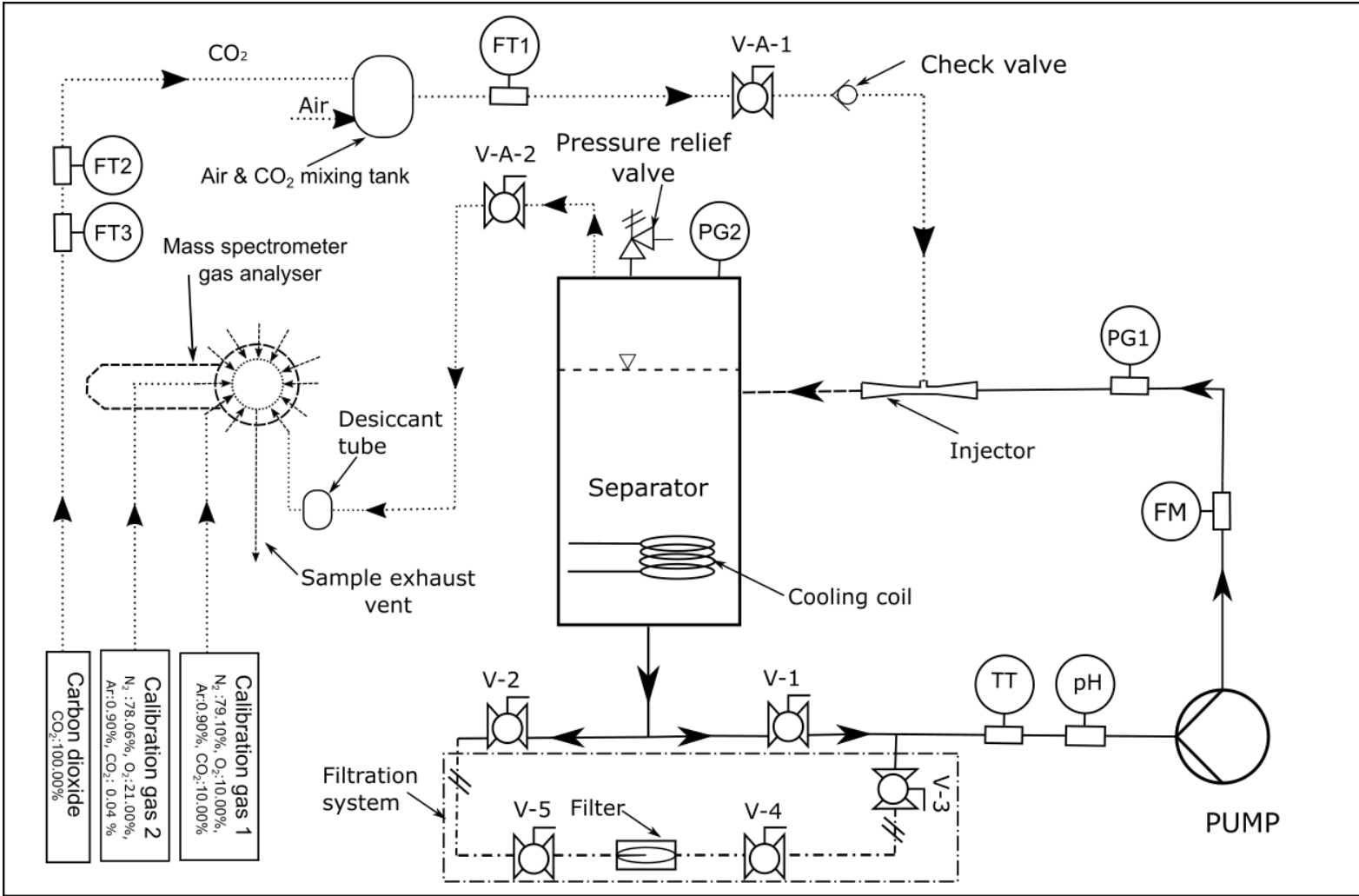


Figure 6-7: The schematic diagram of the horizontal injector loop

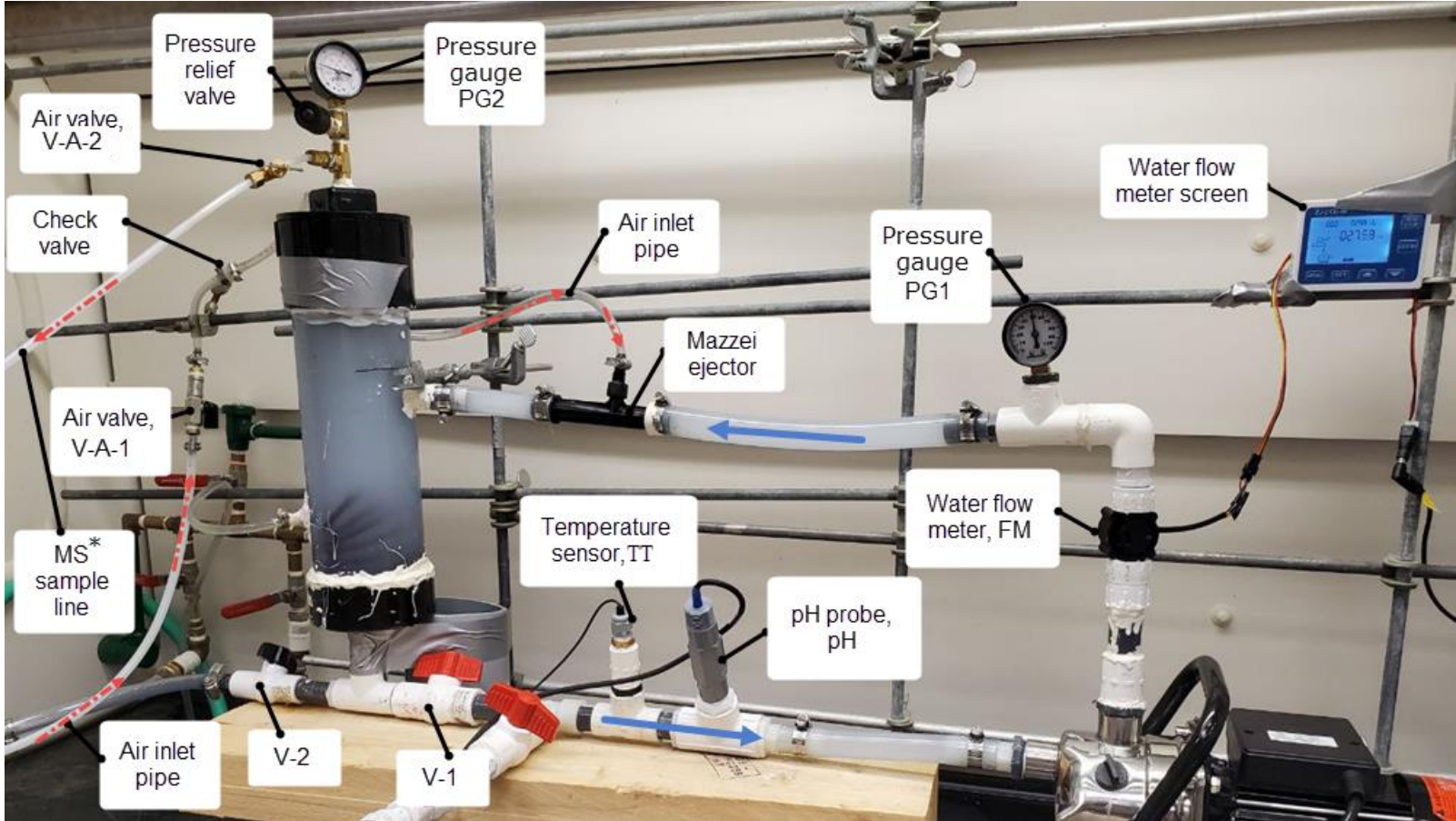


Figure 6-8: The horizontal injector loop with instrument labels (the cloudy liquid visible in the separator is a solution and suspension of $\text{Ca}(\text{OH})_2$ that progressive reacts with admitted CO_2 to form CaCO_3 as experiments proceed).

6.2.3 Instrumentation

Figure 6-7 shows a process and instrumentation diagram (PID) of the HIL. Figure 6-8 presents a corresponding photograph. Alongside the injector, gas-liquid separator, and centrifugal pump, the locations of liquid control valves (V1, V2), air control valves (V-A-1, V-A-2) pressure relief valve (PV), pressure gauges (PG1, PG2), temperature and pH sensors (TT, pH), and flow meters (FM, FT1, FT2) are illustrated.

The specifications of the measuring instruments are described in the following sections:

- Water flow rate

The flow rate on the horizontal injector loop is measured using a GREDIA water flow sensor (FM). This sensor comes with a digital LCD display water flow quantitative controller. The flow range of this flow meter is 1-60 L/min, and the maximum water pressure is 1.2 MPa (174 psi). This is a real-time flow rate monitoring system. The calibration status of the instrument was checked by using a ‘bucket and stopwatch’ method before installation in the rig. The water flow meter is installed on the discharge of the pump and measures the flow rate before the inlet of the injector.

A throttling valve (V-1) can be used to modulate the water mass flow rate in the rig but when this is full open, the water flow rate in the system is determined by the convergent section (nozzle) of the injector. In the experiments, the outlet pressure of the nozzle section of the injector is always just below 0 psi(g) (atmospheric) – this being finally determined by any additional fittings / tubing fitted to the secondary fluid inlet (such as the injector’s check valve). Then the flow rate through the system depends only on the pump discharge pressure and the (fixed) geometry of the nozzle.

The throttling valve can modify the system behavior but only when the drop at this valve is greater than the drop in the injector nozzle.

- Gas flow rate

Experiments with the BabyHAC confirmed that when the water becomes saturated with dissolved gas, the mass flow at the inlet to the system will equal the mass flow of gas at the outlet. In the horizontal injector loop, gas mass flow inducted into the rig by the injector will be in balance with the gas mass that flows out of the rig at the pressure relief valve. Therefore, the gas mass flow rate is measured only at the gas (secondary) intake line of the injector. A valve (V-A-1) permits manipulation of the gas mass flows into the rig, by reducing the absolute pressure at the injector suction inlet as it is closed. However, when the valve (V-A-1) is fully open, the gas mass flow rate is dictated by the water flow rate, and the inlet, and outlet pressures of the injector. When the (V-A-1) valve is closed, the injector can not induct air into the system, and so it works like a connecting tube between the pump and the separator. An Omega FMA-A2322 digital mass flow meter (FT1) measures the gas mass flow rates at the gas intake line of the injector. As well as the check valve at the injector suction inlet, there is another check valve in the gas intake line that prevents back water flow to the gas mass flow meter.

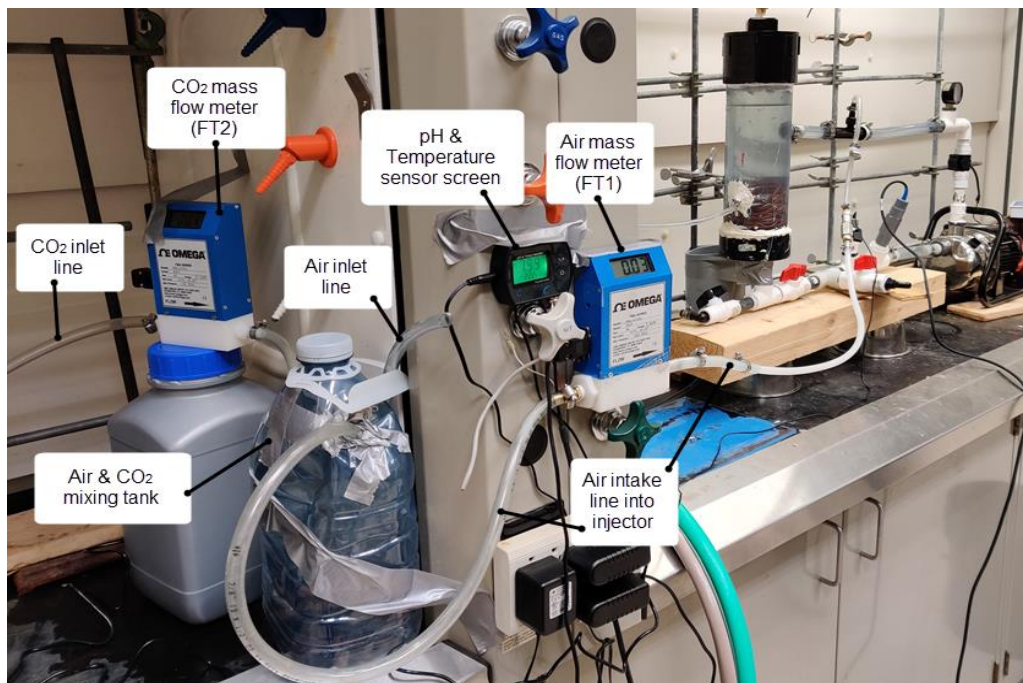


Figure 6-9: Air & CO₂ mixing tank and its instruments

When the HIL works as a reactor for the precipitation of calcium carbonate, the CO₂ (g) is added to the inlet air of the system. To mix CO₂ and air properly, a mixing tank is connected to the gas intake pipe of the injector. Figure 6-9 shows the air and CO₂ mixing tank.

Without the mixing tank, the injector sucks more CO₂ than air to the rig. A ProStar HRF 1425–580 rotameter (FT3) and an Omega FMA-A2308 digital mass flow meter (FT2) are used to measure the CO₂ flow rate which is added to the inlet air.

- Pressure

Measuring the pressure in the rig is a critical quality step to control the performance and safety check to be aware of leaks or the build up of over-pressure in the system. The HIL is equipped with two Bourdon-type pressure gauges (PG1 and PG2). PG1 at the discharge of the pump

measures the water pressure at the inlet of the injector while PG2 measures the pressure at the top of the separator. The pressure range of both gauge pressures is 0-100 psi.

- Temperature

A temperature sensor (AT) is located in the suction line of the pump, and it measures the temperature of the water after the separator. The temperature of the inlet gas to the injector is not measured. However, the HIL is located indoors in a temperature-controlled laboratory, so the air temperature variations are limited.

While the rig is running, if not actively cooled, the temperature of the water increases over time due to pump inefficiency and compression heat arising from the compressed gas. A cooling coil, located in the separator, is thus used for the regulation of water temperature. Liquid temperatures are limited to a maximum of 35°C due to the reduced strength of the PVC materials beyond this temperature.

- pH

The rig is equipped with a Cole-Palmer in-line pH probe (pH). The temperature operating range of this probe is -5 to 80° C, and its epoxy body withstands pressures to 100 psi. The pH meter is calibrated with the pH Buffer solutions including solutions at pH 7 and pH 10. Another handheld pH meter, Dr.meter PH100 is also used for separate measurement of the samples.

- Gas composition

A Hidden Analytical HPR-20 QIC mass spectrometer gas analyzer is used to continuously measure the concentration of discharge gas species from the rig.

6.3 Experimental results of operation of the HIL

The injector manufacturer (Mazzei) provides a performance table that shows the volume of the inducted flow for different inlet pressures and varying injector back pressure (at the outlet). Table 6-1 shows the performance table of the PVDF584 model of the Mazzei injector which is used in this work. The inlet and outlet pressures range from 15 to 80 (psi) and 0 to 65 (psi) respectively. The inducted air flow rate to the injector is also reported at different water flow rates. The manufacturer did not provide the inducted air flow rates for all ranges of the pressure. However, the table can be completed by interpolating the data that are presented by the manufacturer.

Inducted gas (L/min)

Table 6-1: The performance table of the PVDF584 model of Mazzei injector

Inlet pressure (psi)	Motive Flow (L/min)	Injector back pressure (psi)												
		0	5	10	15	20	25	30	35	40	50	60	65	
Inducted gas (L/min)														
15	13.25	8.18	2.16	0.46										
20	15.14	9.64	3.85	1.36	0.41									
25	17.03	10.86	4.75	2.26	0.89	0.35								
30	18.55	12.27	6.39	3.15	1.55	0.85	0.30							
35	20.06	13.35	8.70	4.37	2.44	1.27	0.80							
40	21.58	14.43	9.12	5.12	3.24	1.97	1.27	0.71						
45	22.71	14.85	10.11	5.92	4.42	2.73	1.83	1.18	0.66					
50	23.85	15.56	10.58	7.52	4.84	3.57	2.35	1.65	1.03	0.61				
60	26.12	17.01	12.55	9.87	6.39	4.70	2.68	2.02	1.32	0.94				
70	28.39	17.20	13.54	11.09	8.08	6.02		3.76			2.16	1.26		
80	30.28	17.86	14.57	12.31	10.29	7.52		4.89			3.34	2.16	1.22	0.79

To calculate the losses (resistance) and operating point of the system, a test was conducted to reproduce the injector performance table experimentally. Throughout the test, the inlet and back pressures of the injector were measured by the two pressure gauges (PG1 and PG2). The water flow sensor (FM) and the digital mass flow meter (FT1) measure the inlet water flow rate and the inducted air flow rate of the injector respectively (Figure 6-7). Psychrometric conditions of intake

air were measured with a Kestrel handheld digital psychrometer / anemometer. The amount of electrical power that the pump consumed was also measured by a power meter. The system process / hydrodynamic variables were recorded by continuously monitoring the analog gauges / digital display units with a video camera. Upon completion of the experiment, the video recording was reviewed, and observation sets were taken and referenced against video timestamps. The observations were recorded every 10 seconds.

The hydraulic injector loop was filled with water. The only experimental parameter that was varied during the test was the back pressure of the injector by adjusting the pressure relief valve to varying setpoint pressures. Table 6-2 presents the data collected during the test.

Table 6-2: Experimental measured values

Water flow rate (L/min)	Pump discharge pressure reading (PG1) (psi)	Separator pressure (PG2) (psi)	Inducted gas (L/min)	Temperature of water (°C)	Pump electric power (W)
19.13	30.3	0.0	12.38	20.10	586.25
20.70	35.3	7.0	5.75	20.09	590.13
21.32	38.1	10.0	4.31	21.34	593.50
21.19	36.9	10.0	4.55	20.10	588.13
23.06	45.4	20.0	2.51	21.13	595.14
23.34	45.4	20.0	2.36	20.20	590.80
23.36	46.0	22.0	2.28	20.30	589.75
23.97	47.3	25.0	2.08	21.06	593.56
24.35	50.5	29.0	1.83	20.08	590.00
25.10	52.5	30.0	1.75	20.71	595.09
26.26	55.7	35.0	1.46	20.50	594.11
25.47	55.8	37.0	1.43	20.33	592.17
26.77	60.6	40.0	1.33	20.35	595.13
27.90	68.3	49.2	1.00	20.35	594.17
28.21	66.9	50.0	1.01	20.13	594.77
29.35	72.6	56.0	0.90	20.31	594.38

The separator / injector back pressures ranged from 0 to 56 psi(g) during the experiments. By increasing the back pressure, the water flow rate and pump discharge pressure both increased. The water flow rate increased because the injector primary flow delivery pressure to its nozzle

increased as the system pressure rose. The differential pressure across the injector remained approximately constant as the system pressure (separator pressure / injector back pressure) rose. As expected, as the system pressure rose, reduced mass flow rates of inducted secondary air were noted.

Figure 6-10 shows the measured inducted gas according to the water flow rate (or equivalently injector delivery pressure) during the test. By interpolating the data that are presented in the Mazzei injector performance table a curve representing the continuous behavior of inducted gas mass flow with varying injector water flow can be prepared and this is also plotted in Figure 6-10. It is evident that there is a good agreement between the measured values of the inducted gas and the Mazzei injector performance table; the injector was behaving as designed in the rig.

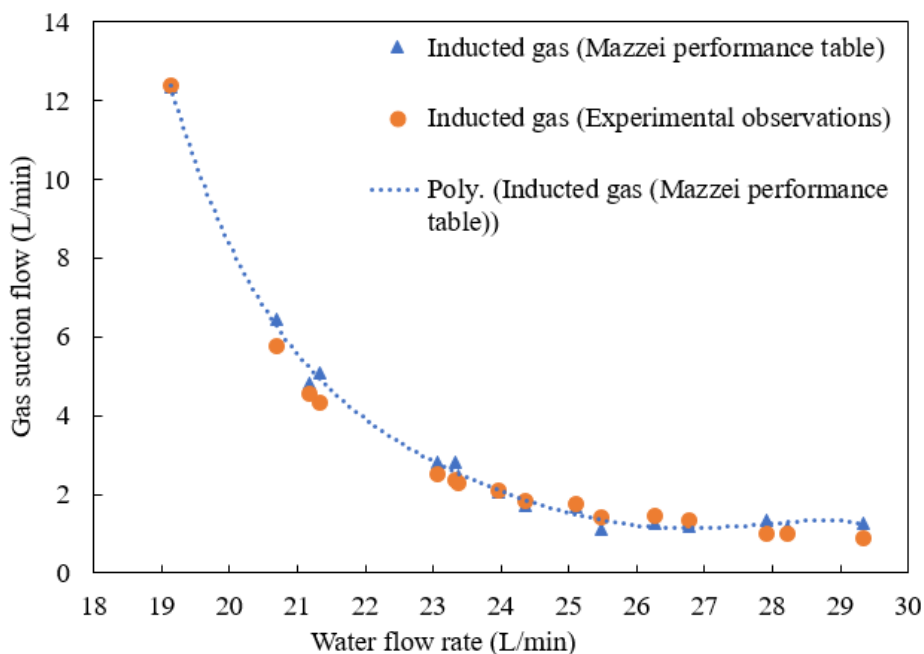


Figure 6-10: Gas suction flow rate versus water flow rate

6.3.1 Pump performance

Table 6-3 shows the pump performance table provided by the pump manufacturer. The role of a pump is to provide sufficient pressure to move fluid through the system at the required flow rate. This energy compensates for the energy losses due to friction, elevation, velocity, and pressure differences between the inlet and outlet of the system (Tuzson, 2000). The hydraulic work of the pump is calculated by Eq. (6.1)

$$\dot{W}_{pump} = \dot{Q}_L(P_{delivery} - P_{suction}) \quad (6.1)$$

where \dot{Q}_L is the liquid volumetric flow rate, $P_{delivery}$ and $P_{suction}$ are the discharge and the suction pressures of the pump, respectively. In Table 6-3, the measured values of the electrical power which the pump consumed during the operation are also presented.

Table 6-3: The pump performance table provided by the pump manufacturer

Parameters	Values			
Head (m)	6.1	18.3	27.4	30.5
Pressure rise (psi)	8.7	26.0	38.9	43.3
Discharge flow rate (L/min)	50.5	29.7	18.9	12.0
Mass flow rate (Kg/s)	0.839	0.493	0.315	0.199
Hydraulic work (W)	50.2	88.5	84.6	59.6
Measured electric power (W)	595	585	585	595
Efficiency (%)	8.44	15.13	14.46	10.02

The pump efficiency is characterized by the ratio of hydraulic power imparted to the flow to the electrical work provided by the motor (Derakhshan *et al.*, 2013).

$$\eta = \frac{\text{Hydraulic power (W)}}{\text{Electric power (W)}} \quad (6.2)$$

As presented in Table 6-3, generally, the efficiency of the pump can be seen to be low. The maximum efficiency of the pump is 15.13%. However, this value appears typical of the efficiency

of small-scale water pumps which are commercially distributed as consumer pumps to North American markets (Emiliawati, 2017).

The pressure vs flow rate performance curve of the pump provided by the manufacturer is plotted in Figure 6-11, the values provided having been fitted to quadratic form. In this figure, the pressure drops across the injector based on the water discharge flow rates are also presented.

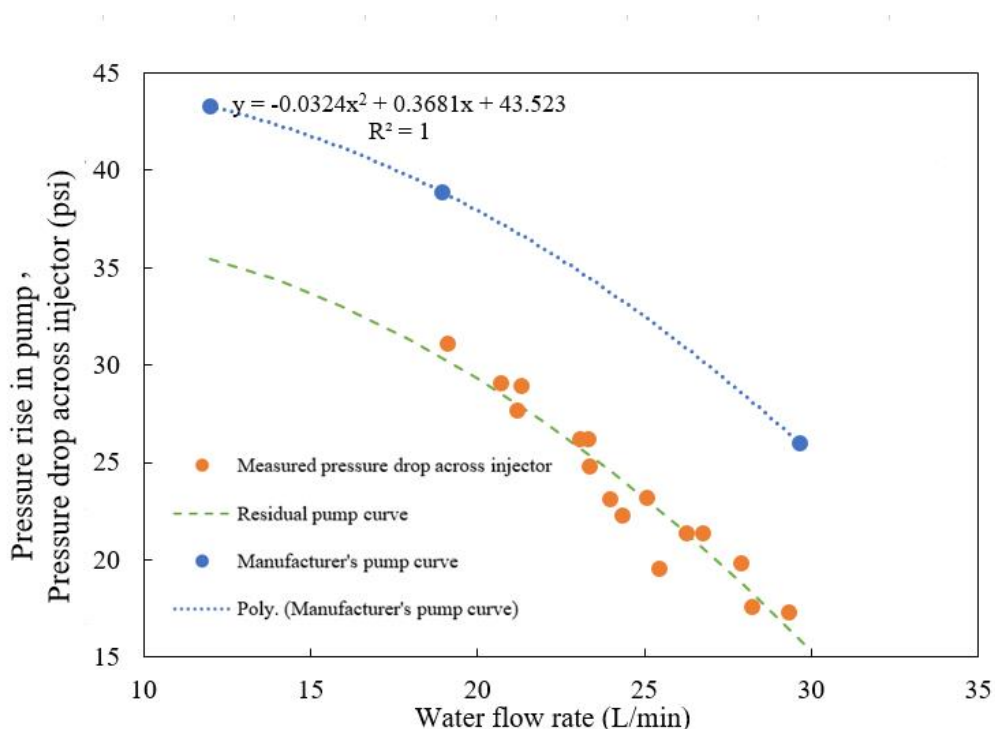


Figure 6-11: The performance curves of the pump and injector

Determination of the pumping system operating point involves equating the relation for the pressure rise across the pump to the pressure fall associated with the components in the circuit with which it is connected and solving for the water flow rate (Millar and Pourmahdavi, 2021). If connecting pipes, tubes and fittings are appropriately sized, the dominant component of the system pressure drop will be that attributable to the injector. If inappropriately sized, the pressure drops

arising from flow through the piping elements such as valves, elbows, barbs, and bends, as well as the separator, will alter the system operating point.

In Figure 6-11, the residual pump curve reflects the performance of the pump after the head losses in serially connected piping elements at a particular discharge rate is subtracted from the pump head at the same discharge rate. This figure shows the separator, pipework, valves, flow meter, etc. account for a 7.4 (psi) (downward) offset of the pump curve, or a $0.003Q^2$ varying pressure drop.

6.3.2 Injector performance

The Mazzei injector consists of a nozzle, suction chamber, throat, and diffuser (Figure 6-12). In this injector, the diameter of the nozzle inlet (d_p) and outlet (d_n) are 1.24 (cm) and 0.43 (cm) respectively. The diffuser outlet (d_d) is 1.24 (cm).

In the injector, a pressure drop accompanies the change in velocity of the water as it passes through the convergent section (nozzle). The pressure drop through the injector convergent section must be sufficient to create a slight negative pressure (vacuum) measured relative to atmospheric pressure at the throat. Under these conditions, the gas will flow into the injector. Most venturi injectors require at least a 20% differential pressure to initiate a vacuum (Li *et al.*, 2020).

The nozzle is an important part of an injector because it determines the water flow rate and, the vacuum level at the suction chamber and thus, the amount of secondary fluid (gas) that can be entrained into the system (Wang *et al.*, 2021).

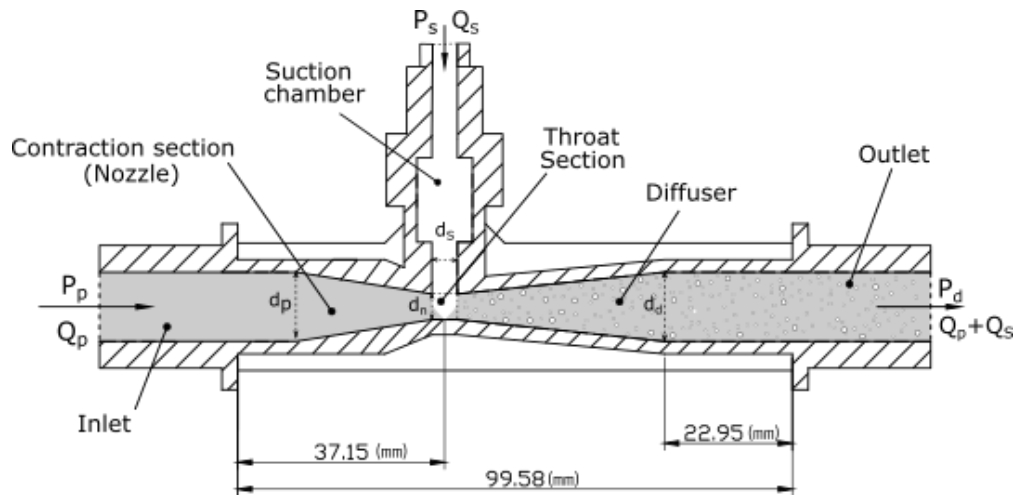


Figure 6-12: Configuration of Mazzei injector

The pump provides sufficient pressure to move water through the system at the required flow rate. The water with flow rate Q_p and high pressure P_p supplies the energy utilized for gas entrainment, compression, and dispersion of phases in the injector. Water is accelerated through the nozzle and creates a low-pressure P_s (vacuum) at the suction chamber of the injector. The air, with flow rate Q_s , flows through the secondary feed pipe to the suction chamber. The nozzle converts the pressure energy (static pressure) of the motive fluid (water) to the kinetic energy by increasing the local velocity (creating a high-velocity jet). Kinetic energy can be divided into two components: axial kinetic energy and turbulent kinetic energy. A main part of the axial kinetic energy of the jet is converted back to the pressure energy by mixing shock resulting from the dispersion of the gas phase into fine bubbles. A part of the turbulent kinetic energy promotes the disintegration of the free jet and improves the gas entrainment rate. (Opletal *et al.*, 2018; Wang *et al.*, 2021)

Pressure drop of water flow across the nozzle ($P_p - P_s$) can be calculated from the Bernoulli equation by assuming the density of water is constant:

$$P_p + \rho_L \frac{v_p^2}{2} = P_s + \lambda \rho_L \frac{v_n^2}{2} \quad (6.3)$$

where v_p is liquid velocity at the injector inlet (m s^{-1}), v_n is jet velocity at the nozzle exit (m s^{-1}), λ is a frictional losses coefficient, ρ_L is liquid density (kg m^{-3}). Bernoulli's equation is valid for ideal fluids (Opletal *et al.*, 2018; Wang *et al.*, 2021).

The mixing process with energy and momentum exchanging between water and gas occurs through the throat of the injector. Further mixing is achieved when the two-phase flow passes through the diffuser. The pressure of the mixing fluid is P_d at the outlet of the injector. Based on the inlet pressure of the injector, inlet water flow rates of the nozzle are calculated by using the Bernoulli's equation. P_s which is the pressure in the suction chamber is taken as zero (atmospheric pressure). The frictional losses of the nozzle are also neglected ($\lambda=1$). Figure 6-13 shows the calculated water flow rates of the nozzle and the Mazzei injector performance table versus inlet pressures. There is a good agreement between the calculated values and Mazzei injector performance table.

Figure 6-13 also presents observations of pressure and water flow rate from the rig trials. The water pressure and flow rate are measured at the discharge of the pump. 1 (psi) pressure deficit has been found to occur between the gauge and the inlet of the injector. This 1 (psi) loss is part of the total losses considered in the residual pump curve. When the 1 (psi) loss is subtracted from the pump discharge pressures, the measured water flow rates are close to the calculated water flow rates and those of the Mazzei injector performance table. The results of the conducted test also

confirm that the water flow rate of the system depends principally on the injector inlet pressure and the injector nozzle dimensions.

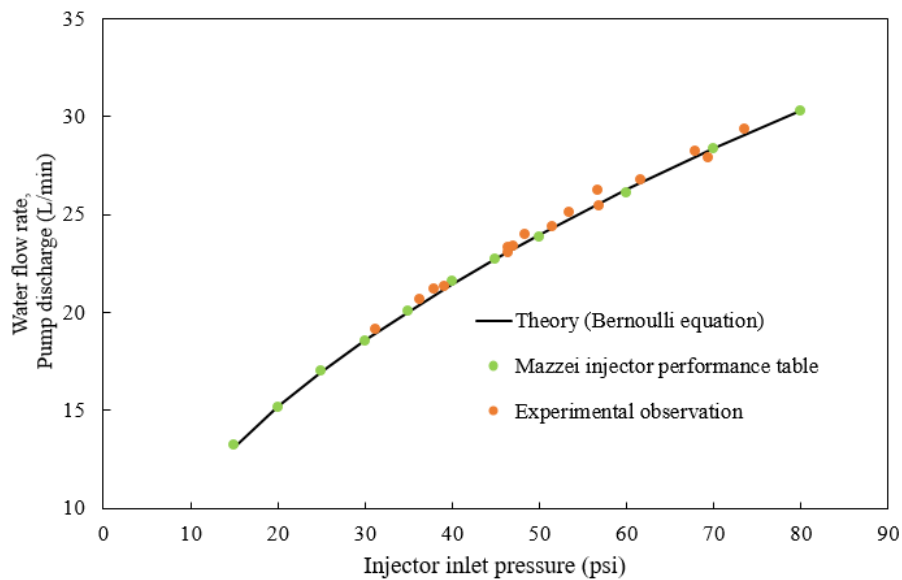


Figure 6-13: The injector water flow rate according to the inlet pressure.

The pressure drops across the injector ($P_p - P_d$) are estimated by considering the following assumptions:

- Both phases are intensely mixed in the throat, and due to the high thermal conductivity of water, the process is considered to be isothermal.
- Static pressure at the ejector outlet, P_d , is equal to the separator pressure.
- The kinetic energy of the gas is negligible compared to that of the liquid (zero slip).
- The water density is assumed for the combined two-phase flow at the outlet of the injector

Figure 6-14 shows the dynamic pressure ($\rho_L \frac{v_d^2}{2}$) which represents the kinetic energy per unit volume of a fluid for the two-phase flow at the end of the injector. The values of the dynamic pressures are small and can be ignored.

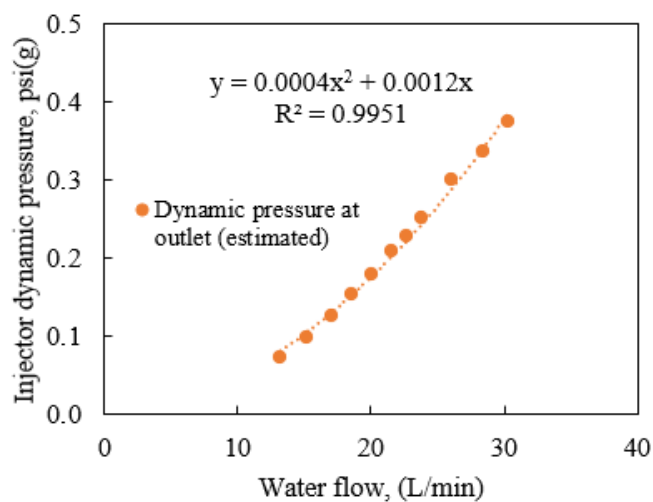


Figure 6-14: Inlet pressure and outlet dynamic pressure of the injector versus inlet water flow rate

In Figure 6-14, the injector outlet pressures are calculated as the sum of the static pressure (P_d) and dynamic pressure at the outlet of the injector. The difference in pressure between the pressure rise across the pump and the pressure drop across the injector represents the frictional head losses of the system.

Table 6-4: The performance of the system (injector and pump)

Water flow rate (L/min)	Pump discharge pressure (PG1) (psi)	Injector inlet pressure (psi)	Separator pressure (PG2) (psi)	Injector outlet pressure (psi)	Pressure drop across injector (psi)	Pressure rise across pump (psi)	Measured inducted air (L/min)	Pump electric power (W)	Work of gas compression (W)	Pump hydraulic work (W)
19.13	30.3	31.3	0.0	0.1	31.1	38.7	12.38	586.25	0.00	85.1
20.70	35.3	36.3	7.0	7.2	29.1	37.3	5.75	590.13	3.79	88.6
21.32	38.1	39.1	10.0	10.2	28.9	36.7	4.31	593.50	3.81	89.8
21.19	36.9	37.9	10.0	10.2	27.7	36.8	4.55	588.13	4.02	89.6
23.06	45.4	46.4	20.0	20.2	26.2	34.8	2.51	595.14	3.70	92.2
23.34	45.4	46.4	20.0	20.2	26.2	34.5	2.36	590.80	3.48	92.5
23.36	46.0	47.0	22.0	22.2	24.8	34.4	2.28	589.75	3.58	92.5
23.97	47.3	48.3	25.0	25.2	23.1	33.7	2.08	593.56	3.57	92.9
24.35	50.5	51.5	29.0	29.2	22.3	33.3	1.83	590.00	3.46	93.1
25.10	52.5	53.5	30.0	30.2	23.2	32.4	1.75	595.09	3.38	93.3
26.26	55.7	56.7	35.0	35.3	21.4	30.9	1.46	594.11	3.10	93.1
25.47	55.8	56.8	37.0	37.3	19.6	31.9	1.43	592.17	3.16	93.3
26.77	60.6	61.6	40.0	40.3	21.3	30.2	1.33	595.13	3.06	92.8
27.90	68.3	69.3	49.2	49.5	19.9	28.6	1.00	594.17	2.59	91.6
28.21	66.9	67.9	50.0	50.3	17.6	28.1	1.01	594.77	2.64	91.2
29.35	72.6	73.6	56.0	56.3	17.3	26.4	0.90	594.38	2.51	89.2

The major part of the pressure energy provided by the pump is used in the injector mainly for fine dispersing and compressing gas into the liquid phase. In Table 6-4, the work utilized on the gas compression (W_{comp}) is calculated by Eq. (6.4)

$$W_{comp} = \dot{m}_G \mathcal{R}_{air} T_s \ln \frac{P_d}{P_s} \quad (6.4)$$

where \dot{m}_G is the gas mass flow (kg/s), \mathcal{R}_{air} is specific gas constant (J/ kg K), and T_s is temperature in suction section (K). By increasing the back pressure, the amount of the air inducted to the system decreases. The gas compression work also decreases. In Table 6-4, the hydraulic work of the pump is calculated by Eq. (6.1).

6.4 Summary

The HIL test rig which is a variation on the HAC systems, was designed, fabricated/assembled and tested. The height of HAC units, following the Millar, (2014) design paradigm, is invariably high. Therefore, the capital cost of HAC construction is considerable in all variations that have been explored thus far. The HIL is a type of HAC with a small elevation difference. The momentum, mass, and energy formulations for the injector are identical to those of the AWMH of the HAC. A huge advantage of HIL is that the delivery pressure is simply controllable without requiring a change of HAC height.

Another advantage of the HIL is that practical isothermal compression was achieved for the gas. According to the work of Opletal *et al.* (2018) and Witte (1969), gas compression in the injector can be treated with good accuracy as being isothermal. Therefore, the temperature can be controlled in the HIL.

In the HIL test rig, the mass flow rates of gas inducted matched those expected from the manufacturer's injector performance table, for specific conditions of injector delivery and separator pressure.

In the next chapter, the operation of HIL as a CO₂ capture and sequestration device/process has been investigated experimentally. The rig is operated with CO₂ gas being mixed with the inducted air (to simulate a combustion off gas), and with Ca(OH)₂ solution circulating rather than water.

7. Experimental investigation of CO₂ capture and sequestration by means of HIL

In the last Chapter, the basic design of the HIL was explained, and the experimental performance of the unit was found to be ‘as designed’ when tested with air as the inducted secondary fluid and with water as the primary circulating fluid. In this chapter, the performance of the HIL is revisited, but with 2 key differences in operation compared with Chapter 6. First, a suspension solution of Ca(OH)₂ (a dilute slurry) is used to replace water as the primary circulating liquid. Second, the air enriched with controlled mass flows of CO₂ constitutes a secondary inducted gas stream. In addition to inducting and compressing the secondary gaseous phase, the injector behaves as a gas distributor to create bubbles enriched with CO₂ so that the CO₂ dissolves in the alkaline solution. The remaining gas phase is pressurized in the diffuser of the injector. As Ca(OH)₂ dissolves and reacts with the dissolved CO₂ in the HIL, a CaCO₃ precipitate is formed, and the circulating fluid remains a dilute slurry with altered chemistry.

As a result, the design objectives of the HIL in this configuration are CO₂ capture (through dissolution) and sequestration (to CaCO₃ precipitate). The HIL should be conceived as a continuous pressurized chemical reactor to understand the performance of the system as a CO₂ capture and sequestration device. The results of the experiments conducted in this chapter aim to provide a proof-of-concept that the HIL is a credible potential CO₂ capture and sequestration technology. Because the experiments planned for the device involve relatively high concentrations of CO₂, conducting these trials in a fume hood was preferable for health and safety reasons.

7.1 Experimental procedures for CO₂ carbonation

7.1.1 Purpose of experiment

The purpose of the experiments beyond the HIL design trials is to confirm that the reaction between CO₂ and Ca(OH)₂ to form CaCO₃ and water can be sustained within the HIL.

In testing rigs beyond the lab-scale unit presented herein, it is envisaged that finely ground alkaline earth minerals will be entrained in water in a separate reactor, some of which will be dissolved to create alkaline or suspension solutions that will be continuously admitted to the HIL simultaneously as combustion off-gas is inducted. However, in the lab-scale unit discussed herein, instead of continuously admitting an alkaline solution/suspension, the unit is pre-charged with a liquid comprising a saturated solution of Ca(OH)₂ and suspended, initially undissolved Ca(OH)₂ particles for better control in these early-stage experiments. As dissolved Ca(OH)₂ reacts with CO₂, the Ca(OH)₂ solution will tend to become depleted from its saturated state. However, the expectation is that the solid suspended Ca(OH)₂ particles will progressively dissolve, ‘topping up’ the solution to a saturated state so that the starting pH will be maintained (at approximately pH=12.5). When all the suspended excess Ca(OH)₂ is dissolved and consumed in the precipitation reactions, further creation of CO₂(aq) causes the pH of the solution to decrease. The principal observation from each experiment is the duration from the start of admission of CO₂ gas when the pH is approximately 12.5 to when the pH decreases to 10.

7.1.2 Preparation of circulating liquid solutions/suspensions

The first step in the experimental process is the preparation of a Ca(OH)₂ solution to fill the rig. Five different solutions are prepared for the CO₂ capture and sequestration experiments. The first,

named 1C-F, comprised 3.55 L of Ca(OH)_2 -saturated aqueous solution in which Ca(OH)_2 is dissolved to its maximum solubility of 5.34 g in 3540 g of deionized water (D.I.) at 22° C. The 1C-F solution is filtered using a 5-micron filter to remove undissolved, suspended particles.

The remaining solutions/suspensions, labeled 1.7C-S, 2.2C-S, 2.9C-S, and 5C-S, are 3.55 L of water containing 9.09, 11.76, 15.68, and 26.72 g of Ca(OH)_2 , respectively. In all the suspension solutions, 5.34 g of Ca(OH)_2 is commonly dissolved, and any excess co-exists as undissolved Ca(OH)_2 to form a slurry.

In this work, D.I. water is used to prepare the Ca(OH)_2 solution. The pH of D.I. water is 6.0 to 6.4, depending on the temperature. However, the pH of pure water is 7.

7.1.3 Filling the injector loop with liquid

Before each individual experimental run, the rig is filled with deionized water and operated for approximately 10 minutes. The objective is to flush out any remaining reactants or products from previous experimental runs. In this work, eight experimental runs are reported with the rig containing varying amounts of Ca(OH)_2 , either in dissolved or suspended states, or both. After each experiment, the rig is washed with dilute acetic acid to remove any CaCO_3 that may have remained from a previous run. A contaminated or dirty apparatus could lead to inaccurate results from the experimental run.

The fill-up line of the rig is shown in Figure 5-6. The horizontal injector loop is filled with 3.55 L of solution/suspension. After the solution/suspension is added to the rig, valve V-2 is closed, and the system is ready to operate.

7.1.4 Phase I Start-up and steady state operation without CO₂ being inducted.

After loading the rig with the solution, the pump is turned on, and the solution is circulated in the system while the injector inducts atmospheric air. In phase I, the pressure relief valve is adjusted to the desired separator pressure (24 psi) after the circulating pump is operated.

When the pressure gauge at the top of the separator (PG2) indicates 24 psi, the mass spectrometer gas-sampling line is connected to the rig to measure the separator off-gas composition. During phase I, the mass spectrometer supplies compressed gas through the sampling line from the separator and reports the composition of the discharge gas from the rig. Concurrent analyses of atmospheric air intake are also performed. The sampling stream is passed through a desiccant tube containing a calcium chloride and calcium sulfate mixture to absorb water vapor from the off-gas stream, and the gas is then supplied to the mass spectrometer at a rate of ~60 mL/min. A mass spectrometer is used to record the CO₂ composition of the discharge gas every 25 s. Phase I requires 1–2 min to complete.

According to the Young *et al.* (2022) bubbly flow model prediction and Figure 5-15, the required pressure to dissolve (90%) of the CO₂ admitted to the circulating fluid is 18.2 psi(g) for mineral carbonation purposes. The operating pressure of the HIL is set to 24 psi to ensure complete dissolution of the admitted CO₂. If this occurs experimentally, the CO₂ concentrations in the off-gas composition readings should decrease to zero.

7.1.5 Phase II Steady state operation without CO₂ being inducted.

In phase II, the rig is operated for another 5-7 min to reach a steady state before CO₂ is added to the inlet air. A steady operating state condition is assumed when the HIL delivery pressure,

circulating fluid temperature, and off-gas composition readings of the mass spectrometer do not vary over time. During this phase, the injector inducts atmospheric air into the system, and the mass spectrometer reports the CO₂ concentration in the discharge gas in real-time.

7.1.6 Phase III Admission of the air/CO₂ mixture

Once the system reaches steady-state conditions, CO₂ is added to the inlet gas, which constitutes the start of Phase III of the experiment.

The experiment uses a gas feed stream with 15% (by volume) CO₂ to simulate expected CO₂ concentrations in the combustion of off-gases/exhausts. The gas feed composition of the air/CO₂ mixture is achieved by maintaining the air and CO₂ mass flow rates at 2.7 L/min and 0.40 L/min, respectively.

The pH of the solution/suspension is continuously measured and recorded every 10 s throughout the experiment.

According to the mineral carbonation chemistry described in Section 3.1, when the pH is greater than 10, the predominant carbon-containing species are carbonate ions (CO₃²⁻). The reaction between Ca²⁺ ions and dissolved CO₂ leads to the precipitation of CaCO₃, which is practically insoluble in water with pH > 9. If the experiment is started with a saturated solution (i.e., no suspended Ca(OH)₂), the pH value will decrease gradually as the pH is lowered during the formation of CaCO₃. The increased H⁺ ion content triggers the re-dissolution of suspended CaCO₃, releasing calcium ions into the solution.

The nucleation stage of calcium carbonate formation in the system (formation of nuclei or critical clusters) occurs at pH over 12.5, followed by precipitation and crystal growth until pH 10

(Montes-Hernandez *et al.*, 2009). During the experiment, when the pH of the solution reaches 10, the pump is turned off, and the valve (V-A-1) of the gas intake line is closed, marking the end of phase III of the rig operation.

7.1.7 Recovery of precipitate

To separate the precipitated calcium carbonate, the sampling line of the mass spectrometer is disconnected, and an air bypass valve (V-A-2) is opened to depressurize the rig. Subsequently, a 5-micron filter is connected to the rig in parallel to a so-called ‘filtration loop’.

The filtration loop is illustrated in Figure 7-1. During filtration, the valve (V-1) is closed so that the pump circulates the solution/suspension through the filtration loop. The model of the filter used is Waterra 5 Micron groundwater. This filter has 600 cm² of polyethersulfone 5-micron filter media.



Figure 7-1: 5-micron filter showing a white slurry at input and a clear fluid at outlet

Figure 7-1 shows the 5C-S solution flow before and after filtration. The solution was milky prior to filtering. After filtering, the solution became clear and colorless.

The precipitate recovered from the filtration system was dried, and its total mass was measured. A sample was collected and sent for X-ray diffraction analysis to confirm the composition of the solid.

7.2 Experimental results

The chemistry and kinetics of the expected carbonation process are described in Chapter 3. The conditions of the experimental trials and variations in the experimental procedure are summarized in Table 7.1. The initial Ca(OH)_2 concentrations of the solutions used in experiments E4 and E6 were subject to uncertainty. The rig was not completely empty of DI water prior to the experiment. It is believed that there was already some D.I. water in the pump manifold when the rig was filled with the 2.2 C-S and 2.9 C-S solutions in experimental trials E4 and E6, respectively. The presence of D.I. water changed the initial Ca(OH)_2 concentration in the solution.

During experiments E4, E5, E6, and E8, the pressure at the inlet of injector PG1 was set to 50 psi. In experiments E1, E2, E3, and E7, PG1 showed 52 psi.

In all the experiments except E1 and E6, the average pressure at the top of the separator measured using PG2 was 24 psi. In experiments E1 and E6, the average pressure of PG2 was slightly lower (23 psi).

Table 7-1: Details of experimental conditions and principal results

Experiment	E1	E2	E3	E4	E5	E6	E7	E8
Date	27 June	1 July	29 June	29 June	1 July	28 July	27 July	1 July
CO ₂ absorption solution	D.I. W ¹	1 C-F ²	1.7 C-S ³	2.2 C-S	2.2 C-S	2.9 C-S	5 C-S	5 C-S
Solution state	-	S ⁴	S-S ⁵	S-S	S-S	S-S	S-S	S-S
Mass of the Ca(OH) ₂ added to solution (g)	0	5.34	9.09	11.76	11.76	15.68	26.72	26.72
Total mass of water in the rig (kg)	3.54	3.54	3.54	3.54	3.54	3.51	3.54	3.54
Initial pH of the solution	6	12.24	12.29	12.15	12.22	12.28	12.26	12:35
pH of the solution at the start of adding CO ₂	7.15	12.25	12.31	12.22	12.26	12.28	12.26	12.35
Final pH of the solution	4.96	10.01	10.04	10.15	10.08	9.97	10.05	9.95
Duration of experiment (mm:ss)	19:30	09:10	12:10	14:10	15:40	19:50	18:30	24:40
Time of adding CO ₂ to inlet air (mm:ss)	07:30	05:00	05:40	10:00	11:40	11:00	11:40	20:10
Average [CO ₂] added into inlet air (mol%)	16.56	15.48	15.06	14.12	15.46	14.61	15.02	16.17
Average input gas mass flow rate (L/min)	2.60	2.53	2.79	2.92	2.55	2.74	2.52	2.47
Average water volume flow rate (L/min)	28.36	28.17	28.48	26.33	24.12	25.56	28.36	26.10
Average circulating water temperature (°C)	23.6	22.05	22.0	21.8	22.2	22.8	24.59	21.3
Average pressure of GP1 (psi)	52	52	52	50	50	50	52	50
Average pressure of GP2 (psi)	23	24	24	24	24	23	24	24

¹ Deionized water² Ca(OH)₂ saturated solution³ Ca(OH)₂ suspension solution (Supersaturated solution)⁴ Saturated⁵ Suspension solution

The average temperature (°C) of circulating water in all experiments except experiments E1 and E7 was 22 °C. In experiments E1 and E7, the circulating water temperatures were slightly higher at 23.6°C and 24.6°C respectively.

7.2.1 CO₂ dissolution in deionized water

In experiment E1, the rig is filled with D.I. D.I is a form of pure, clean water purified by removing atoms, ions, and molecules from tap water through an ion exchange process. Deionization removes dissolved particles such as salt (sodium chloride), minerals, carbon dioxide, organic contaminants, and other impurities from water. In theory, the lack of ions means that D.I water should have a pH of 7. However, when D.I water comes into contact with atmospheric carbon dioxide (during handling and transfer), its absorption of the gas produces weak carbonic acid, which can reduce the pH of the water to 5.5. Therefore, the pH of D.I. water is typically below 7.

Some pH meters cannot measure the pH of D.I. water because ions are required to provide accurate readings. The initial pH of the D.I. water before carbon dioxide has an effect is 7. To maintain a pH of 7, it is necessary to either prevent the D.I. water from being exposed to air or boil the water to remove carbon dioxide (Riche *et al.*, 2006).

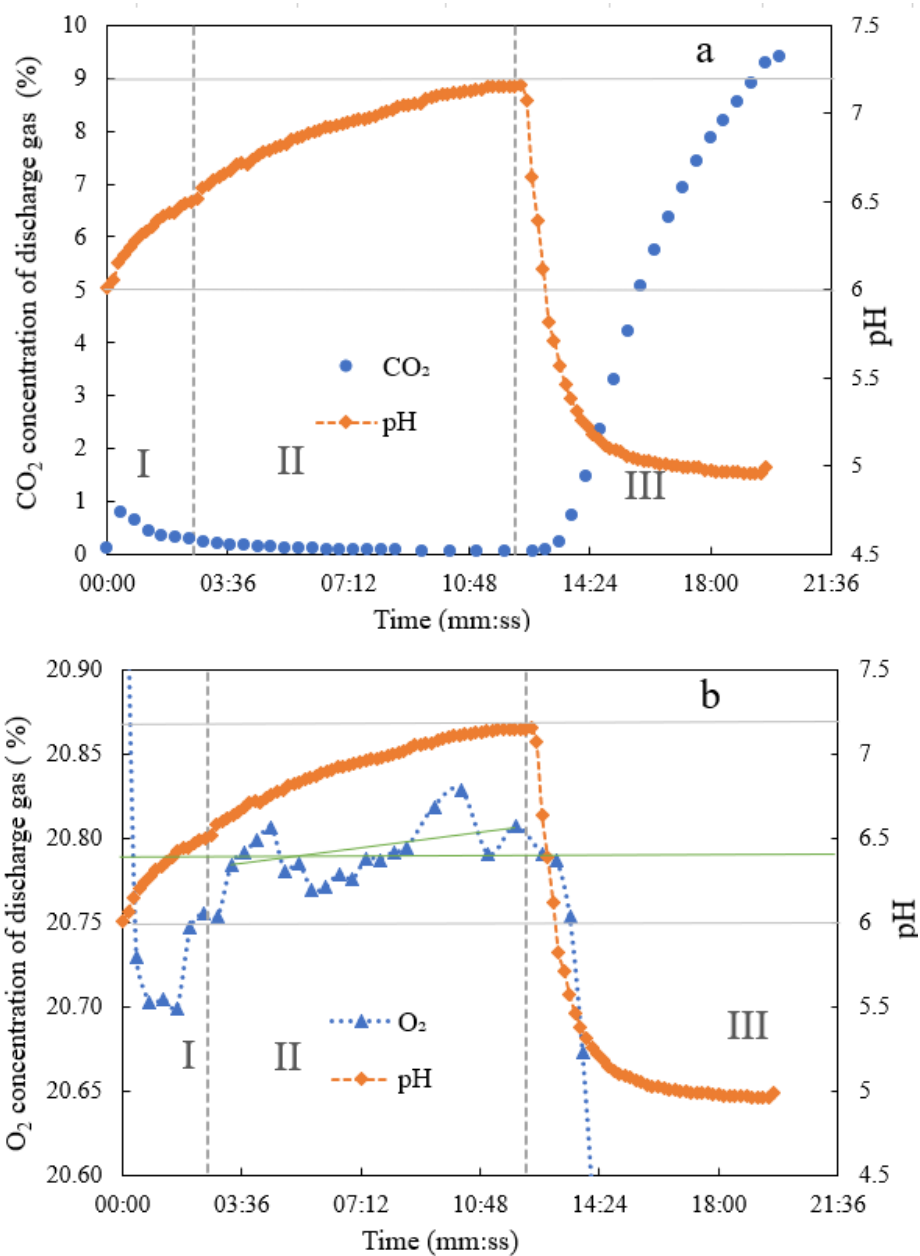


Figure 7-2: Variations of discharge CO₂ and O₂ concentrations and pH of the D.I. water throughout phases I to III of the experimental of the experimental trial according to the time

In this experiment, the initial pH of the D.I. water was 6. During phases I and II, the pH increased and finally reached a constant value after approximately 11:30 min. Lab atmospheric air

was inducted into the water during this time using an injector. The D.I. water was depleted in dissolved O₂, and injecting air into the water increased the dissolved O₂ of the solution and increased its pH. As the O₂ (aq) gradually increased, lesser amounts of O₂ dissolved in the water until the [O₂ (aq)] tended toward an asymptotic value that mirrored the increase in pH.

The D.I. water with dissolved O₂ (DO) would be a fairly aggressive fluid toward metals. Carbon steel was present in the pump casing, and copper was in the separator. DO could readily react with these to create metal oxides, which would rapidly hydrate to produce metal hydroxides. Thus, an increased prevalence of OH⁻ would consume protons to cause the pH to increase.

As shown in Figure 7-2, CO₂ is added to the inlet air during phase III. This is now in much higher partial pressure, and its 10x higher solubility in water means that CO₂ dissolution chemistry in water dominates over the chemistry of O₂ dissolution in water. As CO₂ is dissolved in water, reactions (3.5) - (3-8) proceed, and the pH of the solution decreases until CO₂ saturation. The final pH of the CO₂-saturated D.I. water is 4.99.

7.2.2 CO₂ dissolution in Ca(OH)₂ saturated solution

The Ca(OH)₂ saturated solution, 1C-F, was prepared by mixing 5.34 g of Ca(OH)₂ powder in 3540 g of D.I. water at 22° C. The 1C-F solution was filtered by a 5-micron filter, and it had no undissolved particles. The initial pH of the solution was 12.25. However, the pH of the standard saturated Ca(OH)₂ solution was 12.34 at 22° C (Bates *et al.*, 1956; Lito *et al.*, 1998b). The experiment required 9.16 min, and CO₂ was added to the inlet air at 3:30 (mm:ss) onward.

As listed in Table 7-1, the average percentage of CO₂ (g) concentration added to inlet air was 15.48 %. The average gas mass flow rates of the inlet air and the CO₂ added to the inlet were 2.53 and 0.39 L/min. The water volume flow rate was 28.17 L/min.

Figure 7-3 shows the change in the CO₂ concentration of the discharge gas and the pH of the solution with respect to the time of the experiment. At the start of the addition of CO₂ to the inlet gas, the pH of the solution was 12.25, and mass spectrometry revealed that the concentration of CO₂ in the discharge gas was near zero.

When the pH was greater than 10 ($10 < \text{pH} < \text{initial}$), reaction (3.19) did not proceed because the C-F solution was prepared by filtering the Ca(OH)₂ suspension solution and did not contain any undissolved particles. In this pH range, reactions (3.7)–(3.9) and (3.21) proceed in the reactor, and the carbonate (CO₃²⁻) ions, which are the dominant carbonate species (according to the distribution of dissolved carbonate species based on the pH value (Figure 3-2), react with calcium ions and CaCO₃ precipitates based on reaction (3.31).

The pH began to decrease after adding CO₂ to the inlet gas. Simultaneously, the mass spectrometer showed increased CO₂ concentration in the discharge gas. When the pH reached 10.01, the mass detected more CO₂ in the discharged gas (~0.01%, still orders of magnitude below the concentrations provided at the input to the system.

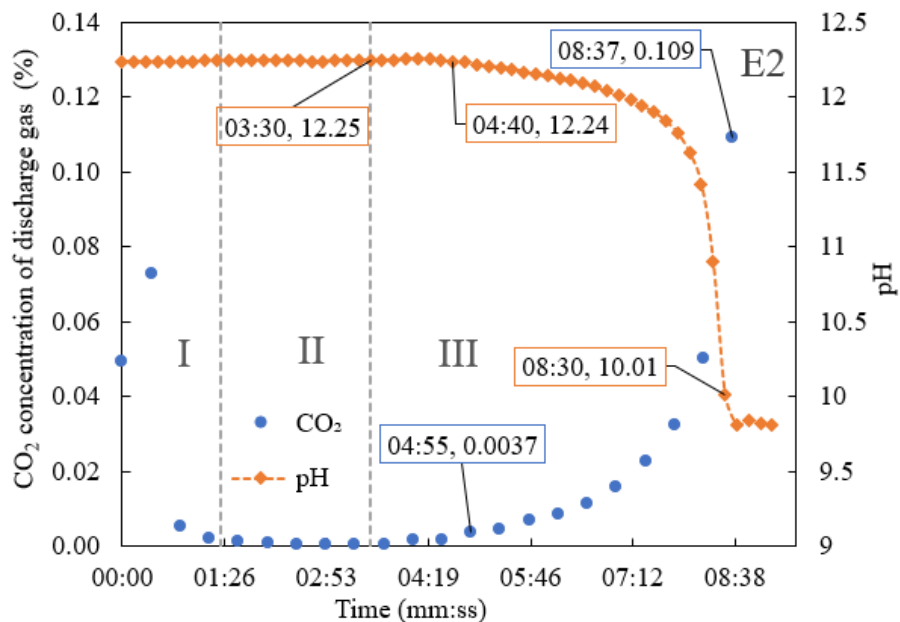


Figure 7-3: Variation of discharge CO₂ concentration and pH of the saturated solution according to the time of the experiment E2

7.2.3 CO₂ dissolution in Ca(OH)₂ suspension solution

- 1.7C-S solution

This solution comprised 5.34 g of dissolved Ca(OH)₂ coexisting with 3.74 g of undissolved Ca(OH)₂. The initial pH of the solution was 12.31. Because the pH was measured solely from ions dissolved in the liquid state, the initial pH in the suspension solution (1.7C-S) should theoretically be the same as that in the saturated solution (1C-F). In practice, the pH varied from the prior values by a small amount.

As listed in Table 7-1, the average percentage of CO₂ (g) concentration added to inlet air was 15.06 %. The average gas mass flow rates of the inlet air and the CO₂ added to the inlet were 2.79 and 0.39 L/min. The water volume flow rate was 28.48 L/min.

Figure 7-4 shows the variations in the CO₂ concentration and pH as the duration of the experiment increased. The behavior of this solution was similar to that of 1C-F. The duration of the experiment was 12.00 min. CO₂ was added to the mixing air at 04:40.

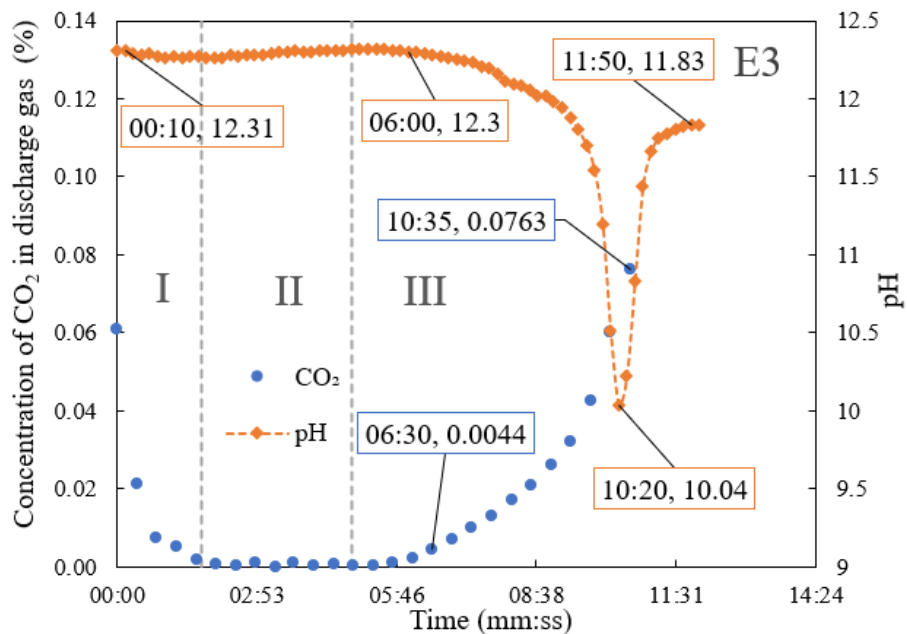


Figure 7-4: Variation of discharge CO₂ concentration and pH of the suspension solution (1.7C-S) according to the time of the experiment E3

The pH started to drop to 10.20 after mixing CO₂ with the inlet gas. Simultaneously, the mass spectrometer showed increased CO₂ concentration in the discharge gas. However, the pH did not reach a constant value, and after entering a trough, it increased and appeared to plateau at pH=11.83 at the end of the record. Possibly, the duration of the experiment was insufficient to produce a complete and consistent decrease in pH to < 10.

- 2.2C-S, 2.9C-S and 5C-S solutions

The 2.2C-S solution consisted of 5.34 g of dissolved Ca(OH)_2 coexisting with 6.41 g and undissolved Ca(OH)_2 in 3.54 kg of D.I. water. Two experiments (E4 and E5) were conducted using this solution. However, the Ca(OH)_2 concentration in the solution used in experiment E4 was unclear.

As shown in Table 7-1, , the average percentage of CO_2 (g) concentration added to inlet air in experiment E4 was 14.12 %. In this experiment, the average gas mass flow rates of the inlet air and CO_2 were 2.92 and 0.38 L/min. The water volume flow rates in experiments E4 and E5 were 26.33 and 24.12 L/min, respectively. Although the water volume flow rate in experiment E4 was greater than that in experiment E5, the percentage of CO_2 (g) concentration added to the inlet air in experiment E5 was higher than that in experiment E4. In this experiment, the average gas mass flow rates of the inlet air and inlet CO_2 were 2.55 and 0.40 L/min respectively.

Figure 7-5 shows the change in the CO_2 concentration of the discharge gas and the pH of the solution with respect to the experimental time. The lengths in experiments E4 and E5 were 14:10 and 15:40, respectively. The reading of the pH meter fluctuated during phase I of experiment E5. The initial pH of the solutions used in the experiment was 11.91. The length of phase III of experiment E5 was 1.67 min longer than that of experiment E4.

Both experiments showed similar behaviors. CO_2 was added to the gas mixture at 3:40 and 3:30 in experiments E4 and E5, respectively. The gas mass spectrometer showed changes in the CO_2 concentration of the discharge gas at 5:40 and 6:09 in experiments E4 and E5, respectively. At E4, pH decreased from 12.21 at 3:40 to 10.41 at 10:50, then increased to 11.95 at 11:30 and after a small peak, and finally decreased again to 10.15 at 13:40.

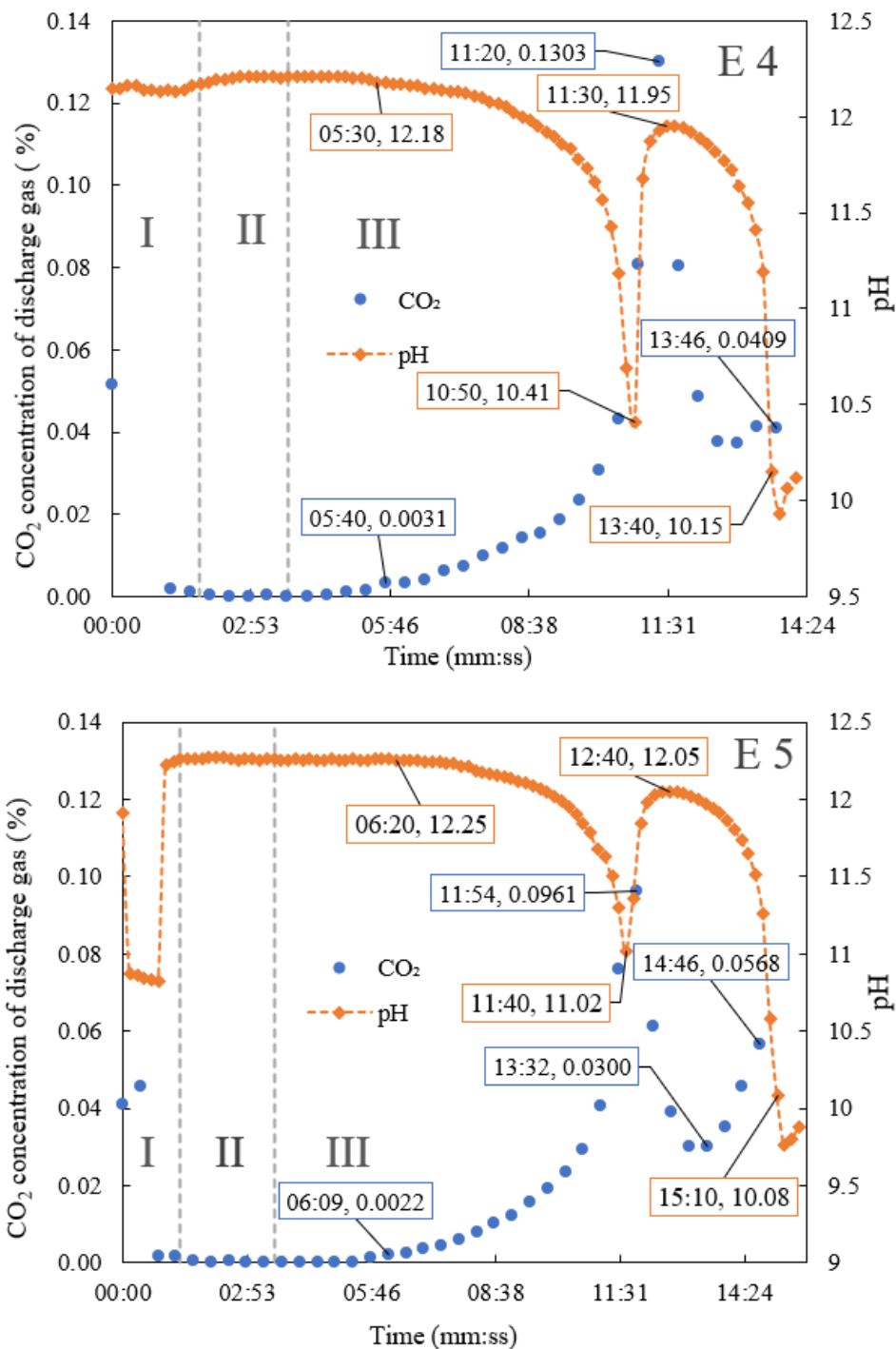


Figure 7-5: Variation of discharge CO₂ concentration and pH of the 2.2C-S suspension solutions according to the time of the experiment

A concentration 'rebound' is also observed in the CO₂ concentration of discharge gas during this time. The trends of the CO₂ concentration of the discharge gas and the pH of experiment E5 are similar to those of experiment E4. It is suggested that the reason for this phenomenon is a non-continuous dissolution of 'clumps' of undissolved Ca(OH)₂ existing within the HIL. It is further suggested that when the pH decreases to 10.41 in experiment E4, a 'clump' of solid Ca(OH)₂ suspended in the solution but somehow obstructed from dissolution starts to dissolve, causing the pH to increase again, and the off-gas CO₂ concentration decrease as the CO₂ reacts with CaCO₃(s). This behavior is evident in all experimental trials with suspension solutions, with the possible exception of E7, possible because E7 may have been halted prematurely. However, it is asserted that when a circulating solution of Ca(OH)₂ entrains and suspends excess solid Ca(OH)₂ particles, they may accumulate somewhere in the horizontal injection loop before ultimately becoming dissolved with a more prolonged operation. An alternative explanation is that some manner of Ca(OH)₂ dissolution activation or threshold exists that is not represented in the chemical conceptual framework. Either way, a more robust investigation of this pH 'dip' behaviour was determined to be a subject for further investigation, beyond the scope of this thesis.

The 2.9C-S solution consisted of 5.34 g of dissolved Ca(OH)₂ coexisting with 10.36 g of undissolved Ca(OH)₂ in 3.51 kg of D.I. water. However, the Ca(OH)₂ concentration in the solution used in experiment E6 was unclear.

The mass of water in the rig in experiment E6 was 5.41 kg. The average gas mass flow rates of the inlet air and the CO₂ added to the inlet air were 2.74 and 0.4 L/min. The water mass flow rate was also 25.56 L/min.

As shown in Figure 7-6, the length of phase II in this experiment was longer than that in the other experiments. However, phase III started when the $[\text{CO}_2]$ and pH values were similar to those in other experimental trials at the beginning of phase III. The length of phase III in experiment E6, which was 11 min, was shorter than that in experiment E5. However, the $\text{Ca}(\text{OH})_2$ concentration in the solution in experiment E6 was greater than that in experiment E5. It was this concluded that, the remnant D.I. water in the rig significantly changed the $\text{Ca}(\text{OH})_2$ concentration in the solution.

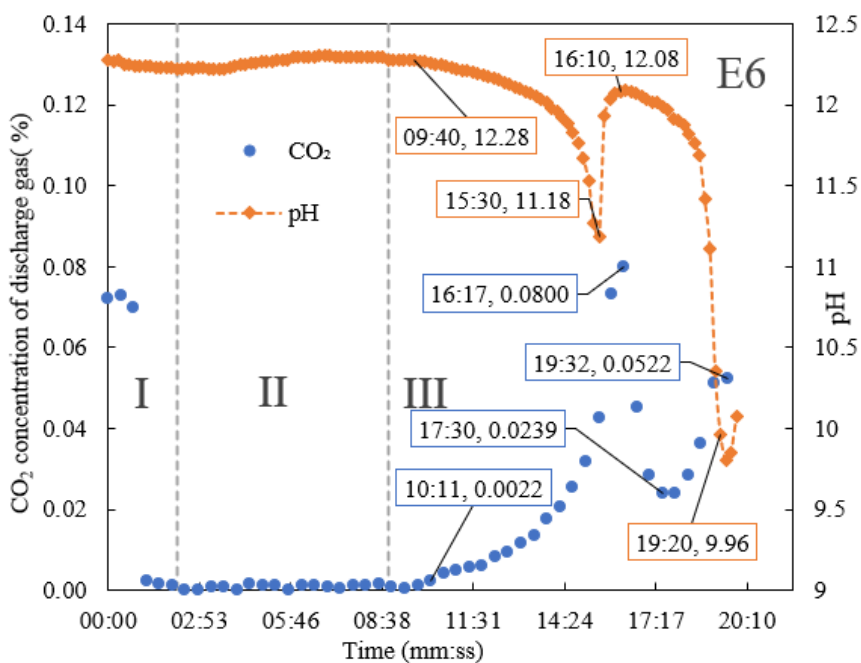


Figure 7-6: Variation of discharge CO_2 concentration and pH of the 2.9C-S suspension solutions according to the time of the experiment E6

The 5C-S solution consisted of 5.34 g dissolved $\text{Ca}(\text{OH})_2$, which was suspended in 21.38 g undissolved $\text{Ca}(\text{OH})_2$ in 3.54 kg of D.I. water. As shown in Table 7-1, the average pressure of PG1, water temperature, and the water flow rate in experiment E7 were higher than those in experiment E8.

Figure 7-7 shows the time evolution of $[\text{CO}_2]$ in the separator discharge gas and pH of the solution in experiments E7 and E8. Experiment E7 might have been curtailed prematurely due to a fall of $[\text{CO}_2]$ due to ‘clumping,’ which is the reason why the experimental run was repeated in E8 a few days later.

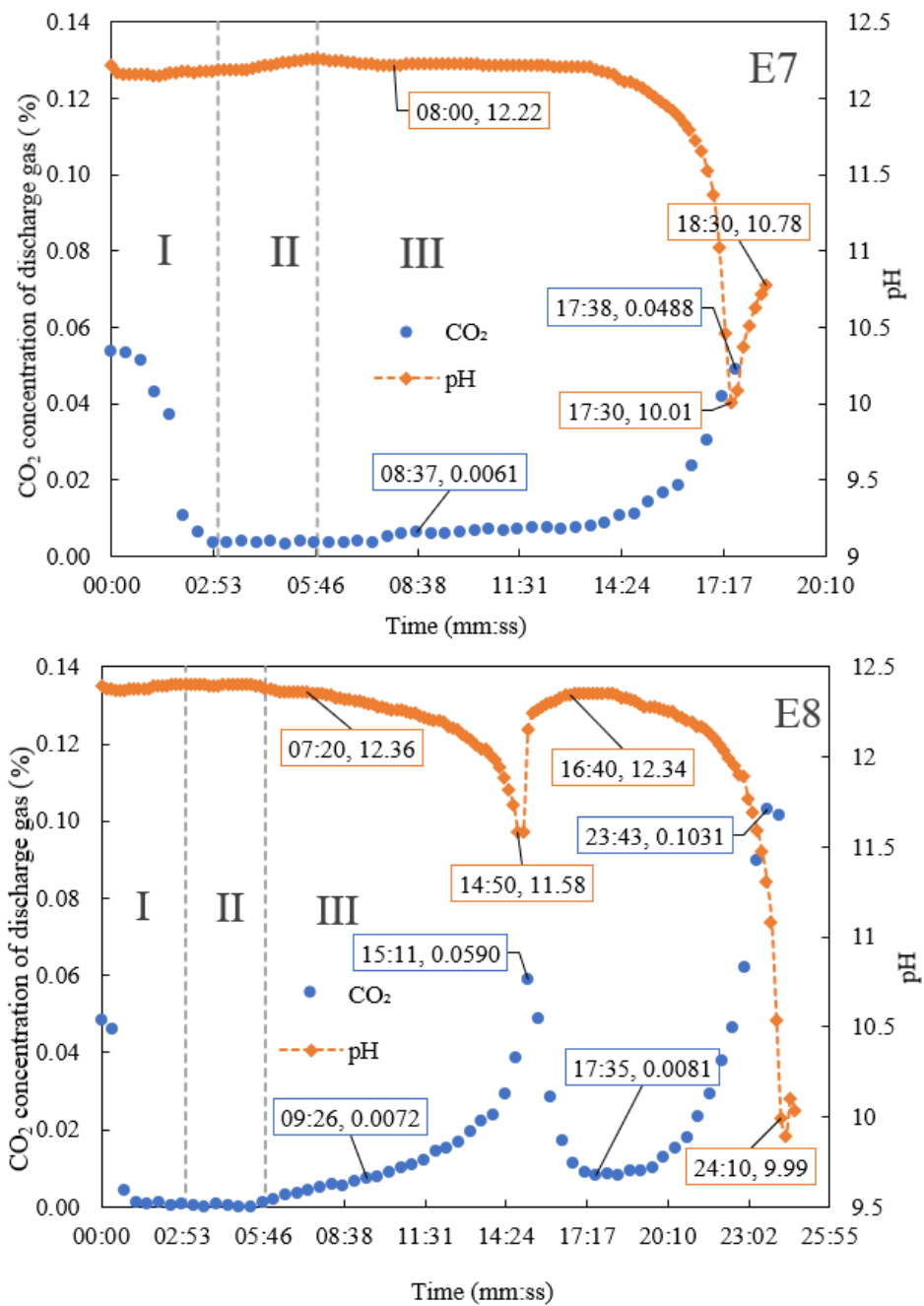


Figure 7-7: Variation of discharge CO₂ concentration and pH of the 5C-S suspension solutions according to the time of the experiment

7.2.4 Summary of results from experimental trials

The key observations identified from various experimental trials are presented in Table 7-2.

Table 7-2: The value of CO₂ consumed in each experiment

Experiment	E2	E3	E4	E5	E6	E7	E8
CO ₂ absorption solution	1C-F	1.7C-S	2.2C-S	2.2C-S	2.9C-S	5C-S	5C-S
Solution state	S ¹	S-S ²	S-S	S-S	S-S	S-S	S-S
Duration from first time adding CO ₂ to pH=10 (minutes)	5	5.67	10	11.66	11	11.67	20.16
Mass of consumed CO ₂ (g)	3.77	4.37	7.53	8.75	8.84	9.16	15.99
Mass of the Ca(OH) ₂ in the solution (g)	5.34	9.09	11.76	11.76	15.68	26.72	26.72
Average [CO ₂] added into inlet air (%)	15.48	15.06	14.12	15.46	14.61	15.02	16.17

7.2.5 Mass of suspension solids at the conclusion of each experimental run.

Various filtration methods were tested on the solution. Connecting Waterra 5 micron groundwater filters to the HIL within a filtration loop effectively separated suspension solids from the circulating fluid. These filters were also used in experiments E5 and E8. The solids then had to be removed from the filters. However, it was evident that the solid mass remaining on the filters could not be recovered for the assay (denoted as F in Table 7-3). The filtrate was collected was dried in an oven at approximately 60° C overnight, and the mass of dried filtrate was measured.

At the end of experimental trials E2 and E4, the 1C-F and 2.2C-S suspensions were decanted from the HIL and dried in an oven. The masses of the recovered dried suspension solids were 3.572 g and 10.631 g for experimental trials E2 and E4, respectively. In these trials, it was established that solids remaining in the HIL could not be recovered for the assay. Samples of the solutions

¹ Saturated

² Suspension

were collected at the end of experiments E3 and E6. The masses of dried solids in these samples are presented in Table 7-3.

Thus, for every experimental run, it proved challenging to recover all suspension solids, irrespective of the filtration method trialled. Table 7-3 shows the suspension solids collected from the HIL at the conclusion of each experimental trail.

Table 7-3: Concentrations of Ca²⁺ and mass of recovered solid CaCO₃

Experiment	E2	E3	E4	E5	E6	E7	E8
CO ₂ absorption solution	1C-F	1.7C-S	2.2C-S	2.2C-S	2.9C-S	5C-S	5C-S
Initial concentration of Ca(OH) ₂ (g)	5.35	9.09	11.76	11.76	15.56	26.72	26.72
pH of the solution at the end of phase III	10.01	10.04	10.15	10.08	9.96	10.01	9.95
Measured pH, before filtering solution	9.81	11.83	10.12	9.88	9.85	10.78	9.99
Mass of recovered solid (g)	3.57	1.31	10.63	6.38+F ¹	1.25	-	18.39+F

The expectation of the experiment was that the recovered solids were principally CaCO₃ (s), and all suspended Ca(OH)₂ dissolved and reacted with CO₂ (aq) during the experimental trials. However, it was deemed possible that some solid Ca(OH)₂ could have remained. Consequently, samples of the dried suspended solids in the HIL were subjected to XRD analysis to confirm the presence or absence of the reactant and expected product species.

7.2.6 XRD analysis of products

X-ray diffraction (XRD) is one of the most powerful tools to identify the crystal structure and mineral phases in geological samples. This method has also been proven effective in the

¹ Unknown mass of unrecovered CaCO₃

quantification of mineralogical data. Quantification is based on the fact that the peak intensities of an individual mineral are proportional to the latter's content in the sample. Measurement of peak intensities should, therefore, provide information regarding the relative amount of the corresponding mineral phase (Al-Jaroudi *et al.*, 2007).

While it was reasonably certain that the CO₂ was being absorbed by the solution/suspension by reacting with the Ca(OH)₂ and precipitating as CaCO₃, the suspended particles of Ca(OH)₂ and the CaCO₃ in the circulating liquid were both white, fine, crystalline solids that were indistinguishable visually. XRD of the dried filtrate from the rig was thus used to confirm that the filtrate obtained was in fact CaCO₃ and to see if any Ca(OH)₂ could be detected in the product. Quantification analysis of the filtrate by such methods was not part of this work. The XRD analysis were qualitative only and aimed to identify CaCO₃ and Ca(OH)₂ in the filtrate samples of experiments E2, E5, E8, and also of the Ca(OH)₂ reactant powder.

After drying, the filtrate powder sample is back-packed into an aluminum sample holder and analyzed using the XRD-100 instrument at the Geoscience Laboratories, situated in the Willett Green Miller Centre on the campus of Laurentian University. Scans are run from diffraction angles from 20° to 80° 2θ at a scanning speed of 0.01 °/s. The resulting spectra are presented in Figure 7-8 and Figure 7-9.

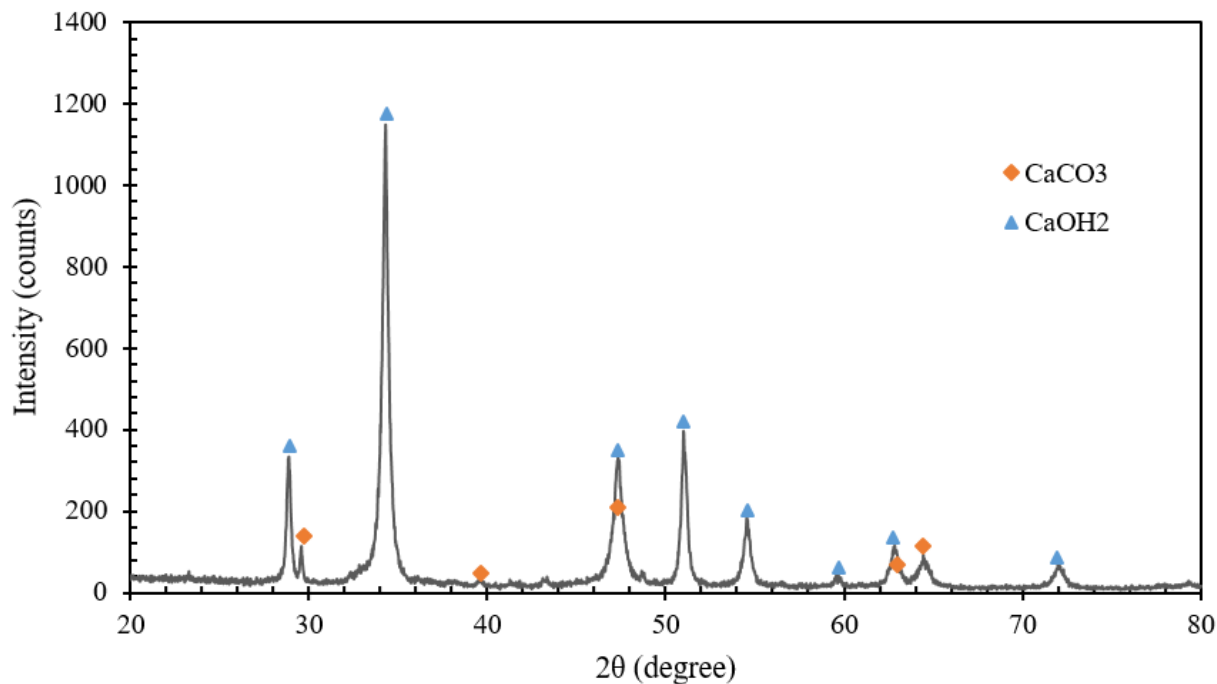


Figure 7-8: XRD patterns of Ca(OH)₂ powder

Figure 7-8 shows the XRD spectrum of the Ca(OH)₂ powder reactant used, which claimed 99.5% purity. Sensor intensity peaks at angles that are characteristic of both CaCO₃ and Ca(OH)₂ are denoted with orange diamonds and blue triangles, respectively. In this spectrum, there are 2 minor intensity peaks at $2\theta = 29.5^\circ$ and $2\theta = 64.5^\circ$ which might be expected in CaCO₃ whereas they are not expected in Ca(OH)₂. High intensity peaks at $2\theta = 29.0^\circ$, $2\theta = 34.0^\circ$, $2\theta = 51.0^\circ$, $2\theta = 54.5^\circ$ and $2\theta = 72.0^\circ$ are characteristic of Ca(OH)₂. The XRD spectrum of Figure 5-16 thus suggests a sample of Ca(OH)₂ with trace amounts of CaCO₃.

Figure 7-9 illustrates the XRD patterns of filtrate samples from experiments E2, E5, and E8. The peaks identified in these spectra are all characteristic of CaCO₃ and there are no intensity peaks present at any value of 2θ that are consistent with Ca(OH)₂ presence in the sample. Expert testimony from the technician who customarily operates the instrument suggests that the CaCO₃

present in the sample from experimental run E2 is very highly crystallized CaCO_3 , whereas the filtrates from experimental runs E5 and E8 are less well crystallized.

In the spectra from experimental runs E2, E5 and E8, it is possible that Ca(OH)_2 particles have acted as seeding points for crystallization/precipitation of CaCO_3 on their surfaces; Ca(OH)_2 could remain in the filtrate but be shielded from x-rays by a CaCO_3 coating. Were this to be the case, it would still be expected that among the billions of particles present in the specimens, patches of Ca(OH)_2 would be exposed to leave lower intensity yet visible intensity peaks in the spectrum at values of 2θ corresponding to those expected for Ca(OH)_2 . As there were none of these at all evident in Figure 7-9, it seems unlikely there is any Ca(OH)_2 remaining at all in the filtrate samples.

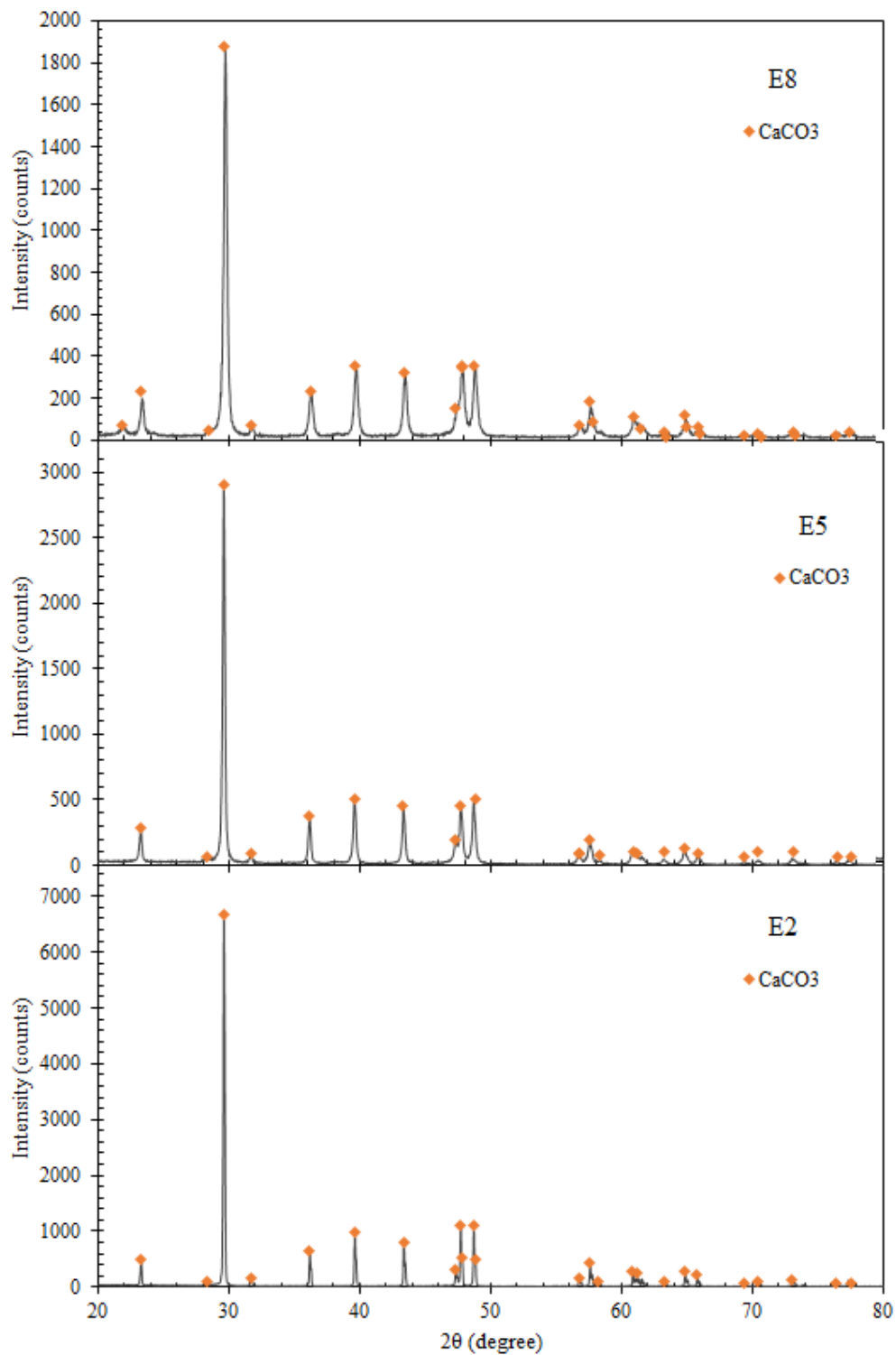


Figure 7-9: XRD patterns of CaCO_3 produced in the experiments E2, E5, and E8

7.3 Discussion

7.3.1 Did the reactor operate as intended?

According to the results of experiments presented in this chapter:

- During phase III of each experimental run, when $[\text{CO}_2 (\text{g})] \sim 15\%$ was admitted at the inlet, $[\text{CO}_2 (\text{g})]$ in discharge gas was lower than 0.01% of the inlet gas. This implies that 99.99% of the CO_2 that is added to the inlet air dissolves in the $\text{Ca}(\text{OH})_2$ solution/suspension solution under these conditions. This is expected behavior if the HIL operated as intended.
- With one exception, collectively, the results of the experimental runs show that the amount of CO_2 absorbed in each experiment increases proportionately with the total $\text{Ca}(\text{OH})_2$ in solution and suspended – as would be expected if the HIL operated as intended.
- With one exception, collectively, the results of the experimental runs show that the duration from the start of phase III to the time the pH of the solution was measured to be 10 increases proportionately with the total $\text{Ca}(\text{OH})_2$ in solution and suspended – as would be expected if the HIL operated as intended.
- A saturated solution was used during experimental E2. Without suspended $\text{Ca}(\text{OH})_2$ in the HIL, the amount of CO_2 absorbed would be lower than in other experimental runs, if the HIL operated as intended.
- At the end of phase III of the experimental run, when the admission of CO_2 ceased and the circulation pump was deactivated, XRD analysis of samples of the solid particles suspended in the formerly circulating liquid was found to be exclusively CaCO_3 , not $\text{Ca}(\text{OH})_2$. This was the expectation if the HIL operated as intended.

- Although samples from only 3 experimental runs and the reactant Ca(OH)_2 material were sent for XRD analysis, the XRD results lead to a confident presumption that in every experimental run, the suspended solid material in the HIL at the end of the experimental run was CaCO_3 only. This being the case, for experimental run E4, the mass of CaCO_3 recovered was 10.63g while the mass of CaCO_3 expected to be produced, based on the overall reaction stoichiometry was 15.87g. This suggests that for one experimental run at least, the yield of $\text{CaCO}_3(\text{s})$ was at least 67%. The actual yield for E4 will be higher than this when it is recalled that the remnant solid was visible in the HIL after the circulating solution had been decanted.

Taking the above listed evidence into account, the overall assertion is that the experimental runs confirm the successful performance of the HIL as a CO_2 capture and sequestration device. Proof of concept has been generated.

7.3.2 Problems evident in the results of the experimental runs.

During the conducted experiments, experimental control is applied to ensure that all process and environmental parameters are held constant, at steady state, as far as practicable. However, some unwanted variations of experimental variables affect the results of the experiments.

The consumed CO_2 in experiment E6 is lower than in experiment E5, and this is thought to be a result of the factor that before the E5 experimental run, the HIL may not have been completely emptied of D.I. water. If there was some D.I. water in the pump manifold when the rig was filled

up with the 2.9C-S solution, the D.I. water would change the Ca(OH)_2 concentration of the solution, and the calculation of the amount of CO_2 absorbed would be in error.

The 2.2C-F solution is used in experimental runs E4 and E5. Although the percentage of CO_2 added into the inlet air of experiment E5 is more than experiment E4, the length of phase III of experimental run E5 is longer than that of experimental run E4. The amount of CO_2 absorbed in experiment E5 is more than in experiment E4. Taken together, these results confirm that there is a lower amount of Ca(OH)_2 in the solution of experiment E4 in comparison with that of experiment E5.

As experiments E3 and E7 may have been stopped early, the results of these experiments may not be completely consistent with those of other experimental runs.

The trends of CO_2 concentration of discharge gas and pH of the experiments E4, E5, E6, and E8 are similar. The 'rebound' values of CO_2 (g) concentration and pH are consistently observed in the results of those experimental runs which at least indicates reliable instrumentation. It is thought that when a circulating solution of Ca(OH)_2 entrains and suspends excess solid Ca(OH)_2 particles, these may be able to accumulate somewhere in the HIL before ultimately becoming dissolved with more prolonged operation.

The pressure relief valve was always set to open at 24 psi to reliably regulate the separator delivery pressure. The intent was to maintain the pressure drop across the injector constant during all of the experimental runs, the pressure at the inlet of the injector measured by the PG1 gauge was 52 psi during experiments E1, E2, E3, and E7, meaning that for those runs, the pressure drop across the injector was slightly higher than for other experimental runs. The pressure drop across the injector during experiments E4, E5, and E8 was 26 psi.

The temperature of the circulating solution into the rig is another important variable of the experiment. A cooling coil in the separator regulates the circulating liquid temperature. The temperature of the solution was maintained approximately constant at 22°C during all of the experiments, with one exception: the average temperature of experiment E7 solution was slightly higher at 24.59°C.

It is now thought plausible that D.I. water could have remained present in the pump involute may lead to some variance between calculated and actual starting concentrations of Ca(OH)_2 in the HIL for experimental runs E4 and E6.

At the stage of writing, it is known that the experimental procedures would be much improved with i) better suspended solids filtration, ii) more consistent HIL washing and DI water flush at the conclusion after each experimental run, and iii) better methods of preparation of the suspension solutions used. However, as the experiments reported simply aimed to generate proof of concept that the HIL reactor ‘worked’ as designed, and such proof has been generated, the various experimental methodological improvements identified have been devolved to the realm of further work.

7.4 Summary

In this chapter the use of a HIL as a CO_2 capture and sequestration device/process was investigated experimentally, and a description of the hydrodynamic design and operation of the HIL was presented in Chapter 6. The results of the Chapter 7 experiments confirmed that the reaction between CO_2 and Ca(OH)_2 to form CaCO_3 could be conducted within the HIL and that the performance of the HIL was consistent with the design expectations. Numerous problems were

encountered during carbonation experiments. HIL systems configured for CO₂ capture and sequestration required much refinement to demonstrate that the process could be effectively scaled up from the lab-scale work reported herein. The use of a rather pure Ca(OH)₂ feedstock to maintain the high pH necessary to sustain sequestration and air with a dosed CO₂ gas stream represents an ideal situation. Practical and theoretical investigations will be necessary to demonstrate that the HIL process can accommodate more complex mineralogical feedstocks containing alkaline earth metal oxides and hydroxides. Moreover, the combustion of flue gas streams that more realistically contain potentially contaminating gas species may be problematic because they will ‘upset’ the basic chemistry being applied.

Consequently, while some proof-of-concept of an effective CO₂ capture and sequestration technique has been generated, the work presented in this Chapter essentially establishes a starting point for an appreciable body of ‘further work’ to deal with more complicated feedstock materials to achieve commercially viable systems. Regardless of the nature of such further work, it will undoubtedly be appreciably assisted by some predictive capability for the performance of HIL as a CO₂ capture and sequestration device that specifically embodies the reaction equilibria and kinetics governing carbonation. Establishing such a predictive capability is the topic of the following Chapter.

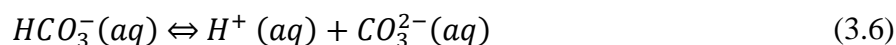
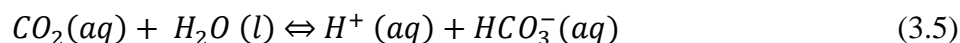
8. Dynamic simulation of mineral carbonation experiments

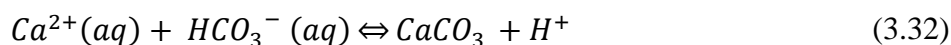
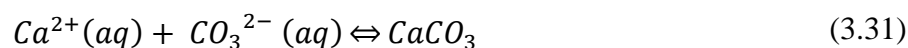
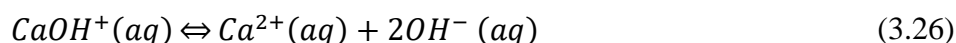
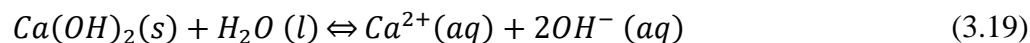
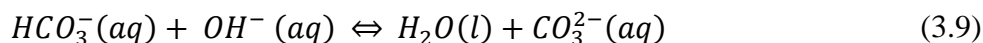
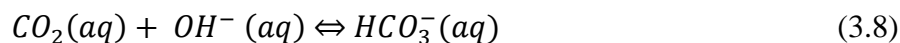
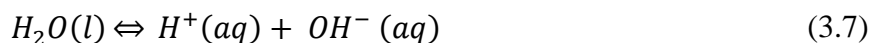
This Chapter reports the results dynamic kinetic modeling of the type introduced in Chapter 3 of the carbonation experiments detailed in Chapter 7 with the HIL, which is designed and proven hydrodynamically in Chapter 6. The objective of this chapter is to show that a sufficient understanding of the process in the HIL has been obtained to predict its performance as a CO₂ capture and sequestration system for design purposes.

8.1 Dynamic kinetic model of carbonation experiments

Because the reaction producing CaCO₃ is strongly pH-dependent, understanding the kinetics of the reactions in the HIL reactor is important for successfully operating a HIL reactor to sequester carbon through a mineral carbonation reaction. In addition, the accurate prediction of CO₂ absorption by alkaline solutions is significant for designing and optimizing large-scale CO₂ capture and sequestration devices.

In this chapter, the dynamic kinetic model developed in Chapter 3 is used to predict the concentration time series of all species participating in the precipitation process of the carbonation experiments conducted using the HIL in Chapter 7. For convenience, the relevant reactions described in Chapter 3 are repeated.





The dynamic kinetic model which is the subject of this Chapter constitutes a set of differential equations representing the above chemical system, which are presented as equations (3.59)–(3.60) in Chapter 3, together with the tabulated equilibria and kinetic coefficients presented in Table 3-1. The parameters driving the set of equations are set to represent the experimental trials of Chapter 7, such that the time series of the species concentration and pH predicted by this model can be compared with the experimental time series and the veracity of system (3.1) to (3.32) can be identified.

8.1.1 The conditions of the experiments

In the following sections, the $CaCO_3$ precipitation process during phase III of experiments E2, E4, E5, and E8 is modeled. Experiments E3 and E7 were found to have stopped early, leading to inconsistencies in their results compared to other experiments. The measured consumption of CO_2 in experiment E6 was lower than that in experiment E5, probably because the HIL was not fully emptied of D.I. water before the E5 experimental trial. The presence of rinsing D.I. water in the

pump manifold might have caused a change in the Ca(OH)_2 concentration in the circulating solution. Calculations of CO_2 absorbed were known to be erroneous. Consequently, only the results of the remaining experiments, E2, E4, E5, and E8, were simulated using a kinetic model. Table 8-1 summarizes the key input parameters used to simulate the experiments. In all the experiments, the volume of the alkaline solution in the HIL rig was 3.54 L.

Table 8-1: Summary of input parameters for the simulation of selected experiments

Experiment	E2	E4	E5	E8
CO_2 absorption solution	1C-F	2.2C-S	2.2C-S	5C-S
Mass of Ca(OH)_2 added to solution (g)	5.34	11.76	11.76	26.72
Average CO_2 (g) flow rate added into inlet air (SLPM)	0.39	0.38	0.40	0.40
Average inlet gas mass flow rate (SLPM)	2.79	2.92	2.55	2.47
Average circulating water temperature ($^{\circ}\text{C}$)	22.05	21.8	22.8	21.9

In experiment E2, the rig was filled with saturated Ca(OH)_2 solution. The remaining experimental trials used suspension solutions containing varying amounts of excess solid Ca(OH)_2 suspended in a Ca(OH)_2 solution at saturation.

When the alkaline solution was saturated, no Ca(OH)_2 solid particles were present in the solution. Therefore, the total surface area of the Ca(OH)_2 particles, A_s , was zero. In other cases, the diameter of the Ca(OH)_2 particles was considered as 2.4 μm . When the suspended Ca(OH)_2 solutions were modeled, the value of A_s was calculated using Eq. (3.45) to (3.48). The volume of gas in the gas–liquid mixture was 0.235 L. This value was calculated by using the Young *et al.* (2022) bubbly flow model. According to the volume of the reactor and the mass of the alkaline solution in it, the volume of gas in the empty space above the reaction mixture V_{G2} was estimated as 1.16 L.

8.1.2 Estimating the values of k_La and enhancement factor

Chapter 4 detailed how carbon dioxide is dissolved in water through a gas–liquid mass transfer phenomenon, the experimentally verified in Chapter 5. To calculate the rate of carbon dioxide dissolution in HIL systems, first, calculate an appropriate gas-liquid volumetric mass transfer coefficient (k_La) when no chemical reactions are present, and then consider the value of the enhancement factor E, which accounts for the altered mass transfer behavior when chemical reactions are present. k_La is an indicator of how quickly gas species are diffused and transferred at the gas–liquid interface of a bubbly two phase flow and is a critical parameter in the design of reactors (Cho and Choi, 2019).

The bubble size estimation at the point of initial mixing of the liquid and gas phases in the Young *et al.* (2022) bubbly flow model was based on Akita and Yoshida (1974) and Wilkinson (1994). This procedure produced the initial bubble size and the initial bubble flux. Thereafter, the bubble flux remained constant. Both models were empirical in nature, and the nature of the flow in the HIL preferred the Wilkinson (1994) model. When the HIL was simulated, the initial bubble size was found to be of the same order as the diameter of the Venturi’s throat, which was inconsistent with the observations made through the transparent tubing connecting the outlet of the injector to the inlet of the separator of the HIL. To explicitly model the Venturi injector, a refinement of the model for the initial bubble size estimation during mixing was required, subject to further work beyond the scope of this thesis.

Consequently, an approximate approach was used to estimate the appropriate values of $k_La_{CO_2}$ for the HIL. Following the procedure illustrated in Section 4.4.4, a vertical HAC downcomer was modeled with the same diameter as the HIL outlet (25.4 mm). However, the

downcomer lengths were varied between 5 and 20 m so that the values of $k_L a_{CO_2}$ could be tabulated for increasing outlet pressures. Table 8-2 presents the input parameters of the model, which are the same as those in experiment E2. The input CO₂ (g) concentration was 0.1655 (mol%). Table 8-3 shows the estimated values of $k_L a_{CO_2}$ based on the outlet pressure.

Table 8-2: Summary of input parameters for the simulation

Input parameter	HIL 'Downcomer'
Input water mass flow rate (kg/s)	0.4717
Input air mass flow rate (g/s)	5.603×10^{-2}
Input CO ₂ mass flow rate (g/s)	1.25×10^{-2}
Gas pressure at injector suction inlet (kPa)	99.078
Water temperature (K)	295.145
Input gas relative humidity (%)	100
Absolute roughness (m)	1.5×10^{-5}
No. segments	60
Diameter (m)	2.54×10^{-4}
Flow direction (°)	-90

Table 8-3: The estimated values of $k_L a_{CO_2}$ according to the outlet pressure

Length of downcomer (m)	Outlet gauge pressure (psi(g))	Total Interfacial area (m ²)	Volume $\times 10^{-3}$ (m ³)	Specific interfacial area (m)	Average $k_{LCO_2} \times 10^{-4}$ (m/s)	$k_L a_{CO_2} \times 10^{-2}$ (s ⁻¹)
5.00	6.16	0.396	2.534	157.329	4.792	7.53
7.50	9.33	0.561	3.8	147.803	4.891	7.12
10.00	12.54	0.707	5.067	139.705	4.842	6.67
12.50	15.76	0.839	6.334	132.573	4.846	6.44
15.00	19.01	0.959	7.601	126.200	4.883	6.16
17.50	22.43	1.446	8.867	163.171	5.128	8.36
18.75	23.90	1.517	9.501	159.429	5.133	8.18
20.00	25.72	1.579	10.13	155.859	5.139	8.01

From these results, the value of the $k_L a_{CO_2}$ used in the following calculation was 8.18×10^{-2} s⁻¹ for 23.9 psi(g) to correspond with the outlet pressure of the injector diffuser in the HIL rig during the experimental trials of Chapter 7 (24 psi(g)). Note that this value of $k_L a_{CO_2}$ was for a 'no chemistry' condition, meaning that the bulk concentration of dissolved CO₂ was not depleted by participating in a CaCO₃ precipitation reaction.

According to the results of CO₂ capture and sequestration experiments reported in Chapter 7, it was observed that during phase III of each experimental trial, 99.99% of the CO₂ added to the inlet air dissolved in the Ca(OH)₂ solution/suspension solution. To determine the enhancement factor E , it was assumed that only 0.01% of inlet CO₂ was present in the discharge gas. Subsequently, the volumetric mass transfer coefficient of the chemical reaction ($k_L a_{CO_2}^R$) was estimated. As shown in equation (3.42), E is the ratio of $k_L a_{CO_2}^R$ to $k_L a_{CO_2}$. Table 8-4 shows the summary of calculations of E and $k_L a_{CO_2}^R$ based on Equation (4.1). The value of E used in the following simulations is 32.

Table 8-4: Summary of calculation for E and $k_L a_{CO_2}^R$

Parameter	Value	Unit
Volume, V	9.501×10^{-3}	m ³
Addition rate of CO ₂ to the liquid phase, \dot{n}	2.52×10^{-4}	mol/s
Log mean concentration different CO ₂ , ΔC	9.46×10^{-4}	mol/m ³
$k_L a_{CO_2}^R = \frac{\dot{n}}{V \times \Delta C}$	2.625	s ⁻¹
$E = \frac{k_L a_{CO_2}^R}{k_L a_{CO_2}}$	32.04	-

8.2 Results of dynamic kinetic model

8.2.1 CO₂ dissolution in Ca(OH)₂ saturated solution

The measured pH of the 1C-F solution at the beginning of phase III was 12.25. However, the pH of the standard saturated Ca(OH)₂ solution was 12.34 at 22° C (Bates *et al.*, 1956; Lito *et al.*, 1998b). The measured pH was lower than that of a standard saturated solution at the same temperature. The dynamic kinetic model calculated the initial pH of the solution as 12.62, which

is higher than the measured pH. One of the reasons of this difference is the activity coefficients were not considered in the pH calculation.

Generally, activity coefficients are correction factors used in calculating pH, particularly for solutions containing ions or molecules that interact strongly with each other. These coefficients account for the effect of other ions or molecules in solution on the activity or effective concentration of a particular ion or molecule of interest (Atkins *et al.*, 2014). In the context of pH calculations, activity coefficients are typically used to calculate the equilibrium concentrations of acid and conjugate base species and the concentrations of other ions that may affect the pH of the solution. By considering the activity coefficients, a more accurate estimate of the actual concentrations of the species in the solution can be obtained, leading to more accurate pH calculations (Robinson and Stokes, 2002). However, it is difficult to find a formula that accurately calculates the pH of calcium hydroxide solutions while accounting for the effects of the activity coefficients.

Figure 8-1 shows the modeling of the variations in the pH and CO₂ concentration of the discharge gas during phase III of experiment E2. According to the model prediction, it required 4.30 min for the pH to decrease from 12.63 to 10 as the reaction progressed. However, the experimentally measured time was longer, at 5.00 min. Additionally, the initial pH of the model was higher than that measured during the experiments. Therefore, the model-predicted time for the pH to decrease to 10 was shorter than the actual time observed in the experiment.

The modeled variation in the CO₂ concentration of the discharge gas was in close agreement with the experimental results. The root mean square error between the model's predicted of the CO₂ concentration of the discharge gas and the experimental results is 3.4×10^{-3} . Figure 8-1 shows

that the concentration of discharged CO_2 (g) remained lower than 0.1 % until pH decreased to 10, indicating that almost all of the added CO_2 in the inlet air was consumed in the reaction system during the experiment. In the dynamic kinetic model, the concentration of dissolved CO_2 in solution was determined using the values of $k_L a$ and E .

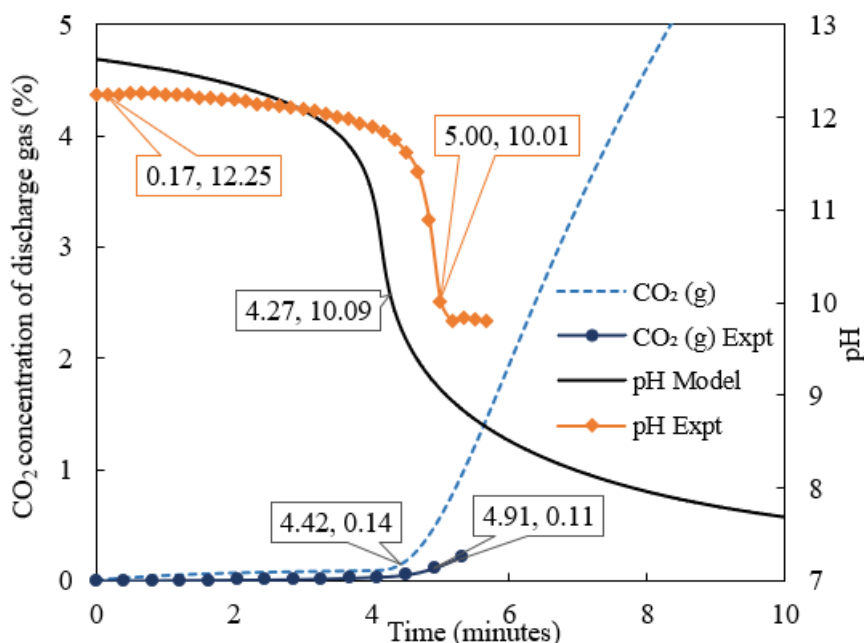


Figure 8-1: Modeling of the variations of discharge CO_2 concentration and pH of 1C.F solution according to the time to phase III

Figure 8-2 and Figure 8-4 present the variations in the concentrations of Ca^{2+} , CaOH^+ , CaCO_3 , and carbon species (CO_2 (aq), HCO_3^- , and CO_3^{2-}) predicted by the model during phase III of experimental trial E2.

When the pH was greater than 10 ($10 < \text{pH} < \text{initial pH}$), the dissolved CO_2 was converted to CO_3^{2-} ions, which reacted with Ca^{2+} ions. The latter originated from the dissolution of $\text{Ca}(\text{OH})_2$ (Ca^{2+} and CaOH^+ ions). The CaCO_3 precipitates were based on reaction (3.31), which proceeded until all calcium ions in the reactor were consumed.

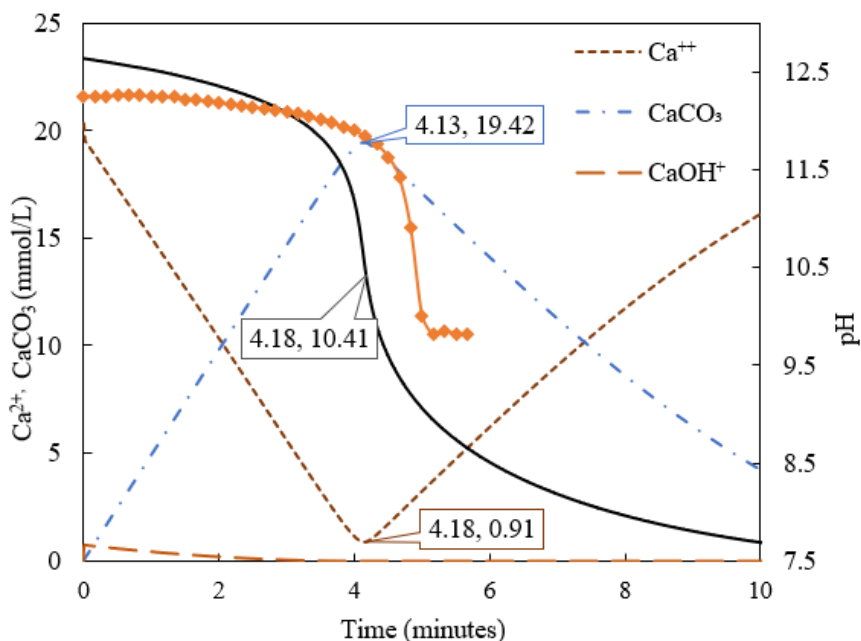


Figure 8-2: Modeling of the variations of Ca²⁺, CaOH⁺, and CaCO₃ concentrations of the 1C.F solution according to the time of phase III

In Figure 8-2, the sum of the initial concentrations of Ca²⁺ and CaOH⁺ was 20.32 mmol/L, which is the same as that of [Ca²⁺] in a saturated solution. The initial concentration of CaCO₃ was zero. According to the model prediction, the maximum concentration of precipitated CaCO₃ was 19.42 mmol/L when the pH of the solution was 10.45 at 4.13 min. The concentrations of Ca²⁺, CaOH⁺, and CO₃²⁻ ions were 0.90, and 0, respectively. When the pH was decreased below 10, the precipitated CaCO₃ quickly dissolved into calcium and carbonate ions. When the pH was 7.74 at 9.48 min, the concentrations of Ca²⁺ and CaCO₃ were 15.09 and 5.21 mmol/L, showing that most of the precipitated CaCO₃ was converted into calcium and carbonate ions.

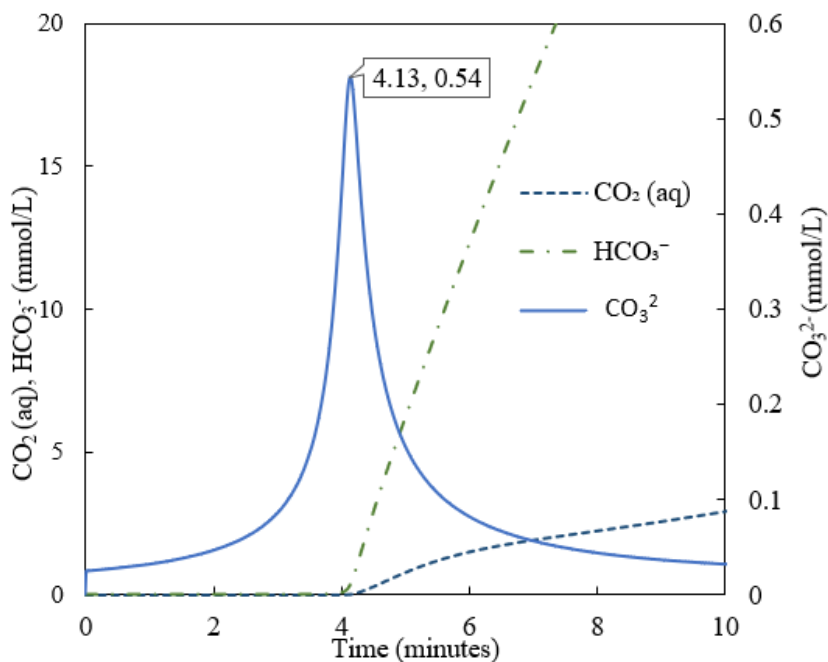


Figure 8-3: Modeling of the variations of $\text{CO}_2(\text{aq})$, HCO_3^- , and CO_3^{2-} concentrations of the 1C.F solution according to the time of phase III

In Figure 8-4, by decreasing the concentration of Ca^{2+} in the reactor, the model predicted $[\text{CO}_3^{2-}]$ increased to its peak (54.02×10^{-2} mmol/L) at pH 10.49 and then decreased to 0.03 mmol/L at pH 7.74. Continuing to admit CO_2 in the simulation caused the pH to decrease further below 10 so that the dissolved CO_2 was converted to HCO_3^- . In the simulation, when the pH was 7.74 at 9.48 min, the model predicted $\text{CO}_2(\text{aq})$ and HCO_3^- concentrations 2.74 and 30.11 mmol/L, respectively.

The accuracy of the predictions of the dynamic kinetic model was influenced by the calculated values of $k_L a$, E , and pH. As these values were estimated more accurately, the experimental observations were more likely to align with the model's predicted performance, leading to a greater degree of agreement between the model and the experiment.

8.2.2 CO₂ dissolution in Ca(OH)₂ suspension solutions

- *2.2C-S solutions*

Experiments (E4 and E5) were conducted with a 2.2C-S solution which consisted of 5.34 g of dissolved Ca(OH)₂ that coexist with 6.41 g of undissolved Ca(OH)₂ in 3.54 kg of D.I. water. However, as mentioned in Section 7.3.2, the amount of Ca(OH)₂ in the solution in experiment E4 was lower than that in experiment E5.

For the initial conditions of the model, it was assumed that 20.30 mmol/L of Ca(OH)₂ was dissolved in the solution, and 6.41 g of Ca(OH)₂ remained as undissolved solids in 3.54 kg of D.I. water. In accordance with this assumption, the total surface area of the CaOH₂ particles (A_s) and the initial pH of the solution were calculated. The initial pH of the model was 12.63, principally because of the concentration of OH⁻ added to the water. In comparison, the initial pH values in experiments E4 and E5 were 12.22 and 12.26, respectively.

The average percentage of CO₂ (g) concentration added to the inlet gas in experiment E4 was 14.12 %. In this experiment, the average gas mass flow rates of the inlet air and CO₂ were 2.92 and 0.38 L/min. The water volume flow rates in experiments E4 and E5 were 26.33 and 24.12 L/min, respectively. Although the water volume flow rate in experiment E4 was higher than that in experiment E5, the percentage of CO₂ (g) concentration added to the inlet air in experiment E5 was higher than that in experiment E4. In experiment E5, the average gas mass flow rates of the inlet air and inlet CO₂ were 2.55 and 0.40 L/min, respectively.

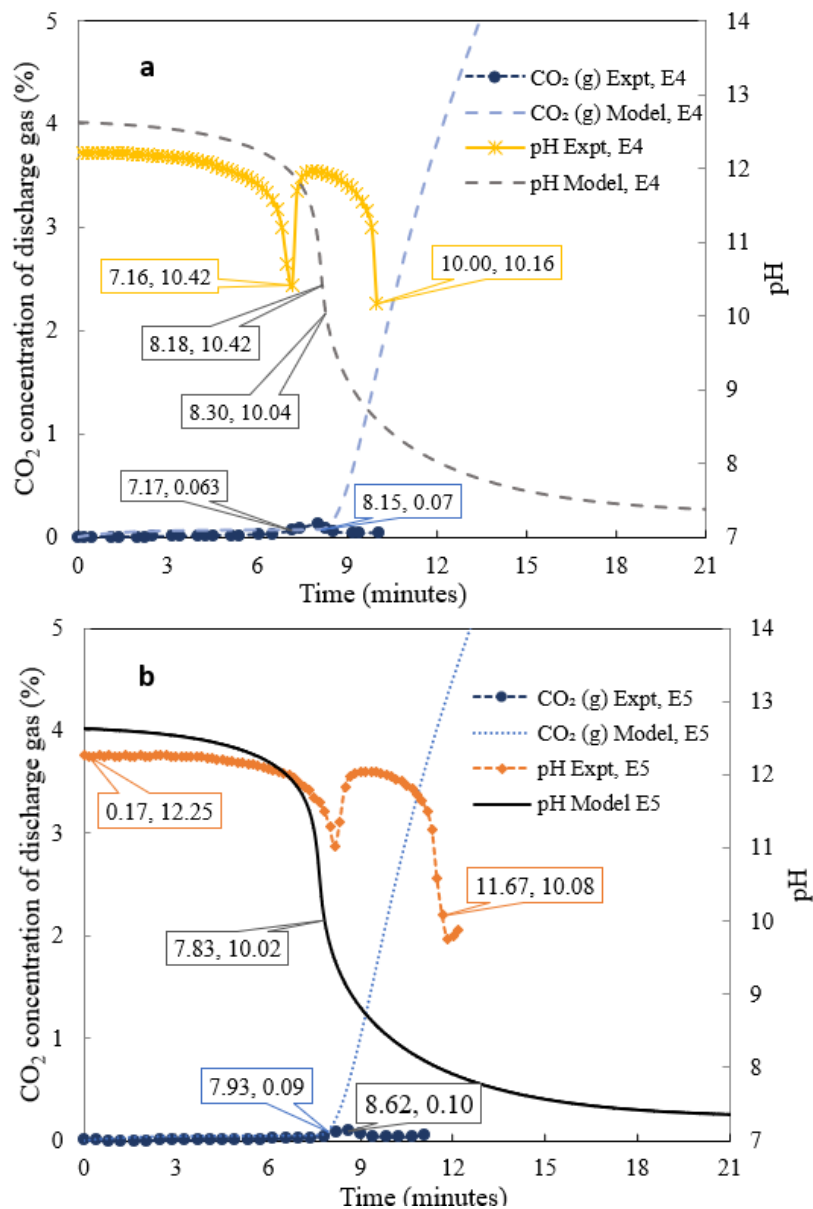


Figure 8-4: Modeling of the variations of discharge CO₂ concentration and pH of 2.2C.S suspension solution according to the time phase III of experiments (a) E4 and (b) E5

The length of phase III in experiment E5 was greater than that in experiment E4, indicating that the Ca(OH)₂ concentration of the solution used in experiment E4 was lower than that in experiment E5.

Figure 8-4 shows the modeling of the variations in the pH and CO₂ concentration of the discharge gas during phase III of experiments E4 and E5. For the initial conditions of the model, the percentage of CO₂(g) added to the inlet air in experiment E4 was lower than that in experiment E5. The model predicted that the length of phase III in experiment E4 would be greater than that in experiment E5.

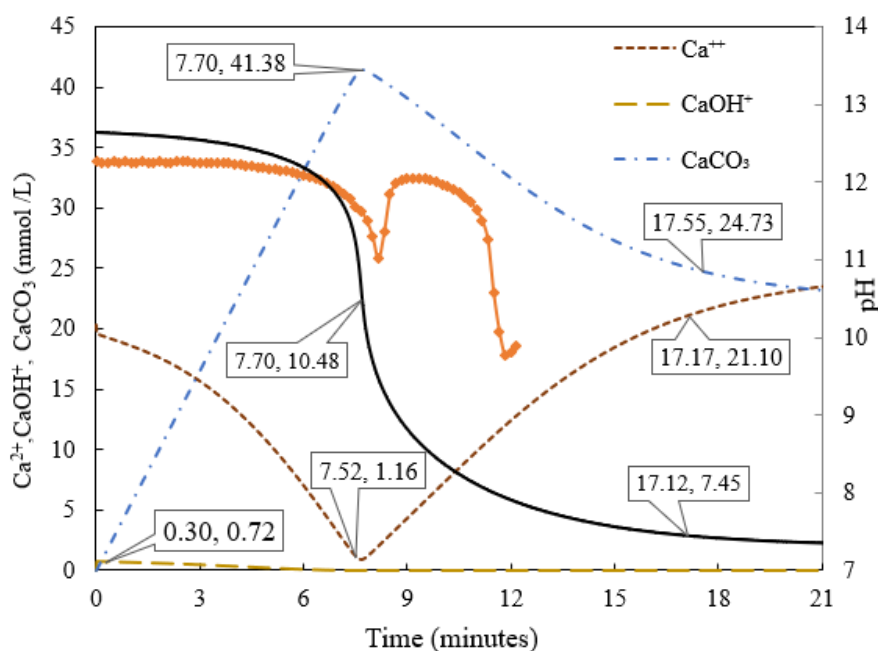


Figure 8-5: Modeling of the variations of Ca²⁺, CaOH⁺, and CaCO₃ concentrations of the 2.2C.S solution according to the time of phase III of experiment E5

The model predicted that the pH of experiments E4 and E5 decreased from 12.63 to 10.02 over 8.32 and 7.83 (min), respectively. However, the model's predicted duration for the pH drop was shorter than the actual phase III duration in both experiments. The duration of phase III of experiment E4 was 10:00 min, while E5 had a duration of 11.67 min. Figure 8-4 also showed that the concentration of discharged CO₂ (g) remained lower than 0.1 % until pH decreased to 10,

indicating that almost all of the added CO_2 in the inlet air was consumed in the reaction system during the experiments.

The variations in the Ca^{2+} , CaOH^+ , and CaCO_3 concentrations, and carbon species ($\text{CO}_2(\text{aq})$, HCO_3^- , CO_3^{2-}) predicted by the model during phase III of experiment E5 are illustrated in Figure 8-5 and Figure 8-6, respectively.

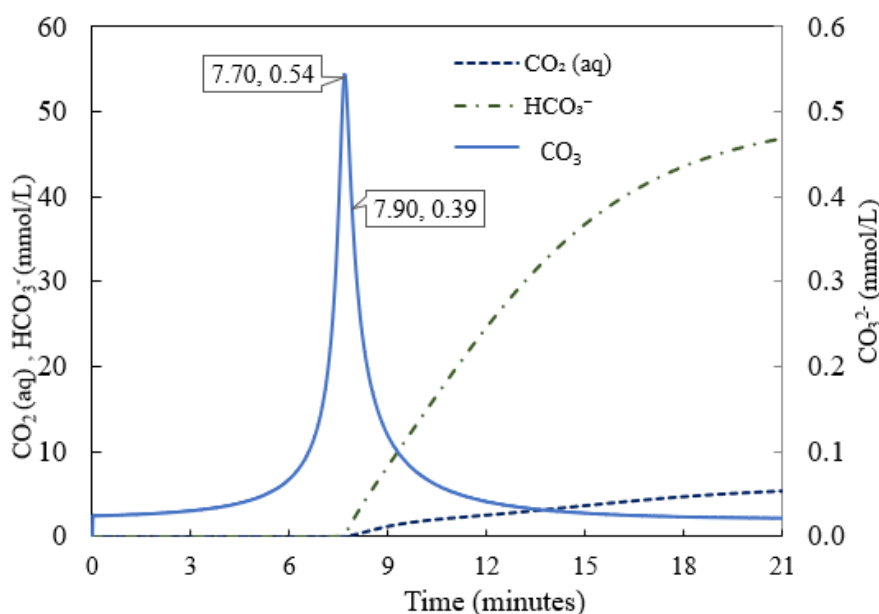


Figure 8-6: Modeling of the variations of $\text{CO}_2(\text{aq})$, HCO_3^{2-} , and CO_3^{2-} concentrations of the 2.2C.S solution according to the time of phase III of experiment E5

According to the model results in Figure 8-6, when the pH decreased from 12.63 to 10.48, the $\text{Ca}(\text{OH})_2$ solid particles dissolved in the solution and reacted with CO_3^{2-} ions. The CaCO_3 precipitated during this time. The highest concentration of CaCO_3 in the solution existed at pH 10.48, after which CaCO_3 dissolved to Ca^{2+} and CO_3^{2-} . However, the dissolution rate of CaCO_3 in the 2.2C-S suspension was lower than that in the 1C-F saturated solution. When pH was 7.39 at 20.55 min, the concentrations of Ca^{2+} and CaCO_3 were approximately the same, at 23.29 mmol/L.

Figure 8-6 shows the trends of the CO_2 (aq), HCO_3^{2-} , and CO_3^{2-} concentrations of the 2.2C.S suspension solution predicted by the model, which is similar to those of the C.F saturated.

- **5C-S solutions**

Experiment E8 was conducted using a 5C-S solution consisting of 5.34 g of dissolved $\text{Ca}(\text{OH})_2$, which was suspended in 21.38 g of undissolved $\text{Ca}(\text{OH})_2$ in 3.54 kg of D.I. water. In the model, it was assumed that 20.30 mmol/L of $\text{Ca}(\text{OH})_2$ dissolved in D.I. water, reaching saturation, while 21.38 g of $\text{Ca}(\text{OH})_2$ remained as an undissolved suspended solid in 3.54 kg of D.I. water.

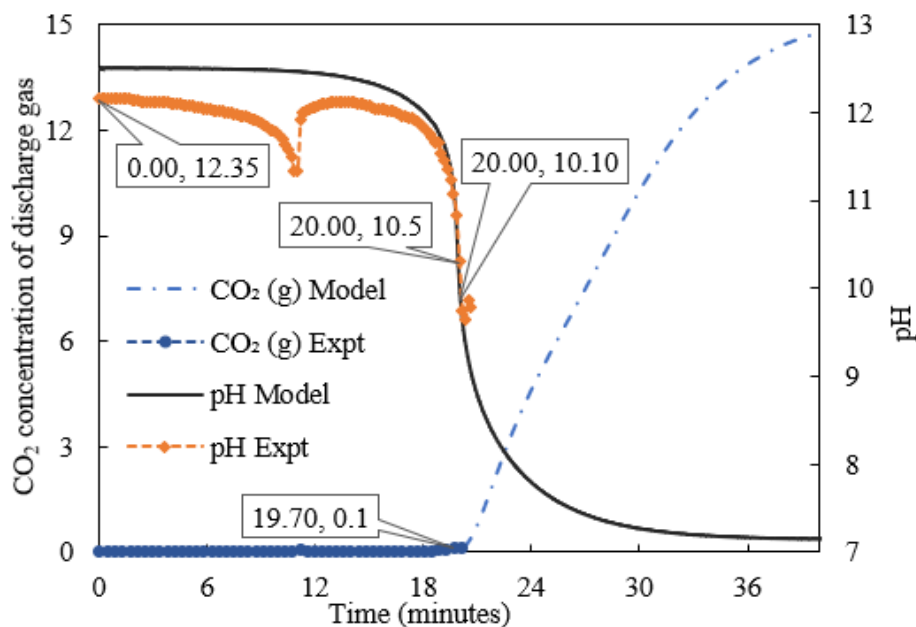


Figure 8-7: Modeling of the variations of discharge CO_2 concentration and pH of 5C.S solution according to the time of phase III

Figure 8-7 shows the model prediction of the variations in the discharge CO_2 concentration and pH of the circulating solution, starting with 5C.S. The initial pH of the experiment and model were 12.35 and 12.69, respectively. The model prediction of $[\text{CO}_2$ (g)] of discharged gas was close

to the measured values and was 'low' in any case. The root mean square error between the modeled prediction of the CO₂ concentration of the discharge gas and the experimentally measured value is 2.2×10^{-3} . The model predicted that it would take 20.03 min to reduce the pH from 12.69 to 10.02, which was very close to the duration of phase III in experiment E8. Furthermore, Figure 8-7 showed that once the pH of the model reached 7.35, all CO₂ added to the inlet air was present in the discharge gas.

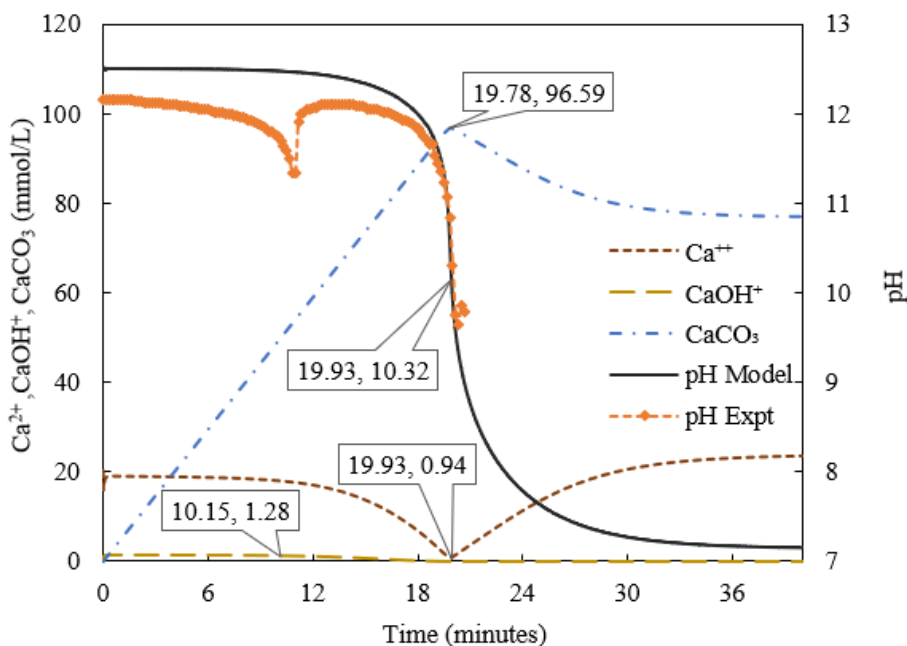


Figure 8-8: Modeling of the variations of the concentrations of Ca²⁺, CaCO₃, and pH of the 5C.S solution according to the time

As shown in Figure 8-8, the highest concentration of CaCO₃ in the solution was 96.73 mmol/L at 19.90 min when the pH was 10.45. After that, the CaCO₃ dissolved into Ca²⁺ and CO₃²⁻. However, the rate of dissolving CaCO₃ was lower than in the other experiments. When

pH was 7.35 at 39.20 min, the concentration of CaCO_3 was 77.04 (mmol/L), which was higher than the Ca^{2+} concentration (23.48 mmol/L) at that time.

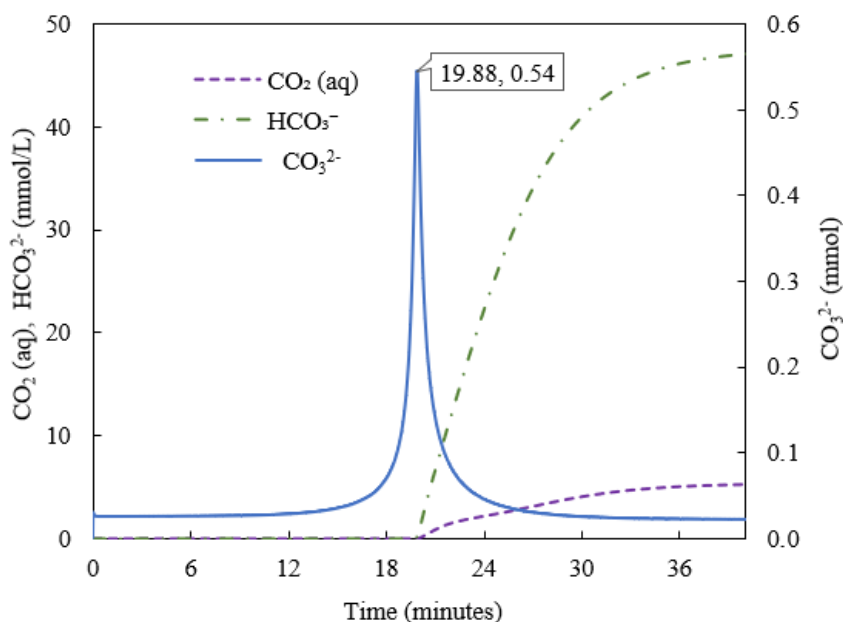


Figure 8-9: Modeling of the variations of CO_2 (aq), HCO_3^{2-} , and CO_3^{2-} concentrations of the 5C.S solution according to the time of phase III

Figure 8-9 shows the variations in the concentrations of the carbon species CO_2 (aq), HCO_3^- , and CO_3^{2-} predicted by the model during phase III, which are similar to those presented for the earlier experiments.

8.3 Discussion

8.3.1 Comparison between experimental and modeled results

Table 8-5 provides a comparison between the experimental results and model predictions. This table indicates that the predicted mass of precipitated CaCO_3 (s) is more than the collected solid

CaCO₃ from the filter after the experiments. This is likely due to some of the CaCO₃ solid not being recovered from the filter.

Table 8-5: The comparison between the experimental results and model predictions

Experiment / Model	E2	E4	E5	E8
CO ₂ absorption solution	1C-F	2.2C-S	2.2C-S	5C-S
Mass of the Ca(OH) ₂ in the solution (g)	5.34	11.76	11.76	26.72
Experiments				
Duration from time adding CO ₂ to pH=10 (minutes)	5	10.00	11.66	20.16
Mass of consumed CO ₂ (g)	3.77	7.53	8.75	15.94
Mass of produced of CaCO ₃ (s) (g)	3.57	10.63	6.38+F	18.39+F
Model				
Model's predicted duration of time to pH=10 (minutes)	4.3	8.32	7.83	20.03
Model's predicted mass of consumed CO ₂ (g)	3.28	7.66	7.61	15.46
Model's predicted mass of CaCO ₃ (s) to pH=10 (g)	6.79	14.55	14.65	34.33
The root mean square error ((RMSE) calculation				
The RMSE between the model's predicted of the CO ₂ concentration of the discharge gas and the experimental measured values	3.1×10^{-3}	1.55×10^{-1}	2.38×10^{-1}	2.1×10^{-3}

According to Figure 8-10 and Figure 8-11, in experiment E2, although the model predicts a shorter duration of time to reach a pH of 10 compared to the actual time required during the experiment, the mass of consumed CO₂ (g) in this experiment is consistent with the model's prediction.

In experiment E5, it is observed that the duration of phase III is longer than the predicted value by the model and the mass of CO₂ (g) consumed during the experiment is higher than the value predicted by the model.

While the Ca(OH)₂ concentration in the solution of experiment E4 is lower than that of experiment E5, the percentage of CO₂ (g) added to the inlet air of experiment E5 is higher than experiment E4. As a result, the model predicts a longer time for experiment E4 to reach a pH of

10 compared to experiment E5, however, this duration is also shorter than phase III of experiment E4. The results of experiment E8 showed a close agreement between the actual duration of phase III and the amount of consumed CO_2 (g) during this period with the values predicted by the model.

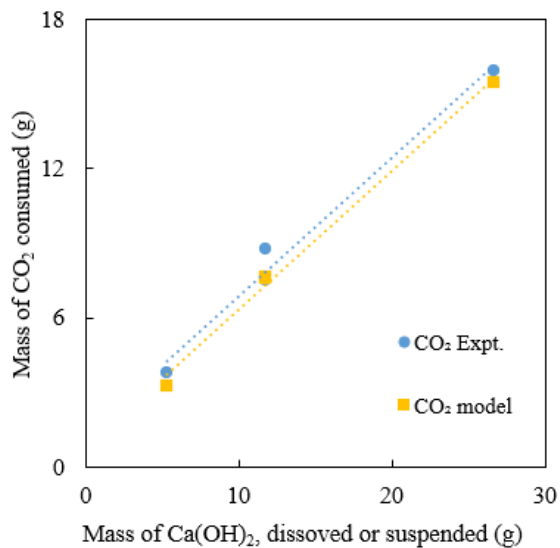


Figure 8-10: Mass of absorbed CO_2 and versus the mass of Ca(OH)_2 in the solution

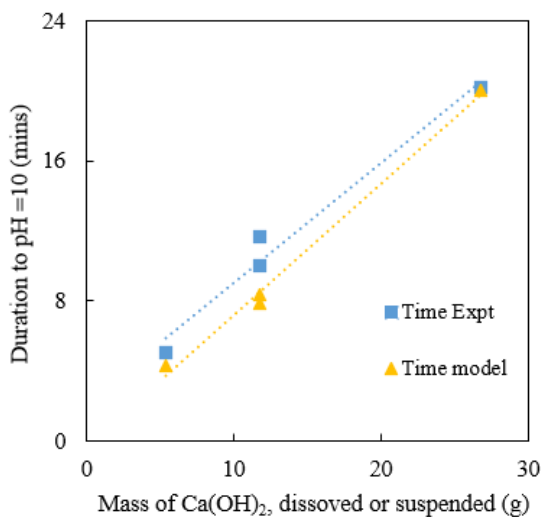


Figure 8-11: Duration of time to reach pH=10 versus the mass of Ca(OH)_2 in the solution

Table 8-5 also presents the RMSE between the model's predicted of the CO₂ concentration of the discharge gas and the experimental measured values. In experiments E2 and E8, the calculated errors are quite small, with values in the order of 10⁻³. According to Figure 8-1, the modeled variation in the CO₂ concentration of the discharge gas closely aligns with the experimental results, resulting in a small RMSE between these values. Moreover, as shown in Figure 8-7, the model prediction of CO₂ (g) concentration of discharged gas was close to the measured values. Thus, the root mean square error between these values is also small as 2.2×10⁻³.

In experiments E4 and E5, as shown in Figure 8-4, the model predicts a shorter duration of time to reach a pH of 10 compared to the actual time required during the experiments. Therefore, the modeled variation in the CO₂ concentration of the discharge gas is lower than experimental results. So, the root mean square errors between the model's predicted of the CO₂ concentration of the discharge gas and the experimentally measured values are considerable.

The results presented in this section indicate that the model predictions provide only a moderate degree of quantitative agreement with the experimental observations. However, it is known with certainty that some of the durations to pH = 10 established experimentally are a consequence of the local 'dipping' behavior in the pH curve which are thought to be associated with 'clumps' of undissolved Ca(OH)₂ solid particles becoming 'stuck' in the system somewhere that allow the circulating suspension solution to dip below Ca(OH)₂ saturation conditions. That experimentally established behavior (which the results collectively show is repeatable) potentially 'masks' an establishing agreement between simulated and experimental times to pH=10 with high precision.

In all cases of model versus experiment, the model's predicted CO₂ concentrations in the discharge gas are found to be lower than the measured concentration of CO₂ (g) in the discharge gas during experimental runs, although these concentrations are far lower than CO₂(g) concentrations in the input gas mixture.

Such performance from the model simulations perhaps casts doubt on the efficacy of the HIL as a device in which to perform carbonation processes and the degree of understanding of the carbonation process embedded in the dynamic kinetic model of the reactions or the controlling parameter values within them. However, re-running the simulations using values $k_L a_{CO_2} = 0.0194 \text{ s}^{-1}$ and $E = 1.8$ transposed directly obtained from Velts' experiments (Velts *et al.*, 2011d) as presented in Section 3.3.3, produces a far greater discord between model predictions and experimental results. Variances in the time to pH=10 are much greater, and the simulated off gas concentrations are orders of magnitude greater than observed. The values of $k_L a_{CO_2} = 0.0818 \text{ s}^{-1}$ and $E = 32$ found predictively in this work (rather than through empirical fitting) clearly illustrate the superiority of the HIL as a mineral carbonation device, enhanced process understanding and the veracity of the Young *et al.* (2022) model.

8.3.2 Sensitivity analysis

A sensitivity analysis was conducted on the model predictions of experiment E2. This analysis aimed to assess the experiment's robustness and the model's reliability. It assists in understanding the sensitivity of the model's output to changes in its inputs and parameters.

The reason for selecting experiment E2 for sensitivity analysis is that it did not include the complication of the 'dip' in the experimentally measured pH curves, suspected to be caused by

'stuck' or 'clumped' $\text{Ca}(\text{OH})_2$ evident in all other experimental runs. The alkaline solution of experiment E2 was saturated, so no $\text{Ca}(\text{OH})_2$ solid particles were present in the solution. Therefore, the total surface area of the $\text{Ca}(\text{OH})_2$ particles, A_s , was zero.

The sensitivity analysis evaluated the impact of varying all selected parameters on the duration required for the pH of the 1C-F solution to decrease to 10. This duration was also measured during the experiment, allowing for a comparison of the model results with the actual time observed in the experiment.

The following input model parameters were systematically varied individually: i) mass of $\text{Ca}(\text{OH})_2$ added to solution, ii) solution volume, iii) average inlet gas mass flow rate, iv) average input gas CO_2 flow rate added into inlet air, v) $k_L a_{\text{CO}_2}$ vi) E .

With the immediately following exceptions, other parameters governing experimental conduct or model simulations were considered but were concluded not to be material. Changes in temperature affect the rate constants; but because experimental temperatures were controlled and exhibited little practical variation, temperature variation was not considered in the sensitivity analysis. The effects of pressure variation are accounted for by the Young *et al.* (2022) bubbly flow model and again, separator pressure was well controlled by the regulating valve and so pressure variation was not considered in the sensitivity analysis either.

Each flexed parameter was varied over an interval of $\pm 10\%$ from the base value during the simulation of the experiment E2. The reason for this choice of variation was because 10% was the maximum error considered credible for the experimentally established variables, simulating what

could be argued to represent a blunder in measurement of mass, volume or flow rates. Table 8-6 presents the results of the sensitivity analysis of experiment E2.

According to Table 8-6, the duration for pH to drop to 10 is highly sensitive to changes in the mass of Ca(OH)₂ added to the solution. In experiment E2, the alkaline solution was saturated. When the mass of Ca(OH)₂ is 10% lower than the base value, the solution is no longer saturated. The initial pH of the solution is 12.58, which is lower than the pH of saturated solution. The duration for the pH to drop to 10 significantly reduces. The likelihood of a 10% lower error on this parameter is zero.

Table 8-6: The results of sensitivity analysis of experiment E2

Experiment E5		Mass of Ca(OH) ₂ added to solution (g)	Solution volume (L)	Inlet gas mass flow rate (SLPM)	Inlet CO ₂ (g) flow rate (SLPM)	$k_L a_{CO_2} \times 10^{-2}$ (s ⁻¹)	Enhancement factor, <i>E</i>
Variable parameters	10% lower than base value	4.788	3.186	2.511	0.3528	7.362	28.8
	Likelihood of 10% lower error	very unlikely	likely	likely	likely	very likely	very likely
	Base value	5.32	3.54	2.79	0.392	8.18	32
	10% more than base value	5.852	3.894	3.069	0.4312	8.998	35.2
	Likelihood of 10% more error	very unlikely	likely	likely	likely	very likely	very likely
Duration for dropping pH to 10	10% lower than base value (minutes)	3.883	4.367	4.321	5.35	4.283	4.286
	Base Value, Model (minutes)	4.300	4.300	4.300	4.300	4.300	4.300
	10% more than base value (minutes)	4.432	5.371	4.298	4.210	4.320	4.351

Conversely, when the mass of Ca(OH)_2 is 10% more than the base value, the solution is a suspension solution; 20.30 mmol/L of Ca(OH)_2 is dissolved in the solution, and 0.532 g of Ca(OH)_2 remained as undissolved solids in D.I. water. The duration for the pH to drop to 10 increases. The likelihood of a 10% more error on this parameter is zero.

The variations in solution volume also affect the gas volume in the empty space above the reaction mixture. Therefore, this parameter is also adjusted during the sensitivity analysis. A 10% lower solution volume (3.186 L) generally results in a shorter duration for pH drop compared to the base value. Conversely, when the solution volume is increased by 10% to 3.894 L, it results in slightly longer durations for the pH to drop, taking approximately 5.371 minutes. This duration closely aligns with the actual time observed in experiment E2. The chances of a 10% error in this parameter are considered likely.

The inlet gas mass flow rate shows minimal sensitivity in this experiment. Even when the flow rate varies by 10% in both directions, there is virtually no noticeable impact on the time it takes for the pH to reach 10. The likelihood of a 10% error in this parameter is quite high.

The flow rate of CO_2 gas has a moderate sensitivity. When the amount of CO_2 being added to the solution is reduced by 10% from the base value (0.392 SLPM), it results in a longer time for the pH to drop to 10, specifically 5.35 minutes. This duration closely aligns with the actual time observed in experiment E2. While increasing the flow rate of CO_2 gas reduces the time needed for the pH to reach 10 compared to the base value. The likelihood of a 10% error in this parameter is quite high. The gas-liquid volumetric mass transfer coefficient ($k_L a$) and enhancement factor (E) have a relatively minor impact on the duration, with small variations having minimal effects. These

parameters are estimated by using Young *et al.* (2022) bubbly flow mode. This model is known to require improvement in accuracy to effectively simulate the gas-liquid mass transfer in the injector diffuser and include the reaction kinetics of carbonate equilibrium in aqueous systems. 10% swings in these values do not produce material variations in the time to pH = 10.

8.3.3 Potential improvements to the dynamic kinetic model for better agreement with experimental conditions

- The bubbly flow model cannot solve two-phases flow in the short length of the injector's diffuser. Therefore, the $k_L a_{CO_2}$ is estimated for a selection of downcomers with a range of outlet pressures similar to that observed during the operation of the HIL rig during the mineral carbonation experiments. The downcomer is vertical, with a diameter of 25.4 mm, and its height is adjusted from 5 to 20 m to create different outlet pressures. The bubbly flow model needs improvement to accurately model the gas-liquid mass transfer in the injector's diffuser. The comparison of simulation results with volumetric mass transfer coefficient from Velts with those adopted from Young indicate that the bubbly flow model nevertheless produces plausible values of these parameters.
- The chemical effect of the reaction of CO₂ with Ca(OH)₂ solution on the rate of absorption and increasing the capacity of the liquid solution to dissolve more CO₂ is considered by E in the dynamic kinetic model. To enhance the accuracy of the dynamic kinetic model, a more precise method for calculating E is required.
- The pH value calculated by the model is higher than the pH value measured during the experiment, and this is thought to be due to the activity coefficients not being considered

in the pH calculation over basic concentrations. To improve the accuracy of the dynamic kinetic model, it is necessary to include the activity coefficients in the pH calculation.

- The equilibrium and kinetic coefficients used in the set of differential equations for the dynamic kinetic model were calculated based on the experimental conditions outlined in their references. However, to ensure a completely objective assessment of the accuracy of the simulation model for the HIL experiments, all equilibrium and kinetic coefficients need to be established consistently, at all-times using activity coefficients for all values, and recalculated for specific experimental conditions of the HIL.
- Accurate measurement of the initial diameter of the Ca(OH)_2 particles is crucial for modeling their dissolution in the suspension solution. This allows for a more precise calculation of the total surface area of the Ca(OH)_2 particles, leading to improved agreement between the results of the dynamic kinetic model and the experimental conditions.
- The problems due to local ‘dips’ of the pH curve and the corresponding local ‘peaks’ in the CO_2 off gas concentration curve, thought to be due to ‘clumps’ of suspended solid particles of Ca(OH)_2 becoming ‘stuck’ in the system, and these need to be eliminated, to prevent masking of the phase III duration to $\text{pH}=10$ when compared to simulation results. This is just one aspect of the experimental procedures that require upgrade. Another aspect includes improving the method of recovery of CaCO_3 (s) so that the yield of the process can be more reliably estimated.

8.4 Summary

This chapter presented the utilization of the dynamic kinetic model, as discussed in Chapter 3, to predict the concentration time series of all species participating in the precipitation process of carbonation experiments conducted via the HIL, as discussed in Chapter 7. The initial conditions and process for estimating the values of k_{LA} and E were described in detail. Overall, the results of the dynamic kinetic model agreed well with the experimental findings. Some potential improvements to the dynamic kinetic model were identified to enhance its compatibility with the experimental conditions.

9. Discussion

9.1 Summary of purpose or findings of prior chapters

The principal functions of the preceding chapters of this thesis are summarized below:

Chapter 2 – Review of the state of technical development and diverse process pathways explored for mineral carbonation processes for carbon capture and sequestration.

Chapter 3 – Focuses on the details of mineral carbonation reaction equilibria, chemical kinetics, and gas mass transfer with the understanding gained embedded in a dynamic kinetic model of mineral carbonation using alkaline earth metal oxide or hydroxide solutions. This also highlighted the importance of solutions, alkaline earth metal oxide/hydroxide dissolution, and CO₂ gas mass transfer to ‘de-bottleneck’ the process for mineral carbonation.

Chapter 4 – General review and explanation of HACs, devices that have hitherto been principally developed for the purpose of efficient gas compression, but which are considered to have their purpose augmented in this thesis as improved gas-liquid contactors that enhance gas mass transfer.

Chapter 5 – Report of experimental procedures that verified the Young *et al.* (2022) 1D process model for hydrodynamics and mass transfer in 2-phase bubbly flows, typical of hydraulic air compressors. A procedure for calculating the volumetric gas mass transfer coefficient from the results of numerical simulations using the Young *et al.* (2022) model is also presented.

Chapter 6 – Design, fabrication, and testing of a bench scale so-called ‘horizontal induction loop’ (HIL), a type of HAC that does not rely on great elevation difference to pressurize inducted

gas but instead is more compact by relying on a venturi injector geometry to pressurize inducted gas and to recover pressure of the injector's primary motive fluid.

Chapter 7 – Use HIL to undertake proof-of-concept experiments to capture (that is, separate) CO₂ present in mixtures of atmospheric gases and sequester CO₂ to a solid carbonate product.

Chapter 8 – Reports of simulations of the proof-of-concept mineral carbonation experiments undertaken with the HIL, using the Young *et al.* (2022) model to back-calculate values of the volumetric mass transfer coefficient and a comparison of the results from the HIL experiments with the dynamic kinetic model simulations. The degree of agreement between the simulation and the experiment was deemed satisfactory at this stage of concept development.

In this discussion chapter:

The efficacy of the gas mass transfer behavior of the HAC, and more specifically, its downcomer, is tested against that of a bubble column contactor on a commercial scale. This is because a conventional bubble column reactor appears to be the closest competitor to an HAC downcomer in terms of mass transfer performance alone. The focus is retained on the predicted gas mass transfer behavior to illustrate the ability to use the now experimentally verified Young *et al.* (2022) model in process design calculations.

9.2 Hydrodynamic and mass transfer comparison of HAC downcomers and upward co-current flow bubble column reactors.

This section presents the simulation results of the hydrodynamic and mass transfer behaviors of the HAC downcomer and bubble column. The input parameters of the model, composition of dry air and input gas mixtures, and initial concentration of each species in water closely resemble those

used in the simulation described in Section 4.4.3. For convenience, a summary of the input parameters is presented in Table 9-1 and Table 9-2. The shaft lengths of the HAC downcomer and bubble column were 80.95 m.

It is important to recognize that in the case of the co-current up-flow bubble column, the gas injected into the column at the column base would first have to be compressed to the column base pressure. In contrast, in the HAC system, the gas was inducted at ambient pressure and compressed (to 829.440 kPa) with the maximum conceivable efficiency as part of its contactor process. Consequently, significant energy savings associated with gas compression/CO₂ dissolution should be expected by adopting a HAC system as a liquid/gas contactor over a co-current up-flow bubble column. The input pressures of the HAC downcomer and bubble column were 101.325 and 884.860 kPa, respectively. When the inlet pressure of the upward co-current bubble column was considered the same as the delivery pressure of the HAC downcomer, the outlet pressure of the bubble column became slightly negative. Thus, in the simulation, the inlet pressure of the bubble column was set slightly higher than the delivery pressure produced by the HAC downcomer. The pressure loss in the air-water mixing process of the HAC downcomer was the principal reason for this small difference.

Figure 9-1 shows the concentration profiles of gases dissolved in water predicted by the model. The concentrations of N₂(aq) and Ar (aq) increased as the lengths of the HAC downcomer and bubble column increased. The HAC downcomer provided more dissolved gases in the water than the bubble column.

Table 9-1: Summary of input parameters for the simulation

Input parameter	Downcomer HAC	Bubble column
Input water mass flow rate (kg/s)	401.27	401.27
Input air mass flow rate (kg/s)	0.109	0.109
Input pressure (kPa)	101.325	884.860
Input temperature (K)	293.15	293.15
Shaft diameter (m)	0.368	0.368
Shaft length (m)	80.95	80.95
Flow direction (°)	-90	90
Absolute roughness (m)	1×10^{-3}	1×10^{-3}
Input gas relative humidity (%)	100	100
No. segments	60	60

Table 9-2: Mixtures of air and input gas

Mixture	N₂	O₂	Ar	CO₂
Atmospheric dry mol fractions	0.7808	0.2095	0.0093	0.0004
Input gas dry mol fractions	0.75	0.05	0.01	0.19

The concentrations of dissolved CO₂ at the end of the HAC downcomer and bubble column are 1.59 and 1.49 mol/m³ respectively. The CO₂ dissolved by the HAC is consistently higher than an equivalent upward co-current flow bubble column. This statement holds true across all comparative simulations, despite the small difference. As shown in Figure 9-1, the concentration of dissolved CO₂ in the HAC downcomer increased to 1.50 mol/m³ at 21.95 m and then asymptotically increased to 1.59 mol/m³ at the end of the HAC downcomer. However, the concentration of dissolved CO₂ in the bubble column increased to 1.59 mol/m³ at 35.08 m up its length and then decreased to 1.49 mol/m³ at the uppermost end of its column. The HAC downcomer provided approximately 6.25% more dissolved CO₂(aq) than the bubble column. This HAC downcomer performance margin of superiority was lower than expected. However, based on the work presented earlier in this thesis, the reasons for this are i) saturated solution with CO₂ and ii) system losses.

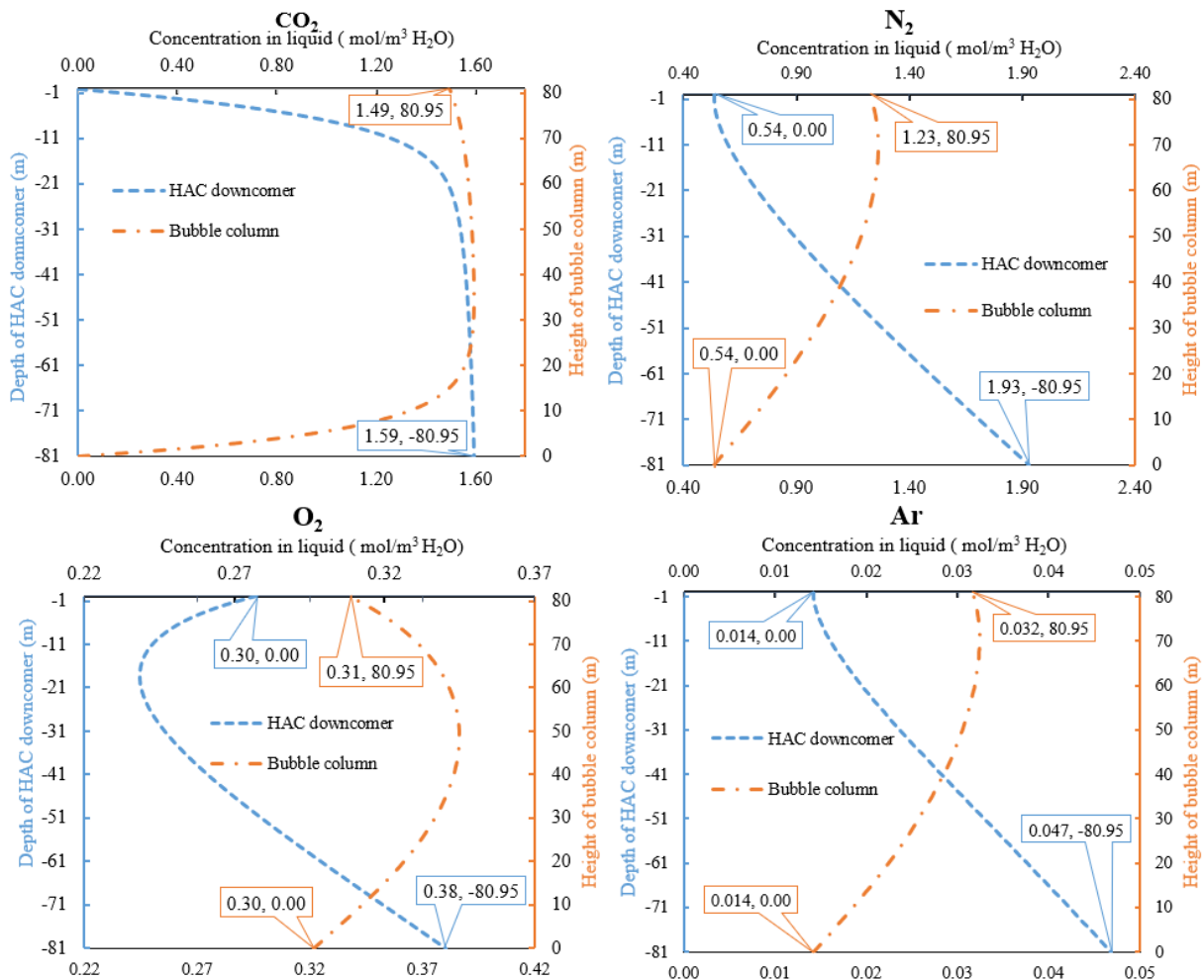


Figure 9-1: Concentration profiles of the liquid in the HAC downcomer and bubble column predicted by the model

Figure 9-1 shows that the water was supersaturated with O_2 at the HAC inlet. Because the HAC downcomer had a lower inlet pressure than the bubble column, the dissolved O_2 first exited the solution in the HAC downcomer. However, a higher initial pressure in the bubble column caused more O_2 to dissolve in the water. As the lengths of the HAC downcomer and bubble column increased, the pressure in the HAC downcomer also increased, resulting in more O_2 being initially dissolved in the water. In contrast, the pressure in the bubble column decreased, causing O_2 to escape from the solution. Figure 9-2 shows that the concentration of the remaining oxygen gas in

the HAC off-gas increased and then decreased along the length of the HAC downcomer. However, the remaining O₂ in the off gas increased in the bubble column.

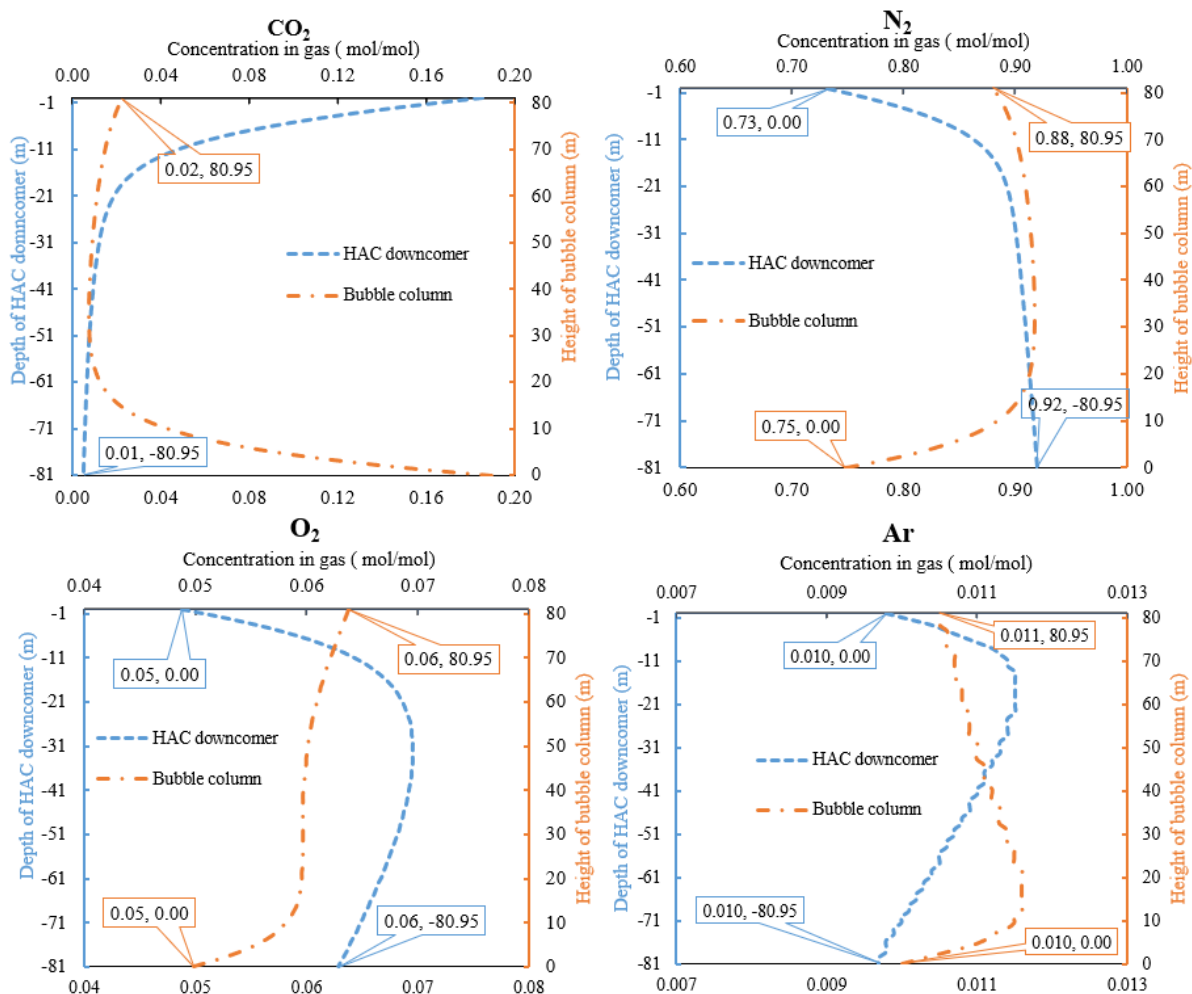


Figure 9-2: Concentration profiles of the gas in the HAC downcomer and bubble column predicted by the model

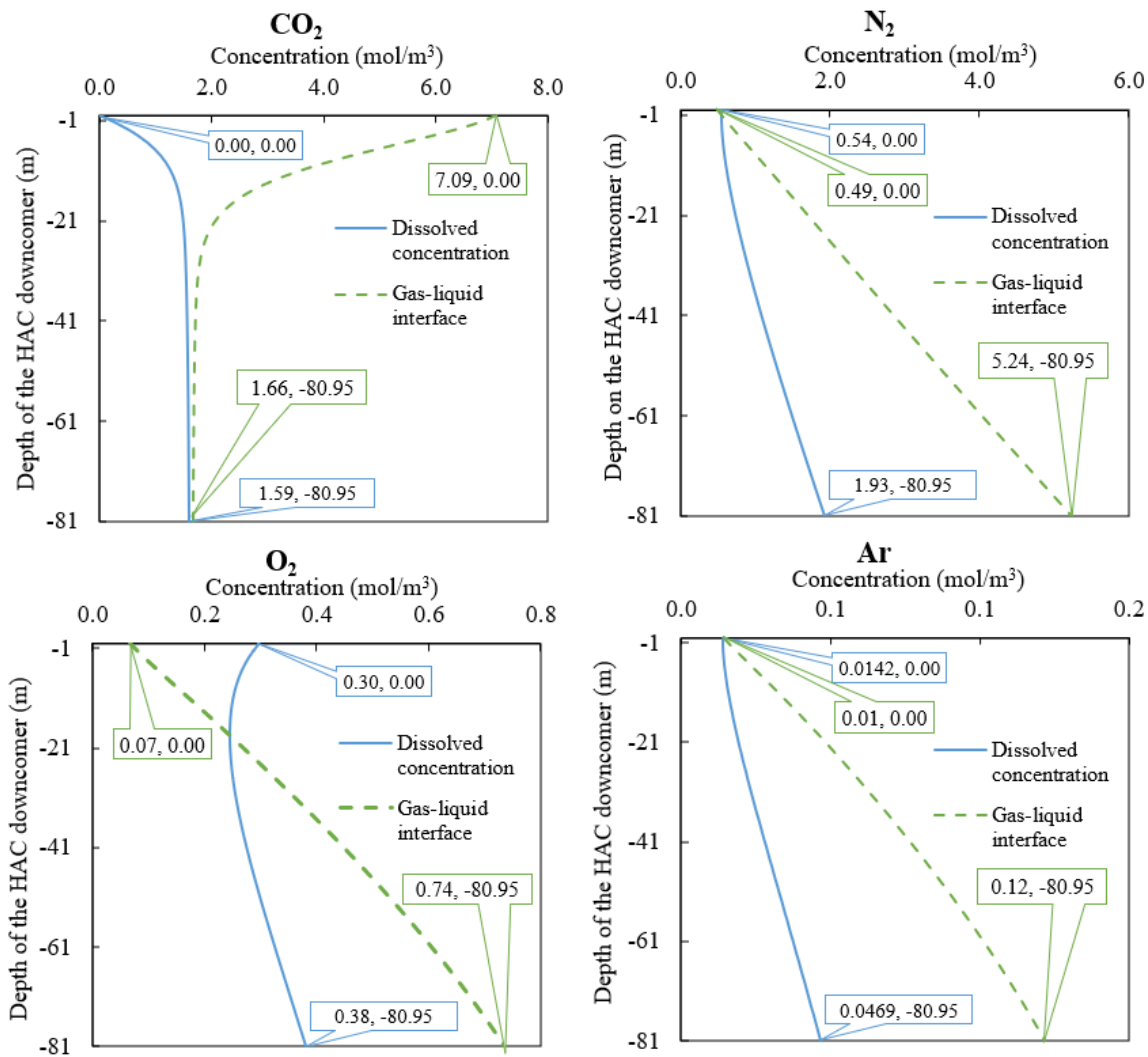


Figure 9-3: Liquid concentration profile of the gas species at the gas-liquid interface in each section of the downcomer

Figure 9-3 and Figure 9-4 show the concentration of CO₂ at the gas-liquid interface was high when the pressure was high in both systems. The concentration of CO₂ at the gas-liquid interfacial area was calculated according to the local gas composition and pressure.

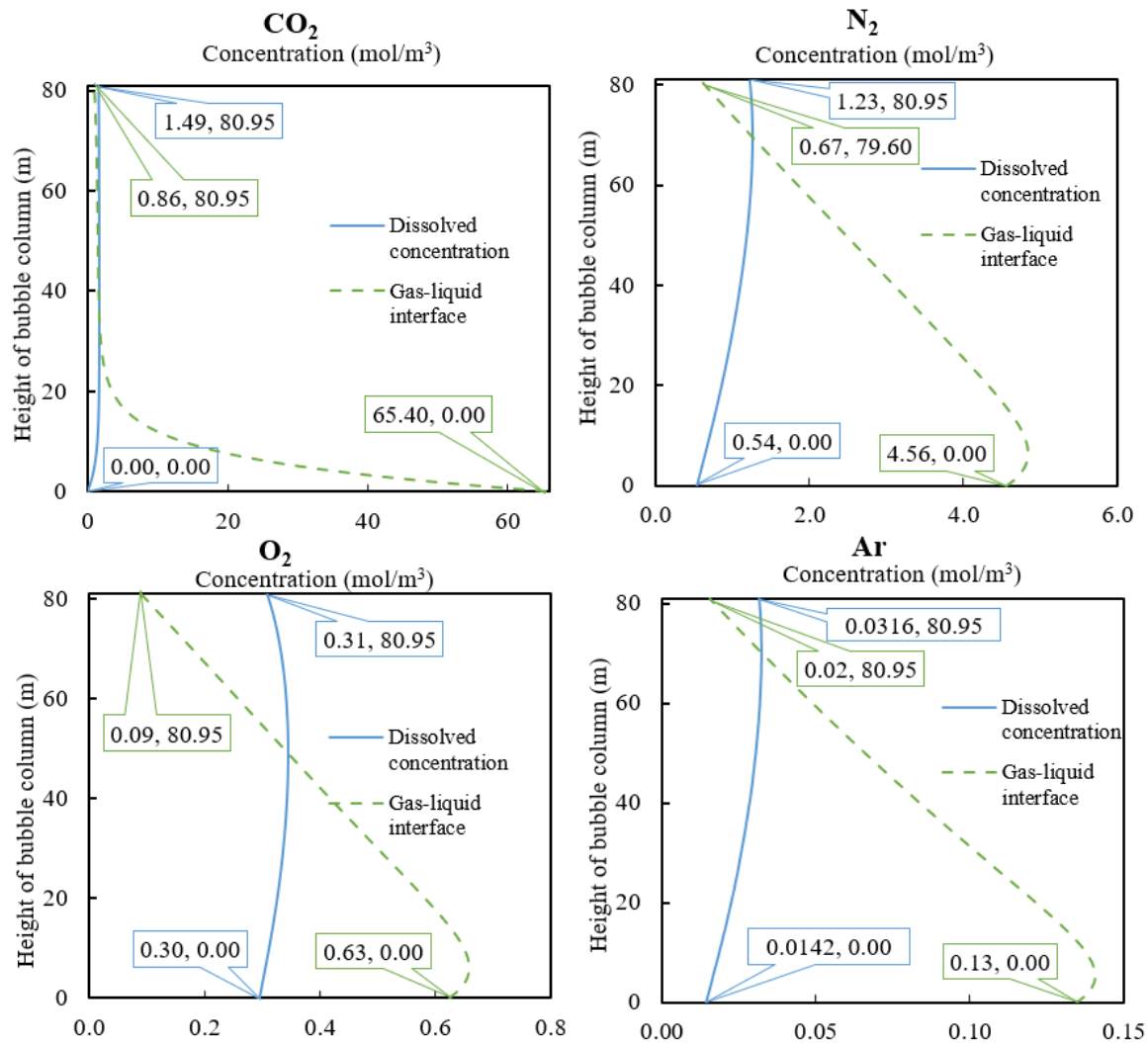


Figure 9-4: Liquid concentration profile of the gas species at the gas-liquid interface in each section of the downcomer

In Young *et al.* (2022) the sign convention adopted for gas slip velocity was positive in the flow direction. Therefore, the gas-slip velocity of the HAC downcomer was positive. The gas bubbles moved in the direction of water flow through the downcomer, and their slip velocity decreased from 0.36 m/s to 0.27 m/s. However, the gas bubbles in the bubble column moved in the opposite direction of the water flow, and their slip velocity also decreased from -0.34 to -0.41 m/s (Figure 9-5). A positive slip velocity indicated that the liquid moved faster than the gas,

whereas a negative slip velocity indicated the opposite. As the slip velocity became more negative in the flow direction within the bubble column, the absolute velocity of the gas increased as the bubbles increased in the column.

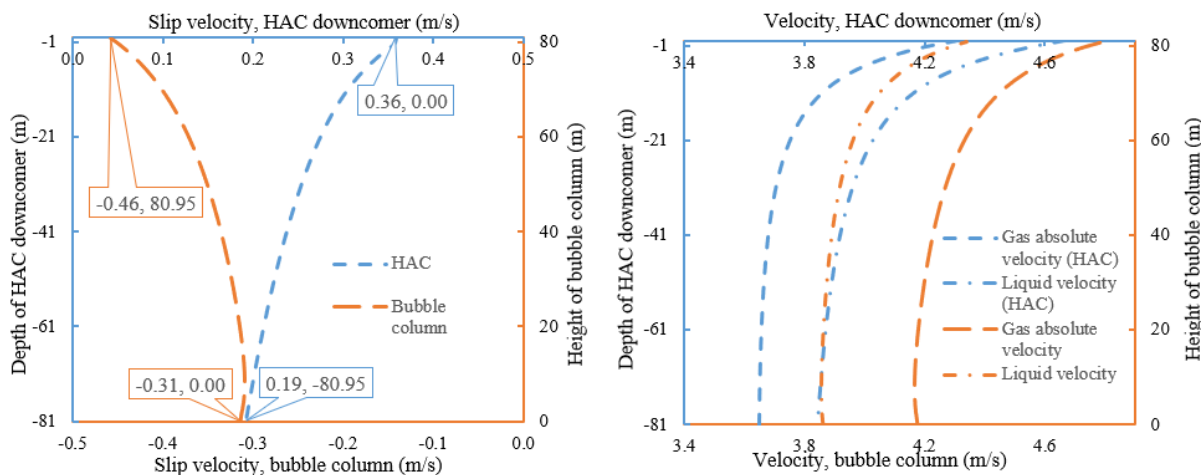


Figure 9-5: The variation of slip velocity, gas and liquid velocity in the HAC downcomer and bubble column

The bubble size decreased throughout the HAC system in the flow direction, whereas the number of gas bubbles remained constant in the bubbly flow model. As the size of the bubbles decreased, the interfacial area between the gas and liquid phases also decreased. The total interfacial area available for the HAC downcomer was 414.35 m².

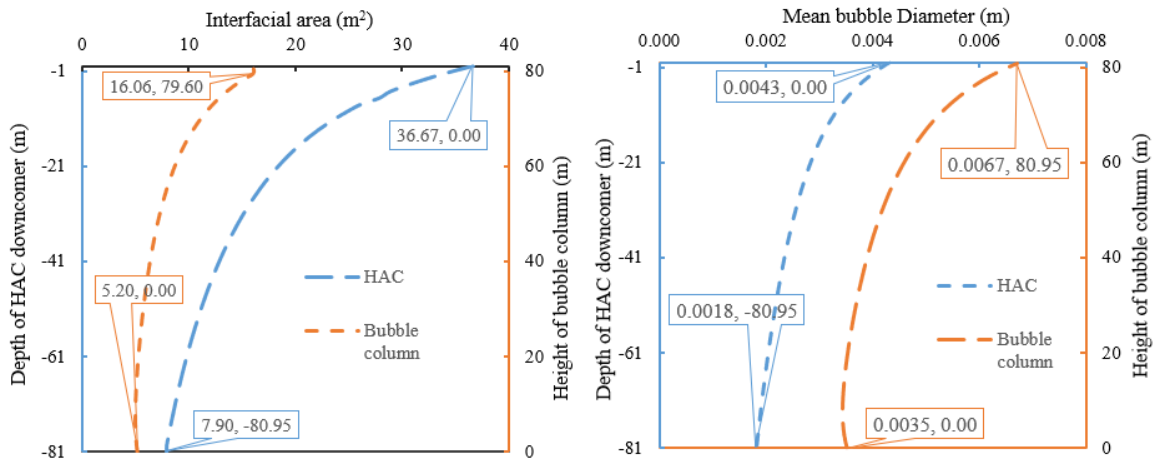


Figure 9-6: The mean bubble diameter and interfacial area of the HAC downcomer and bubble column

The size of air bubbles in the HAC downcomer was smaller than those in the bubble column. However, the HAC produced a larger interfacial area than the bubble column.

The higher inlet pressure for the bubble column increased the interfacial concentration and initially drove more gas into the solution at the inlet end compared to the mass transfer at the HAC inlet end, where the pressure was low. The local interfacial area of the HAC at the inlet was larger than that of the bubble column at the inlet due to lower gas density.

9.3 The advantage of HAC downcomer over bubble column

The HAC could be considered a co-current downward bubble column that provides slightly higher mass transfer rates compared to co-current upward bubble columns. This is due to the increased contact time between the gas and liquid phases, resulting in longer residence time, and better mixing of the phases. As mentioned earlier, the HAC downcomer yields a 6.26% increase in dissolved CO₂ (aq) compared to the bubble column.

In the context of liquid/gas contactor systems, it is crucial to acknowledge the fundamental differences between the co-current up flow bubble column and the HAC downcomer. Specifically, in the case of the co-current up flow bubble column, any gas that is introduced into the column at its base must undergo compression first to reach the requisite column base pressure. In contrast, the HAC system operates by inducing gas at ambient pressure and achieving maximum compression efficiency as an integral part of the contactor process. As a result, it is reasonable to anticipate that significant energy savings associated with gas compression and CO₂ dissolution can be realized by adopting the HAC system as a liquid/gas contactor instead of the co-current up flow bubble column.

9.4 Comparison of the HAC and HIL

The horizontal injector loop (HIL) was developed specifically to investigate the at-pressure aqueous mineral carbonation of this work, but in design, fabrication and testing of the HIL as a compressor only, not a pressurized flow chemical reactor, a new variant of HAC, the HIL, has emerged which is expected to possess the energy efficiency characteristics of a HAC and has been shown to possess the mass transfer performance characteristics of a HAC, without the requirement for significant vertical extent of the process structure.

Irrespective of the progress relating to CO₂ capture and sequestration presented in this work, as a gas compressor alone, the HIL developed in this work appreciably improves the commercial prospects of HAC technology by substantially reducing the capital expenditures required for commercial developments. The significant vertical extent has been the determining factor in the capital expenditure required for the construction of HACs of commercial scale. The reduced (i.e. nominal) height of the HIL coupled with the lower energy input costs, and the expected reduced

maintenance costs, may permit HAC systems to compete more strongly with incumbent, mainstream compressor technologies.

A second significant development enabled by the HIL, which is absent in the HAC, is the ability to adjust the compressed gas delivery pressure in the HIL. Such a capability is simply absent in the HAC, as the delivery pressure is essentially fixed by the elevation difference between the separator operating water level (SOWL) and the tailrace operating water level (TOWL) in the HAC – at design time. Relatively small variations in HAC delivery pressure are possible, but the range of delivery pressure variation is restricted to the permissible elevation head variation in either of the aforementioned vessels (the vessel height). In contrast, in the HIL, the gas delivery pressure can be varied from zero to close to the circulating pump delivery pressure at the HIL nozzle inlet, albeit with corresponding variations in the mass flow rate of induced gas. Against this benefit, there is also a minor loss. The variation of water levels in a HAC essentially provided variable, nearly constant pressure, receiver capacity which at periods of very low demand for compressed gas enabled the circulating pump to be shut down completely while compressed air demand was met from storage. With the HIL concept, all liquid levels are steady during operation and while stopped. There is no available constant pressure, variable volume, and energy storage capacity.

It is said that the HIL is “expected” to possess the same gas compression energy efficiency performance as HACs of great vertical extent because this has yet to be proven through direct experimental observation of nearly isothermal compression between injector throat and separator inlet. Against this circumstance, the assertion remains because every mathematical formulation of liquid-gas injectors, educators, venturi mixers, etc. found in the literature (Atay, 1986; Bhat *et al.*, 1972; Choi *et al.*, 2015; Kandakure *et al.*, 2005; Manzano *et al.*, 2018; Opletal *et al.*, 2018; Witte,

1969b; Zahradník *et al.*, 1997) features isothermal or near isothermal compression of the gas phase, for the same reasons as have been identified to explain the superior gas compression efficiency of the HAC. These are high interfacial heat transfer area between the phases, of order 1000 times higher mass transfer of the denser, liquid phase and approximately 4 times higher specific heat capacity of the liquid over the gas. The interfacial heat transfer area is the same as the interfacial mass transfer area: the surface area of the bubbles in the 2 phase flow. Most of the seminal works on injector formulations also publish experimental data confirming the performance expected on the bases of their respective models. Direct experimental confirmation of the near isothermal nature (~ 10 mK) of the compression of gas has been proven for a demonstration scale HAC with a 23 m tall vertical downcomer by Millar *et al.* (2019), but direct experimental verification of such nearly isothermal compression for the gas remains to be found for HACs following the HIL HAC variant developed as part of this thesis. Given the contributions of so many injector investigators in the literature, such experimental proof was deemed outside the scope of this thesis, but experimental verification is already the subject of ongoing research.

Consequently, the HIL delivers comparable performance with reduced height and lower capital cost, thereby increasing its feasibility for carbon capture and sequestration projects constrained by capital resources. The experimental results presented in this study provide evidence that HIL is a potentially viable technology for CO₂ capture and sequestration.

9.5 The HAC or the HIL as a carbon capture and sequestration device

Work presented in this thesis has shown that there are two products to be expected of either a HAC of significant vertical extent, or a HIL of nominal vertical extent, when integrated in a process designed for CO₂ capture and sequestration from a post-combustion flue gas:

- 1) a solid CaCO₃ filtrate,
- 2) pneumatic power,

The conversion efficiency of CO₂ to CaCO₃ was not definitively shown to be close to 100% in this work, but the highest yield of CaCO₃ proven was 73% of the amount expected, despite the difficulties associated with filtrate recovery from the HIL laboratory apparatus. Experimental concentrations of CO₂ in offgas were proven to be around 2 orders of magnitude lower than concentrations provided at inlet. Solid-liquid separation technology is well established for many industrial processes, including those for the commercial production of precipitated calcium carbonate (Li *et al.*, 2016; Svarovsky, 2000; Wakeman and Tarleton, 2005; Wu *et al.*, 2013). This is why, the work in this thesis did not prioritize high precipitate recovery in the design of the lab apparatus and this aspect of poor performance of the lab scale HIL apparatus is in no way envisaged to be an impediment to process scale up for commercial capture and sequestration applications.

As a post-combustion product, the CO₂ rich flue gas that was inducted into the HAC/HIL is expected to have high temperature. When the hot gas and the circulating water initially mix, the inlet gas temperature is expected to fall as a result of heat transfer to the circulating liquid. While the gas compression process thereafter may still be near isothermal, the elevated circulating liquid

temperature will diminish the compression efficiency of the appliance due to psychrometric behavior. Elevated temperature, at the low pressure gas inlet to the HAC/HIL, increases the saturation moisture content of the gaseous phase which permits greater mass transfer of water from the circulating liquid solution. Consequently, as the circulating liquid temperature rises, an increasing proportion of the compression work applied by the HAC/HIL ends up compressing water vapour that will ultimately condense as the pressure rises and the liquid water will rejoin the circulating solution. The compression work expended becomes lost.

To avoid this deleterious mechanism, the HAC/HIL circulating liquid requires active cooling to maintain the circulating liquid temperature to below $\sim 35^{\circ}\text{C}$. This could be achieved by means of a conventional cooling loop present within the HAC/HIL flow circuit coupled to an external reservoir of cooling: the atmosphere or, if available, cooling water from a river or a lake. If, at the site of carbon capture and sequestration, no demand exists for pneumatic power, then the gases compressed by the HAC/HIL may simply be expanded by passing them through a turbine stage. Thereby the compressed gas stream will develop work as it depressurizes and expands so that some of the input power used in circulating pumps can be recovered. Given that the gas expansion will commence from a temperature around 35°C , the gas temperature after expansion will be appreciably below zero for compressor pressure ratios between 4 and 8. Passing the cold expanded gas through an indirect heat exchanger across the hot inlet post-combustion flue gas will cause the latter to be pre-cooled before being inducted into the HAC/HIL system. The mass flow of the expanded coolant gas will be approximately equal to the mass flow of the inlet flue gas (less that mass flow of CO_2 separated and sequestered), reducing (but not eliminating) the demand for HAC/HIL liquid phase cooling from external sources. Even if the coolant gas completely reduces

the inlet gas temperature to that of the circulating liquid, the gas compression heat will still require discharge from the system. A key point in this discourse is that even if there is no demand for the pneumatic power product at the capture and sequestration site, it can nevertheless be used to develop appreciable cooling.

9.5.1 CO₂ mineralization via HAC/HIL

Direct aqueous carbonation is generally considered the most promising mineral carbonation route due to its relatively low energy requirements, high carbonation efficiency, and scalability potential (Bobicki *et al.*, 2012a; O'Connor *et al.*, 2000; Pan *et al.*, 2018d, 2015b; Sanna *et al.*, 2014b). In the work presented in this thesis, Ca(OH)₂ aqueous solution is considered as the source of calcium ions for carbonation process. Simple oxides and hydroxides of Ca display the highest carbonation yields, while neutral silicate materials and alkaline waste residues are less susceptible to carbonation and exhibit varying carbonation degrees depending on their specific structural composition and chemical properties.

A number of factors may affect the ranking of affinity toward CO₂ observed for pure mineral phases in real industrial residues, including the size of the particles, the presence of impurities, the degree of ion substitutions in crystals, and the accessibility of reactive components within the crystal (Chiang and Pan, 2017a; Poletini *et al.*, 2016; Zheng *et al.*, 2022).

CaO is rarely present in pure form in alkaline solid wastes, thus the leaching of calcium in solid particles plays a critical role in determining the efficiency of mineral carbonation. The dissolution of calcium components in solid wastes is favored at low pH and high temperature, which is, however, not favored for the precipitation of CaCO₃. To determine the feasibility of using

alkaline solid wastes as the feedstock for mineral carbonation, a series of experiments by HIL is necessary.

The dynamic kinetic model should also be modified to simulate the performance of mineral carbonation using a CaO-based material (heterogeneous solution). The current model does not feature the particle size of the produced CaCO₃. The system is considered homogeneous in that the kinetics of the nucleation and growth of calcium carbonate particles are not considered. When the system is heterogeneous, focus is retained on the dynamics of solid particle growth and several theoretical models have been put forward, such as the random pore model (RPM) when mineral wastes are considered the feedstock (Morales-Flórez *et al.*, 2015), the overlapping grain model (Liu *et al.*, 2012) the shrinking core model (for dissolution of, e.g. Ca(OH)₂, mineral silicates) (Johnsen *et al.*, 2006), and the surface coverage model (Pan *et al.*, 2014).

9.5.2 Prospects for commercial scale CO₂ capture and sequestration

The purpose of the present research was investigation of the feasibility of carbon capture and sequestration of CO₂ by Ca(OH)₂ aqueous mineral carbonation in a pressurized continuous reactor. Generally, CCS methods often involve significant capital and operating costs due to the large reactor sizes required to overcome the significant mass transfer resistances between phases.

The capture and sequestration of CO₂ from flue gases or other industrial processes requires specialized equipment which makes the process energy-intensive and complicated. The reaction time of capturing CO₂ from the gas stream is inversely proportional to the concentration of CO₂ present in the gas stream, meaning that when the concentration of CO₂ is low, the duration of the

capturing process is longer (Chiang and Pan, 2017b). Therefore, it is essential to develop technologies to capture and sequester CO₂ from industrial processes even at low concentrations.

This study provides significant information on post-combustion CO₂ capture and sequestration techniques, with a specific focus on mineral carbonation process routes and potential feedstocks for CO₂ sequestration. There is no doubt that mineral carbonation is a promising technology due to its abundant resource availability and enhanced security over other methods of sequestering CO₂. However, this technology is still relatively new, and transport and storage costs could remain higher compared to geological storage in sedimentary basins.

According to Sanna *et al.* (2014), the cost of mineral carbonation technology was estimated to be \$17 per tCO₂, whereas geological storage in sedimentary basins is estimated at \$8 per tCO₂. However, there have been many developments and process improvements in mineral carbonation concepts and technologies, as exemplified by the work in this thesis, that means the nearly decade old estimate of Sanna *et al.* (2014) needs to be revisited. Augmenting the work presented herein with a robust economic assessment is a priority topic for further work. However, the potential of using industrial waste materials as feedstocks for mineral carbonation offers a sustainable and cost-effective approach to reducing CO₂ emissions and promoting sustainable waste management practices.

10. Conclusions, contributions, and future work

10.1 Conclusions

In recent years, there has been a significant focus on reducing the capital and operating expenses associated with CO₂ capture and minimizing the energy impact. This study presented a literature review of the equilibria and kinetics of reactions related to the mineral carbonation process. This review aimed to collect relevant equilibrium, solubility, and kinetic constants to develop a mathematical dynamic kinetic model for chemical systems. The accuracy of the dynamic kinetic model was verified by comparing the model results with experimental data reported in the literature, and the comparison indicated a good level of agreement between them.

The carbonation reaction rate was influenced by the gas-liquid mass transfer rate, availability of CO₂ (aq) species in solution, and rate of dissolution of solid Ca(OH)₂ under varying pH conditions. In contrast, the dissolution of CO₂ (g) into CO₂ (aq) was slow because of the resistance between the two phases. Increasing the pressure could accelerate the carbonation reaction rate, making HAC a better technology for intensifying carbon capture and sequestration because of its high mass transfer performance compared to conventional bubble columns or spray towers. However, a high rate of Ca(OH)₂ dissolution was necessary to maintain carbonation at high pH; otherwise, higher rates of CO₂ dissolution would lower the pH and produce soluble bicarbonate species. In a reaction sequence using Ca(OH)₂, the rate of CaCO₃ production or CO₂ sequestration depended on the solution rate of alkaline earth metal oxides and hydroxides. The chemical effect of the Ca(OH)₂ in solution on the CO₂ absorption rate was represented by an enhancement factor.

Young *et al.* (2022) bubbly flow models, which simulated the hydrodynamic and mass transfer processes in HAC downcomers and bubble column reactors, demonstrated how HACs could achieve high rates of CO₂ dissolution from flue gas streams, leading to high concentrations of CO₂ (aq). The accuracy of the model was verified experimentally, and there was good agreement between the experimental results and model predictions. The verified model was utilized to estimate the required pressure for dissolving enough CO₂ for a carbon capture and sequestration process and the volumetric mass transfer coefficient of CO₂ in the solution ($k_L a_{CO_2}$) for the dynamic kinetic model of mineral carbonation.

Despite the HAC's high mass transfer performance compared to conventional bubble columns, the suitability of HAC technology for carbon capture and sequestration was constrained by the significant size and capital cost of its unit, particularly when following the general Millar (2014) design paradigm. To address this challenge, a new apparatus, the HIL, was introduced to increase the mass transfer rates between the phases and improve mixing while retaining desirable gas compression efficiencies.

The HIL test rig, a variation of the HAC system, incorporated a Venturi injector that effectively distributed gas into the circulating liquid within the system, making it an ideal test reactor for validating the expected performance of the CO₂ capture and sequestration system. It had a significantly larger bubble contact area and promoted effective agitation through the circulation of solids, liquids, and gases within the rig. One significant advantage of the HIL was its ability to easily control the delivery pressure without requiring changes in the HAC height. Another benefit of the HIL is its anticipated ability to achieve practical isothermal gas compression, making temperature control possible.

During testing in the HIL rig, the gas mass flow rates generated by the injector were aligned with the values specified in the manufacturer's injector performance table, considering the particular conditions of injector delivery and separator pressure. Overall, the HIL worked as designed, using air and water.

The HIL, conceived as a pressurized continuous chemical reactor, was subsequently tested to determine its capability as a CO₂ capture and sequestration device. Therefore, the rig was filled with a Ca(OH)₂ suspension solution, and air, enriched with controlled mass flows of CO₂, was inducted into the system via the injector. The injector served not only to induct and compress the gas phase but also to distribute the gas and create CO₂-enriched bubbles for effective dissolution into the alkaline solution. The gas phase was pressurized in the injector-diffuser. As Ca(OH)₂ dissolved and reacted with the dissolved CO₂ in the HIL, a CaCO₃ precipitate was formed, which altered the chemistry of the circulating fluid into a dilute slurry with a different solid component. These experiments confirmed the feasibility of using the HIL as a carbon capture and sequestration device. The results of these experiments were simulated using a dynamic kinetic model which showed good agreement with the experimental results. Despite this, certain enhancements to the dynamic kinetic model have been identified to improve its compatibility with the experimental conditions.

10.2 Original contributions

Major contributions of this thesis are summarized below:

- Provide a comprehensive literature review on the process chemistry and kinetics of the reactions for CO₂ capture and sequestration using aqueous Ca(OH)₂ solutions to formulate a mathematical model for the chemical reactions within the systems (Chapter 3).
- Introduce and characterize HAC as a gas-liquid contactor systems that utilize a co-current downward bubble column to enhance the gas-liquid mass transfer (Chapter 4).
- Discuss the effect of different variables on the mass transfer coefficient in a bubble flow column and introduce a new method for calculating $k_L a$ in the gas-liquid contactor using the Young *et al.* (2022) bubbly flow model. The hydrodynamic and mass transfer of the HAC downcomer is investigated (Chapter 4).
- Experimental verification of a one-dimensional steady-state Young *et al.*, (2022) bubbly flow model. This work also offered the first direct experimental proof of the exsolution of dissolved gas in a HAC riser, measured at the tailrace (Chapter 5).
- Introduce and characterize HIL as a new apparatus to improve mass transfer rates and overcome the limitations of HAC technology for carbon capture and sequestration. A significant advantage of the HIL is that the delivery pressure can be easily controlled without changing the HAC height (Chapter 6).
- Experimental investigation of HIL as pressurized continuous chemical reactors for CO₂ capture and sequestration (Chapter 7).
- Simulate the mineral carbonation experiments of the HIL using the dynamic kinetic model and show good agreement with the experimental results (chapter 8).
- Compare the hydrodynamics and mass transfer of HAC downcomers and upward co-current flow bubble column reactors (Chapter 9).

10.3 Future work

Future work to be conducted from this work are as follows:

- Enhance the accuracy of the bubbly flow model to simulate the gas-liquid mass transfer in the injector diffuser effectively and include the reaction kinetics of carbonate equilibrium in aqueous systems to improve the prediction of CO₂ separation
- Improve dynamic kinetic model accuracy by addressing potential improvements such as recalculating equilibrium and kinetic coefficients based on experimental conditions, including activity coefficients in pH calculations, obtaining precise Ca(OH)₂ particle diameter measurements, and accurately determining k_{LA} .
- HIL systems configured for CO₂ capture and sequestration require refinement to demonstrate that the process can be effectively scaled up from the laboratory scale reported herein.
- The HIL process uses pure Ca(OH)₂ and a gas stream containing CO₂ to sustain sequestration. Further research is required to investigate the ability of this process to accommodate more complex alkaline earth metal ion feedstocks and more realistic simulated gas streams containing potentially contaminating gas species.
- Further investigations are required to study the possibility of the separation of separating precipitated CaCO₃ in a continuous reactor and utilizing the by-product for commercial purposes. If the use of CaCO₃ becomes commercialized, there is a risk that the sequestered CO₂ will be de-sequestered. Life cycle analysis of the process using CaCO₃ should be

undertaken to determine whether it is more favorable to permit CaCO_3 precipitates to sediment and consolidate for permanent storage, as in geological processes.

- Undertake carbonation experiments at the pilot plant scale using the same experimental conditions as those tested at the laboratory scale. Then, perform a comparative study between the two scales.
- Perform a life cycle assessment and energy requirements analysis to evaluate the economic and technical feasibility of mineral carbonation under specific experimental conditions.

10.4 PhD Journey: learnings and future directions

Throughout my PhD journey, I gained important knowledge and abilities. I discovered that persistence is crucial in research, even when things don't go as planned. I improved my thinking and problem-solving skills, which helped me tackle the complex issues prevalent in the research.

Looking ahead, I want to share my research by publishing papers and presenting at conferences. I'm also excited about collaborating with others and mentoring students. In the long run, I aim to work in the mining industry where I can apply my skills to solve real-world problems.

In summary, my PhD has prepared me to make a positive impact in my field. I'm eager to continue learning and contributing to my future endeavors.

11. References

- Abdul Majeed Saed, R., 2003. Bubble Column Hydrodynamic Study with Experimental Investigation and CFD Computations (Master Thesis). Nahrain University.
- Abu Reesh, I.M., 2021. Acrylonitrile Process Enhancement through Waste Minimization: Effect of Reaction Conditions and Degree of Backmixing. *Sustainability* 13, 7923. <https://doi.org/10.3390/su13147923>
- Aghajanian, S., Koiranen, T., 2020. Dynamic modeling and semibatch reactive crystallization of calcium carbonate through CO₂ capture in highly alkaline water. *Journal of CO₂ Utilization* 38, 366–374. <https://doi.org/10.1016/j.jcou.2020.02.018>
- Al-Jaroudi, S.S., Ul-Hamid, A., Mohammed, A.-R.I., Saner, S., 2007. Use of X-ray powder diffraction for quantitative analysis of carbonate rock reservoir samples. *Powder Technology* 175, 115–121. <https://doi.org/10.1016/j.powtec.2007.01.013>
- Allen, D.T., 2019. Gaseous Carbon Waste Streams Utilization: Status and Research Needs. Committee on Developing a Research Agenda for Utilization of Gaseous Carbon Waste Streams. <https://doi.org/10.17226/25232>
- Altiner, M., Top, S., Kaymakoğlu, B., Seçkin, İ.Y., Vapur, H., 2019. Production of precipitated calcium carbonate particles from gypsum waste using venturi tubes as a carbonation zone. *Journal of CO₂ Utilization* 29, 117–125. <https://doi.org/10.1016/j.jcou.2018.12.004>
- Amaral, A., Gillot, S., Garrido-Baserba, M., Filali, A., Karpinska, A.M., Plósz, B.G., De Groot, C., Bellandi, G., Nopens, I., Takács, I., Lizarralde, I., Jimenez, J.A., Fiat, J., Rieger, L., Arnell, M., Andersen, M., Jeppsson, U., Rehman, U., Fayolle, Y., Amerlinck, Y., Rosso, D., 2019. Modelling gas–liquid mass transfer in wastewater treatment: when current knowledge needs to encounter engineering practice and vice versa. *Water Science and Technology* 80, 607–619. <https://doi.org/10.2166/wst.2019.253>
- Andrade, C., Sanjuán, M., 2018. Updating Carbon Storage Capacity of Spanish Cements. *Sustainability* 10, 4806. <https://doi.org/10.3390/su10124806>
- Andreussi, P., Paglianti, A., Silva, F.S., 1999. Dispersed bubble flow in horizontal pipes. *Chemical Engineering Science* 54, 1101–1107. [https://doi.org/10.1016/S0009-2509\(98\)00289-9](https://doi.org/10.1016/S0009-2509(98)00289-9)
- Annan, M., Gooda, E.A., 2018. Effect of minor losses during steady flow in transmission pipelines – Case study “water transmission system upgrade in Northern Saudi Arabia.” *Alexandria Engineering Journal* 57, 4299–4305. <https://doi.org/10.1016/j.aej.2018.12.002>

- Arakaki, T., Mucci, A., 1995. A continuous and mechanistic representation of calcite reaction-controlled kinetics in dilute solutions at 25C and 1 atm total pressure. *Aquat Geochem* 1, 105–130. <https://doi.org/10.1007/BF01025233>
- Atay, I., 1986. Fluid flow and gas absorption in an ejector venturi scrubber. New Jersey Institute of Technology.
- Atkins, P., Atkins, P.W., Paula, J. de, 2014. *Atkins' Physical Chemistry*. OUP Oxford.
- Azadi, M., Edraki, M., Farhang, F., Ahn, J., 2019. Opportunities for Mineral Carbonation in Australia's Mining Industry. *Sustainability* 11, 1250. <https://doi.org/10.3390/su11051250>
- Azdarpour, A., Asadullah, M., Mohammadian, E., Hamidi, H., Junin, R., Karaei, M.A., 2015. A review on carbon dioxide mineral carbonation through pH-swing process. *Chemical Engineering Journal* 279, 615–630. <https://doi.org/10.1016/j.cej.2015.05.064>
- Baes, C.F., Mesmer, R.S., 1977. The Hydrolysis of Cations. *Berichte der Bunsengesellschaft für physikalische Chemie* 81, 245–246. <https://doi.org/10.1002/bbpc.19770810252>
- Bai, W. (Wei), 2010. Experimental and numerical investigation of bubble column reactors (PhD). Eindhoven University of Technology.
- Balamurugan, S., Lad, M.D., Gaikar, V.G., Patwardhan, A.W., 2007. Hydrodynamics and mass transfer characteristics of gas–liquid ejectors. *Chemical Engineering Journal* 131, 83–103. <https://doi.org/10.1016/j.cej.2006.12.026>
- Bałydyga, J., Henczka, M., Sokolnicka, K., 2010. Utilization of carbon dioxide by chemically accelerated mineral carbonation. *Materials Letters* 64, 702–704. <https://doi.org/10.1016/j.matlet.2009.12.043>
- Bates, R.G., Bower, V.E., Smith, E.R., 1956. Calcium hydroxide as a highly alkaline pH standard. *J. RES. NATL. BUR. STAN.* 56, 305. <https://doi.org/10.6028/jres.056.040>
- Besagni, G., Inzoli, F., Ziegenhein, T., 2018. Two-Phase Bubble Columns: A Comprehensive Review. *ChemEngineering* 2, 13. <https://doi.org/10.3390/chemengineering2020013>
- Bhat, P.A., Mitra, A.K., Roy, A.N., 1972. Momentum transfer in a horizontal liquid-jet ejector. *Can. J. Chem. Eng.* 50, 313–317. <https://doi.org/10.1002/cjce.5450500301>
- Biń, A.K., Duczmal, B., Machniewski, P., 2001. Hydrodynamics and ozone mass transfer in a tall bubble column. *Chemical Engineering Science, Proceedings of the 5th International Conference on Gas-Liquid and Gas-Liquid-Solid Reactor Engineering* 56, 6233–6240. [https://doi.org/10.1016/S0009-2509\(01\)00213-5](https://doi.org/10.1016/S0009-2509(01)00213-5)

- Blomen, E., Hendriks, C., Neele, F., 2009. Capture technologies: Improvements and promising developments. *Energy Procedia* 1, 1505–1512. <https://doi.org/10.1016/j.egypro.2009.01.197>
- Bobicki, E.R., Liu, Q., Xu, Z., Zeng, H., 2012. Carbon capture and storage using alkaline industrial wastes. *Progress in Energy and Combustion Science* 38, 302–320. <https://doi.org/10.1016/j.pecs.2011.11.002>
- Bockris, V.J.O., Reddy, A.K.N., 1972. *Modern electrochemistry. An Introduction to an Interdisciplinary Area.* London und Plenum Press.
- Boiler Combustion, 2022. URL <http://cleanboiler.org/learn-about/boiler-efficiency-improvement/boiler-combustion/> (accessed 3.1.22).
- Briens, C.L., Huynh, L.X., Large, J.F., Catros, A., Bernard, J.R., Bergougnou, M.A., 1992. Hydrodynamics and gas-liquid mass transfer in a downward venturi-bubble column combination. *Chemical Engineering Science* 47, 3549–3556. [https://doi.org/10.1016/0009-2509\(92\)85069-N](https://doi.org/10.1016/0009-2509(92)85069-N)
- Carpenter, S.M., Long, H.A., Wang, T., Stiegel, G., 2017. 13 - Integration of carbon capture in IGCC systems, in: *Integrated Gasification Combined Cycle (IGCC) Technologies.* Woodhead Publishing, pp. 445–463. <https://doi.org/10.1016/B978-0-08-100167-7.00036-6>
- Carroll, J.J., Slupsky, J.D., Mather, A.E., 1991. The Solubility of Carbon Dioxide in Water at Low Pressure. *Journal of Physical and Chemical Reference Data* 20, 1201–1209. <https://doi.org/10.1063/1.555900>
- Cents, A.H.G., Brillman, D.W.F., Versteeg, G.F., 2005. CO₂ absorption in carbonate/bicarbonate solutions: The Danckwerts-criterion revisited. *Chemical Engineering Science* 60, 5830–5835. <https://doi.org/10.1016/j.ces.2005.05.020>
- Chai, S.Y.W., Ngu, L.H., How, B.S., 2022. Review of carbon capture absorbents for CO₂ utilization. *Greenhouse Gases* 12, 394–427. <https://doi.org/10.1002/ghg.2151>
- Chakraborty, S., Jo, B.W., 2018. Aqueous-based carbon dioxide sequestration, in: *Carbon Dioxide Sequestration in Cementitious Construction Materials.* Elsevier, pp. 39–64. <https://doi.org/10.1016/B978-0-08-102444-7.00003-4>
- Chang, E.-E., Chiu, A.-C., Pan, S.-Y., Chen, Y.-H., Tan, C.-S., Chiang, P.-C., 2013. Carbonation of basic oxygen furnace slag with metalworking wastewater in a slurry reactor. *International Journal of Greenhouse Gas Control* 12, 382–389. <https://doi.org/10.1016/j.ijggc.2012.11.026>
- Chang, E.-E., Pan, S.-Y., Yang, L., Chen, Y.-H., Kim, H., Chiang, P.-C., 2015. Accelerated carbonation using municipal solid waste incinerator bottom ash and cold-rolling

- wastewater: Performance evaluation and reaction kinetics. *Waste Management* 43, 283–292. <https://doi.org/10.1016/j.wasman.2015.05.001>
- Chang, E.E., Wang, Y.-C., Pan, S.-Y., Chen, Y.-H., Chiang, P.-C., 2012. CO₂ Capture by Using Blended Hydraulic Slag Cement via a Slurry Reactor. *Aerosol Air Qual. Res.* 12, 1433–1443. <https://doi.org/10.4209/aaqr.2012.08.0210>
- Chang, R., Kim, S., Lee, S., Choi, S., Kim, M., Park, Y., 2017. Calcium Carbonate Precipitation for CO₂ Storage and Utilization: A Review of the Carbonate Crystallization and Polymorphism. *Frontiers in Energy Research* 5.
- Charpentier, J.-C., 1981. Mass-Transfer Rates in Gas-Liquid Absorbers and Reactors, in: *Advances in Chemical Engineering*. Elsevier, pp. 1–133. [https://doi.org/10.1016/S0065-2377\(08\)60025-3](https://doi.org/10.1016/S0065-2377(08)60025-3)
- Chen, H., Wei, S., Ding, W., Wei, H., Li, L., Saxén, H., Long, H., Yu, Y., 2021. Interfacial Area Transport Equation for Bubble Coalescence and Breakup: Developments and Comparisons. *Entropy* 23, 1106. <https://doi.org/10.3390/e23091106>
- Chen, L.-T., Rice, W., 1982. Some Psychometric Aspects of a Hydraulic Air Compressor (HAC). *Journal of Energy Resources Technology* 104, 274–276. <https://doi.org/10.1115/1.3230415>
- Chen, T.-L., Jiang, W., Shen, A.-L., Chen, Y.-H., Pan, S.-Y., Chiang, P.-C., 2020a. CO₂ Mineralization and Utilization Using Various Calcium-Containing Wastewater and Refining Slag via a High-Gravity Carbonation Process. *Ind. Eng. Chem. Res.* 59, 7140–7150. <https://doi.org/10.1021/acs.iecr.9b05410>
- Chen, T.-L., Pei, S.-L., Chiang, P.-C., 2020b. Integrated leaching–carbonation kinetic model on CO₂ mineralization of alkaline solid wastes in a high-gravity rotating packed bed. *React. Chem. Eng.* 5, 1929–1938. <https://doi.org/10.1039/D0RE00239A>
- Chiang, P.-C., Pan, S.-Y., 2017a. *Carbon Dioxide Mineralization and Utilization*. Springer Singapore, Singapore. <https://doi.org/10.1007/978-981-10-3268-4>
- Cho, H.-J., Choi, J., 2019. Calculation of the Mass Transfer Coefficient for the Dissolution of Multiple Carbon Dioxide Bubbles in Sea Water under Varying Conditions. *Journal of Marine Science and Engineering* 7, 457. <https://doi.org/10.3390/jmse7120457>
- Choi, S.H., Ji, H.S., Kim, K.C., 2015. Comparative study of hydrodynamic characteristics with respect to direction of installation of gas-liquid ejector system. *J Mech Sci Technol* 29, 3267–3276. <https://doi.org/10.1007/s12206-015-0725-6>
- Compton, R.G., Daly, P.J., 1987. The dissolution/precipitation kinetics of calcium carbonate: An assessment of various kinetic equations using a rotating disk method. *Journal of Colloid and Interface Science* 115, 493–498. [https://doi.org/10.1016/0021-9797\(87\)90066-X](https://doi.org/10.1016/0021-9797(87)90066-X)

- Cortes Garcia, G.E., van der Schaaf, J., Kiss, A.A., 2017. A review on process intensification in HiGee distillation: Process intensification in HiGee distillation. *J. Chem. Technol. Biotechnol* 92, 1136–1156. <https://doi.org/10.1002/jctb.5206>
- Covington, A.K., Bates, R.G., Durst, R.A., 1985. Definition of pH scales, standard reference values, measurement of pH and related terminology (Recommendations 1984). *Pure & Appl. Chem.*, 57, 531–542.
- Danckwerts, P.V., 1955. Gas absorption accompanied by chemical reaction. *AIChE Journal* 1, 456–463. <https://doi.org/10.1002/aic.690010412>
- Danckwerts, P.V., Sharma, M.M., 1966. The absorption of carbon dioxide into solutions of alkalis and amines: (with some notes on hydrogen sulphide and carbonyl sulphide), I. *Chem. E. review series*. Institution of Chemical Engineers, London.
- Daval, D., Martinez, I., Corvisier, J., Findling, N., Goffé, B., Guyot, F., 2009. Carbonation of Ca-bearing silicates, the case of wollastonite: Experimental investigations and kinetic modeling. *Chemical Geology, CO2 geological storage: Integrating geochemical, hydrodynamical, mechanical and biological processes from the pore to the reservoir scale* 265, 63–78. <https://doi.org/10.1016/j.chemgeo.2009.01.022>
- David Glasstone, S.L., 1962. *Elements of Physical Chemistry, Second Edition*. ed. Van Nostrand Company.
- Dean, C.C., Blamey, J., Florin, N.H., Al-Jeboori, M.J., Fennell, P.S., 2011. The calcium looping cycle for CO₂ capture from power generation, cement manufacture and hydrogen production. *Chemical Engineering Research and Design* 89, 836–855. <https://doi.org/10.1016/j.cherd.2010.10.013>
- Deckwer, W.-D., Adler, I., Zaidi, A., 1978. A comprehensive study on CO₂-interphase mass transfer in vertical cocurrent and countercurrent gas-liquid flow. *Can. J. Chem. Eng.* 56, 43–55. <https://doi.org/10.1002/cjce.5450560107>
- Derakhshan, S., Pourmahdavi, M., Abdollahnejad, E., Reihani, A., Ojaghi, A., 2013. Numerical shape optimization of a centrifugal pump impeller using artificial bee colony algorithm. *Computers & Fluids* 81, 145–151. <https://doi.org/10.1016/j.compfluid.2013.04.018>
- Dey, S., Ali, S.Z., Padhi, E., 2019. Terminal fall velocity: the legacy of Stokes from the perspective of fluvial hydraulics. *Proceedings of the Royal Society A: Mathematical, Physical and Engineering Sciences* 475, 20190277. <https://doi.org/10.1098/rspa.2019.0277>
- Dijkstra, J.J., Meeussen, J.C.L., Comans, R.N.J., 2004. Leaching of Heavy Metals from Contaminated Soils: An Experimental and Modeling Study. *Environ. Sci. Technol.* 38, 4390–4395. <https://doi.org/10.1021/es049885v>

- Ding, W., Yang, H., Ouyang, J., Long, H., 2016. Modified wollastonite sequestrating CO₂ and exploratory application of the carbonation products. *RSC Adv.* 6, 78090–78099. <https://doi.org/10.1039/C6RA13908F>
- Dodds, W.S., Stutzman, L.F., Sollami, B.J., 1956. Carbon Dioxide Solubility in Water. *Ind. Eng. Chem. Chem. Eng. Data Series* 1, 92–95. <https://doi.org/10.1021/i460001a018>
- Doran, P.M., 2013. Chapter 10 - Mass Transfer, in: Doran, P.M. (Ed.), *Bioprocess Engineering Principles* (Second Edition). Academic Press, London, pp. 379–444. <https://doi.org/10.1016/B978-0-12-220851-5.00010-1>
- Doucet, F.J., 2010. Effective CO₂-specific sequestration capacity of steel slags and variability in their leaching behaviour in view of industrial mineral carbonation. *Minerals Engineering* 23, 262–269. <https://doi.org/10.1016/j.mineng.2009.09.006>
- Drew, T.B., Hoopes, J.W., Cokelet, G.R., 1981. *Advances in chemical engineering*, Advances in chemical engineering. Academic Press, New York London Toronto.
- Duggirala, P.Y., 2005. Formation of Calcium Carbonate Scale and Control Strategies in Continuous Digesters 34.
- Dutta, B.K., 2009. *Principles Of Mass Transfer And Separation Process*. Malaysia.
- Edwards, T.J., Maurer, G., Newman, J., Prausnitz, J.M., 1978. Vapor-liquid equilibria in multicomponent aqueous solutions of volatile weak electrolytes. *AIChE Journal* 24, 966–976. <https://doi.org/10.1002/aic.690240605>
- Eigen, M., 1963. Protonenübertragung, Säure-Base-Katalyse und enzymatische Hydrolyse. Teil I: Elementarvorgänge. *Angewandte Chemie* 75, 489–508. <https://doi.org/10.1002/ange.19630751202>
- Eigen, M., 1954. Methods for investigation of ionic reactions in aqueous solutions with half-times as short as 10⁻⁹ sec. Application to neutralization and hydrolysis reactions. *Discuss. Faraday Soc.* 17, 194–205. <https://doi.org/10.1039/DF9541700194>
- Ekberg, L.E., 1994. Outdoor Air Contaminants and Indoor Air Quality under Transient Conditions. *Indoor Air* 4, 189–196. <https://doi.org/10.1111/j.1600-0668.1994.t01-1-00007.x>
- Emiliawati, A., 2017. A study of water pump efficiency for household water demand at Lubuklinggau 1903, 100003. <https://doi.org/10.1063/1.5011613>
- Fara, A.M.A., 2018. *Experimental and Modelling Studies on Direct Aqueous Carbonation of Thermally Activated Lizardite*. The University of Newcastle, Callaghan, NSW, Australia.

- Fioravante, I., Nunes, R., Acciari, H., Codaro, E., 2019. Films Formed on Carbon Steel in Sweet Environments - A Review. *Journal of the Brazilian Chemical Society* 30. <https://doi.org/10.21577/0103-5053.20190055>
- Fuel Oil Combustion (No. AP 42), 2010. . U.S. Environmental Protection Agency, U.S.
- Galán Sánchez, L.M., Meindersma, G.W., de Haan, A.B., 2011. Kinetics of absorption of CO₂ in amino-functionalized ionic liquids. *Chemical Engineering Journal* 166, 1104–1115. <https://doi.org/10.1016/j.cej.2010.12.016>
- Gerdemann, S.J., O'Connor, W.K., Dahlin, D.C., Penner, L.R., Rush, H., 2007a. Ex Situ Aqueous Mineral Carbonation. *Environ. Sci. Technol.* 41, 2587–2593. <https://doi.org/10.1021/es0619253>
- Goff, F., Guthrie, G., Lipin, B., Fite, M., Chipera, S., Counce, D., Kluk, E., Ziock, H., 2000. Evaluation of ultramafic deposits in the Eastern United States and Puerto Rico as sources of magnesium for carbon dioxide sequestration (No. LA-13694-MS). Los Alamos National Lab. (LANL), Los Alamos, NM (United States). <https://doi.org/10.2172/754045>
- Gopinath, S., Mehra, A., 2018. Carbon dioxide sequestration using steel slag—modeling and experimental investigation, in: *Carbon Dioxide Sequestration in Cementitious Construction Materials*. Elsevier, pp. 65–80. <https://doi.org/10.1016/B978-0-08-102444-7.00004-6>
- Gough, C., 2016. *Carbon Capture and its Storage: An Integrated Assessment*. Routledge.
- Greenberg, S.A., Copeland, L.E., 1960. Thermodynamic Functions for Calcium Hydroxide in Water. *J. Phys. Chem.* 64, 1057–1059. <https://doi.org/10.1021/j100837a023>
- Gruenewald, M., Radnjanski, A., 2016. Gas–liquid contactors in liquid absorbent-based PCC, in: *Absorption-Based Post-Combustion Capture of Carbon Dioxide*. Elsevier, pp. 341–363. <https://doi.org/10.1016/B978-0-08-100514-9.00014-7>
- Gunjal, P.R., Ranade, V.V., 2016. Chapter 7 - Catalytic Reaction Engineering, in: Joshi, S.S., Ranade, Vivek V. (Eds.), *Industrial Catalytic Processes for Fine and Specialty Chemicals*. Elsevier, Amsterdam, pp. 263–314. <https://doi.org/10.1016/B978-0-12-801457-8.00007-0>
- Han, D.-R., Namkung, H., Lee, H.-M., Huh, D.-G., Kim, H.-T., 2015. CO₂ sequestration by aqueous mineral carbonation of limestone in a supercritical reactor. *Journal of Industrial and Engineering Chemistry* 21, 792–796. <https://doi.org/10.1016/j.jiec.2014.04.014>
- Han, S.-J., Yoo, M., Kim, D.-W., Wee, J.-H., 2011a. Carbon Dioxide Capture Using Calcium Hydroxide Aqueous Solution as the Absorbent. *Energy Fuels* 25, 3825–3834. <https://doi.org/10.1021/ef200415p>

- Haque, F., Santos, R.M., Chiang, Y.W., 2019. Using nondestructive techniques in mineral carbonation for understanding reaction fundamentals. *Powder Technology, Expanding Boundaries in Particle Technology: A select collision of papers from the World Congress in Particle Technology VIII* 357, 134–148. <https://doi.org/10.1016/j.powtec.2019.08.089>
- Hariharan, S., Leopold, C., Werner, M.R., Mazzotti, M., 2017. A Two-step CO₂ Mineralization Process. *Energy Procedia* 114, 5404–5408. <https://doi.org/10.1016/j.egypro.2017.03.1684>
- Harris, D.C., Lucy, C.A., 2020. *Quantitative Chemical Analysis*. Austin.
- Hassan-Beck, H.M., 1997. *Process Intensification: Mass Transfer and Pressure Drop for Countercurrent Rotating Packed Beds*. (PhD). University of Newcastle, Newcastle upon Tyne, England.
- Hassanpour, A., Khalili, B., Gholamzadeh, M., 2016. Solubility of calcium hydroxide in water at different temperatures and pressures. 2016 61, 2403–2408.
- Haynes, W.M., 2011. *CRC Handbook of Chemistry and Physics*, 92nd Edition. CRC Press, Hoboken.
- Hemmati, A., Shayegan, J., Bu, J., Yeo, T.Y., Sharratt, P., 2014a. Process optimization for mineral carbonation in aqueous phase. *International Journal of Mineral Processing* 130, 20–27. <https://doi.org/10.1016/j.minpro.2014.05.007>
- Hemmati, A., Shayegan, J., Sharratt, P., Yeo, T.Y., Bu, J., 2014b. Solid products characterization in a multi-step mineralization process. *Chemical Engineering Journal* 252, 210–219. <https://doi.org/10.1016/j.cej.2014.04.112>
- Hendriks, C., de Visser, E., Jansen, D., Carbo, M., Ruijg, G.J., Davison, J., 2009. Capture of CO₂ from medium-scale emission sources. *Energy Procedia, Greenhouse Gas Control Technologies* 9 1, 1497–1504. <https://doi.org/10.1016/j.egypro.2009.01.196>
- Higbie, R., 1935. The rate of absorption of a pure gas into still liquid during short periods of exposure. [New York.
- Hikita, H., Asai, S., Takatsuka, T., 1976. Absorption of carbon dioxide into aqueous sodium hydroxide and sodium carbonate-bicarbonate solutions. *The Chemical Engineering Journal* 11, 131–141. [https://doi.org/10.1016/S0300-9467\(76\)80035-4](https://doi.org/10.1016/S0300-9467(76)80035-4)
- Ho, Iizuka, A., Shibata, E., 2019. Carbon Capture and Utilization Technology without Carbon Dioxide Purification and Pressurization: A Review on Its Necessity and Available Technologies. *Ind. Eng. Chem. Res.* 58, 8941–8954. <https://doi.org/10.1021/acs.iecr.9b01213>

- Ho, M.T., Wiley, D.E., 2016. Liquid absorbent-based post-combustion CO₂ capture in industrial processes, in: *Absorption-Based Post-Combustion Capture of Carbon Dioxide*. Elsevier, pp. 711–756. <https://doi.org/10.1016/B978-0-08-100514-9.00028-7>
- Hu, W., Berdugo, C., Chalmers, J.J., 2011. The potential of hydrodynamic damage to animal cells of industrial relevance: current understanding. *Cytotechnology* 63, 445–460. <https://doi.org/10.1007/s10616-011-9368-3>
- Huijgen, Wouter J. J., Comans, R.N.J., 2005. Mineral CO₂ Sequestration by Steel Slag Carbonation. *Environ. Sci. Technol.* 39, 9676–9682. <https://doi.org/10.1021/es050795f>
- Huijgen, W J J, Comans, R.N.J., 2005. Carbon Dioxide Storage by Mineral Carbonation.
- Huijgen, W.J.J., Comans, R.N.J., Witkamp, G.-J., 2007. Cost evaluation of CO₂ sequestration by aqueous mineral carbonation. *Energy Conversion and Management* 48, 1923–1935. <https://doi.org/10.1016/j.enconman.2007.01.035>
- Huijgen, W.J.J., Ruijg, G.J., Comans, R.N.J., Witkamp, G.-J., 2006. Energy Consumption and Net CO₂ Sequestration of Aqueous Mineral Carbonation. *Ind. Eng. Chem. Res.* 45, 9184–9194. <https://doi.org/10.1021/ie060636k>
- Huntzinger, D.N., Gierke, J.S., Kawatra, S.K., Eisele, T.C., Sutter, L.L., 2009. Carbon Dioxide Sequestration in Cement Kiln Dust through Mineral Carbonation. *Environ. Sci. Technol.* 43, 1986–1992. <https://doi.org/10.1021/es802910z>
- Hutchison, A., 2018. Air entrainment and air-water separation in hydraulic air compressors (PhD). Laurentian University, Ontario, Canada.
- IEA, 2016. *Energy, Climate Change and Environment 2016 Insights*. Paris, France.
- Ionics Instrument Business Group, 2004. Sievers 800 Total Organic Carbon Analyzer Operation and Maintenance Manual URL <https://www.manualslib.com/manual/1302819/Sievers-Toc-800.html> (accessed 2.4.23).
- IPCC, 2007. IPCC, Fourth Assessment Report, Climate change: Synthesis Report. Cambridge.
- IPCC, 2005a. *Carbon dioxide capture and storage*. Cambridge University Press, New York.
- IPCC, 2005b. IPCC special report on carbon dioxide capture and storage, Intergovernmental Panel on Climate Change. Cambridge.
- IPCC, 2001. IPCC, Third Assessment Report, Climate change, Impacts, adaptation and vulnerability. Cambridge.
- Iron and Steel Technology Roadmap Analysis 2022. . IEA. URL <https://www.iea.org/reports/iron-and-steel-technology-roadmap> (accessed 6.1.22).

- Jakobsen, H.A., 2014. Bubble Column Reactors, in: Jakobsen, H.A. (Ed.), *Chemical Reactor Modeling: Multiphase Reactive Flows*. Springer International Publishing, Cham, pp. 883–935. https://doi.org/10.1007/978-3-319-05092-8_8
- Ji, L., Yu, H., 2018. Carbon dioxide sequestration by direct mineralization of fly ash, in: *Carbon Dioxide Sequestration in Cementitious Construction Materials*. Elsevier, pp. 13–37. <https://doi.org/10.1016/B978-0-08-102444-7.00002-2>
- Johannsen, K., Rademacher, S., 1999. Modelling the Kinetics of Calcium Hydroxide Dissolution in Water. *Acta hydrochim. hydrobiol.* 27, 72–78. [https://doi.org/10.1002/\(SICI\)1521-401X\(199902\)27:2<72::AID-AHEH72>3.0.CO;2-H](https://doi.org/10.1002/(SICI)1521-401X(199902)27:2<72::AID-AHEH72>3.0.CO;2-H)
- Johnsen, K., Grace, J.R., Elnashaie, S.S.E.H., Kolbeinsen, L., Eriksen, D., 2006. Modeling of Sorption-Enhanced Steam Reforming in a Dual Fluidized Bubbling Bed Reactor. *Ind. Eng. Chem. Res.* 45, 4133–4144. <https://doi.org/10.1021/ie0511736>
- Julcour, C., Bourgeois, F., Bonfils, B., Benhamed, I., Guyot, F., Bodéan, F., Petiot, C., Gaucher, É.C., 2015. Development of an attrition-leaching hybrid process for direct aqueous mineral carbonation. *Chemical Engineering Journal* 262, 716–726. <https://doi.org/10.1016/j.cej.2014.10.031>
- Kandakure, M.T., Gaikar, V.G., Patwardhan, A.W., 2005. Hydrodynamic aspects of ejectors. *Chemical Engineering Science* 60, 6391–6402. <https://doi.org/10.1016/j.ces.2005.04.055>
- Khodayari, A., 2010. Experimental and theoretical study of carbon dioxide absorption into potassium carbonate solution promoted with enzyme (Master Thesis). University of Illinois at Urbana-Champaign.
- Kimweri, H.T.H., 2001. Enhancement of gas-liquid mass transfer in hydrometallurgical leaching systems (Doctor of Philosophy - PhD). University of British Columbia.
- King, L., 2022. Mineral Properties, Photos, Uses and Descriptions URL <https://geology.com/minerals/> (accessed 4.19.22).
- Kohl, A.L., Nielsen, R., 1997. *Gas Purification*, 5th edition. ed. Gulf Professional Publishing, Houston, Tex.
- Kolawole, T.O., 2019. Intensified Post-Combustion Carbon Capture using a Pilot Scale Rotating Packed Bed and Monoethanolamine Solutions. Newcastle University.
- Kornmüller, U.C.R., 1995. Limestone dissolution kinetics in upflow reactor systems (Master Thesis). University of Cape Town.
- Krevor, S.C.M., Lackner, K.S., 2011a. Enhancing serpentine dissolution kinetics for mineral carbon dioxide sequestration. *International Journal of Greenhouse Gas Control* 5, 1073–1080. <https://doi.org/10.1016/j.ijggc.2011.01.006>

- Krevor, S.C.M., Lackner, K.S., 2011b. Enhancing serpentine dissolution kinetics for mineral carbon dioxide sequestration. *International Journal of Greenhouse Gas Control* 5, 1073–1080. <https://doi.org/10.1016/j.ijggc.2011.01.006>
- Krishna, R., van Baten, J.M., 2003. Mass transfer in bubble columns. *Catalysis Today, Catalysis in Multiphase Reactors* 79–80, 67–75. [https://doi.org/10.1016/S0920-5861\(03\)00046-4](https://doi.org/10.1016/S0920-5861(03)00046-4)
- Kutus, B., Gácsi, A., Pallagi, A., Pálinkó, I., Peintler, G., Sipos, P., 2016. A comprehensive study on the dominant formation of the dissolved $\text{Ca}(\text{OH})_2(\text{aq})$ in strongly alkaline solutions saturated by $\text{Ca}(\text{II})$. *RSC Adv.* 6, 45231–45240. <https://doi.org/10.1039/C6RA05337H>
- Kwon, S., Fan, M., DaCosta, H.F.M., Russell, A.G., 2011. Factors affecting the direct mineralization of CO_2 with olivine. *Journal of Environmental Sciences* 23, 1233–1239. [https://doi.org/10.1016/S1001-0742\(10\)60555-4](https://doi.org/10.1016/S1001-0742(10)60555-4)
- Kwon, T.-H., Cho, G.-C., Santamarina, J.C., 2008. Gas hydrate dissociation in sediments: Pressure-temperature evolution. *Geochemistry, Geophysics, Geosystems* 9. <https://doi.org/10.1029/2007GC001920>
- Lackner, K.S., 2003. A Guide to CO_2 Sequestration. *Science* 300, 1677–1678. <https://doi.org/10.1126/science.1079033>
- Lackner, K.S., Wendt, C., Butts, D.P., Joyce, E.L., Sharps, D.H., 1995. Carbon dioxide disposal in carbonate minerals 18.
- Last, G.V., Schmick, M.T., 2011. Identification and Selection of Major Carbon Dioxide Stream Compositions (No. PNNL-20493, 1019211). <https://doi.org/10.2172/1019211>
- Lc, M., Kalaga, D., Sathe, M., Turney, D., Griffin, D., Li, X., Kawaji, M., Nandakumar, K., Joshi, J.B., 2018. Experimental study and CFD simulation of the multiphase flow conditions encountered in a Novel Down-flow Bubble Colum. *Chemical Engineering Journal* 350. <https://doi.org/10.1016/j.cej.2018.04.211>
- Lee, D., Na, J., Park, D., Lee, J.M., 2021. Bayesian Optimization of Semicontinuous Carbonation Process Operation Recipe. *Ind. Eng. Chem. Res.* 60, 9871–9884. <https://doi.org/10.1021/acs.iecr.1c01322>
- Lemus-Ruiz, S., Rojas-Cervantes, M.L., Flores-Rojas, G., 2012. Solubility of calcium hydroxide in water at different temperatures. *Journal of Chemical & Engineering Data* 3, 781–784.
- Leung, D.Y.C., Caramanna, G., Maroto-Valer, M.M., 2014. An overview of current status of carbon dioxide capture and storage technologies. *Renewable and Sustainable Energy Reviews* 39, 426–443. <https://doi.org/10.1016/j.rser.2014.07.093>

- Li, Hao, Li, Hong, Huang, X., Han, Q., Yuan, Y., Qi, B., 2020. Numerical and Experimental Study on the Internal Flow of the Venturi Injector. *Processes* 8, 64. <https://doi.org/10.3390/pr8010064>
- Li, J., Hitch, M., 2018. Mechanical activation of magnesium silicates for mineral carbonation, a review. *Minerals Engineering* 128, 69–83. <https://doi.org/10.1016/j.mineng.2018.08.034>
- Li, J., Hitch, M., 2017. A Review on Integrated Mineral Carbonation Process in Ultramafic Mine Deposit. *GREE* 2. <https://doi.org/10.15273/gree.2017.02.027>
- Li, J., Hitch, M., 2016. Mechanical activation of ultramafic mine waste rock in dry condition for enhanced mineral carbonation. *Minerals Engineering* 95, 1–4. <https://doi.org/10.1016/j.mineng.2016.05.020>
- Li, Jiajie, Hitch, M., Power, I.M., Pan, Y., 2018. Integrated Mineral Carbonation of Ultramafic Mine Deposits—A Review. *Minerals* 8, 147. <https://doi.org/10.3390/min8040147>
- Li, J., Jacobs, A.D., Hitch, M., 2019. Direct aqueous carbonation on olivine at a CO₂ partial pressure of 6.5 MPa. *Energy* 173, 902–910. <https://doi.org/10.1016/j.energy.2019.02.125>
- Li, Jie, Sun, C., Tao, W., Cao, Z., Qian, H., Yang, X., Wang, J., 2018. Photoinduced PEG deshielding from ROS-sensitive linkage-bridged block copolymer-based nanocarriers for on-demand drug delivery. *Biomaterials* 170, 147–155. <https://doi.org/10.1016/j.biomaterials.2018.04.015>
- Li, Q., 2016. Calcium Carbonate Formation in Energy-Related Subsurface Environments and Engineered Systems (PhD). Washington University in St. Louis, Missouri.
- Li, X., Fan, L., Zhou, M., 2016. Solid-liquid separation of ultrafine Calcium carbonate (CaCO₃) suspensions by using therm-compression filtration technology. *MATEC Web of Conferences* 62, 04007. <https://doi.org/10.1051/mateconf/20166204007>
- Liang, Z. (Henry), Rongwong, W., Liu, H., Fu, K., Gao, H., Cao, F., Zhang, R., Sema, T., Henni, A., Sumon, K., Nath, D., Gelowitz, D., Srisang, W., Saiwan, C., Benamor, A., Al-Marri, M., Shi, H., Supap, T., Chan, C., Zhou, Q., Abu-Zahra, M., Wilson, M., Olson, W., Idem, R., Tontiwachwuthikul, P. (PT), 2015. Recent progress and new developments in post-combustion carbon-capture technology with amine based solvents. *International Journal of Greenhouse Gas Control, Special Issue commemorating the 10th year anniversary of the publication of the Intergovernmental Panel on Climate Change Special Report on CO₂ Capture and Storage* 40, 26–54. <https://doi.org/10.1016/j.ijggc.2015.06.017>
- Liendo, F., Arduino, M., Deorsola, F.A., Bensaid, S., 2022. Factors controlling and influencing polymorphism, morphology and size of calcium carbonate synthesized through the carbonation route: A review. *Powder Technology* 398, 117050. <https://doi.org/10.1016/j.powtec.2021.117050>

- Lito, M.J.G.H.M., Camões, M.F.G.F.C., Covington, A.K., 1998a. Equilibrium in Saturated Ca(OH)₂ Solutions: Parameters and Dissociation Constants. *Journal of Solution Chemistry* 27, 925–933. <https://doi.org/10.1023/A:1022663212760>
- Lito, M.J.G.H.M., Camões, M.F.G.F.C., Covington, A.K., 1998b. Equilibrium in Saturated Ca(OH)₂ Solutions: Parameters and Dissociation Constants. *Journal of Solution Chemistry* 27, 925–933. <https://doi.org/10.1023/A:1022663212760>
- Liu, M., Hohenshil, A., Gadikota, G., 2021. Integrated CO₂ Capture and Removal via Carbon Mineralization with Inherent Regeneration of Aqueous Solvents. *Energy Fuels* 35, 8051–8068. <https://doi.org/10.1021/acs.energyfuels.0c04346>
- Liu, W., Dennis, J.S., Sultan, D.S., Redfern, S.A.T., Scott, S.A., 2012. An investigation of the kinetics of CO₂ uptake by a synthetic calcium based sorbent. *Chemical Engineering Science* 69, 644–658. <https://doi.org/10.1016/j.ces.2011.11.036>
- Liu, Z., 1997. Dissolution kinetics of calcium carbonate minerals in H₂O-CO₂ solutions in turbulent flow: The role of the diffusion boundary layer and the slow reaction $\text{H}_2\text{O} + \text{CO}_2 \rightleftharpoons \text{H}^+ + \text{HCO}_3^-$. 11.
- Liu, Z., Li, X., Mao, Z.-S., Yuan, S., Yang, C., 2020. Hydrodynamics of gas phase in a shallow bubble column from in-line photography. *Chemical Engineering Science* 221, 115703. <https://doi.org/10.1016/j.ces.2020.115703>
- Majumder, S., Kundu, G., Mukherjee, D., 2006. Bubble size distribution and gas–liquid interfacial area in a modified downflow bubble column. *Chemical Engineering Journal* 122, 1–10. <https://doi.org/10.1016/j.cej.2006.04.007>
- Majumder, S.K., 2016a. 1 - Introduction, in: Majumder, S.K. (Ed.), *Hydrodynamics and Transport Processes of Inverse Bubbly Flow*. Elsevier, Amsterdam, pp. 1–24. <https://doi.org/10.1016/B978-0-12-803287-9.00001-1>
- Majumder, S.K., 2016b. 8 - Mass Transfer Characteristics, in: Majumder, S.K. (Ed.), *Hydrodynamics and Transport Processes of Inverse Bubbly Flow*. Elsevier, Amsterdam, pp. 307–381. <https://doi.org/10.1016/B978-0-12-803287-9.00008-4>
- Majumder, S.K., 2016c. 6- Mixing in Inverse Bubbly Flow, in: *Hydrodynamics and Transport Processes of Inverse Bubbly Flow*. Elsevier, pp. 183–253. <https://doi.org/10.1016/B978-0-12-803287-9.00006-0>
- Mandal, A., 2010. Characterization of gas-liquid parameters in a down-flow jet loop bubble column. *Braz. J. Chem. Eng.* 27, 253–264. <https://doi.org/10.1590/S0104-66322010000200004>

- Mandal, A., Kundu, G., Mukherjee, D., 2005. Comparative Study of Two-Phase Gas-Liquid Flow in the Ejector Induced Upflow and Downflow Bubble Column. *International Journal of Chemical Reactor Engineering* 3. <https://doi.org/10.2202/1542-6580.1203>
- Manzano, J., Palau, C.V., Azevedo, B.M. de, Bomfim, G.V. do, Vasconcelos, D.V., 2018. Characterization and selection method of Venturi injectors for pressurized irrigation. *REVISTA CIÊNCIA AGRONÔMICA* 49. <https://doi.org/10.5935/1806-6690.20180023>
- Maroto-Valer, M.M., Fauth, D.J., Kuchta, M.E., Zhang, Y., Andrésen, J.M., 2005. Activation of magnesium rich minerals as carbonation feedstock materials for CO₂ sequestration. *Fuel Processing Technology* 86, 1627–1645. <https://doi.org/10.1016/j.fuproc.2005.01.017>
- Mastercraft 3/4 HP Stainless Steel Irrigation Jet Pump | Canadian Tire, 2022. URL <https://www.canadiantire.ca/en/pdp/mastercraft-3-4-hp-stainless-steel-irrigation-jet-pump-0623424p.html> (accessed 3.8.23).
- Mazzei venturi Injectors 2022. Mazzei. URL <https://mazzei.net/products/venturi-injectors/> (accessed 9.22.22).
- McCabe, W.L., Smith, J.C., Harriott, P., 2005. Unit operations of chemical engineering.
- Millar, D.L., Pourmahdavi, M., 2021. A Method for Pump Manifold Performance Calculations in Hydraulic Air Compressors. *Journal of Fluids Engineering* 143. <https://doi.org/10.1115/1.4049672>
- Millar, D.L., 2014. A review of the case for modern-day adoption of hydraulic air compressors. *Applied Thermal Engineering* 69, 55–77. <https://doi.org/10.1016/j.applthermaleng.2014.04.008>
- Mitchell, M.J., Jensen, O.E., Cliffe, K.A., Maroto-Valer, M.M., 2010. A model of carbon dioxide dissolution and mineral carbonation kinetics. *Proc. R. Soc. A* 466, 1265–1290. <https://doi.org/10.1098/rspa.2009.0349>
- Mokhtari, K., 2016. Chemical alteration of oil well cement with basalt additive during carbon storage application (M.S). Louisiana State University.
- Moler, C., 2022. Stiff Differential Equations Mathworks. URL <https://www.mathworks.com/company/newsletters/articles/stiff-differential-equations.html> (accessed 12.2.22).
- Montes-Hernandez, G., Concha-Lozano, N., Renard, F., Quirico, E., 2009. Removal of oxyanions from synthetic wastewater via carbonation process of calcium hydroxide: Applied and fundamental aspects. *Journal of Hazardous Materials* 166, 788–795. <https://doi.org/10.1016/j.jhazmat.2008.11.120>

- Montes-Hernandez, G., Renard, F., Geoffroy, F., 2006. Kornmüller. *Journal of Crystal Growth* 800, 228–236.
- Morales-Flórez, V., Santos, A., Romero-Hermida, I., Esquivias, L., 2015. Hydration and carbonation reactions of calcium oxide by weathering: Kinetics and changes in the nanostructure. *Chemical Engineering Journal* 265, 194–200. <https://doi.org/10.1016/j.cej.2014.12.062>
- Na, J., Park, S., Bak, J.H., Kim, M., Lee, D., Yoo, Y., Kim, I., Park, J., Lee, U., Lee, J.M., 2019a. Bayesian Inference of Aqueous Mineral Carbonation Kinetics for Carbon Capture and Utilization. *Ind. Eng. Chem. Res.* 58, 8246–8259. <https://doi.org/10.1021/acs.iecr.9b01062>
- Nasser, A., 2010. Factors effects the Growth of Chinese Hamster Ovary (CHO) cell on Microcarriers Culture.
- Nduagu, E., Björklöf, T., Fagerlund, J., Wärnå, J., Geerlings, H., Zevenhoven, R., 2012. Production of magnesium hydroxide from magnesium silicate for the purpose of CO₂ mineralisation – Part 1: Application to Finnish serpentinite. *Minerals Engineering* 30, 75–86. <https://doi.org/10.1016/j.mineng.2011.12.004>
- Neeraj, Yadav, S., 2020. Carbon storage by mineral carbonation and industrial applications of CO₂. *Materials Science for Energy Technologies* 3, 494–500. <https://doi.org/10.1016/j.mset.2020.03.005>
- O'Connor, W., Dahlin, D.C., Rush, G.E., Gerdemann, S.J., Penner, L.R., Nilsen, D.N., 2005. Aqueous Mineral Carbonation: Mineral Availability, Pretreatment, Reaction Parametrics, and Process Studies. <https://doi.org/10.13140/RG.2.2.23658.31684>
- O'Connor, W.K., Dahlin, D.C., Nilsen, D.N., Gerdemann, S.J., Rush, G.E., Walters, R.P., Turner, P.C., 2001a. Research status on the sequestration of carbon dioxide by direct aqueous mineral carbonation. Pittsburgh Coal Conference, University of Pittsburgh, 1249 Benedum Hall, Pittsburgh, PA 15261.
- O'Connor, W.K., Dahlin, D.C., Nilsen, D.N., Walters, R.P., Turner, P.C., 2000. Carbon dioxide sequestration by direct aqueous mineral carbonation.
- O'Connor, W.K., Dahlin, D.C., Rush, G.E., Dahlin, C.L., Collins, W.K., 2001b. Carbon dioxide sequestration by direct mineral carbonation: process mineralogy of feed and products (No. DOE/ARC-2001-027). Society for Mining, Metallurgical, and Exploration, Inc., 8307 Shaffer Parkway, Littleton, CO 80127.
- Opletal, M., Novotný, P., Linek, V., Moucha, T., Kordač, M., 2018. Gas suction and mass transfer in gas-liquid up-flow ejector loop reactors. Effect of nozzle and ejector geometry. *Chemical Engineering Journal* 353, 436–452. <https://doi.org/10.1016/j.cej.2018.07.079>

- Padurean, A., Cormos, C.-C., Agachi, P.-S., 2012. Pre-combustion carbon dioxide capture by gas–liquid absorption for Integrated Gasification Combined Cycle power plants. *International Journal of Greenhouse Gas Control* 7, 1–11. <https://doi.org/10.1016/j.ijggc.2011.12.007>
- Pakzad, P., Mofarahi, M., Lee, C.-H., 2021. Sensitivity analysis of mass transfer and enhancement factor correlations for the absorption of CO₂ in a Sulzer DX packed column using 4-diethylamino-2-butanol (DEAB) solution. *Separation and Purification Technology* 268, 118696. <https://doi.org/10.1016/j.seppur.2021.118696>
- Pallagi, A., Tasi, Á., Gácsi, A., Csáti, M., Pálinkó, I., Peintler, G., Sipos, P., 2012a. The solubility of Ca(OH)₂ in extremely concentrated NaOH solutions at 25°C. *Open Chemistry* 10, 332–337. <https://doi.org/10.2478/s11532-011-0145-0>
- Pallagi, A., Tasi, Á., Gácsi, A., Csáti, M., Pálinkó, I., Peintler, G., Sipos, P., 2012b. The solubility of Ca(OH)₂ in extremely concentrated NaOH solutions at 25°C. *Open Chemistry* 10, 332–337. <https://doi.org/10.2478/s11532-011-0145-0>
- Pan, S.-Y., Chang, E.E., Chiang, P.-C., 2012. CO₂ Capture by Accelerated Carbonation of Alkaline Wastes: A Review on Its Principles and Applications. *Aerosol Air Qual. Res.* 12, 770–791. <https://doi.org/10.4209/aaqr.2012.06.0149>
- Pan, S.-Y., Chiang, A., Chang, E.-E., Lin, Y.-P., Kim, H., Chiang, P.-C., 2015. An Innovative Approach to Integrated Carbon Mineralization and Waste Utilization: A Review. *Aerosol Air Qual. Res.* 15, 1072–1091. <https://doi.org/10.4209/aaqr.2014.10.0240>
- Pan, S.-Y., Chiang, P.-C., Chen, T.-L., Pei, S.-L., 2018. CO₂ Mineralization and Utilization by a High-Gravity Carbonation Process: Past, Present, and Future, in: Cledon, M., Brar, S.K., Galvez, R., Oyanedel-Craver, V. (Eds.), *ACS Symposium Series*. American Chemical Society, Washington, DC, pp. 97–104. <https://doi.org/10.1021/bk-2018-1302.ch005>
- Pan, S.-Y., Chiang, P.-C., Chen, Y.-H., Tan, C.-S., Chang, E.-E., 2014. Kinetics of carbonation reaction of basic oxygen furnace slags in a rotating packed bed using the surface coverage model: Maximization of carbonation conversion. *Applied Energy* 113, 267–276. <https://doi.org/10.1016/j.apenergy.2013.07.035>
- Pan, S.Y., Chiang, P.C., Chen, Y.H., Tan, C.S., Chang, E.E., 2013. Ex Situ CO₂ Capture by Carbonation of Steelmaking Slag Coupled with Metalworking Wastewater in a Rotating Packed Bed. *Environ. Sci. Technol.* 47, 3308–3315. <https://doi.org/10.1021/es304975y>
- Pankow, J.F., 1991. *Aquatic Chemistry Concepts*. CRC Press.
- Parivazh, M.M., Rahmani, M., Akrami, M., 2022. Numerical Investigation on a Liquid–Gas Ejector for Carbon Dioxide Removal Using Amine Solution: Hydrodynamics and Mass Transfer Evaluation. *Applied Sciences* 12, 4485. <https://doi.org/10.3390/app12094485>

- Park, A.-H.A., 2005. Carbon dioxide sequestration: Chemical and physical activation of aqueous carbonation of Mg-bearing minerals and pH swing process (PhD). The Ohio State.
- Park, A.-H.A., Fan, L.-S., 2004. CO₂ mineral sequestration: physically activated dissolution of serpentine and pH swing process. *Chemical Engineering Science*, ISCRE18 59, 5241–5247. <https://doi.org/10.1016/j.ces.2004.09.008>
- Park, S., Song, K., Jeon, C.W., 2016. A study of mineral recovery from waste ashes at an incineration facility using the mineral carbonation method. *International Journal of Mineral Processing* 155, 1–5. <https://doi.org/10.1016/j.minpro.2016.08.001>
- Parmar, R., Majumder, S.K., 2013. Microbubble generation and microbubble-aided transport process intensification—A state-of-the-art report. *Chemical Engineering and Processing: Process Intensification* 64, 79–97. <https://doi.org/10.1016/j.cep.2012.12.002>
- Pavese, V., Millar, D., Verda, V., 2017. Hydraulic gas compressor: a low energy intensive and low cost option for CO₂ capture 16.
- Pavri, R., Moore, G., 2007. Gas turbine emissions and control (No. GRE-4211). GE Energy Services, Atlanta, GA.
- Pei, S.-L., Pan, S.-Y., Li, Y.-M., Chiang, P.-C., 2017. Environmental Benefit Assessment for the Carbonation Process of Petroleum Coke Fly Ash in a Rotating Packed Bed. *Environ. Sci. Technol.* 51, 10674–10681. <https://doi.org/10.1021/acs.est.7b00708>
- Pellegrini, L.A., De Guido, G., Moioli, S., 2020. Design of the CO₂ Removal Section for PSA Tail Gas Treatment in a Hydrogen Production Plant. *Front. Energy Res.* 8, 77. <https://doi.org/10.3389/fenrg.2020.00077>
- Pinto, D., Emonds, R., Versteeg, G.F., 2016. Experimental Determination of Mass-transfer Coefficients and Area of Dumped Packing Using Alkanolamine Solvents. *Energy Procedia* 86, 219–228. <https://doi.org/10.1016/j.egypro.2016.01.023>
- Plummer, L.N., Busenberg, E., 1982. The solubilities of calcite, aragonite and vaterite in CO₂-H₂O solutions between 0 and 90°C, and an evaluation of the aqueous model for the system CaCO₃-CO₂-H₂O. *Geochimica et Cosmochimica Acta* 46, 1011–1040. [https://doi.org/10.1016/0016-7037\(82\)90056-4](https://doi.org/10.1016/0016-7037(82)90056-4)
- Plummer, L.N., Wigley, T.M.L., Parkhurst, L.D., 1978. The kinetics of calcite dissolution in CO₂-water systems at 5 degrees to 60 degrees C and 0.0 to 1.0 atm CO₂. *American Journal of Science* 278, 179–216. <https://doi.org/doi:10.2475/ajs.278.2.179>
- Pohorecki, R., Moniuk, W., 1988. Kinetics of reaction between carbon dioxide and hydroxyl ions in aqueous electrolyte solutions. *Chemical Engineering Science* 43, 1677–1684. [https://doi.org/10.1016/0009-2509\(88\)85159-5](https://doi.org/10.1016/0009-2509(88)85159-5)

- Polettini, A., Pomi, R., Stramazzo, A., 2016. CO₂ sequestration through aqueous accelerated carbonation of BOF slag: A factorial study of parameters effects. *Journal of Environmental Management* 167, 185–195. <https://doi.org/10.1016/j.jenvman.2015.11.042>
- Pourmahdavi, M., Young, S.M., Hutchison, A., Noula, C., Millar, D.L., 2022. Gas absorption in a hydraulic air compressor. Part II: Experimental verification. *Chemical Engineering Science* 117870. <https://doi.org/10.1016/j.ces.2022.117870>
- Power, I.M., Wilson, S.A., Dipple, G.M., 2013. Serpentinite Carbonation for CO₂ Sequestration. *Elements* 9, 115–121. <https://doi.org/10.2113/gselements.9.2.115>
- Rackley, S.A., 2017. Mineral carbonation, in: *Carbon Capture and Storage*. Elsevier, pp. 253–282. <https://doi.org/10.1016/B978-0-12-812041-5.00010-6>
- Ragipani, R., Bhattacharya, S., Suresh, A.K., 2019. Kinetics of steel slag dissolution: from experiments to modelling. *Proc. R. Soc. A* 475, 20180830. <https://doi.org/10.1098/rspa.2018.0830>
- Rakymkul, Y., 2011. solubilities and mass transfer coefficients of gases in heavy synthetic hydrocarbons Liquids (Master Thesis). University of Pittsburgh.
- Rao, A.D., 2010. 2 - Gas-fired combined-cycle power plant design and technology, in: Roddy, D. (Ed.), *Advanced Power Plant Materials, Design and Technology*, Woodhead Publishing Series in Energy. Woodhead Publishing, pp. 32–53. <https://doi.org/10.1533/9781845699468.1.32>
- Rashid, M.I., Benhelal, E., Farhang, F., Oliver, T.K., Rayson, M.S., Brent, G.F., Stockenhuber, M., Kennedy, E.M., 2019. Development of Concurrent grinding for application in aqueous mineral carbonation. *Journal of Cleaner Production* 212, 151–161. <https://doi.org/10.1016/j.jclepro.2018.11.189>
- Rasi, S., 2009. Biogas composition and upgrading to biomethane. JYVÄSKYLÄ.
- Reddy, K.R., Gopakumar, A., Chetri, J.K., 2019. Critical review of applications of iron and steel slags for carbon sequestration and environmental remediation. *Rev Environ Sci Biotechnol* 18, 127–152. <https://doi.org/10.1007/s11157-018-09490-w>
- Reynes, J.F., Mercier, G., Blais, J.-F., Pasquier, L.-C., 2021. Aqueous mineral carbonation of Fe rich olivine by cation complexation using 2,2'-bipyridine; concept validation and parameters optimization. *Applied Geochemistry* 131, 105029. <https://doi.org/10.1016/j.apgeochem.2021.105029>
- Riche, E., Carrie, A., Andin, N., Mabic, S., 2006. High-purity water and pH. *American laboratory* 38, 22–24.

- Robinson, R.A., Stokes, R.H., 2002. *Electrolyte Solutions: Second Revised Edition*, Second Edition, Revised. ed. Dover Publications, Mineola, NY.
- Romano, M.C., Anantharaman, R., Arasto, A., Ozcan, D.C., Ahn, H., Dijkstra, J.W., Carbo, M., Boavida, D., 2013. Application of Advanced Technologies for CO₂ Capture From Industrial Sources. *Energy Procedia* 37, 7176–7185. <https://doi.org/10.1016/j.egypro.2013.06.655>
- Romanov, V., Soong, Y., Carney, C., Rush, G.E., Nielsen, B., O'Connor, W., 2015. Mineralization of Carbon Dioxide: A Literature Review. *ChemBioEng Reviews* 2, 231–256. <https://doi.org/10.1002/cben.201500002>
- Sánchez-Cotte, E.H., Pacheco-Bustos, C.A., Fonseca, A., Triana, Y.P., Mercado, R., Yepes-Martínez, J., Lagares Espinoza, R.G., 2020. The Chemical-Mineralogical Characterization of Recycled Concrete Aggregates from Different Sources and Their Potential Reactions in Asphalt Mixtures. *Materials (Basel)* 13, 5592. <https://doi.org/10.3390/ma13245592>
- Sander, R., 2015. Compilation of Henry's law constants (version 4.0) for water as solvent. *Atmospheric Chemistry and Physics* 15, 4399–4981. <https://doi.org/10.5194/acp-15-4399-2015>
- Sanna, A., Dri, M., Hall, M.R., Maroto-Valer, M., 2012. Waste materials for carbon capture and storage by mineralisation (CCSM) – A UK perspective. *Applied Energy* 99, 545–554. <https://doi.org/10.1016/j.apenergy.2012.06.049>
- Sanna, A., Dri, M., Maroto-Valer, M., 2013. Carbon dioxide capture and storage by pH swing aqueous mineralisation using a mixture of ammonium salts and antigorite source. *Fuel, Advances in Coal Science and Technology, ICCS&T 2011* 114, 153–161. <https://doi.org/10.1016/j.fuel.2012.08.014>
- Sanna, Aimaro, Lacinska, A., Styles, M., Maroto-Valer, M.M., 2014a. Silicate rock dissolution by ammonium bisulphate for pH swing mineral CO₂ sequestration. *Fuel Processing Technology* 120, 128–135. <https://doi.org/10.1016/j.fuproc.2013.12.012>
- Sanna, A., Uibu, M., Caramanna, G., Kuusik, R., Maroto-Valer, M.M., 2014. A review of mineral carbonation technologies to sequester CO₂. *Chem. Soc. Rev.* 43, 8049–8080. <https://doi.org/10.1039/C4CS00035H>
- Saran, R.K., Arora, V., Yadav, S., 2018. CO₂ sequestration by mineral carbonation: a review. *Global Nest Journal* 20, 497–503. <https://doi.org/10.30955/gnj.002597>
- Sazonov, R.V., Serov, A.A., Kuznetsov, V.V., 2014. The solubility of calcium hydroxide in water at high temperatures and pressures. *The Journal of Supercritical Fluids* 94, 64–72.
- Schulze, L.E., 1954. *Hydraulic air compressors*. United States Department of the Interior.

- Seifritz, W., 1990. CO₂ disposal by means of silicates. *Nature* 345, 486–486. <https://doi.org/10.1038/345486b0>
- Sethi, V.K., Dutta, P.S., 2018. An Innovative Approach in Post Combustion Carbon Capture and Sequestration towards Reduction of Energy Penalty in Regeneration of Solvent. *Carbon Capture, Utilization and Sequestration*. <https://doi.org/10.5772/intechopen.78394>
- Singh, J., Dhar, D., 2019. Overview of Carbon Capture Technology: Microalgal Biorefinery Concept and State-of-the-Art. *Frontiers in Marine Science* 6, 29. <https://doi.org/10.3389/fmars.2019.00029>
- Sipilä, J., Teir, S., Zevenhoven, R., 2008. Carbon Dioxide Sequestration by Mineral Carbonation: Literature Review Update 2005–2007 (No. 2008–1). Abo Akademi University, Turku.
- Song, C., Pan, W., Srimat, S.T., Zheng, J., Li, Y., Wang, Y.-H., Xu, B.-Q., Zhu, Q.-M., 2004. Tri-reforming of Methane over Ni Catalysts for CO₂ Conversion to Syngas With Desired H₂/CO Ratios Using Flue Gas of Power Plants Without CO₂ Separation, in: *Studies in Surface Science and Catalysis*. Elsevier, pp. 315–322. [https://doi.org/10.1016/S0167-2991\(04\)80270-2](https://doi.org/10.1016/S0167-2991(04)80270-2)
- Straelen, J. van, Geuzebroek, F., Goodchild, N., Protopapas, G., Mahony, L., 2009. CO₂ capture for refineries, a practical approach. *Energy Procedia* 179–185. <https://doi.org/10.1016/j.egypro.2009.01.026>
- Stumm, W., Morgan, J.J., 1995. *Aquatic Chemistry: Chemical Equilibria and Rates in Natural Waters*, 3rd ed.
- Sun, J., 2010. Carbonation kinetics of cementitious materials used in the geological disposal of radioactive waste (PhD). University College London, London.
- Svarovsky, L., 2000. *Solid-Liquid Separation*. Elsevier.
- Teir, S., 2008. Fixation of carbon dioxide by producing carbonates from minerals and steelmaking slags. Helsinki University of Technology.
- Thonemann, N., Zacharopoulos, L., Fromme, F., Nühlen, J., 2022. Environmental impacts of carbon capture and utilization by mineral carbonation: A systematic literature review and meta life cycle assessment. *Journal of Cleaner Production* 332, 130067. <https://doi.org/10.1016/j.jclepro.2021.130067>
- Trambouze, P., 2004. *Chemical Reactors*. Editions OPHRYS.
- Tsonopoulos, C., Coulson, D.M., Inman, L.B., 1976. Ionization constants of water pollutants. *J. Chem. Eng. Data* 21, 190–193. <https://doi.org/10.1021/je60069a008>
- Tuzson, J., 2000. *Centrifugal pump design*. John Wiley & Sons, New York.

- US Department of Commerce, N., 2022. Global Monitoring Laboratory - Carbon Cycle Greenhouse Gases. URL <https://gml.noaa.gov/ccgg/trends/> (accessed 5.24.22).
- Vacassy, R., Lemaître, J., Hofmann, H., Gerlings, J.H., 2000. Calcium carbonate precipitation using new segmented flow tubular reactor. *AIChE J.* 46, 1241–1252. <https://doi.org/10.1002/aic.690460616>
- Vanderzee, S.S.S., 2016. Carbon sequestration through the production of precipitated calcium carbonate from waste concrete (Master Thesis). Queen's University, Canada.
- Veetil, S.P., Hitch, M., 2020a. Recent developments and challenges of aqueous mineral carbonation: a review. *Int. J. Environ. Sci. Technol.* 17, 4359–4380. <https://doi.org/10.1007/s13762-020-02776-z>
- Veetil, S.P., Hitch, M., 2020b. Recent developments and challenges of aqueous mineral carbonation: a review. *Int. J. Environ. Sci. Technol.* 17, 4359–4380. <https://doi.org/10.1007/s13762-020-02776-z>
- Veetil, S.P., Pasquier, L.-C., Blais, J.-F., Cecchi, E., Kentish, S., Mercier, G., 2015. Direct gas–solid carbonation of serpentinite residues in the absence and presence of water vapor: a feasibility study for carbon dioxide sequestration. *Environ Sci Pollut Res* 22, 13486–13495. <https://doi.org/10.1007/s11356-015-4580-x>
- Velts, O., 2011. Oil shale ash as a source of calcium for calcium carbonate: process feasibility, mechanism and modeling (PhD). TTU Press, Tallinn.
- Velts, O., Uibu, M., Kallas, J., Kuusik, R., 2011a. CO₂ mineral trapping: Modeling of calcium carbonate precipitation in a semi-batch reactor. *Energy Procedia* 4, 771–778. <https://doi.org/10.1016/j.egypro.2011.01.118>
- Velts, O., Uibu, M., Kallas, J., Kuusik, R., 2011b. Waste oil shale ash as a novel source of calcium for precipitated calcium carbonate: Carbonation mechanism, modeling, and product characterization. *Journal of Hazardous Materials* 195, 139–146. <https://doi.org/10.1016/j.jhazmat.2011.08.019>
- Verduyn, M., Geerlings, H., Mossel, G. van, Vijayakumari, S., 2011. Review of the various CO₂ mineralization product forms. *Energy Procedia*, 10th International Conference on Greenhouse Gas Control Technologies 4, 2885–2892. <https://doi.org/10.1016/j.egypro.2011.02.195>
- Vinu, R., 2017. Chapter 4 - Gas–Liquid and Gas–Liquid–Solid Reactors, in: Ravi, R., Vinu, R., Gummadi, S.N. (Eds.), *Coulson and Richardson's Chemical Engineering (Fourth Edition)*. Butterworth-Heinemann, pp. 273–342. <https://doi.org/10.1016/B978-0-08-101096-9.00004-2>

- Wakeman, R., Tarleton, S., 2005. *Solid/ Liquid Separation: Principles of Industrial Filtration*. Elsevier.
- Walke, S., Sathe, V., 2011. Review of Gas Holdup Characteristics of Bubble Column Reactors. *International Journal of Chemical Engineering Research* 3, 71–80. <https://doi.org/10.37622/IJChER/3.1.2011.71-80>
- Wang, C., Xu, Z., Lai, C., Sun, X., 2018. Beyond the standard two-film theory: Computational fluid dynamics simulations for carbon dioxide capture in a wetted wall column. *Chemical Engineering Science* 184, 103–110. <https://doi.org/10.1016/j.ces.2018.03.021>
- Wang, T., Huang, H., Hu, X., Fang, M., Luo, Z., Guo, R., 2017. Accelerated mineral carbonation curing of cement paste for CO₂ sequestration and enhanced properties of blended calcium silicate. *Chemical Engineering Journal* 323, 320–329. <https://doi.org/10.1016/j.cej.2017.03.157>
- Wang, W., Sanku, M., Karlsson, H., Hulteberg, C., Karlsson, H.T., Balfe, M., Stallmann, O., 2017. Medium Temperature Desulfurization for Oxyfuel and Regenerative Calcium Cycle. *Energy Procedia* 114, 271–284. <https://doi.org/10.1016/j.egypro.2017.03.1169>
- Wang, X., Li, H., Dong, J., Wu, J., Tu, J., 2021. Numerical study on mixing flow behavior in gas-liquid ejector. *Exp. Comput. Multiph. Flow* 3, 108–112. <https://doi.org/10.1007/s42757-020-0069-z>
- Wang, X., Maroto-Valer, M.M., 2011. Integration of CO₂ Capture and Mineral Carbonation by Using Recyclable Ammonium Salts. *ChemSusChem* 4, 1291–1300. <https://doi.org/10.1002/cssc.201000441>
- Wang, Y., Zhao, L., Otto, A., Robinius, M., Stolten, D., 2017. A Review of Post-combustion CO₂ Capture Technologies from Coal-fired Power Plants. *Energy Procedia*, 13th International Conference on Greenhouse Gas Control Technologies, GHGT-13, 14-18 November 2016, Lausanne, Switzerland 114, 650–665. <https://doi.org/10.1016/j.egypro.2017.03.1209>
- Wardhaugh, L.T., Solnordal, C.B., Allport, A., 2017. Design and performance of the rotating liquid sheet contactor. *Chemical Engineering and Processing: Process Intensification*, EPIC2015 113, 102–117. <https://doi.org/10.1016/j.cep.2016.09.002>
- Wee, J.-H., 2013. A review on carbon dioxide capture and storage technology using coal fly ash. *Applied Energy* 106, 143–151. <https://doi.org/10.1016/j.apenergy.2013.01.062>
- Whitman, W.G., 1962. The two film theory of gas absorption. *International Journal of Heat and Mass Transfer* 5, 429–433. [https://doi.org/10.1016/0017-9310\(62\)90032-7](https://doi.org/10.1016/0017-9310(62)90032-7)
- Wiechers, H.N.S., Sturrock, P., 1975. Calcium carbonate crystallization kinetics.

- Wiechert, H.N.S., Sturrock, P., 1975. calcium carbonate crystallization kinetics. *Water Research* 9, 11.
- Wiley, D.E., Ho, M.T., Bustamante, A., 2011. Assessment of opportunities for CO₂ capture at iron and steel mills: An Australian perspective. *Energy Procedia* 4, 2654–2661. <https://doi.org/10.1016/j.egypro.2011.02.165>
- Witte, J.H., 1969a. Mixing shocks and their influence on the design of liquid-gas ejectors (PhD). TUDelft.
- Woodall, C.M., McQueen, N., Pilorgé, H., Wilcox, J., 2019. Utilization of mineral carbonation products: current state and potential. *Greenhouse Gases: Science and Technology* 9, 1096–1113. <https://doi.org/10.1002/ghg.1940>
- Wu, N., Wyart, Y., Liu, Y., Rose, J., Moulin, P., 2013. An overview of solid/liquid separation methods and size fractionation techniques for engineered nanomaterials in aquatic environment. *Environmental Technology Reviews* 2, 55–70. <https://doi.org/10.1080/09593330.2013.788073>
- Yadav, S., Mehra, A., 2021. A review on ex situ mineral carbonation. *Environ Sci Pollut Res* 28, 12202–12231. <https://doi.org/10.1007/s11356-020-12049-4>
- Yadav, S., Mehra, A., 2017. Dissolution of steel slags in aqueous media. *Environ Sci Pollut Res* 24, 16305–16315. <https://doi.org/10.1007/s11356-017-9036-z>
- Yan, H., Zhang, J., Zhao, Y., Liu, R., Zheng, C., 2015a. CO₂ Sequestration by Direct Aqueous Mineral Carbonation under Low-Medium Pressure Conditions. *J. Chem. Eng. Japan / JCEJ* 48, 937–946. <https://doi.org/10.1252/jcej.14we381>
- Yi, H., Xu, G., Cheng, H., Wang, J., Wan, Y., Chen, H., 2012. An Overview of Utilization of Steel Slag. *Procedia Environmental Sciences* 16, 791–801. <https://doi.org/10.1016/j.proenv.2012.10.108>
- Yildirim, I.Z., Prezzi, M., 2011. Chemical, Mineralogical, and Morphological Properties of Steel Slag. *Advances in Civil Engineering* 2011, 1–13. <https://doi.org/10.1155/2011/463638>
- Young, S.M., 2017. Simulating air absorption in a hydraulic air compressor. (MAsc) Laurentian University.
- Young, S.M., Pourmahdavi, M., Hutchison, A., Millar, D.L., 2022. Gas absorption in a hydraulic air compressor. Part I: Simultaneous hydrodynamic and mass transfer bubbly flow model. *Chemical Engineering Science* 260, 117871. <https://doi.org/10.1016/j.ces.2022.117871>
- Zahradník, J., Fialová, M., 1996. The effect of bubbling regime on gas and liquid phase mixing in bubble column reactors. *Chemical Engineering Science, Chemical Reaction Engineering:*

- From Fundamentals to Commercial Plants and Products 51, 2491–2500. [https://doi.org/10.1016/0009-2509\(96\)00107-8](https://doi.org/10.1016/0009-2509(96)00107-8)
- Zahradník, J., Fialová, M., Linek, V., Sinkule, J., Řezníčková, J., Kaštánek, F., 1997. Dispersion efficiency of ejector-type gas distributors in different operating modes. *Chemical Engineering Science* 52, 4499–4510. [https://doi.org/10.1016/S0009-2509\(97\)00294-7](https://doi.org/10.1016/S0009-2509(97)00294-7)
- Zeebe, R.E., Wolf-Gladrow, D., 2001a. *CO₂ in Seawater: Equilibrium, Kinetics, Isotopes*, 1st ed. Elsevier Science.
- Zeebe, R.E., Wolf-Gladrow, D. (Eds.), 2001b. Chapter 2 Kinetics, in: *Elsevier Oceanography Series, CO in Seawater: Equilibrium, Kinetics, Isotopes*. Elsevier, pp. 85–140. [https://doi.org/10.1016/S0422-9894\(01\)80003-9](https://doi.org/10.1016/S0422-9894(01)80003-9)
- Zeebe, R.E., Wolf-Gladrow, D.A., Jansen, H., 1999. On the time required to establish chemical and isotopic equilibrium in the carbon dioxide system in seawater. *Marine Chemistry* 65, 135–153. [https://doi.org/10.1016/S0304-4203\(98\)00092-9](https://doi.org/10.1016/S0304-4203(98)00092-9)
- Zevenhoven, R., Wiklund, A., Fagerlund, J., Eloneva, S., In't Veen, B., Geerlings, H., Van Mossel, G., Boerrigter, H., 2010. Carbonation of calcium-containing mineral and industrial by-products. *Front. Chem. Eng. China* 4, 110–119. <https://doi.org/10.1007/s11705-009-0238-x>
- Zhang, Z., Pan, S.Y., Li, H., Cai, J., Olabi, A.G., Anthony, E.J., Manovic, V., 2020. Recent advances in carbon dioxide utilization. *Renewable and Sustainable Energy Reviews* 125, 109799. <https://doi.org/10.1016/j.rser.2020.109799>
- Zheng, P., Zhou, G., Li, W., Zhao, C., Huang, P., Hua, J., Sun, J., Guo, Y., 2022. Characteristics of carbide slag slurry flow in a bubble column carbonation reactor. *International Journal of Chemical Reactor Engineering* 20, 765–778. <https://doi.org/10.1515/ijcre-2021-0204>
- Zhengchao, W., Guo, K., Liu, H., Liu, C., Geng, Y., Lu, Z., Jiao, B., Chen, D., 2020. Effects of bubble size on the gas-liquid mass transfer of bubble swarms with Sauter mean diameters of 0.38–4.88 mm in a co-current up-flow bubble column. *Journal of Chemical Technology & Biotechnology* 95. <https://doi.org/10.1002/jctb.6445>
- Zhu, Y., Frey, H.C., 2012. Integrated gasification combined cycle (IGCC) systems, in: *Combined Cycle Systems for Near-Zero Emission Power Generation*. Elsevier, pp. 129–161. <https://doi.org/10.1533/9780857096180.129>

Appendix A: Experimental data

Averaged set point data for process parameters measured during experiment A.

Set point	Start time (hh:mm:ss)	End time (hh:mm:ss)	Atmospheric pressure (kPa)	Delivery pressure (kPa)	Inlet air temperature (K)	Liquid temperature (K)	Input gas mass flow (g/s)	TOWL (m)
1	15:19:06	16:04:24	100.05	132.10	297.55	289.05	1.031	0.22
2	16:57:15	17:52:38	100.02	132.01	295.65	289.05	1.052	0.21
3	18:41:51	19:33:31	100.02	131.79	294.55	289.15	1.046	0.21
4	20:35:03	21:30:49	100.02	131.94	292.65	288.55	1.052	0.21
5	22:12:38	22:28:37	100.15	132.15	293.05	289.05	1.049	0.21
Average	-	-	100.05	132.00	294.65	288.95	1.046	0.21

Averaged set point data for process parameters measured during experiment B.

Set point	Start time (hh:mm:ss)	End time (hh:mm:ss)	Atmospheric pressure (kPa)	Delivery pressure (kPa)	Inlet air temperature (K)	Liquid temperature (K)	Input gas mass flow (g/s)	TOWL (m)
1	11:49:38	12:53:28	99.13	131.56	302.23	294.1	0.839	0.23
2	13:28:36	14:14:28	99.10	131.63	305.23	294.37	0.870	0.23
3	15:03:50	15:38:17	99.09	131.60	304.48	294.02	0.879	0.23
4	16:09:02	16:34:53	99.07	131.64	304.17	294.46	0.876	0.23
5	17:04:24	17:37:38	99.07	131.63	303.96	294.60	0.872	0.23
6	18:18:14	18:42:50	99.05	131.51	301.37	293.69	0.861	0.23
7	19:08:40	19:25:54	99.03	131.61	300.68	293.61	0.862	0.23
8	20:35:56	20:45:44	99.02	131.70	299.5	293.41	0.852	0.23
Average	-	-	99.08	132.60	302.7	294.03	0.864	0.23

Averaged set point data for process parameters measured during experiment C.

Set point	Start time (hh:mm:ss)	End time (hh:mm:ss)	Atmospheric pressure (kPa)	Delivery pressure (kPa)	Inlet air temperature (K)	Liquid temperature (K)	Input gas mass flow (g/s)	TOWL (m)
1	10:31:08	10:55:41	99.05	131.68	297.23	297.16	0.839	0.24
2	11:43:32	12:15:29	99.07	132.05	299.40	296.88	0.870	0.25
3	12:51:06	13:20:35	99.08	131.82	301.11	296.86	0.879	0.24
4	13:59:54	14:30:32	99.11	131.82	300.94	296.86	0.876	0.24
5	15:11:04	15:44:13	99.13	131.77	301.02	296.85	0.872	0.22
6	16:45:39	17:28:36	99.12	131.69	299.81	296.82	0.861	0.24
7	18:17:41	18:45:57	99.08	131.67	299.85	296.86	0.862	0.24
8	0:01:53	20:26:23	99.07	131.62	298.49	296.76	0.852	0.23
Average	-	-	99.09	131.76	299.73	296.88	0.864	0.24

Averaged set point data for process parameters measured during experiment D.

Set point	Start time (hh:mm:ss)	End time (hh:mm:ss)	Atmospheric pressure (kPa)	Delivery pressure (kPa)	Inlet air temperature (K)	Liquid temperature (K)	Input gas mass flow (g/s)	TOWL (m)
1	11:49:38	12:21:01	98.88	131.55	302.70	2946.87	1.022	0.19
2	13:28:36	14:14:05	98.78	131.36	306.20	297.03	1.040	0.18
3	15:00:47	15:43:50	98.81	131.41	306.99	296.88	1.069	0.18
4	16:51:27	17:22:09	98.75	131.30	305.15	296.82	1.054	0.18
5	18:05:12	18:35:57	98.76	131.21	303.42	296.79	1.092	0.18
6	19:12:50	19:31:15	98.74	131.27	301.92	296.97	1.091	0.18
7	20:08:05	20:26:30	98.70	131.25	300.21	297.03	1.063	0.18
Average	-	-	98.78	131.34	308.80	296.91	1.062	0.18

Averaged gas species concentrations measured at each set point during experiment A.

Set point	Mole fraction measured at AWMH (a) (mol/mol)				Mole fraction measured in off-gas (b) (mol/mol)			
	N ₂	O ₂	Ar	CO ₂	N ₂	O ₂	Ar	CO ₂
1	0.7839	0.2067	0.0088	0.0005	0.7840	0.2067	0.0088	0.0005
2	0.7657	0.2032	0.0086	0.0224	0.7666	0.2034	0.0086	0.0214
3	0.7490	0.2003	0.0085	0.0422	0.7478	0.2001	0.0084	0.0436
4	0.7256	0.1963	0.0082	0.0698	0.7229	0.1959	0.0082	0.0730
5	0.7830	0.2073	0.0089	0.0008	0.7829	0.073	0.0089	0.0009

Averaged gas species concentrations measured at each set point during experiment B.

Set point	Mole fraction measured at AWMH (a) (mol/mol)				Mole fraction measured in off-gas (b) (mol/mol)			
	N ₂	O ₂	Ar	CO ₂	N ₂	O ₂	Ar	CO ₂
1	0.7849	0.2058	0.0088	0.0004	0.7850	0.2058	0.0088	0.0004
2	0.7706	0.2032	0.0087	0.0175	0.7716	0.2034	0.0087	0.0163
3	0.7528	0.2001	0.0085	0.0387	0.7502	0.1996	0.0085	0.0417
4	0.7393	0.1976	0.0084	0.0547	0.7359	0.1969	0.0083	0.0589
5	0.7183	0.1936	0.1936	0.0800	0.71301	0.1925	0.0081	0.0864
6	0.7606	0.2021	0.0086	0.0288	0.7602	0.2020	0.0086	0.0292
7	0.767	0.2033	0.0087	0.0211	0.7676	0.2033	0.0087	0.0204
8	0.7844	0.2063	0.0088	0.0005	0.7843	0.2061	0.0088	0.0008

Averaged gas species concentrations measured at each set point during experiment C.

Set point	Mole fraction measured at AWMH (a) (mol/mol)				Mole fraction measured in off-gas (b) (mol/mol)			
	N ₂	O ₂	Ar	CO ₂	N ₂	O ₂	Ar	CO ₂
1	0.7831	0.2074	0.0089	0.0006	0.7850	0.2058	0.0088	0.0004
2	0.7719	0.2037	0.0087	0.0157	0.7722	0.2037	0.0087	0.0155
3	0.7546	0.1978	0.0083	0.0393	0.7538	0.1976	0.0083	0.0402
4	0.7461	0.1964	0.0083	0.0493	0.7443	0.196	0.0083	0.0514
5	0.7442	0.1949	0.0082	0.0528	0.7415	0.1943	0.0082	0.056
6	0.7755	0.2011	0.0085	0.0149	0.7758	0.2011	0.0085	0.0146
7	0.7159	0.1876	0.0078	0.0887	0.7092	0.1861	0.0077	0.0969
8	0.7879	0.2027	0.0086	0.0009	0.7878	0.2027	0.0086	0.001

Averaged gas species concentrations measured at each set point during experiment D.

Set point	Mole fraction measured at AWMH (a) (mol/mol)				Mole fraction measured in off-gas (b) (mol/mol)			
	N ₂	O ₂	Ar	CO ₂	N ₂	O ₂	Ar	CO ₂
1	0.783	0.2072	0.0089	0.001	0.7832	0.2069	0.0089	0.001
2	0.7724	0.2056	0.0088	0.0132	0.773	0.2057	0.0088	0.0124
3	0.7553	0.2017	0.0086	0.0345	0.756	0.2018	0.0086	0.0336
4	0.7445	0.1993	0.0085	0.0477	0.7445	0.1993	0.0085	0.0477
5	0.721	0.192	0.0081	0.0789	0.7176	0.1912	0.008	0.0832
6	0.7552	0.2004	0.0085	0.0358	0.756	0.2006	0.0085	0.0348
7	0.7834	0.207	0.0088	0.0007	0.7834	0.2069	0.0088	0.0008

Asymptotic CO₂ concentrations measured at separator (d) for each set point of each experiment.

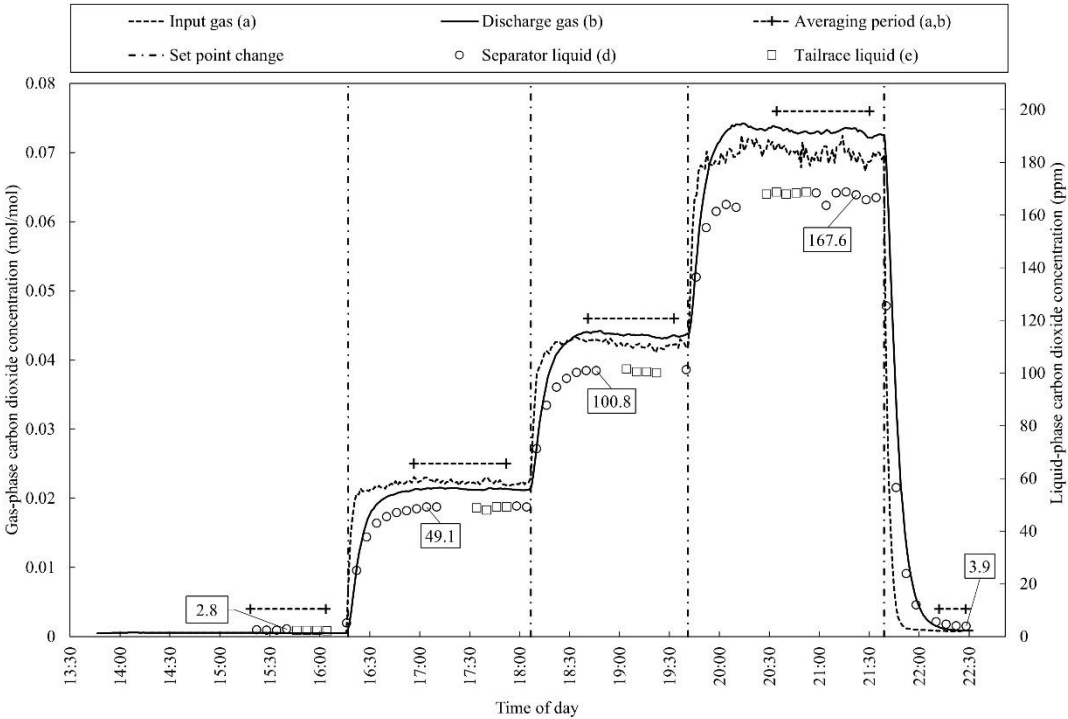
Set point	Separator liquid CO ₂ concentration in experiment (ppm)			
	A	B	C	D
1	2.21	1.51	3	3.31
2	49.13	30.58	28.51	22.13
3	100.1	81.03	73	57.75
4	168.3	112.57	94.71	81.31
5	2.21	165.37	104.41	151.54
6	-	58.3	28.27	62.37
7	-	39.23	182.49	4.11
8	-	3.07	-	-

Asymptotic CO₂ concentrations measured at separator (e) for each set point of each experiment.

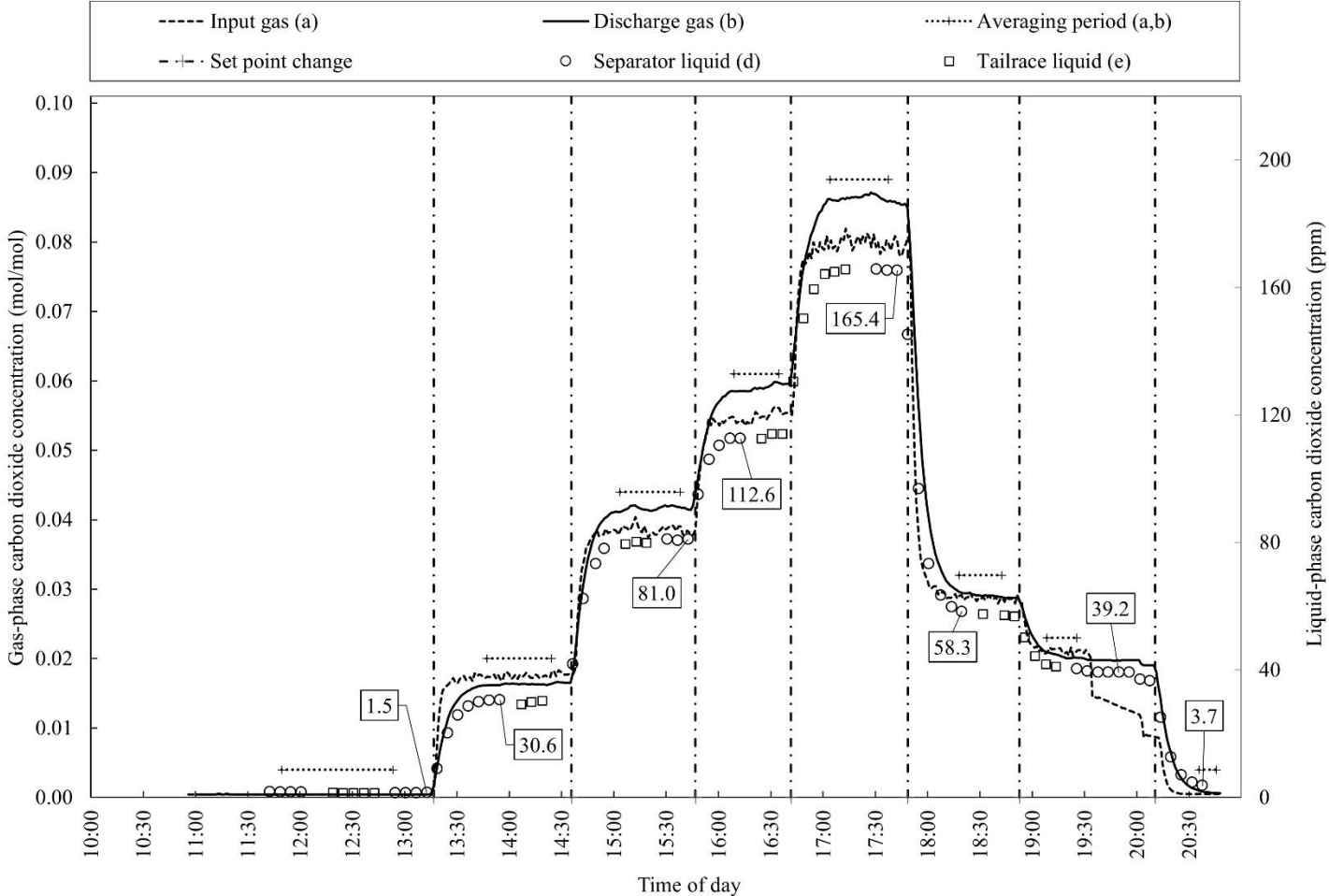
Set point	Separator liquid CO ₂ concentration in experiment (ppm)			
	A	B	C	D
1	2.21	1.43	3.00	3.18
2	49.13	30.29	28.51	21.71
3	100.1	79.93	73	57.75
4	168.3	114.03	94.71	82.24
5	2.21	165.73	104.41	-
6	-	56.83	28.27	-
7	-	41.07	182.49	-
8	-	-	-	-

Appendix B: Time series of experimental observations of CO₂ concentrations for experiments A and B

CO₂ concentration monitored in gas phase and liquid phase during experiment A. Mass flow rates of CO₂ added for each of the 5 set points are as consecutively listed in Table 5-2. For each set point, average steady state concentrations were computed over the time durations indicated by the horizontal dashed lines.



CO₂ concentration monitored in gas phase and liquid phase during experiment B. Mass flow rates of CO₂ added for each of the 8 set points are as consecutively listed in Table 5-2. For each set point, average steady state concentrations were computed over the time durations indicated by the horizontal dashed line



Appendix C: Sample MATLAB Code

This appendix contains the MATLAB code required to run the dynamical kinetic model

```

clear
clc

% Define constant values ----

T      = 21.3 + 273.3;           % Water Temperature
rho_w  = 997.52;                % Density of water (kg/m3)
rho_CO2 = 1.977;                % Density of CO2 (kg/m3)
rho_CaCO3 = 2.3;                % Density of Ca(OH)2 (g/cm3)

P_air  = 1;                     % Atmospheric pressure (atm)
P_CO2  = 1;

Q_g    = 2.53/60;                % air volumetric flow rate (L/S)
Q_CO2  = 0.39/60;                % CO2 volumetric flow rate (L/s)

MW_CO2 = 44;                    % Molecular weight of CO2, (g/mole)
MW_Ca   = 40.078 ;               % Molecular weight of Ca , g/mole
MW_CaOH2 = 74.09 ;              % Molecular weight of Ca(OH)2 , g/mole

V_L    = 3.55;                  % Volume of liquid(L)
V_g    = 0.2355;                % Volume of gas in gas-liquid mixture
V_g2   = 1.1618;                % Volume of gas above liquid

K_H    = 3.5e-2;                % Henry's constant(mol/L.atm)

K1= 10^(-6.3);                  % Equilibrium constant(mol/L)
K2= 10^(-10.3);                 % Equilibrium constant(mol/L)
K_La  = 0.0808;                 % CO2 volumetric mass transfer (1/s)
E     = 30;                      % Enhancement factor
C_CO2 = 12;                      % CO2 concentration in the inlet gas (%)
CaOH  = 0;

% Ksp ----- Nucleation and growth of CaCO3 crystals
Ksp = 10^(2839.319./ T - 171.9065 + 71.595 .* log10(T) - 0.077993 .* T);

Z0 = 0;                          % (g)
Ca  = 0.0203; %0.023;             % Saturated [Ca2+] (mol/L)
CaCO3 = 0 ;                       % (mol/L)
ds  = 2.4 *10^-4;                 % (cm)

% Kw ----- Equilibrium constant for H2O <-----> OH- + H+
Kw=(10.0^(-5839.5/(T)-22.4773*log10(T)+61.2062) * (rho_w^2) ) *10^-6; % (mol/L)^2

OH = 2*Ca;                        % (mol/L)
H  = Kw / OH ;                     % (mol/L)
pH= -log10(H);

```

```

Teta =(K_H *MW_CO2* P_air)/rho_CO2;

Qg_CO2= (Q_CO2*rho_CO2/( MW_CO2));    % CO2 gas flow rat (mol/s)

CO2_g_in = Qg_CO2/Q_g;                % CO2 concentration add into liquid (mol/L)

CO2_aq = 0;                            % (mol/L)
HCO3    = 0;                            % (mol/L)
CO3     = 0;                            % (mol/L)
CO2_g   = K_H*P_CO2;                    % (mol/L)
CO2_gout = 0;                           % (mol/L)

% ----- The initial concentrations -----
Tspan = (0:1000);                        % Time (Second)

% y0 = [ CO2_aq; HCO3; CO3; H; OH]
y0 = [CO2_g ;CO2_aq; HCO3; CO3; H; OH; Ca; CaCO3; CaOH; CO2_gout];

[t,y]=ode23tb(@(t,y)CO2_CaCO3_DxDt_air_solid(t,y,Q_g,CO2_g_in,K_La,Teta,V_L,V
_g,V_g2,E,Z0,ds,Ksp),Tspan,y0); % Solve the system of differential equations

% ----- Plot Figures -----
t=t/60;
pH_f=-log10((y(:,5)));
Y_CO2g_out= y(:,10).* (MW_CO2/rho_CO2)*100;

figure

plot( t,Y_CO2g_out,'LineWidth',1.5)
xlabel('Time(minutes)')
ylabel('Concentration of discharge gas CO_2 (%)')
leg=legend('CO_2out(g)');
leg.ItemTokenSize=[10,10];
title('Concentration Profiles')
grid on

figure
tiledlayout(3,1)
set(gcf,'Position',[0,0.1,800,400])

nexttile
plot(t,y(:,2),'LineWidth',1.5)
xlabel('Time(minutes)')
ylabel('Concentration (mol/L)')
leg=legend('CO_2(aq)');
leg.ItemTokenSize=[10,10];
title('Concentration Profiles')
grid on

nexttile
plot(t,y(:,3),'LineWidth',1.5)
xlabel('Time(minutes)')
ylabel('Concentration (mol/L)')
leg=legend('HCO_3^-');
leg.ItemTokenSize=[10,10];

```

```

title('Concentration Profiles')
grid on

nexttile
plot(t,y(:,4),'LineWidth',1.5)
xlabel('Time(minutes)')
ylabel('Concentration (mol/L)')
leg=legend('CO_3^2-');
leg.ItemTokenSize=[10,10];
title('Concentration Profiles')
grid on

figure
tiledlayout(2,1)
nexttile
plot(t,(-log10((y(:,5)))),'LineWidth',1.5)
xlabel('Time(minutes)')
ylabel('pH')
leg=legend('pH');
leg.ItemTokenSize=[10,10];
title('pH Profiles')
grid on

nexttile
plot(t,y(:,7),t,y(:,8),t,y(:,9),'LineWidth',1.5)
xlabel('Time(minutes)')
ylabel('Concentration (mol/L)')
leg=legend('Ca^2+', 'CaCO_3', 'CaH^+');
leg.ItemTokenSize=[10,10];
title('Concentration Profiles')
grid on
-----
function dYfuncvecdt = CO2_CaCO3_DxDt_air_solid(~,Yfuncvec, Q_g,
CO2_g_in, K_La, Teta, V_L, V_g,V_g2,E,Z0,ds,Ksp)

% Constants -----
CO2_g = Yfuncvec(1); % Concentration of CO2_g
CCO2 = Yfuncvec(2); % Concentration of CO2_aq
CHCO3 = Yfuncvec(3); % Concentration of HCO_3^-
CCO3 = Yfuncvec(4); % Concentration of CO_3^--
CH = Yfuncvec(5); % Concentration of H^+
COH = Yfuncvec(6); % Concentration of OH^-
CCa = Yfuncvec(7); % Concentration of Ca^++
CCaCO3 = Yfuncvec(8); % Concentration of CaCO_3
CCaOH = Yfuncvec(9); % Concentration of CaOH+
CO2_gout= Yfuncvec(10); % Concentration of outlet CO2 (g)

% Reactions & Rate constants -----

k11= 8.4e3; % (L/mol.s)
k12= 2.0e-4; % (1/sec)
k21=6.0e9; % reaction rate constant for

```

```

% HCO3- + OH- -----> CO3-- + H2O, (L/mol.sec)
k22=1.26e6; % (1/sec)
k31=1.4e11; % reaction rate constant
% for OH- + H+ -----> H2O, (L/mol.sec)
k32=1.3e-3; % (mol/L.sec)
k41=2.4e-2; % reaction rate constant for
% CO2 + H2O -----> HCO3+ H+(1/sec)
k42= 5.7e4; % (L/mol.s)
k52 =9e-3 ; % (mol/L.s)
k51 = 1.9e6;
k61 = 400 ; % (L /mol.s)
k62 = 10e6; % (1/ s)
kf = 2.2*10^-8; % (mol/(L.s.cm^2)
kb = 1.9 *10^-3; % (L^2/(mol^2 .s. cm^2)
kf2 = 1958; % (1/ s)
kb2 = 1990; % (L /mol.s) ;%kf2/10^(-1.299)

% Ca(OH)2 and CaCO3 surface area-----

rho_CaCO3 = 2.3; % Density of Ca(OH)2 (g/cm3)
MW_CaOH2 = 74.09 ; % Molecular weight of Ca(OH)2 , (g/mole)

ns = (Z0/(1.333*rho_CaCO3*pi*(ds/2)^3));
V_CaOH = (Z0-((CCa+CCaCO3+CCaOH)*MW_CaOH2*V_L))/rho_CaCO3;
As = ((pi*ns)^(1/3)) * ((6*V_CaOH)^2/3);
I = 0.5* (4*CCa+ CH + COH + CHCO3 +4*CCO3+CCaOH);
F = -0.5*sqrt(I)/(1+1.4*sqrt(I));
f = 10^F;

%% Differential equations -----
dCO2_gdT = (Q_g*(CO2_g_in -CO2_g)-K_La*E*((Teta*CO2_g-
CCO2)*(V_L+V_g)))/V_g;

dCCO2dT = ((K_La*E*(Teta*CO2_g-CCO2)*(V_L+V_g))/V_L) - k11* CCO2* COH
+ k12* CHCO3 - k41* CCO2 + k42* CHCO3* CH;

dCHCO3dT = + k11* CCO2* COH - k12* CHCO3 - k21 *CHCO3* COH + k22* CCO3
+ k41 * CCO2 - k42 * CHCO3* CH + k62* CH - k61 * CCa* CHCO3;

dCCO3dT = + k21* CHCO3* COH - k22* CCO3 -k51* CCa* CCO3 + k52 ;

dCHdT = + k32 - k31 *COH * CH + k41 *CCO2 - k42 * CHCO3 * CH ...
- k62 * CH + k61 * CCa * CHCO3;

dCOHdT = - k11* CCO2* COH + k12* CHCO3 - k21 *CHCO3* COH + k22* CCO3
+ k32 -k31* COH* CH + 1*As *(kf - kb*CCa*(COH^2)*f^6)...
+ kf2 * CCaOH - kb2 * CCa * COH;

```

```

dCCadT = + k52 - k51 * CCa * CCO3 + k62 * CH - k61 * CCa * CHCO3
          + 2*0.01*As * (kf - kb*CCa*(COH^2)*f^6) + kf2 * CCaOH - kb2 *
          CCa * COH;

dCCaCO3dT = - k52 + k51 * CCa * CCO3 - k62 * CH + k61 * CCa * CHCO3;

dCCaOH = - kf2 * CCaOH + kb2 * CCa * COH;

dCO2g_outdT = Q_g*(CO2_g-CO2_gout)/V_g2;

dYfuncvecdt = [ dCO2_gdT ; dCCO2dT; dCHCO3dT; dCCO3dT; dCHdT; dCOHdT;
dCCadT; dCCaCO3dT ;dCCaOH; dCO2g_outdT];

end

```